MECHANICAL DESIGN OF A CUSTOMIZABLE SELF-EXPANDING ENDOVASCULAR STENT

by

Joel C. R. Scott

Submitted in partial fulfillment of the
requirements for the degree of
Master of Applied Science

at

Dalhousie University
Halifax, Nova Scotia
August 2015

Table of Contents

List of Tables

List of Figures

Abstract

Stent migration and endoleak are common failure mechanisms for endovascular repair, both of which can be partially attributed to a lack in understanding of the mechanical properties of endovascular stents. A novel radial extensometer and machine vision system were developed to standardize testing methodology and improve the quality of collected radial force data. A converged finite element model of the radial extensometer was validated using experimental results for an uncovered 12 mm stent. Torsion, t-bending and s-bending moments are all shown to contribute to stent performance. A small batch manufacturing process was developed to produce z-stents that are analogous to those fabricated by industry. A parametric study of stent design parameters showed that a lesser increase in bend diameter was the only characteristic not to be a statistically significant contributor to radial force generation. Results were used to develop radial force prediction software for the design of patient-specific 14 mm stents.

List of Abbreviations Used

AAA	Abdominal Aortic Aneurysm
ADC	Analog-to-Digital Converter
AR	Area Reduction
ASA	American Society of Anesthesiologists
BCC	Body-Centered-Cubic
BCG	Brightness, Contrast and Gamma
BCT	Body-Centered-Tetragonal
BMP	Bitmap
CAD	Computer-Aided Design
CFD	Computational Fluid Dynamics
COM	Communication
CSM	Computational Solid Mechanics
CST	Constant Strain Triangle
CT	Computed Tomography
DAQ	Data Acquisition
EDS	Energy-Dispersive x-Ray Spectroscopy
EMR	Electro-Magnetic-Radiation
EVAR	Endovascular Repair
EVT	Endovascular Technologies
FBD	Free-Body Diagram
FCC	Face-Centered-Cubic
FDA	United States Food and Drug Administration
FE	Finite Element
FFT	Fast Fourier Transform
FSO	Full Scale Output
GUI	Graphical User Interface
ICU	Intensive Care Unit

MAPE	Mean Absolute Percent Error
MPE	Mean Percent Error
NI	National Instruments
OA	Original Area
OSR	Open Surgical Repair
PIV	Particle Image Velocimetry
SE	Standard Error of the Estimate
SEM	Scanning Electron Microscope
SNR	Signal-to-Noise Ratio
UV	Ultraviolet
VI	Virtual Instrument

Acknowledgements

I would like to thank my parents, Anne and Kelly Scott, as well as my family and friends, whose love and motivation supported me through my work and the writing of this dissertation.

Thank-you to my supervisors Drs. Clifton Johnston and Darrel Doman for providing me with their insight as well as my committee members Drs. Ted Hubbard and Chris Lightfoot for their time and effort.

Manufacturing was completed thanks to the generous help of Reg Peters and Angus MacPherson. Thank-you for your immaculate work and training.

This work has been supported by a grant from the Natural Sciences and Engineering Research Council of Canada.

Chapter 1

Introduction

There are currently multiple treatment options available for those who are diagnosed with an abdominal aortic aneurysm (AAA). Preference for a less invasive procedure has lead to a surge in popularity of endovascular repair (EVAR) over open surgical repair (OSR) and promoted the development of a booming industry for stent-graft prosthetics. The majority of current stents used for AAA repair are self-expanding, applying a radial force to artery walls to achieve both strong axial arterial fixation, as well as a strong graft-to-artery seal.

Stent migration due to haemodynamic drag continues to be a common failure mechanism and is the primary cause of stent-graft leakage (endoleak), which can lead to aneurysm rupture. Both failure mechanisms can be partially attributed to deficiencies in stent graft radial spring design. This argument is supported by an investigation into performance of the Zenith (Cook Medical, Bloomingon, IN) self-expanding stainless steel (316L) z-stent by Johnston et al. which discovered that increasing stent diameter corresponded to a decrease in radial force despite higher haemodynamic drag forces in larger arteries[1]. Their findings were successfully reproduced and expanded upon.

The purpose of this work is to both develop investigative tools intended for use in rectifying a deficient understanding of stent mechanics and to characterize the impact of altering stent design parameters on overall stent performance. Results from this analysis are used to predict stent performance based on both varied stent geometry and patient specific characteristics. The Zenith stent-graft is the primary prosthetic studied, however, tools developed in this work can be used to investigate the performance of any available AAA stent-graft.

To quantify radial force generated by various stent diameters and geometries, a novel radial extensometer was developed along with a machine vision system used to calculate the cross sectional area reduction (AR) of stent-grafts during testing. This

system will not only eliminate error contributed by deformation of Mylar used in the radial extensometer but also reduce error by switching from a manually calculated AR to one based on live observation during testing. This system was used to validate and expand upon the radial force results presented by Johnston et al. investigating the impact of stent connections, graft covering and multiple stents on radial force results[1]. Adoption of this radial extensometer by others will establish a consistant platform for comparison of results from study to study.

A finite element model was created to mimic the newly designed radial extensometer. Creating a model that matches the experimental setup makes it possible to validate the simulation against real world values. The completed model provides a tool for analysis of the mechanical function of stents, specifically the mechanisms responsible for radial force generation. Torsion, t-bending and s-bending moments were all shown to contribute to sent radial force generation. It was also demonstrated that both the contact between stent legs and the support rollers of the experimental setup as well as pinching of stent bends between these rollers impact results collected by the radial extensometer. This tool will not only be useful for investigating the relationship between radial force produced by stents and linear force measured by the radial extensometer force gauge but also for simulating novel stent designs.

A small batch method of stent production was developed to manufacture stents which could be used to investigate the impact of altering stent design characteristics (leg length, bend angle, bend radius, wire diameter) on radial force generation. Results from this design parameter study showed that lesser changes in bend diameter had no statistically significant impact on radial force generation. Results gathered for all parameters were used by a new software which was developed to predict stent radial force. Output from this software is calculated based on user input values for design characteristic dimensions as well as patient specific arterial diameter and compliance.

These new tools can be used to collect data required to shift from an inexact stent selection methodology based on a generalized range of prosthetic oversize, to one where stents are developed to generate an ideal radial force for each patient's specific characteristics. There are several other pathologies treated with EVAR that would benefit from the ability to measure and manipulate the radial force generated by their

associated prosthetics. Devices used in more delicate circumstances such as vena cava stenosis and aortic dissection, where it is important to minimize the amount of stress imparted on the weak or weakened vessel, would benefit disproportionately from this ability[2, 3, 4, 5]. Improvements in stent performance will both increase the use of EVAR over OSR and expand the number of possible applications where EVAR can be used. Either of these scenarios will increase the demand for prosthetics and the available market for manufacturers.

AAA stent-grafts are selected based on measurements of the patient's outer arterial diameter. However, while investigating the performance of these prosthetics, diametral oversize is substituted for AR to nondimensionalize collected data, ensuring results are independent of stent diameter. Equations 1.1 and 1.2 can be used to convert from AR to diametral oversize for results presented from this point forward.

$$D_F = 2 * \sqrt{\left[\frac{\left(\pi \frac{{D_O}^2}{2}\right)\left(\frac{100 - AR}{100}\right)}{\pi}\right]} \tag{1.1}$$

$$D_{OVER} = 100 * \left(\frac{D_O}{D_F} - 1\right) \tag{1.2}$$

where

D_F = final diameter (mm)
D_O = original diameter (mm)
AR = area reduction (%)
D_{OVER} = diametral oversize (%)

1.1 Literature Review

Endovascular stents have been used for several years in the management of occlusive (closing off), degenerative (weakening) and aneurysmal (bulging) arterial disease. However, the mechanics of endovascular stents are in need of further investigation.

Generally, an AAA is defined as a section of diseased artery that has ballooned out to over 50 % (1.5 times) the original healthy diameter, or greater than 3 cm diameter total[6, 7, 8]. AAAs are three times more common in men than in women, with an increase in likelihood in those of older age with a history of angina, coronary heart

disease, myocardial infarction or cigarette smoking[7]. Other risk factors include a lower ratio of high-density to low-density lipoprotein cholesterol levels, lower ankle-arm blood pressure ratio, higher creatinine levels, existing carotid stenosis or a greater intima-media thickness of the internal carotid artery[8].

Most AAAs are asymptomatic and are therefore detected by chance. Screening studies in the United Kingdom have estimated the prevalence of asymptomatic AAAs at $1.3 - 12.7\,\%$ depending on age group and how AAAs were defined[9]. For those that are symptomatic (who present with a pulsating sensation in the abdomen, back pain and/or abdominal pain) the rate of AAA in men becomes $\sim$25 per $100,000$ at 50 years of age and $\sim$78 per $100,000$ in those greater than 70 years of age[9]. Melton et al. noted the number of new AAA events from $1971 - 1980$ achieved an incidence of 36.5 per $100,000$ person-years[10].

Preliminary investigations into AAAs revealed steadily decreasing cumulative survival rates following initial diagnosis (Table 1.1). It has become well established that the risk of rupture and mortality increases with aneurysm diameter. Nevitt et al. noted the risk of rupture over five years was $0\,\%$ for patients with an aneurysm less than 5 cm in diameter and $25\,\%$ percent for patients with an aneurysm 5 cm or larger[11]. Furthermore, the National Institute for Health and Care Excellence states that the 5−year survival rate for patients with aneurysms larger than 5 cm was only $\sim$20 %[9]. For those patients who experienced an aneurysm rupture, $38\,\%$ reached the hospital alive and only $19\,\%$ survived overall. For those over the age of 75, the survival rate for those who experienced an aneurysm rupture at home dropped even farther to $5.6\,\%$[12]. Literature has established that it is important to address aneurysms $\geq$5 cm in diameter following diagnosis and to work on identifying aneurysms before rupture.

The first successful attempt at OSR of an aneurysm by removal and replacement of a graft was performed by Dr. Charles Dubost in 1951[15]. An investigation into the success of OSR from $1952 - 1965$ revealed a drop from an overall operative mortality of $14.7\,\%$ for this entire period of observation to $6.3\,\%$ in the last two years of the study[14]. A more recent report on operative mortality of OSR (2007) claims a further reduction to $2.7\,\%$[16]. Mortality and morbidity in the first thirty days following OSR were $1.4\,\%$ and $15\,\%$, with 3 and 5 year survival rates of $93\,\%$ and $88\,\%$ respectively[17,

Table 1.1: Non-surgical survival rates following AAA diagnosis. Standardized values are calculated using age, cardiac status and blood pressure

	Survival Rate (%)			
	Estes, 1950[13]	Szilacyi et al., 1966[14]		
		Standardized		Non-Standardized
Yrs. After Diagnosis	N/A	≤6 cm	>6 cm	All Patients
1	67.0	75.0	47.5	54.3
2	58.1	72.1	25.9	41.3
3	49.2	68.3	12.1	32.1
4	26.9	57.1	8.8	24.0
5	18.9	47.8	6.0	17.2
8	10.0	23.1	0.0	6.1
10	0.0	11.1	0.0	1.5
Deaths Due to Rupture	63.3	-	-	34.9

16].

In the United Kingdom, elective OSR is currently recommended for patients with aneurysms larger than 5.5 cm in diameter or with aneurysms larger than 4.5 cm that have grown by >0.5 cm in the past 6 months. Even though $15 - 20\,\%$ of small aneurysms do not expand substantially, $80\,\%$ have been found to steadily increase in diameter, while $20\,\%$ increase by the required 0.5 cm per year[18]. Patients with aneurysms <4.5 cm in diameter are not generally recommended for surgery but are followed up every $3 - 6$ months as a precaution[7]. Overall, removal of the aneurysm increased the length of survival of patients by 2.1 times, effectively doubling their life expectancy[14].

OSR is still a very invasive procedure which cannot be performed in all cases. Mortality rates may have become very low, however, these rates increase significantly for patients with certain comorbidities. Coronary artery disease, renal failure and chronic obstructive pulmonary disease are of particular concern[19]. It was important that a less invasive approach be developed to treat those that would not be suitable for OSR.

Balloon angioplasty was initially developed by Drs. Charles T. Dotter and Melvin

P. Judkins to address arterial occlusion[20]. Angioplasty proved very effective, however, it was difficult to treat patients who experienced a development of secondary luminal thrombosis following catheter dilatation, as there was no lumen left to dilate[21]. Following an initial investigation into the implantation of tubular grafts by Dr. Dotter, the implantation of coil spring grafts was suggested as a method to treat arterial occlusion and elastic recoil of the vessel with long term patency that avoided the trauma associated with OSR[22]. Along with this investigation came first mention of the possibility of automatically expanding endovascular stents by either stretching out or winding up coil spring stents as a manner of controlling their diameter prior to implantation[21].

Drs. Juan Parodi, Julio Palmaz and Héctor Barone saw the potential to expand intravascular stenting outside of angioplasty as a minimally invasive alternative to OSR. Through their efforts, the first successful treatment of a human AAA was performed in 1990 by transfemoral placement of an aortic graft, anchored using large balloon expandable stents[23, 24, 25, 26, 7].

1.1.1 Current Endovascular Aneurysm Repair

AAA endovascular repair has benefited from several years of evolution and innovation, including the switch from balloon expanded stents as anchors to an interpretation of Dr. Dotter's vision of automatically expanding stents[21]. Arteries undergo diameter changes of $\sim 3-10\,\%$ when subjected to 100 mmHg pulsatile pressure changes, which stiff balloon-expanded stents are not able to track. The switch to self-expanding stents allowed stent-grafts to better match the compliance of vessel walls, enabling better contact at all levels of dilation[27, 28]. The first two self-expanding AAA stent-grafts (AneuRx [Medtronic, Inc., Dublin, Ireland] and Ancure [Guidant Corporation, Marlborough, MA]) gained United States Food and Drug Administration (FDA) approval in September 1999[29]. With the approval of this technology, $2000-2010$ saw the number of AAA treated through EVAR instead of OSR increase from $5.2\,\%$ to $74.0\,\%$[30]. As outlined in Table 1.2, there are currently fourteen self-expanding endovascular stent-grafts approved by the FDA and Conformité Européenne (CE), available on the market today for treatment of AAAs[31, 32, 7, 33, 34]. Several other models including the Lifepath (Edward Lifesciences, Irvine, CA) and Ancure have

Table 1.2: Current self-expanding AAA stent-grafts organized by initial date of approval

Manufacturer	Device	Stent Material	Graft Material	Approval
Medtronic	AneuRx	nitinol	woven polyester	FDA 1999[29]
W.L. Gore & Associates Inc.	Excluder	nitinol	ePTFE	FDA 2002[37]
Cook Medical	Zenith	stainless steel	woven polyester	FDA 2003[38]
Endologix	Powerlink	Co-Cr alloy	woven polyester	FDA 2004[39]
Vasutek	Anaconda	nitinol	woven polyester	CE 2005[40]
Jotec	E-vita	nitinol	woven polyester	CE 2008[41]
Medtronic	Talent	nitinol	woven polyester	FDA 2008[42]
Medtronic	Endurant	nitinol	woven polyester	FDA 2010[42]
TriVascular	Ovation Prime	hardening polymer/ nitinol	PTFE	FDA 2011[42]
Endologix	AFX	Co-Cr alloy	multilayer ePTFE	FDA 2011[43]
Lombard Medical	Aorfix	nitinol	polyester	FDA 2013[42]
Bolton	Treovance	nitinol	woven polyester	CE 2013[44]
Jotec	E-tegra	nitinol	woven polyester	CE 2014[41]
Incraft	Cordis Corp.	nitinol	woven polyester	CE 2014[45]

been discontinued[35, 36].

Self-expanding stents have a number of advantages over their balloon expanded counterparts, most notably of which is their ability to follow pulsatile diameter changes of the vessel wall[46, 47]. A study by Duda et al. showed abrupt and irreversible stent collapse when an ultimate external compressive force or pressure was exceeded for balloon-expanded stents, this did not occur with self-expanding stents[48]. The success of EVAR has been steadily improving and has enabled the treatment of high risk groups due to its less invasive nature when compared to OSR[49, 6]. EVAR has been shown as comparable or superior to OSR for a number of criteria, as shown in Table 1.3. Among several other benefits, patients undergoing EVAR experienced lower short-term mortality rates, lower rates of complication as well as shorter hospital and intensive care unit (ICU) stays than patients undergoing traditional OSR[50]. These significant benefits, despite a higher cost of care, justifies the use of EVAR over OSR for patients with suitable anatomy[30].

EVAR will likely continue to expand in popularity as new prosthetic designs further improve device reliability[51]. Unlike OSR, the risk of rupture following surgery still exists because the aneurysm sac is left inside the patient[52]. Numerical simulations have shown that a securely placed endovascular stent-graft shields the diseased AAA wall from pulsatile blood pressure, keeping the maximum wall stress 20 times below the wall stress value of a non-isolated AAA. Even with this significant improvement, there are still small changes in pressure caused by the interaction of pulsatile cardiac blood flow and the graft membrane, therefore the aneurysm sac itself[53].

EVAR has encountered its own unique and challenging failure mode compared to OSR, called "endoleak". The term "endoleak" was coined by White et al. in 1996 and refers to an endograft seal failure leading to leakage between the vessel wall and stent-graft, resulting in incomplete aneurysm exclusion[54, 55]. Recent data for endoleak following EVAR reveals a prevalence of between $4 - 30\,\%$[56, 57, 58]. Incidence of endoleak has shown generous improvement when compared to older studies (pre$-$2005) involving first and second generation devices, which reported EVAR endoleak rates of $5.4 - 44\,\%$[59, 55, 60, 61, 62, 63, 64, 65]. Several types of endoleak have been characterized and are outlined in Table 1.4. Absence of endoleak types I

Table 1.3: Comparison of OSR and EVAR (American Society of Anesthesiologists [ASA])

Criteria	OSR	EVAR
ASA patient risk level 4 (highest) (%) [59]	17	26
Blood transfusion (ml) [70, 71, 72]	$720 - 1287$	$135 - 408$
Blood lost (ml) [59, 72, 73]	$1596 - 3662$	$500 - 1843$
Surgery time (min) [72, 59]	$188 - 216$	$145 - 186$
ICU utilization (days) [70, 72, 59]	$1.75 - 8.3$	$0.1 - 3.4$
Length of hospital stay (days) [59, 72, 74, 30, 70]	$7 - 20$	$2 - 13$
Anesthesia (hours) [59]	4.9	4.5
Perioperative mortality unruptured (%) [75, 76, 30]	$4 - 4.7$	$0 - 1.3$
Perioperative mortality ruptured (%) [30]	41	27
Early conversion EVAR to OSR $\leq$30 days (%) [77]	N\A	1.5
Early conversion mortality (%) [77]	N\A	12.4
Late conversion EVAR to OSR >30 days (%) [77]	N\A	1.9
Late conversion mortality (%) [77]	N\A	10
30-Day mortality (%) [78, 71, 50]	$1.5 - 5.6$	$0.5 - 3.1$
30-Day morbidity (%) [76]	30	15
1-Year all-cause mortality (%) [78, 50]	12.1	$7.4 - 8.7$
2-Year all-cause mortality (%) [75]	15.2	14.3
3-Year secondary intervention (%) [76]	4.5	16.6
3-Year aneurysm-related mortality (%) [76]	7.6	0
3-4 year all-cause mortality (%) [76, 75]	$15.2 - 33.8$	$34.7 - 42.9$
6.4 Year all-cause mortality (%) [79]	30.1	31.1
6.4 Year secondary intervention (%) [79]	18.1	29.6
Most recent cost estimate unruptured (US$) [30]	$46,935$	$63,623$
Most recent cost estimate ruptured (US$) [30]	$80,574$	$101,928$

and III is required to achieve clinical success as defined by Chaikof et al. in the Reporting Standards for Endovascular Aortic Aneurysm Repair published in 2002[66]. Types II and IV are not desirable but clinical success can still be achieved unless these endoleaks are associated with aneurysm sac expansion[66, 67]. Many type II endoleaks have been shown to resolve spontaneously[68]. The percentage of patients experiencing endoleak may seem quite large, however, endoleak types I and III are significantly less common than types II and IV[68, 62, 64]. In two studies from 2003 by Buth et al. and 2008 by Baril et al., the number of endoleak type I and III cases was found to be between $4.05 - 12\,\%$[60, 58]. A fifth type of endoleak is referred to

as "endotension". This term refers to a scenario where the aneurysm sac continues enlarging and is presumably still pressurized, however, the origin of leakage cannot be determined[69].

Table 1.4: Classification of the five types of endoleak[66]

Type	Cause of Perigraft Flow
I	a) Inadequate seal at proximal end of endograft
	b) Inadequate seal at distal end of endograft
	c) Inadequate seal at iliac occluder plug
II	Flow from visceral vessel (lumbar, IMA, accessory renal, hypogastric) without attachment site connection
III	a) Flow from module disconnection
	b) Flow from fabric disruption
	Minor (<2 mm)
	Major (≥2 mm)
IV	Flow from porous fabric (<30 days after graft placement)
Endoleak of undefined origin	Flow visualized but source unidentified

Endoleak is concerning as it has been shown to cause aneurysm sac expansion in 21.1 % of patients[57]. Type I and III endoleaks have been shown to significantly increase pressure inside the aneurysm sac[80]. Due to the fact that aneurysm wall stress is directly related to sac pressure, these high pressure endoleaks increase the chance of rupture substantially (3.4 % with endoleak vs. 0.25 % without) as a result of a lack of appropriate outflow[60, 80, 81, 82, 53]. Patients with high pressure endoleaks show a larger change in aneurysm volume than those with type II endoleaks, 13.23 % vs. 8.55 %, and a significantly larger change in diameter, 19.8 % vs. 5.4 % respectively[56, 60].

Because of this increase in probability of rupture and therefore mortality, endoleak is widely considered the main problem associated with EVAR failure[7]. In an article published by Buth et al. in 2003, secondary intervention was required in 54 % of patients with endoleak types I and III compared to 6 % in the group without. Conversion to open surgery was also higher in this group at 11 % vs. 0.8 % respectively[60]. In 2006, Brewster et al. published combined EVAR primary outcome statistics for

ten different stent-graft devices as seen in Table 1.5.

Table 1.5: Cumulative probability of primary AAA EVAR outcome measures [78]

Freedom From:	**30 Days**	**1 Year**	**5 Years**	**9 Years**
Rupture	99.9	99.1 ± 0.4	97.6 ± 0.9	94.0 ± 2.2
Aneurysm-related mortality	98.2	97.1 ± 0.6	96.1 ± 0.9	92.6 ± 2.1
Conversion to open	99.5	98.8 ± 0.4	93.3 ± 1.7	93.3 ± 1.7
All-cause mortality	98.2	92.6 ± 1.0	52.1 ± 2.8	16.8 ± 5.7
Reintervention	100	97.2 ± 0.6	78.2 ± 2.6	62.9 ± 7.0

Prevention of endoleak requires an understanding of its etiology. Analysis of previous failures has informed new generations of devices, increased the integrity of new devices and reduced the likelihood of type III endoleaks[83, 84, 85]. After years of device redesign and improvement, type I endoleak has become the primary cause of stent-graft failure. To avoid endoleak, a seal must be achieved between the proximal and distal ends of the stent-graft and the artery wall[66]. Anything that promotes an immediate or delayed failure in fixation will increase the likelihood of endoleak and aneurysm rupture. It's no surprise then that the primary cause for type I proximal endoleak, and therefore late rupture, is stent-graft migration[7, 86, 87, 88, 89].

Stent migration has been defined in reporting standards by Chaikof et al. as being a displacement of the prosthetic of >10 mm relative to anatomical landmarks, or any migration leading to symptoms or requiring therapy[66]. As seen in Table 1.6, multiple investigators have defined migration as >5 mm axial displacement in order to perform a more sensitive analysis. Upstream migration has even been noted in rare cases [90, 91].

According to vanHerwaarden et al., 68 % of re-intervention was performed for fixation related complication and 75 % of these complications occurred at the proximal neck [92]. Although reservations exist as to how prolific EVAR should become for patients with difficult anatomical preconditions and severe comorbidities, improvements and innovation will open this procedure up as a less invasive method of aneurysmal repair for a greater number of people[68].

With the prevalence of stent-graft migration it is important to understand how

Table 1.6: Incidence of migration

Author	Follow-up Time (Months) Mean	Range	Incidence (%) ≥5 mm	≥10 mm	Unknown
Resch et al.[93]	13.0	$1-36$	45.0	–	–
Mohan et al.[94]	19.8	$1-48$	3.0	–	–
Greenberg et al.[95]	–	$24-36$	1.5	–	–
Conners et al.[96]	–	12	7.0	–	–
	–	24	20.4	–	–
	–	36	42.1	–	–
	–	48	66.7	–	–
Sternbergh et al.[63]	–	12	2.3	0.0	–
Lee et al.[97]	17.0	≤36	–	17.5	–
Cao et al.[98]	28.0	$24-46$	–	15.0	–
	–	36	–	27.0	–
Li, Zhonghua[99]	40.3	40.3 ± 7.5	–	16.7	–
Carpenter et al.[65]	11.0	≤52	–	2.2	–
Zarins et al.[100]	30.0	30 ± 11	–	–	8.4
	–	12	–	–	1.4
	–	24	–	–	6.6
	–	36	–	–	18.8

stent-grafts held in place. Several types of stent-grafts have been released to market with different types of fixation. All stents include some amount of passive fixation–it is also required to generate a seal between artery and graft–using only radial force generated by the stent to hold the graft in place. Additionally to this, some stent-grafts have adopted mechanical fixation in the form of hooks or barbs, such as the first commercial aortic endograft, the Endovascular Technologies (EVT) device, and most AAA stent-grafts used today[101]. The radial force required for passive fixation is generated by over-sizing the stent compared to the diameter of the outer vessel wall.

Stent oversize of a minimum 10 % up to 20 % relative to the computed tomography (CT) generated outer aortic neck diameter is credited with the greatest success of EVAR[102, 103]. These values have been used as the oversize benchmark in the majority of modern studies[64, 104, 6, 95]. Even with general agreement in these values, controversy still exists in higher values of oversize. Some studies suggest

that oversizing above 20 %[103], up to 25 %[105] or even as high as 30 %[63, 100] would still be successful while reducing the rate of endoleaks. Others have warned it may be dangerous to oversize more than 20 %. Conners et al. found an increased rate of migration for those with stents >20 % compared to those oversized <20 %, of 29.2 % and 18.6 % respectively[96]. It has become widely accepted that stent-graft oversize of more than 30 % can lead to future complications such as vessel growth and remodeling[106]. Of particular concern as a contributor to the likelihood of stent-graft migration and type I endoleak is secondary proximal neck dilation following initial dilation during introduction of the prosthetic[93, 105, 63, 96, 98]. Certain reports question whether this dilation is caused by stent oversize or a continuation of the disease process itself, however, it is likely due to a combination[107, 93]. In a study by Sternbergh et al., device oversizing >30 % was associated with a ∼16x increased risk of AAA expansion (9.5 % at >30 % oversize vs. 0.6 % at ≤30 %) at 24 months and a ∼14x increase in risk of device migration greater than 5 mm (14 % at >30 % oversize vs. 0.9 % at ≤30 %)[63]. Radial force may be responsible for passive fixation of AAA stent-grafts, however, indefinitely increasing oversize and radial force until fixation is achieved will likely damage the artery and induce arterial remodeling. Over-sizing has also been shown to introduce folds into prosthetic grafts, thereby promoting endoleak by compromising the seal created between graft and artery wall[47].

The largest contributor to stent-graft migration is due to axial haemodynamic drag force, and its ability to overcome fixation forces generated by the stent-graft device. Average passive fixation forces were found to be between $3.97 - 5.41$ N for stents with 24 mm proximal and 12 mm distal necks using passive proximal fixation and oversizing of 16.67 %[108]. On the other hand, the axial component of proximal migration force ranged between $2.96 - 5.5$ N for a passively fixed stent-graft of the same dimensions[88, 109, 110]. Several other studies have found drag forces of between 2.5 N and 16 N for AAA stent-grafts of various diameters[101, 111, 109]. Resch et al. determined that a Zenith stent with mechanical fixation barbs that penetrate the entire aortic wall require 24 N to dislodge, compared to a passively fixed Talent stent-graft, which required only 4.5 N[112]. It is quite clear that passive stent-graft contact and biological incorporation is generally inadequate to withstand the forces of pulsatile blood flow through the prosthetic, therefore, including mechanical fixation

is important to ensuring fixation. Hypertension, arterial tortuosity, arterial diameter and a large ratio between proximal aortic diameter and smaller distal iliac diameters are particularly notorious for increasing drag force[53, 113, 94, 73, 114, 100, 47, 6, 109, 88]. Improved proximal fixation (mechanical and/ or passive), friction, longitudinal stiffness and arterial in-growth will all help to reduce migration and stent-graft failure[103, 115, 93, 88, 109, 6, 53, 112, 101]. Proximal aortic fixation length is typically shorter in patients who experience migration compared to those that don't, $1.6 - 2.4\,\text{cm}$ vs. $2.3 - 3.3\,\text{cm}$ respectively[100, 63]. In cases where migration was successfully avoided, aneurysm sac regression following EVAR was compelling, with diameter reductions of $-0.09 \pm 4.90\,\text{mm}$ and $-1.48 \pm 2.56\,\text{mm}$ at one and two years respectively[97].

An unfortunate part of having oversize become the standard for determining required fixation force is that the mechanical design of all stent-grafts is slightly different. Each brand of stent will produce a different radial force and distribution of force at equal levels of constriction. The unique arterial compliance of each patient will also affect the final diameter and oversize achieved following deployment of the prosthetic. It would be wise for future research to investigate the relationship between stent-graft type, oversize, radial force generated and radial force required for fixation and seal. Previous research by Johnston et al. found that in stent-grafts of increasing diameter, radial force at similar levels of constriction did not increase as would be expected. It was found that smaller stents exerted greater radial forces than larger stents at similar levels of constriction. Larger arteries experience larger flow and haemodynamic drag and would logically require higher radial forces than smaller arteries for passive fixation[1].

The Cook Medical, Zenith AAA stent-graft was selected for further investigation. As is reflected in Table 1.7, its performance is similar if not superior to the majority of competitors and it benefits from a very simple design. The Zenith stainless steel 316L stent is easy to work with, analyze and reproduce making it a logical starting point. Faries et al. noted that there was no significant difference between device types in freedom from aneurysm rupture, with an overall 98.7 % freedom at 24 months follow-up[19].

Table 1.7: Performance of Cook Medical's Zenith stent-graft[19]

Variable	%
Implant success	99.3
Perioperative conversion to standard open repair	0.8
Device migration	1.4
Reduction in AAA diameter	58.0
AAA diameter unchanged	33.0
Endoleak at 30 days	15.0
Endoleak at 4 years	4.0
Late aneurysm rupture	0.6

1.1.2 Current Modeling of z-Stent Mechanics and Radial Force

Prasad et al. submitted a very complete computational fluid dynamics (CFD) and computational solid mechanics (CSM) investigation in 2012, of nitinol z-stents expanding inside a thoracic aneurysm. Their goal was to investigate the mechanics of endograft stability considering a range of endograft sizes (length and degree of oversizing). Results include the impact of fixation length, aortic curvature, friction between device and aorta, and endograft oversizing on endograft stability. This work and many others investigate important characteristics involved in the interaction between stent-grafts and artery walls, as well as factors governing positional stability of stent grafts in-vivo under haemodynamic loading.

Current numerical analyses of AAAs and EVAR focus on several topics. These include: stent-graft oversize, arterial remodeling due to the interaction of stent-grafts and artery walls[116, 117, 118, 119]; the prediction of aneurysm rupture based on sac pressure and wall stress/ strain[120, 53, 121, 122, 123, 124, 125, 126]; haemodynamics, drag, migration and endoleak[53, 110, 127, 128, 111, 129, 103]; bending and kinking[130, 131, 132]; and finally thrombus and calcification[133, 106, 104, 103]. Some significant results have already been extracted from these studies, for example, Li and Kleinstreuer modeled a stented AAA and were able to show that a securely placed endovascular stent keeps the maximal aneurysmal wall stress 20 times below the wall stress value in a non-stented AAA[53]. Another simulation by Molony et al. found a 92 % decrease in peak wall stress following EVAR[128].

There is a significant lack of investigation into the mechanical functionality of stent-grafts of any kind, let alone the z-type stent graft being studied and the mechanisms by which they produce their radial force[134, 104, 135]. Developing the ability to manipulate the fixation (radial) force to an ideal value for each individual stent and patient instead of relying on inexact "rule-of-thumb" oversizing of $10 - 20\,\%$ will undoubtedly improve the short and long-term success rate of EVAR today.

Some existing analytical works make assumptions in regard to how force is generated in the stent. For example, Wang et al. examines a wire mesh stent as an equivalent thin-walled pressure vessel[136]; and Vad et al. use interference fitting theory for the contact pressure that develops at the interface of two concentric cylinders to experimentally validate their finite element model investigating the coefficient of friction for self-expanding stent-grafts[115]. Future work would benefit from a more complete investigation into the mechanics of stent force generation, avoiding assumptions made in previous works. For example, the assumption made by Snowhill et al. that the mechanical reaction of a single stent bend could be extrapolated to get the radial force of a complete stent, or Fallone et al. assuming that Hooke's law could be used to determine radial force[137, 138, 139].

The design of endovascular devices has progressed for years using a trial and error methodology focused on experimental testing, however, computational design has seen a relatively slow adoption in medical device design[135, 140]. There is a minimal amount of literature that exists examining the mechanical properties, radial force and method of force generation for stainless steel self-expanding endovascular z-stents intended for AAAs. The majority of studies focus on super-elastic nitinol instead of stainless steel[116, 117, 133, 141, 138]. In 2012 and 2013, Nematzadeh et al. agreed that a numerical investigation of the z-shaped open-cell nitinol self-expanding stent was missing in literature, their investigations focused on the effect of material properties and crimping on mechanical performance of these stents[142, 141]. They do not investigate radial forces or the manner by which the stresses they report are created, however, their work does discuss changes in mechanical behavior under different conditions. Unfortunately, as is the case for the majority of works, they present no research on the performance of stainless steel stents.

Focusing more on radial force production and experimental validation, certain

other studies introduce material of interest. Kleinstreuer et al., investigate the radial force generated as a nitinol stent is constricted and compare their results to experimental values[138]. Although their work does not focus on z-stents or stainless steel, they manage to contribute significant information on the location of maximum stress and strain of their investigated nitinol design, as well as fatigue life and the interaction of stent, graft and artery wall.

DeBock et al. examines linear and radial compression tests experimentally and numerically for nitinol and stainless steel AAA z-stents[143]. Although their methodology and the trend of their radial force data is similar to experimental work of Johnston et al., it is difficult to compare their findings or to glean meaningful results as neither study investigates a single, uncovered stent wire, or even stents of similar composition[1]. Each investigator publishes values for prosthetics with different numbers and diameters of graft covered stents at the same time. DeBock et al. did however, publish values for proximal and distal neck radial force during unloading which are presented as experimental results in Section 1.1.3.

Aside from change in radial force and stent properties due to stress-induced transformation of austenite to martensite in super-elastic nitinol, it has not been possible to find any investigations related to computationally investigating the mechanism and resulting magnitude of radial force generation in z-type self-expanding endovascular stents[142]. No resources other than that by DeBock et al. have been found on modeling the mechanics of stainless steel stents. With the apparent difficulty in comparing results from different studies it has become clear why Abel et al. agreed that while significant progress had been made in endovascular graft testing, continued collaboration among all interested parties would provide the most benefit to future designs, predictability and device performance[140].

1.1.3 Current Experimental Options for Measuring the Radial Force of Self-Expanding Stent-Grafts

Over the years the FDA has tried several times to standardize methods of testing and reporting during the pre-clinical stage of stent-graft development, however, significant variation in presented results and method of data collection still exist[144, 66, 67]. There are several different experimental techniques that have been used to collect

radial force data in past investigations.

As seen in Figure 1.1, in 1988 Fallone et al. used a "tire wrap" method to collect radial force data for analysis[139], which has since been mimicked by several others[145, 146, 147, 148, 145, 137]. In this method, a nonelastic strip remains fixed to either a wall or force gauge on one end, while the opposite end is attached to either weights or a force gauge. The advantage of this system is that a uniform radial load is exerted upon the stent. The most recent use of this style of device was by Bashar et al. in 2003. Fallone et al., Sawada et al. and Snowhill et al. measured the radial force of individual stainless steel stents. Their results evaluated the effect of changing different design parameters on measured radial force. Fallone et al. characterized the stent with respect to its wire diameter, length and radius. Sawada et al. investigated the impact of wire diameter, number of bends, stent diameter and length of stent, while Snowhill et al. examined the impact of wire diameter, leg length and number of bends on radial force. These investigations are performed on lab made copies of first generation z-stents. They all found that stents had higher radial force if they were made with larger wire diameter, while Fallone et al. and Sawada et al. found higher radial force in stents of shorter length. It will be interesting to compare results from analysis of these first generation stents to those developed as part of this thesis.

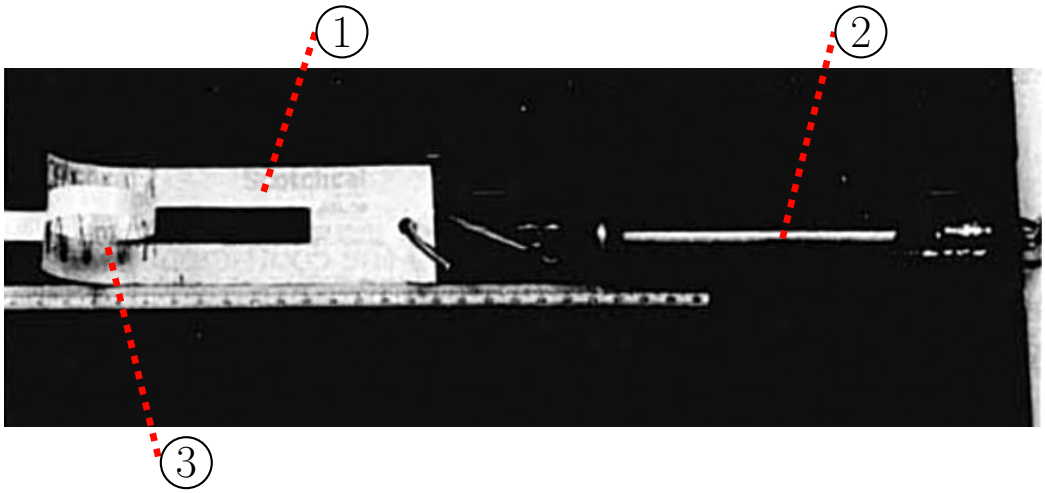

Figure 1.1: "Tire wrap" experimental measurement apparatus[139]: 1 - nonelastic working material, 2 - force gauge, 3 - stent inside "tire wrap" loop

A compression test was first used by Lossef et al. in 1994 with the goal of creating a standardized testing method to compare experimental and commercially available

stents [149]. Several other groups have introduced refinements to this technique[101, 145], the most recent of which was published by Dyet et al. in 2000 (Figure 1.2)[150]. In general, this technique is comprised of a stent fixed to the top of a weigh scale or force gauge and a micrometer which presses down on top of the stent, compressing it during testing, while measuring positional displacement. Johnston et al. expressed concern that point load compression analysis was not representative of loading types experienced in vivo[1].

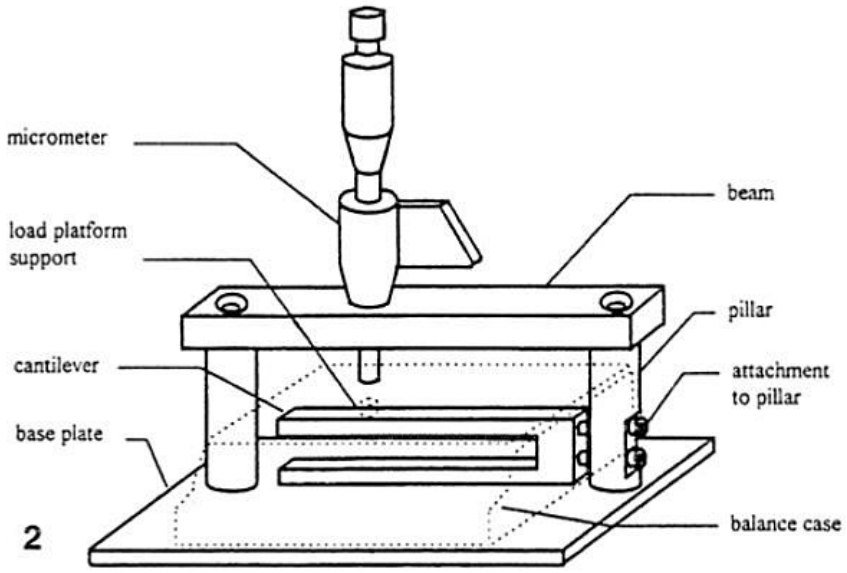

Figure 1.2: Diagram of the balance and micrometer used in the vertical compression test[150]

A hydrostatic method of radial strength testing (Figure 1.3) has been used by several parties, most recently, by Johnston et al. in 2010[151, 152, 153, 1]. This method uses a pressure chamber with a hollow, circular central section that is exposed to atmosphere. This tubular section is made of flexible tubing that will dilate and constrict based on the hydrostatic pressure of the chamber. The hydrostatic pressure required to constrict the stent as well as stent diameter are recorded.

A radial constriction technique was introduced by Duda et al. in 2000 with variations implemented by several others (Figure 1.4), most recently Voute et al. in 2011[48, 1, 154, 155]. The general functionality of this system is the same for all iterations. One end of a film sheet is anchored to a load cell and extends from the load cell to wrap around a leading roller, around the stent being tested, then passes

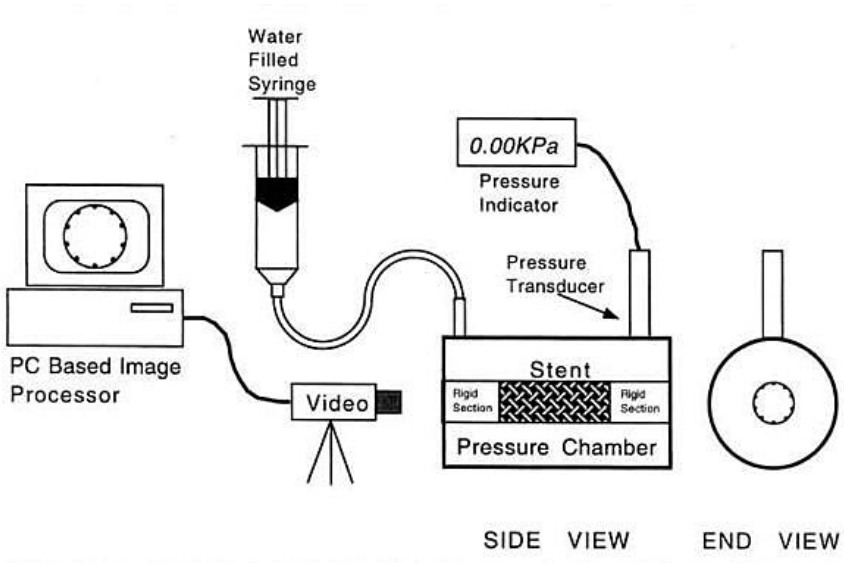

Figure 1.3: Schematic of hydrostatic system schematic and components used to measure stent compliance[151]

around a second roller where its other end is anchored. The stent is constricted by displacing one of the anchors, which tightens the Mylar sheet, constricting the stent. The stent is constricted to a set value of cross-sectional AR before the anchor changes direction and allows the stent begins expanding. As the stent expands, pressure exerted on the Mylar sheet is converted to a linear force which passes down the Mylar to the load cell where it is recorded. Johnston et al. investigated certain design parameters for stainless steel stents such as the effect of stent diameter, placing stent wires in series and overall covered stent length on radial force for stents of different brands[1]. These results are the primary source of comparative data for multi-stent radial force data presented in Chapter 2. A revised version of this apparatus is used for the collection of all experimental radial force data, due to its advantages in ease of control, system stability, affordability, reliability and the ability to collect meaningful, repeatable results.

Another type of radial force testing apparatus is manufactured by industry. The device by Machine Solutions Inc. (Flagstaff, Az) seen in Figure 1.5, uses a constricting iris design to crimp and analyze stents. Vorwerk et al. used a rudimentary version of this collapsing iris design during their work collecting radial force data in 1994[156]. Using an industrial device manufactured by MPT Europe (Leek, The Netherlands)

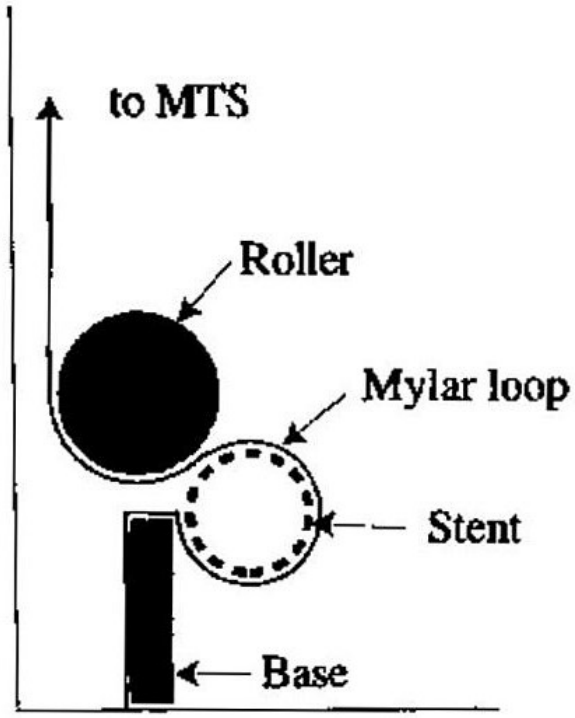

Figure 1.4: Preliminary radial extensometer[48]

similar to the one seen in Figure 1.5, DeBock et al. measured the radial force exerted by the proximal and distal openings of a 20 % oversized stainless steel z-type stent to be 4.5 N and 5.5 N respectively; as well as 5.2 N and 10.3 N respectively for 50 % oversize. This Zenith Flex device had an overall diameter of 30 mm with a proximal wire diameter of 0.45 mm and a distal wire diameter of 0.35 mm. Unfortunately, these results report values for a combination of the first two wire segments of a full, bifurcated AAA stent graft and not of one individual segment which makes comparison with other results difficult[143].

A final experimental setup was used by Snowhill et al. in 2001. Their experimental setup consisted of a silicone elastomer tube filled with a continuous bead of mercury that was placed in a wheatstone bridge circuit connected to an operational amplifier circuit (Figure 1.6)[137]. The diameter change is determined from the voltage change that occurs when a stent expands in the Whitney gauge due to differing resistance of the thinned out mercury. Because material properties of the silicone tube are known, a radial force can be calculated.

Preliminary investigations into the effect of altering z-stent design parameters have

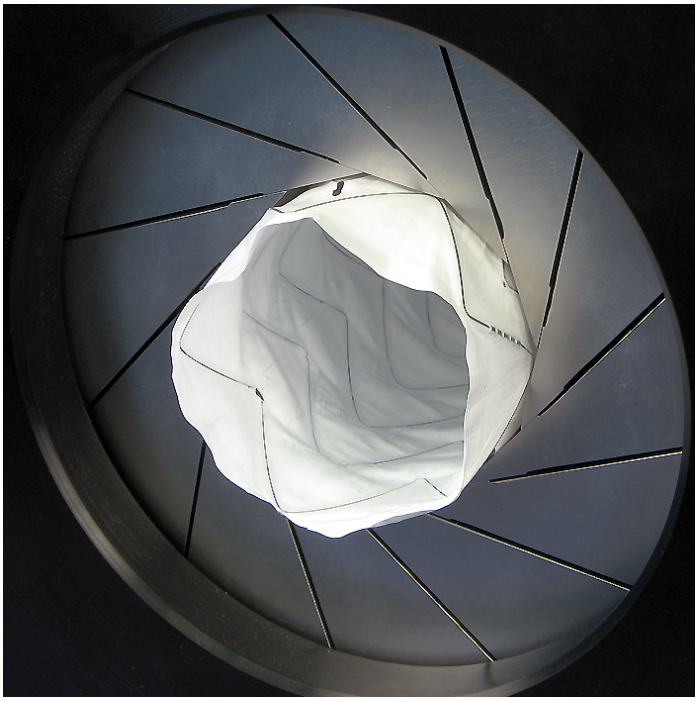

Figure 1.5: Industrial testing equiptment - iris[157]

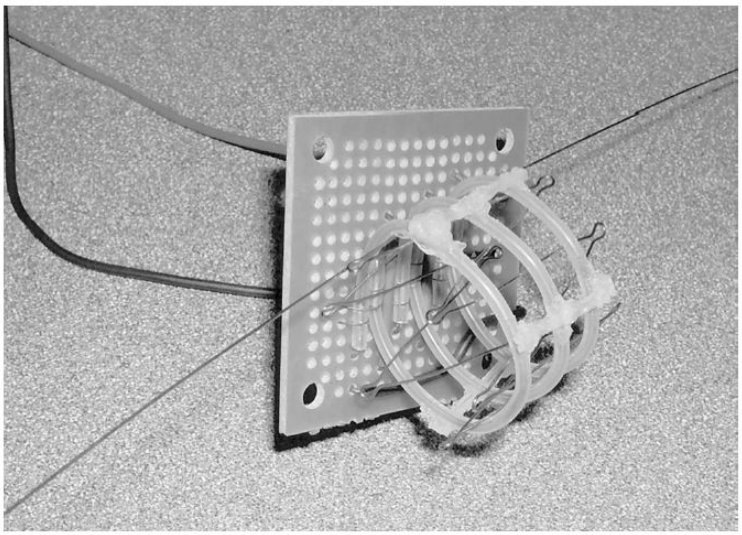

Figure 1.6: A Whitney strain gauge with a z-stent inserted into its center. This gauge is composed of silicone elastomer tubing containing a mercury bead[137]

been pursued. There is very little complete data examining the effect of changing design criteria such as leg length, bend radius, wire diameter and bend angle on

radial force generation for individual stent wire sections of newer generations of self-expanding z-stents. More work is required to analyze the impact of altering stent geometry on stent mechanics and radial force generation.

Chapter 2

Radial Extensometer

A radial extensometer was designed and sized specifically to measure radial force exerted by endovascular stents at different levels of expansion. This system was developed by further refining the measurement process used by Johnston et al., which was initially developed by Duda et al.[1, 48]. This novel device was designed to integrate position, force and machine vision, automatically controlling data collection and post-processing based on user input. The completed apparatus has been successfully used for extensive data collection proving itself as a useful tool in the investigation of endovascular stent-grafts. Adoption of this system by other groups would provide a common platform for analysis of prosthetics and comparison of results.

2.1 Methods

Positional control and data acquisition for this system is performed by a Zaber (Vancouver, BC, Canada) T-LSR150A linear slide with built-in controller[158]. Force data collection is performed by an Omega (Laval, QC, Canada) LCM703, 50 N force transducer, while a Logitech (Newark, CA, USA) C920 webcam is used to collect dynamic measurement of stent AR[159, 160]. The webcam is used at a resolution of 800 x 600 pixels with a focal distance of 55 mm and a field of view of 38.06 x 28.55 mm. All experimental data acquisition (DAQ) is automated and controlled by National Instruments (NI) (Vaudreuil-Dorion, QC, Canada) LabVIEW and the software packages available for each component. NI-DAQmx and the NI9237 Simultaneous Bridge Module for force gauge control; machine vision software package NI-IMAQdx for collection of AR data from the webcam; as well as Zaber drivers for LabVIEW based linear slide control and position data collection[161]. All post-processing and data analysis is completed using Python(x,y), a scientific-oriented Python distribution[162].

The radial extensometer, as seen in Figure 2.1, is composed of a 0.001 in sheet of Mylar polyester film connected to a 50 N load cell at one end and anchored to a linear

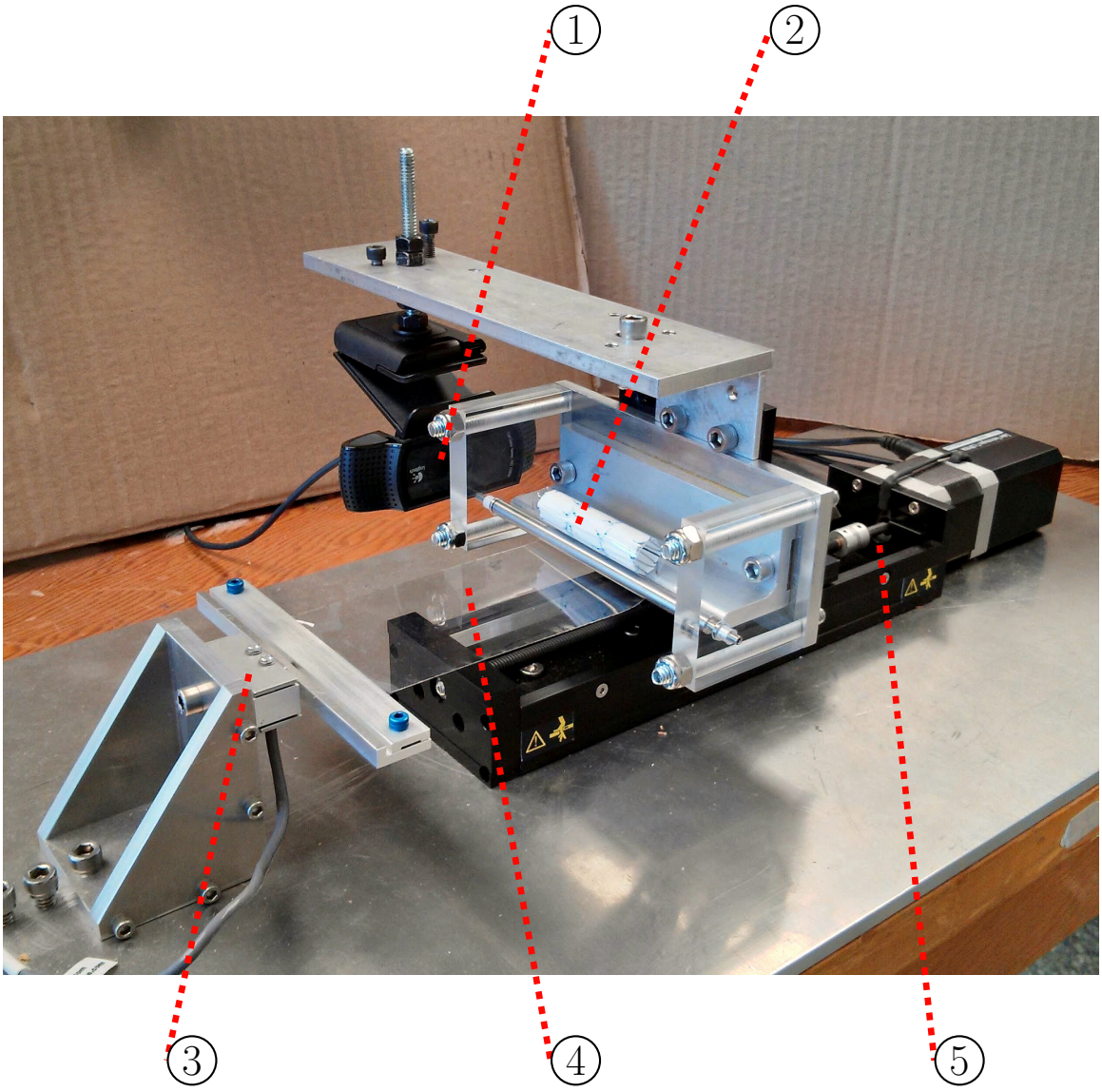

Figure 2.1: Extensometer system: 1 - machine vision webcam, 2 - stent-graft, 3 - force gauge, 4 - Mylar film, 5 - linear slide

slide at the other.

From left to right in Figure 2.2, Mylar is threaded from the load cell clamp, around a first roller, around the stent being tested, and around the round edge of a moving Mylar anchor which has the same radius of curvature as the roller; this anchor is then used to secure the Mylar to the moving platform of the linear slide. The stent is constricted by moving the Mylar anchor which is supported by the linear slide away from the load cell at a rate of 0.329 mm/s. The stent is constricted (crimped) to a predetermined value of cross sectional AR. Once constriction is complete, expansion

begins with the slide moving in the opposite direction toward the force gauge, allowing the Mylar to loosen around the stent. As the stent expands, it exerts a radial force (pressure) back on the Mylar, this radial force is converted into a linear force as it passes down the Mylar to the load cell where it is recorded, as demonstrated in Figure 2.2. Data collected during expansion of the stent represents radial force values at different points of expansion inside a vessel, these results are required for stent performance analysis.

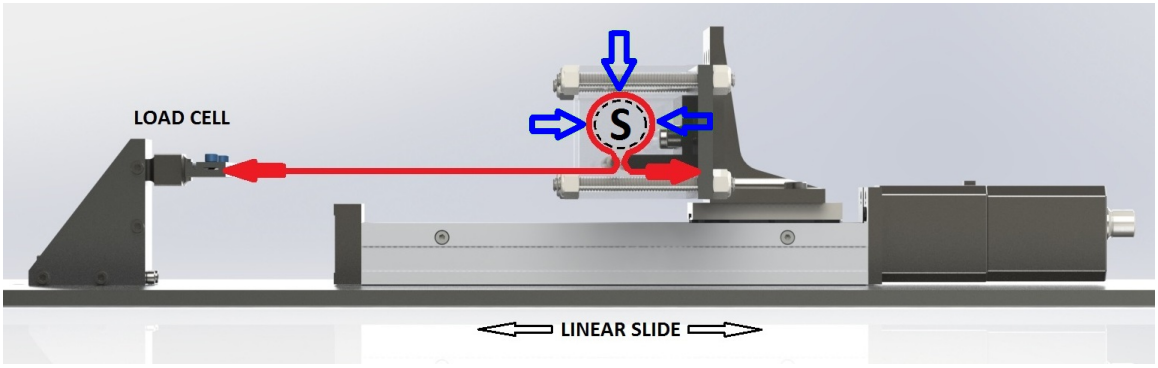

Figure 2.2: Generalized radial extensometer functionality

Compared to the most recent experimental system for radial force measurement by Johnston et al., this new radial extensometer contains several modifications and improvements[1]. The linear slide provides accurate, high resolution position control which can be customized with available LabVIEW drivers. The load cell and associated 24-bit analog-to-digital converter (ADC) are sized specifically for analyzing the range of radial force expected from AAA endovascular stents, providing excellent resolution compared to the existing over-sized system. This apparatus is designed in a horizontal orientation for several reasons including improved system stability, minimization of errors caused by gravitational effects, ease of setup as well as better angles for monitoring and observation. The most significant addition is real time AR monitoring through machine vision, reducing assumptions made to manually calculate system AR. Control and data collection for all components in this system are performed simultaneously by LabVIEW, improving ease of use. System behavior can easily be adjusted for individual test requirements.

2.1.1 Position Logging and Control

The linear slide used in this system is operated with a stepper motor, whose controller is capable of keeping track of the number of steps taken. Displacement of the slide can therefore be measured and controlled without need for an encoder or extensive calibration. The stepper motor controllers are able to regulate the frequency of pulses send to the motor, precisely controlling velocity and acceleration. The Zaber T-LSR150A linear slide has a positional accuracy of ±45 µm, repeatability of <2.5 µm and resolution of 0.0992 µm, contributing minimally to overall system error[163].

The control and data collection for the linear slide is performed through an RS-232 port. Unfortunately, a large limitation of this port is a theoretical max read and write sampling rate of 6.24 ms and a full read/write cycle rate of 12.48 ms[164]. To ensure compatibility, communication is limited to a period of 15 ms. Due to the consistent data transfer and slide velocity it is possible to interpolate between data points to up-sample positional data.

2.1.2 Force

The force gauge used in this system has linearity and hysteresis values of 0.15 % of full scale output (FSO) and a repeatability of 0.05 %FSO[165]. The maximum error at full scale output due to hysteresis is 0.08 N or 0.0076 g. Collected force data will be well below full scale output of 50 N, or even 10 N, avoiding the majority of hysteresis error.

The NI9237 module used for force data acquisition contains a 24 bit delta-sigma ADC and low-pass anti-aliasing filter. This ADC will give a force gauge resolution of 2.9 µN or 30.4 ng. Resolution provided by a 16 bit ADC would be adequate for the purposes of this system, avoiding significant quantization with a resolution of 0.7 mN or 0.07 g.

2.1.3 Machine Vision and Area Reduction

Machine vision was added to the radial extensometer to collect AR and circularity data. The “NI vision Acquisition Express”, “NI Vision Assistant Express” and “Find Circular Edge 1” virtual instruments were used to track these results throughout

testing. A Logitech webcam is mounted on the Radial extensometer and aimed down the center of an open stent to collect data.

During constriction, the camera and software tracks a darkened edge of the Mylar film. The "Find Circular Edge" virtual instrument (VI) locates intersection points between a set of adjustable search lines and the edge of the Mylar film and fits a circle to these points (Figure 2.3). Values for radius of this best fit circle measured in pixels are output and converted to an area value; a mean value of area is calculated for the first 25 data points. Comparing all succeeding values to this original mean area, gives a value for percent of original area (OA), which can be converted to percent AR using: $100 - OA = AR$. It is not necessary to calibrate the camera because no dimensioned values are ever extracted. However, resolution of the camera (pixel size) was determined at different levels of zoom, along with associated diametral errors (Table 2.1). Because the resolution of the camera is constant at different zoom levels, diametral error ranges from 74.1 µm − 125.8 µm for low to high zoom levels respectively. Smaller diameter stents will typically use zoom level '+1' and will therefore have smaller diametral error than larger diameter stents that use lower levels of zoom. Zoom level '+1' corresponds to a field of view of 32.95 x 24.72 mm.

The AR calculation relies on the diameter of a circle, fit to the Mylar's edge. Diametral error is an inaccuracy in measurement due to the resolution of the webcam, which corresponds to the size of one pixel on each side of a circle who's diameter is being measured. The diametral error for a 14 mm stent using a zoom level of '+1', would correspond to an error in oversize of 0.59 %. Even with the higher diametral error experienced by larger stents at a zoom level of '0', the error in oversize still decreases. For example, a 22 mm stent would only experience an oversize error of 0.48 %.

Previous iterations of the radial extensometer by other research groups outlined in Section 1.1.3, either used linear displacement or calculated AR using some form of Equation 2.1, published by Johnston et al.[1]. Using vision to calculate AR should provide more accurate, repeatable results when compared to manual methods because the camera is able to continually track progress of the experiment. Real-time tracking will also circumvent any calculation error due to Mylar elongation due to the applied load during testing. There is a potential for accruing error during the

Table 2.1: Dimensional resolution of a Logitech C920 webcam at different levels of zoom (±SD)

Zoom Level	Pixel Size (µm)	Diametral Error (µm)
+2	37.1 ± 0.1	74.1 ± 0.2
+1	41.2 ± 0.1	82.4 ± 0.1
0	47.6 ± 0.1	95.2 ± 0.2
−1	53.0 ± 1.1	106.0 ± 2.2
−2	62.9 ± 1.4	125.8 ± 2.8

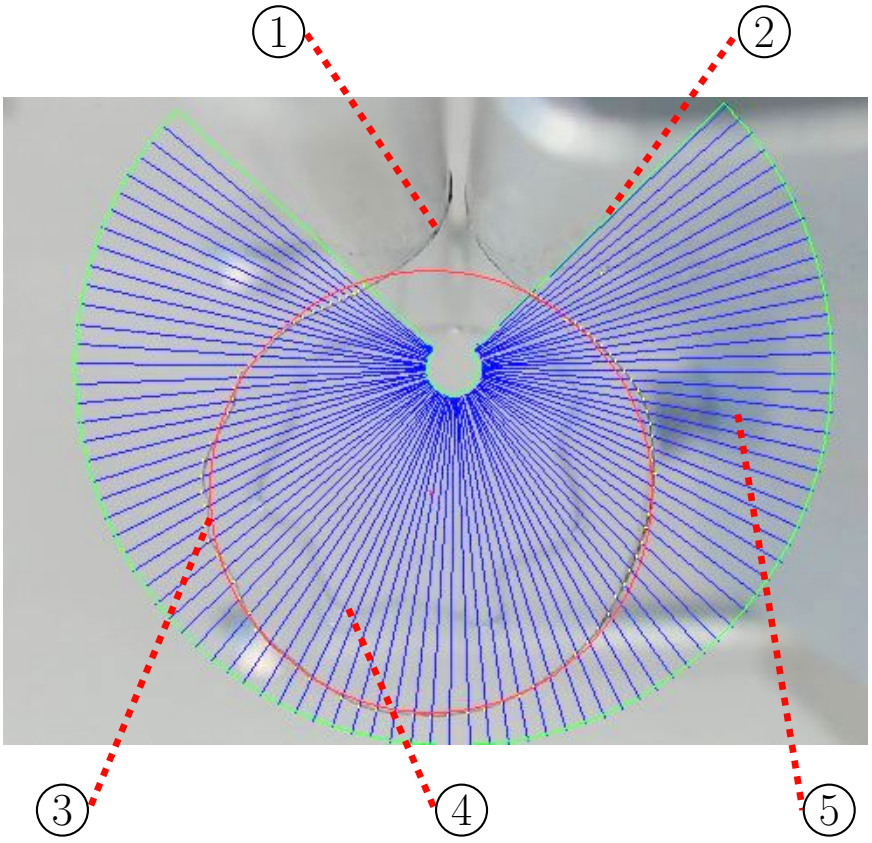

Figure 2.3: Vision capture using the NI "Find Circular Edge 1" VI: 1 - edge of Mylar sheet, 2 - green edge of region of interest, 3 - red circle fit to Mylar edge, 4 - stent expanded in Mylar loop, 5 - blue lines intersect with Mylar edge creating a point for circle fitting

circle fitting process if the Mylar strays too far from its circular shape during testing. Future generations of this device should move away from circle fitting and attempt

to calculate the exact area of the Mylar opening, regardless of circularity.

$$AR = 1 - \left(\frac{C_0 - \Delta C}{\pi D_0} \right)^2 \tag{2.1}$$

where

AR = area reduction
C_0 = circumference of fully-deployed stent (mm)
ΔC = displacement of Mylar film (mm)
D_0 = diameter of fully-deployed stent (mm)

2.2 Design

The radial extensometer system used by Johnston et al. (Figure 2.4), on which these works expand, was designed to be clamped to the work table of a tensile load testing apparatus developed by MTS Systems Corporation (Minneapolis, MN). The basic functionality of the new system is similar to that of Johnston et al., with several notable changes intended to increase extensometer performance and quality of collected data[1]. Drawings and materials are outlined in Appendix D.

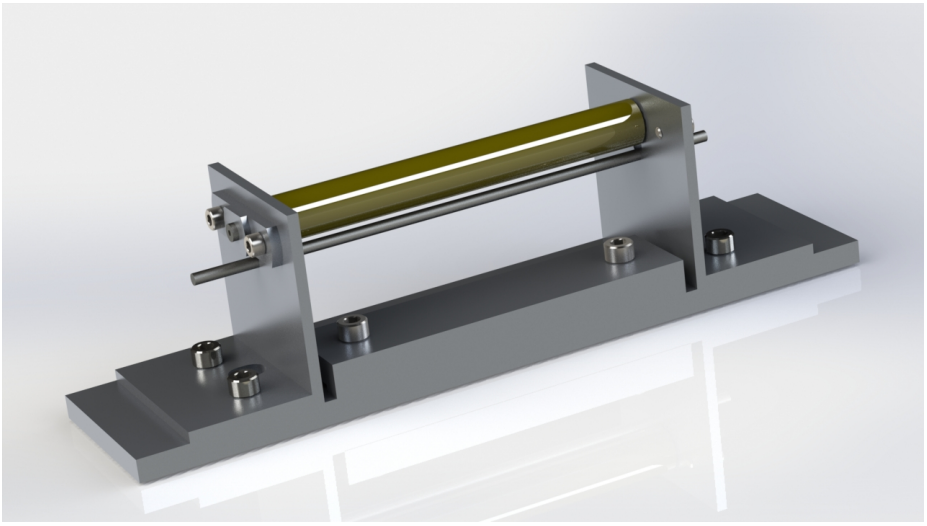

Figure 2.4: Original radial extensometer used by Johnston et al.[1]

The radial extensometer was altered to be symmetric in all three major planes (x-y, x-z, y-z) by employing equal size leading and trailing support sections (a fixed bracket and a free roller). The free roller is made of stainless steel 316 (Appendix D,

page 200) to ensure good stiffness and avoid deformation throughout testing, while the larger fixed bracket section uses Aluminum 6061-T6 (Appendix D, page 197). In the process of improving system symmetry, roller size was chosen to be 0.25 in to minimize inertia as well as to bring contact points underneath the stent as close together as possible on opposing supports without compromising system strength and stiffness.

Certain other small changes were employed such as a horizontal system setup and clear acrylic roller support walls (Appendix D, pages 198 and 199). A horizontal setup minimized the impact of any gravitational effects and made for a much more stable experimental platform. Clear acrylic roller supports were necessary to implement machine vision and monitoring of experimental progress.

Component selection was improved compared to previous designs. Force gauge, position monitoring and data acquisition system were sized appropriately for the small forces expected to be generated during testing of self-expanding stent-grafts. Avoiding over-sized components will improve accuracy and resolution while decreasing error.

Clear Mylar film was selected for stent constriction due to it's favorable material properties. Both it's high modulus of elasticity in comparison to other plastic films and it's low coefficient of friction made this material especially attractive for this application[166, 167]. Alternatives to Mylar were investigated, such as woven fabric made of fiberglass and carbon fiber; none were as well tailored to the functionality of this system as clear Mylar. Selecting a clear material as opposed to the reflective Mylar used by Johnston et al. makes it possible to visually and optically analyze stent-grafts during testing[1]. Mylar sections were laser cut to ensure consistent dimensions, results, and a repeatable setup (Appendix D, page 206). Clamps were designed with screws that fit through holes in laser cut sections of Mylar, automatically aligning the Mylar prior to testing and enabling a faster more easily reproduced testing and assembly process.

The most critical alteration is the introduction of machine vision to monitor stent-graft AR during testing. This system creates an entirely new explicit method of collecting stent AR data for analysis. Using an explicit method of data collection will reduce error caused by assuming a perfect correlation between linear motion of the Mylar and AR of the stent. The combination all of these changes has led to both the

computer aided design (CAD) rendering (without machine vision) shown in Figure 2.5 and the completed experimental setup shown in Figure 2.1.

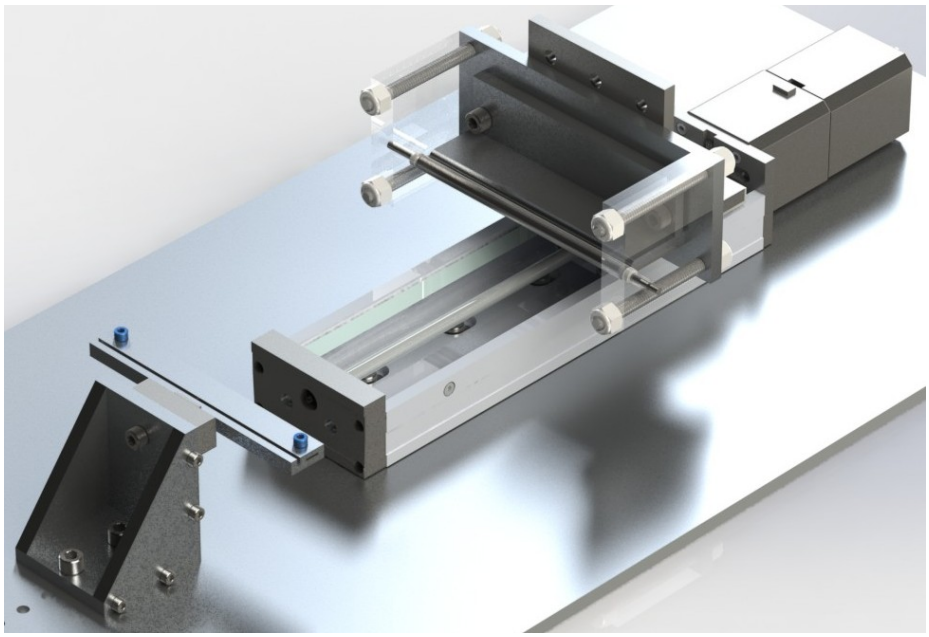

Figure 2.5: New radial extensometer

2.2.1 Calibration Sensitivity, Repeatability and Linearity

The force gauge was calibrated in a tensile horizontal arrangement, identical to the manner in which it is employed. The cantilevered stationary Mylar anchor (Appendix D, pages 201 and 202) is fixed to the horizontally mounted force gauge to ensure the impact of its cantilevered mass is not reflected in measured results. To ensure accurate data collection following calibration, two methods of evaluation were used:

1. Calibration data was collected in the vertical and horizontal directions to characterize the difference in system performance throughout full system range.

2. Low mass calibration was performed with frequent steps to determine the impact of the cantilevered Mylar anchor on collected data. There was concern that error would be introduced in the horizontal setup as the linear Mylar force was required to counteract the moment imposed by gravitational forces acting on

the cantilevered anchor. The Omega linear calibration data sheet can be found found in Appendix E on page 207.

Calibration was performed by collecting ten independent fifteen second long data sets at fifteen separate loads. Load was completely unloaded between data sets to ensure each was unique and complete. System sensitivity was calculated by dividing full scale output voltage (extrapolated from the slope of the calibration output curve) by the 10 V excitation used by the force gauge. Repeatability was calculated by dividing the largest standard deviation calculated from averaged data sets by the full scale output. Force gauge sensitivity and repeatability are shown in Table 2.2.

Table 2.2: Sensitivity and repeatability with 10V excitation

Origin	Sensitivity (mV/V)	Repeatability (%FSO)
Calibrated	2.284	0.035
Data sheet	2.293	0.050

Full force gauge calibration results can be seen in Figure 2.6. The trend line of the horizontal calibration curve has an r^2 value of 0.99996 showing an excellent fit between this data and it's corresponding trend. A very linear increase in the comparison between output voltage and calibration mass.

Low mass results from horizontal and vertical calibration are compared in Figure 2.7. Unlike the vertical setup, a horizontal system would require fewer offsets to account for gravitational effects on hanging system mass. Along with this benefit in data collection, using a horizontal system allows for a more compact and stable system that is more simple to prepare, use and observe.

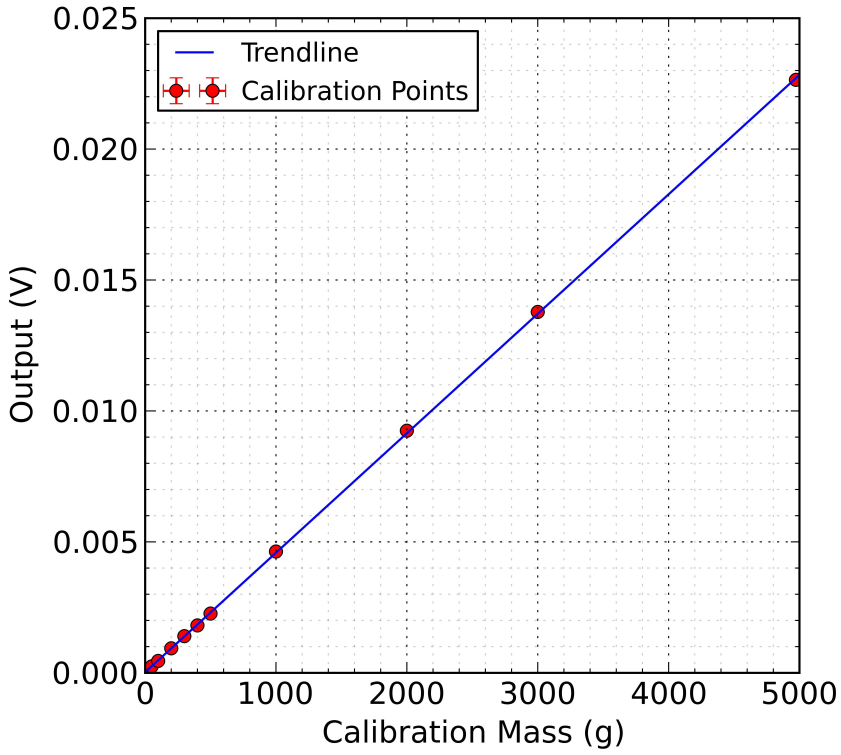

Figure 2.6: Full system horizontal calibration

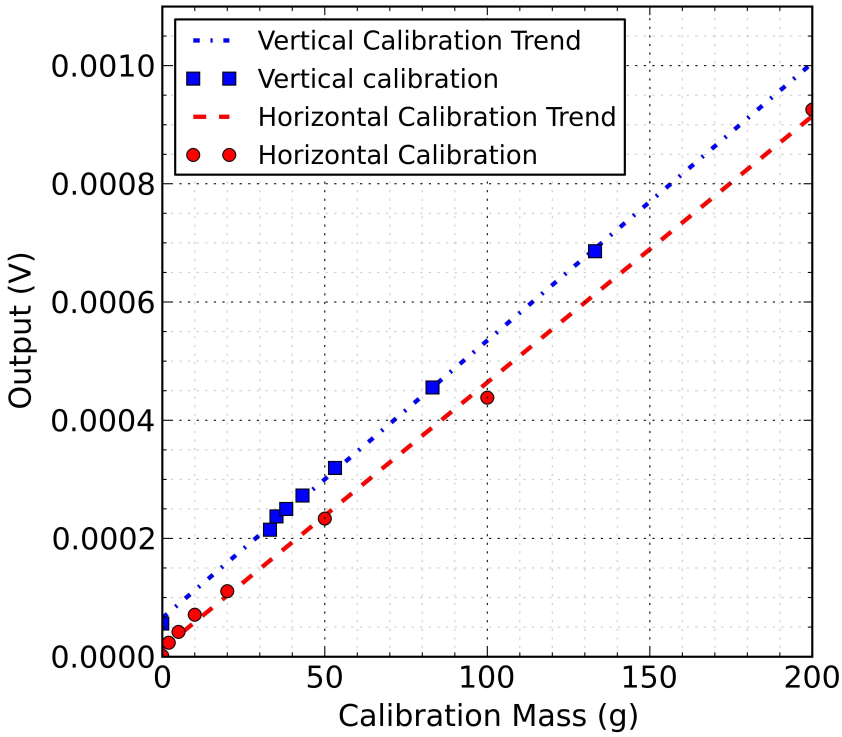

Figure 2.7: Low range vertical and horizontal calibration data

2.2.2 Noise

There are several possible ways for noise to be introduced during data collection such as vibration from the stepper motor; linear stage motion; analog-to-digital conversion and amplification by the NI9237 DAQ module; or 60 Hz electro-magnetic-radiation (EMR). The 24 bit Sigma-Delta ADC provides the load cell with exceptionally high resolution and will therefore produce very little quantization error. Also, "the $\Sigma - \Delta$ modulator shapes the quantization noise so that it lies above the passband of the digital [lowpass] output filter"[168], further reducing noise in collected data.

To test noise in the force gauge DAQ, 10 V excitation voltage leads for the load cell were connected directly to analog inputs of the NI9237 module and data was sampled for 15 sec. After transforming this data to the frequency domain using the fast Fourier transform (FFT), prevalent frequencies become visible at 180 Hz, 360 Hz, 540 Hz and 720 Hz with random noise presenting itself as scattered frequencies throughout the sample range (Figure 2.8). Superposition of 60 Hz EMR is likely the cause of these equally spaced dominant frequencies.

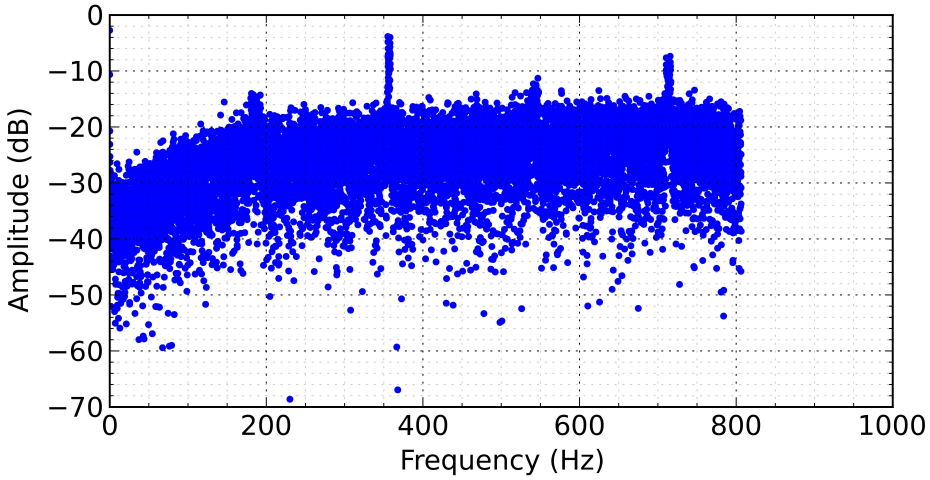

Figure 2.8: Noise contributed by the NI9237 module

As shown in Figure 2.9, frequencies above 46 % of the sampling rate of 1612 Hz are cutoff due to the NI9237 module stopband filter intended to prevent aliasing. This explains the absence of frequencies above 806.4 Hz in Figure 2.8.

Optimization of the corner (cutoff) frequency for a Butterworth low-pass filter is shown in Figure 2.10. Peak signal-to-noise (SNR) is found at a cutoff frequency of

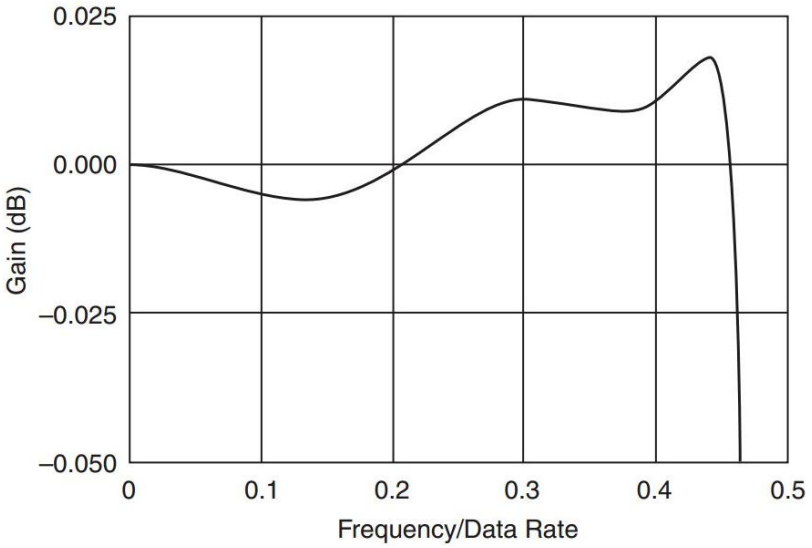

Figure 2.9: Passband flatness of the NI9237 module (Hz/Hz)[169]

18.7 Hz, corresponding to a filtered SNR of 1.388, which compares well to an unfiltered SNR of 1.002. The optimized cutoff frequency is well below the lowest prevalent noise frequency of 60 Hz, effectively damping out the majority of EMR interference.

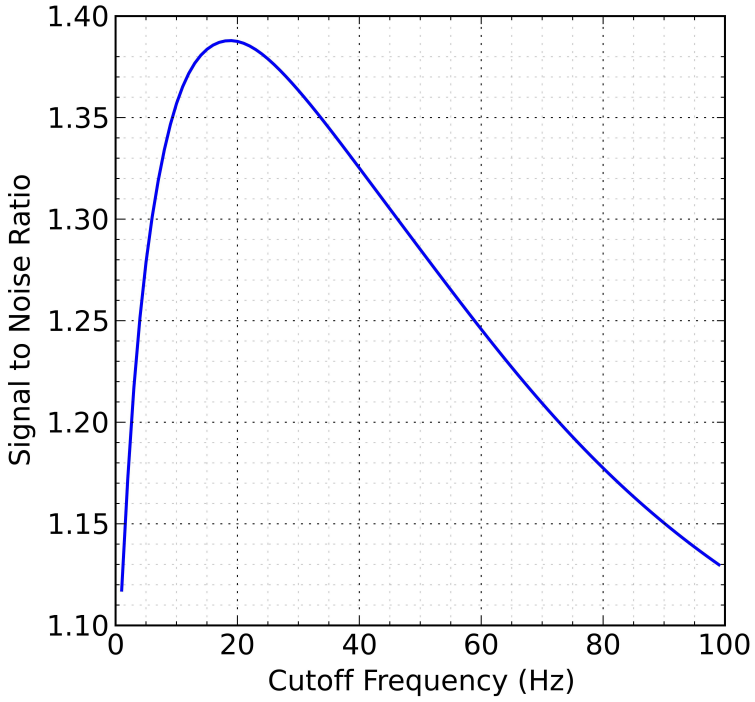

Figure 2.10: Maximized SNR ratio for force gauge sample

2.2.3 Theoretical Linear Force Comparison

Analysis of full system functionality was performed using a simple experiment. Spring force was calculated theoretically using Equation 2.2 and compared to experimental results collected using the radial extensometer.

$$F = \frac{\delta d^4 G}{8 D^3 N} \tag{2.2}$$

where

δ = spring deflection (mm)
D = mean coil diameter (mm)
d = wire diameter (mm)
G = shear modulus of spring material (MPa)
F = external force applied along axis of helix (N)
N = number of active coils

A 302 stainless steel tension spring with 10.25 active coils was used during this test. This spring has an outer spring diameter of 0.438 in (11.125 mm), a mean coil diameter of 0.403 in (10.2362 mm), a wire diameter of 0.035 in (0.889 mm) and a shear modulus of 77.2 GPa. During testing, the spring was extended in tension along its central axis to a maximum displacement of 5 mm at a velocity of 0.33 mm/ sec, then returned to its initial state. Spring test comparison of experimental and theoretical data is shown in Table 2.3.

Table 2.3: Spring test results

Data Type	Value
Average maximum experimental force (N)	2.65
Standard deviation experimental force (N)	0.06
Maximum theoretical force (N)	2.74
Percent error (%)	3.59

Test results show an excellent comparison between theoretical and experimental linear force results with a percent error of 3.59 %. This outcome gives strong evidence that the accuracy of future results collected by the experimental apparatus can be trusted as reliable.

2.3 Results

Several preliminary investigations were performed using the completed radial extensometer. Both machine and stent performance are analyzed in a series of tests designed not only to validate radial extensometer results against those from previous studies but also to fine tune certain aspects of extensometer setup and operation.

2.3.1 Effect of Stent Orientation

All currently available z-wire stents use some method of fixation to connect edges of the stent wire together to make a circular prosthetic. Two of the most common methods, brazing and crimping, will alter mechanical properties of the stent. Experimental results shown in Figures 2.11(a) and 2.11(b) reveal that depending on stent orientation in the radial extensometer (horizontal or vertical joint placement) a different force profile is observed. The coordinate system for the directions shown in the legend of these figures is presented in Figure 3.12.

In Figure 2.11(a), there is a more notable separation of force profiles of $\sim$0.70 N at $\sim$28 % AR for differing orientations during constriction. During expansion, a less pronounced separation of 0.40 N at 40.5 % AR can be observed in Figure 2.11(b). Comparison of experimental constriction and expansion demonstrates a significant hysteresis between the two radial force profiles. Hysteresis is likely caused primarily by the shift in loading mechanisms from the linear slide during constriction to stent radial force during expansion. The linear slide is capable of exerting a peak linear force of 300 N and will not be slowed by friction or any other system mechanics that get in the way. However, the stent radial force value being recorded during expansion is significantly lower and quite susceptible to frictional effects. Stent mechanics also have an impact on the radial force profile and hysteresis, they are examined more in depth in Chapter 4.

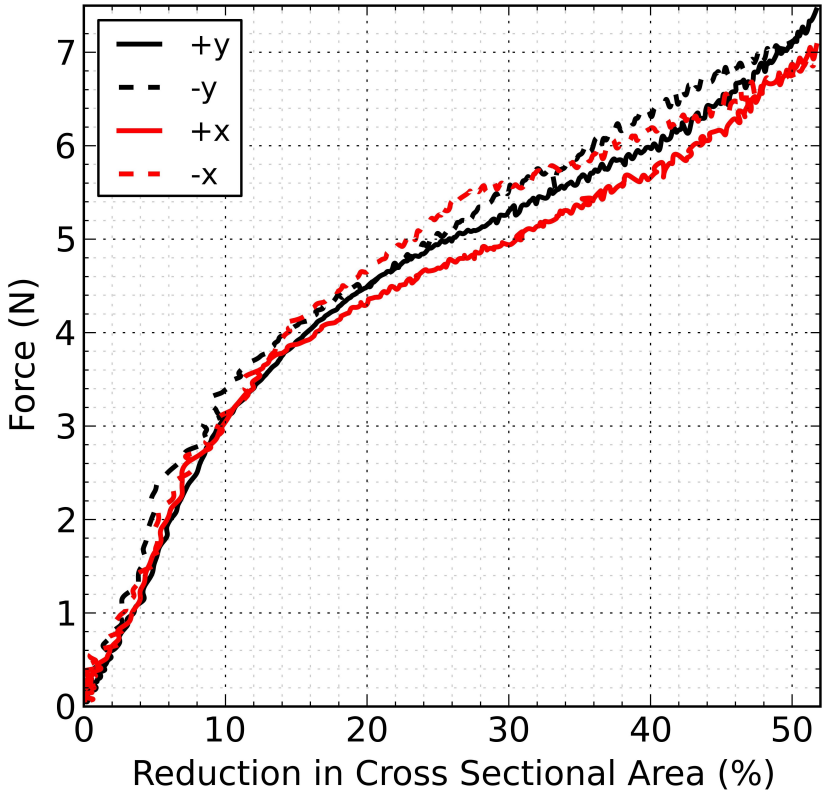

(a) Constriction

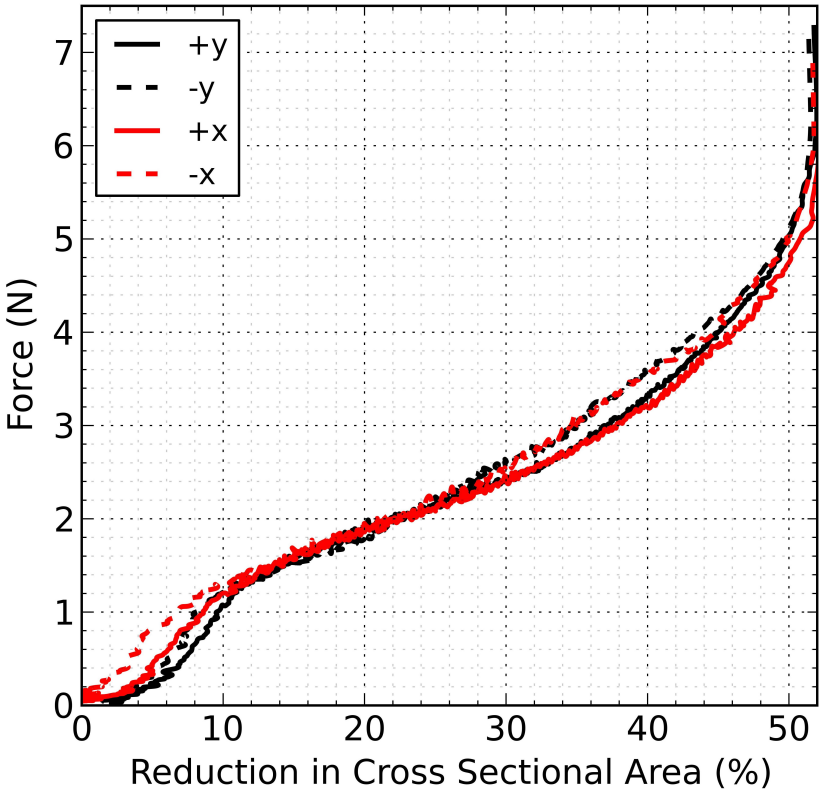

(b) Expansion

Figure 2.11: 22 mm Stent brazed joint orientation - three wire covered

During constriction the linear slide imparts an unforgiving force on the stent through the Mylar, the linear slide is capable of exerting a peak linear force of 300 N and will not be slowed by friction or any system mechanics that get in the way. During expansion the stent's peak radial force at different levels of expansion, after having overcome friction and other system influences, is being collected by the load cell at this stage. The stents ability to exert force is fa

Collection and manipulation of radial extensometer data presented in this chapter used the first iteration of data collection methodology developed for these works. Slide displacement required to achieve 50 % AR was determined using a combination of a calculator (which employed Equation 2.1 solved for displacement[1]) and trial and error for fine tuning. As the first test for a specific diameter of stent is run, the position of the slide at 50 % AR is recorded. Every subsequent test is moved to exactly this position on the slide and the assumption is made that each of these tests will also achieve 50 % AR. Slide displacement is linear and predictable, therefore, the same number of steps is required to move from an AR of $50 - 0$ % for each test of the same stent diameter. Each presented result in this chapter is created by averaging at least three unique data sets. Finding their mean can be done simply by adding values at identical indexes and dividing by the number of data sets. This technique was adjusted for use in later data collection and will be explained in detail in Chapter 6.

Stents are typically oversized for installation by $10 - 20$ % compared to the outer arterial diameter, which corresponds to an AR range of $17.4 - 30.6$ % for the 22 mm stent used in this investigation[102, 103]. From the data shown in Figure 2.4, the maximum force profile separation in this range was calculated to be 0.21 N at 29 % AR. The average peak force of all force profiles at 29 % AR is 2.43 N, which corresponds to a percent error of 8.77 %. Separation of data sets due to stent orientation in the radial extensometer demonstrates that that inclusion of a connected joint in the manufacture of z-type stent grafts does in fact have an impact on radial force generation and distribution. This effect could be compounded if multiple stents were aligned in that same prosthetic.

Directionality should be considered while designing stent-grafts for patients' unique anatomical geometry. To ensure consistency, all future experiments were performed

with a downward ("-y") stent wire connection orientation to ensure repeatability and consistent experimental setup. Removal of the brazed stent joint in future manufactured stents would improve the symmetry of their radial force generation.

Table 2.4: Directionality results during expansion

AR Range (%)	$10-50$	$10-30$
Max separation (N)	0.40	0.21
AR at max separation (%)	40.5	29.0
Mean force at max separation (N)	3.48	2.43
Max standard deviation (N)	0.17	0.09

2.3.2 Impact of Mylar Thickness

The original radial extensometer designed by Johnston et al. used 0.002 in (0.0508 mm) reflective Mylar to constrict stents during testing. Initial trials with the new horizontal experimental setup revealed that this material was impacting stent loading and unloading[1]. The thicker Mylar was more resistant to deformation and would retain its own shape outside of testing. Figure 2.12 demonstrates how with Mylar loading defined to be 0.035 N, the amount of offset between stent and rollers grows with increased Mylar thickness.

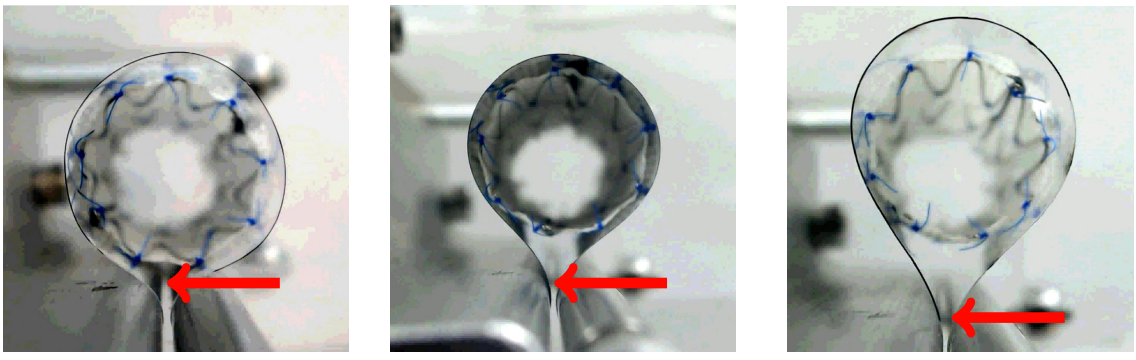

(a) 0.001 in Mylar **(b)** 0.002 in Mylar **(c)** 0.003 in Mylar

Figure 2.12: Stent offsets for differing Mylar thicknesses with 0.035 N Mylar loading

Thicker Mylar requires a greater amount of pre-loading to set the stent against the

rollers and ensure an immediate reduction of AR values. Results of an experimental trial with 0.001 in, 0.002 in and 0.003 in laser cut Mylar sections are shown in Figure 2.13. Although data sets presented in this figure do not show a large separation, the 0.003 in Mylar does present a modestly higher radial force than that of 0.002 in and 0.001 in (0.0254 mm) samples. Regardless of how similarly the samples perform, following this test all future experiments used 0.001 in Mylar. This will minimize the need for pre-loading while also reducing difficulties during experimental setup and post-processing. Avoiding pre-loading is important to reduce contributed by Mylar's effect on collected results.

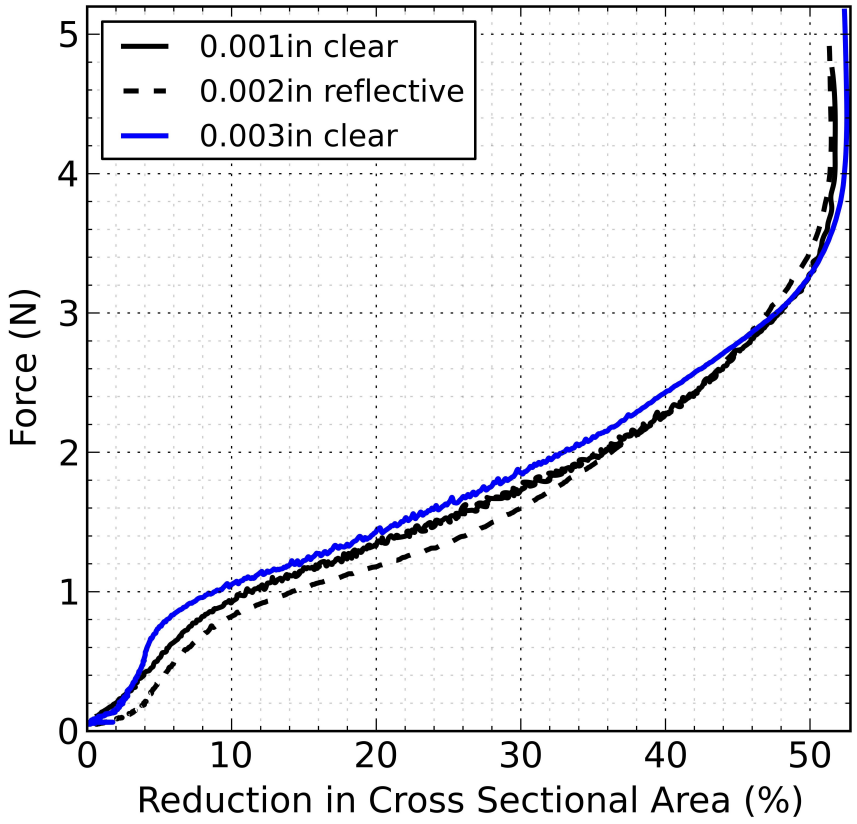

Figure 2.13: Mylar thickness comparison using a covered, two wire, 18 mm stent-graft

2.3.3 Effect of Graft Covering, Multiple Stents and Test Range

Results presented by Johnston et al. explained that the force applied by stents placed in an end-to-end configuration was equivalent to the sum of forces applied by individual stents[1]. Reaffirmation of this claim using the new radial extensometer can be seen in Figure 2.14. This figure also presents a comparison of a stent with and without a graft covering. It is important to note how little the woven polyester covering of the single z-wire Zenith stent affects collected radial force results above an AR of 10 %.

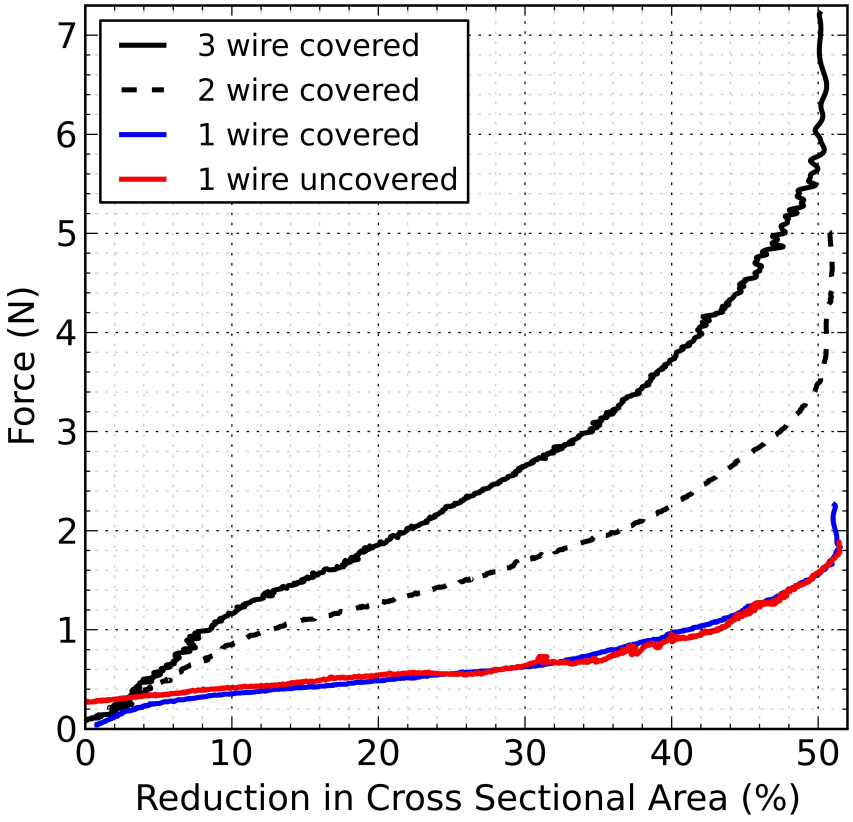

Figure 2.14: Effect of multiple stent wires and configurations

Figure 2.15 demonstrates the impact of peak AR on collected results. Altering the amount of AR seems to have a sizable impact on the trajectory of force data collected during stent expansion. All tests collected for use in this work were constricted to 50 % AR to ensure consistent methodology and tight grouping of results.

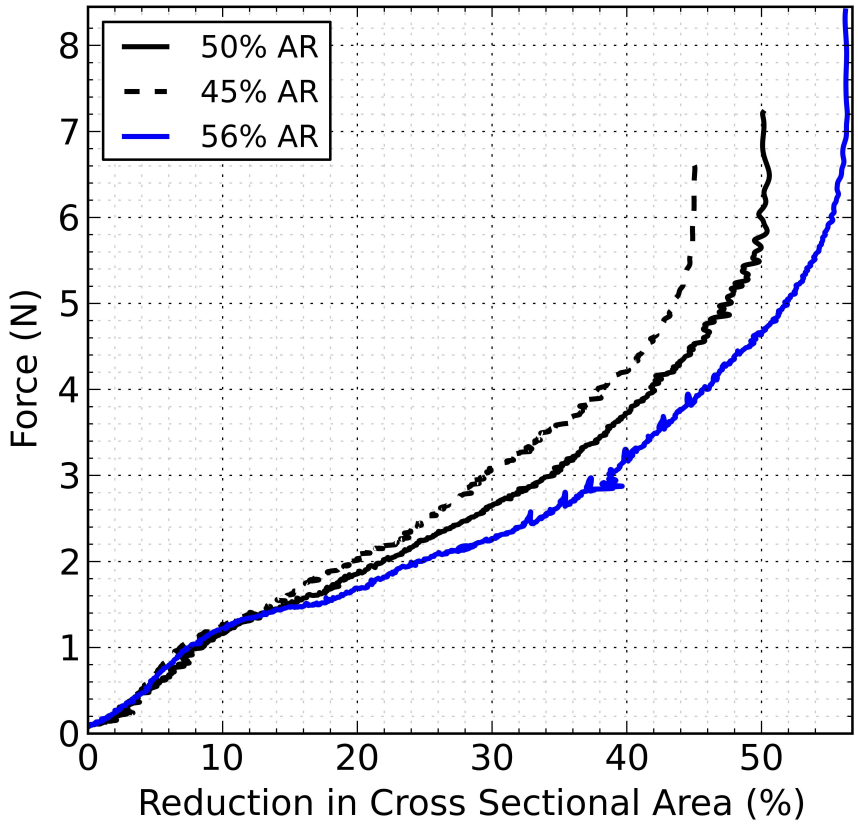

Figure 2.15: Effect of peak AR achieved during testing on results using a covered, three wire, 18mm stent-graft

2.4 Discussion

This chapter is intended to outline the design, calibration and testing of components involved in a novel radial extensometer. As a preliminary investigation into system performance, results initially presented by Johnston et al. regarding a discrepancy between stent diameter and radial force generation have been verified[1]. Figure 2.16 clearly demonstrates that smaller stent diameters exhibit higher radial force than larger diameter stents across the entire range of AR values (Figure 2.16(a)) and oversize (figure 2.16(b)) that may be encountered following implantation. Considering that drag force increases along with arterial diameter, it is logical that the radial force exerted by stent-grafts should also increase with diameter up to a certain plateau intended to avoid vessel remodeling. Future chapters will focus on developing tools necessary to progress toward the design of mechanically correct stents, correcting the issue presented in figure 2.16.

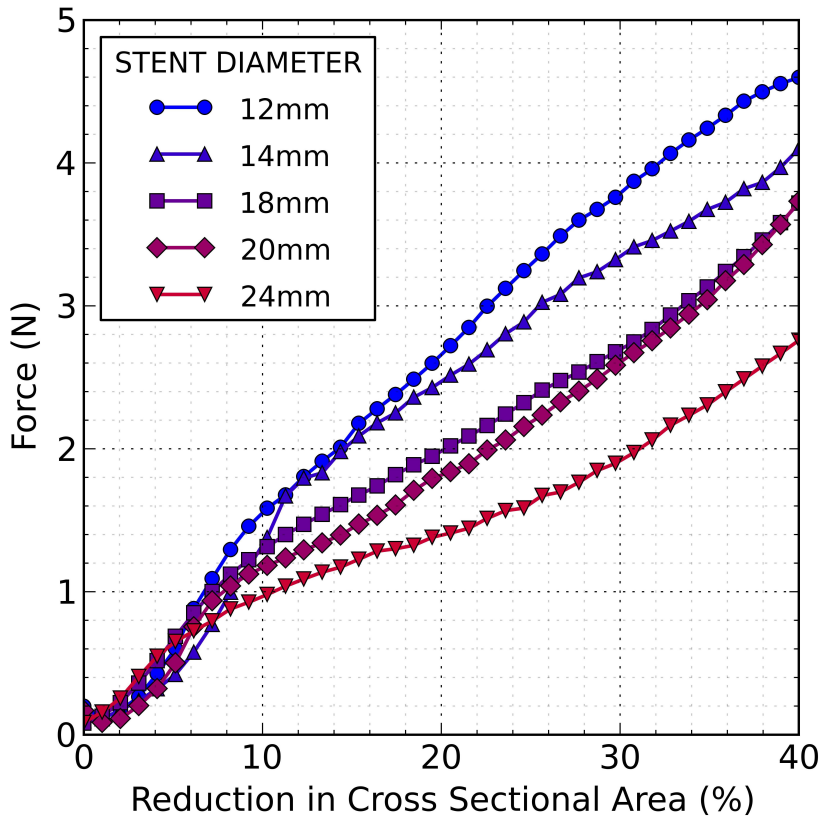

(a) Based on stent-graft cross sectional AR

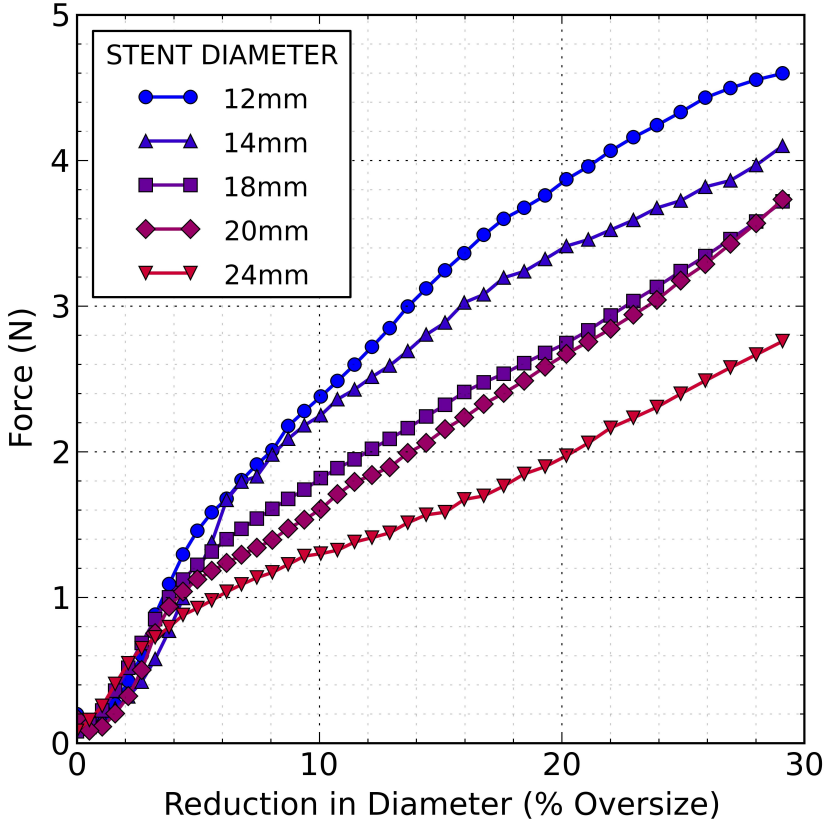

(b) Based on stent-graft diametral oversize

Figure 2.16: Comparison of covered, three wire stent-graft diameter and radial force

Future iterations of the novel radial extensometer described in these works could benefit from lessons learned through multiple rounds of data collection. Changing from a positional control system, to a system managed with AR values collected by machine vision, would eliminate the need to manually ensure all tests switch from compression to expansion at 50 % AR. Shifting to vision control will ensure a precise peak AR value, increasing system accuracy and repeatability.

Expanding upon the current design, functionality could be improved by adding the ability to manipulate temperature and humidity in order to observe their effect on stent expansion and radial force. This would not only allow the system to mimic in-vivo conditions but also facilitate testing of super-alloy nitinol stents while maintaining control over their phase change capabilities.

Chapter 3

Finite Element Modeling

A complete finite element (FE) model which mimics the function of the radial extensometer will be a valuable tool for both investigating the mechanical function of self-expanding stents and aiding in the efficient design of new prosthetics. A validated model can be used to investigate scenarios such as the mechanical systems responsible for stent radial force generation, the conversion of radial force to the linear force measured by the radial extensometer force gauge as well as the impact of design changes on stent performance.

3.1 Software

Five programs were used to create and analyze all FE models outlined in this work.

1. **SolidWorks:** Used for computer aided design (CAD) of component geometries[170].

2. **Hypermesh:** A FE pre-processor used for meshing solid geometries[171].

3. **LS-DYNA:** A dynamic modeling program used to simulate changes in engineering properties throughout meshed geometries[172].

4. **LS-PrePost:** A FE post-processor used for extracting meaningful data and visuals from completed simulations[173].

5. **Python (x,y):** An interpreter for the Python language, as well as a software package catered toward the scientific community.

3.2 Meshing Methodology

A standard method of meshing was established to reduce error and variation between components. All components in the final model are meshed using one-dimensional

beam elements or two-dimensional quadrilateral elements. As explained in the Altair University training manual, quadrilateral elements are better than triangular elements due to their ability to more accurately represent strain[174]. This can be shown through differentiation of the displacement functions for different element types. For a 3 node constant strain triangle, displacement functions are presented in Equations 3.1 and 3.2.

$$u = \alpha_1 + \alpha_2 x + \alpha_3 y \tag{3.1}$$

$$v = \alpha_4 + \alpha_5 x + \alpha_6 y \tag{3.2}$$

where

u = deflection in x (mm)
v = deflection in y (mm)
x = x-coordinate position (mm)
y = y-coordinate position (mm)
α = constant

Strains can be calculated by differentiating Equations 3.1 and 3.2, where ε is the strain (mm/mm).

$$\varepsilon_x = \frac{\partial u}{\partial x} = \alpha_2 \tag{3.3}$$

$$\varepsilon_y = \frac{\partial v}{\partial y} = \alpha_6 \tag{3.4}$$

Equations 3.3 and 3.4 show that by differentiating displacement functions, constant strain triangle (CST) strains are found to be constant. However, using quadrilateral four node elements, displacement is described with eight constants (Equations 3.5 and 3.6).

$$u = \alpha_1 + \alpha_2 x + \alpha_3 y + \alpha_4 xy \tag{3.5}$$

$$v = \alpha_5 + \alpha_6 x + \alpha_7 y + \alpha_8 xy \tag{3.6}$$

Strains are once again calculated, this time by differentiating Equations 3.5 and 3.6.

$$\varepsilon_x = \frac{\partial u}{\partial x} = \alpha_2 + \alpha_4 y \tag{3.7}$$

$$\varepsilon_y = \frac{\partial v}{\partial y} = \alpha_7 + \alpha_8 x \tag{3.8}$$

Finally, Equations 3.7 and 3.8 show that by using four node elements, through-thickness strain (an important quality to have for simulations involving systems in bending) can be calculated and is a linear function of position.

A two-dimensional quadrilateral surface mesh should be optimized to be smooth and regular[174]. A clean, geometrically precise mesh is required for accurate FE analysis because as angles of a quadrilateral deviate from 90 °, stress calculations become more unreliable[175].

3.3 Explicit and Implicit Solver Use

An explicit solver was used for all simulations leading up to the completed model because of the ease at which it can handle nonlinearities, such as contact, material models, and large deformation compared to implicit analysis. Using an explicit solver made it possible to ensure preliminary contact definitions were functioning prior to moving on to the more sensitive implicit iterative solver. An explicit solver can solve for nodal acceleration directly, compared to the implicit solver which much perform several iterations before a solution of acceptable tolerance is reached.

Due to the Courant condition, the time step used in explicit analysis must be lower than the time it takes for sound to travel across a mesh element. Because the time step must be so small, simulation run time would be extremely large unless the duration simulated by the model is reduced. For this reason, an explicit model solver is primarily used in explosive, projectile and crash test simulations, where only a very short time frame needs to be modeled.

Because of the large number of time steps required to meet the Courant condition, the total simulated time of preliminary explicit models was considerably reduced compared to real world values. Simulated duration for each model is shown in Table 3.1, where the final implicit simulated duration represents the real world length of

experimental testing. With such small duration values for the explicit models of Table 3.1, introduction of energy into the system becomes very rapid. This surge of energy could potentially cause shock waves or detrimentally large contact forces to form, negatively impact model results. The simulated duration of the "90 Degree Mylar and Rigid Roller Contact" model was considerably higher than the other explicit simulations, however, model loading was complete by 5000 ms and the simulation was extended to 50 000 ms to observe any changes that may occur leading up to equilibrium.

Table 3.1: Explicit vs. implicit - total simulation time

Model Title	Simulated Duration (ms)	LS-DYNA Solver
Flat Mylar	150	Explicit
90 Degree Mylar and Rigid Roller Contact	50000	Explicit
Full System - Free Mylar; Rigid Rollers and Stent analog	1000	Explicit
Full System - Rigid Rollers; Free Stent Analog and Mylar	1000	Explicit
Completed Simulation - Rigid Rollers; Free Stent and Mylar with Friction	263636.4	Implicit

For the final model, a non-linear implicit solver was used primarily to lengthen simulated duration to real world values without the enormous increase in simulation run time that would be encountered with the explicit solver. Increasing the explicit time step to reduce the run time for an explicit solver would require mass scaling. Scaling the mass of the small components present in the final model would have a significant impact on collected force results ($F = ma$), while also increasing inertia and momentum. The final FE model is considered non-linear because it simulates contacting parts and experiences a large amount of deformation.

3.4 Results

The model constructed as part of this study mimics the function of the radial extensometer described in Chapter 2, facilitating model validation. The final complex

system was divided into five stages of development with each successive stage building upon the success of those before it: a flat 200 mm long by 60 mm wide section of Mylar, used to characterize material performance; a 90 ° angle Mylar over rigid roller contact, for honing initial contact characteristics; a full system model with rigid rollers and stent analog, used to determine convergence of the curved Mylar mesh; a full system model with rigid rollers, free stent analog and free Mylar; and a final model which replaces the stent analog from previous models with an accurate stent geometry. This step-by-step methodology ensures a reliable and accurate foundation for the complete system. All stages demonstrate effective material response, contact effectiveness and mesh convergence.

3.4.1 Flat Mylar

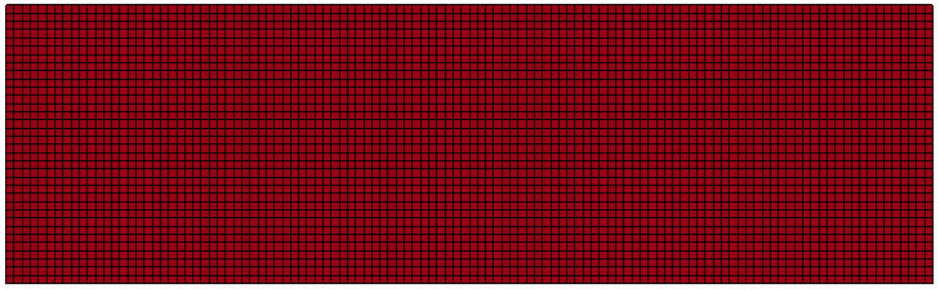

Figure 3.1: Flat Mylar - 0.25 mm quadrilateral mesh

The thin Mylar film was meshed using two-dimensional quadrilateral elements (Figure 3.1, and modeled assuming a Hookean elastic material using LS-DYNA's "*MAT_ELASTIC" constitutive material model with material properties provided by DuPont Teijin Films (Table 3.2)[166]. This Mylar model was used in every subsequent simulation performed leading up to the final simulation, FE model material value inputs can be found in Appendix B.2. In this simulation, a 0.001 in thick, 8 in long by 2.28 in wide section of Mylar has one vertical edge anchored while a 10 N load is applied to the other to determine the resulting magnitude of elongation.

Figure 3.2 shows that when comparing simulation time to elongation, simulation results converge with a mesh element size of 0.25 mm. Under a load of 10 N, a model

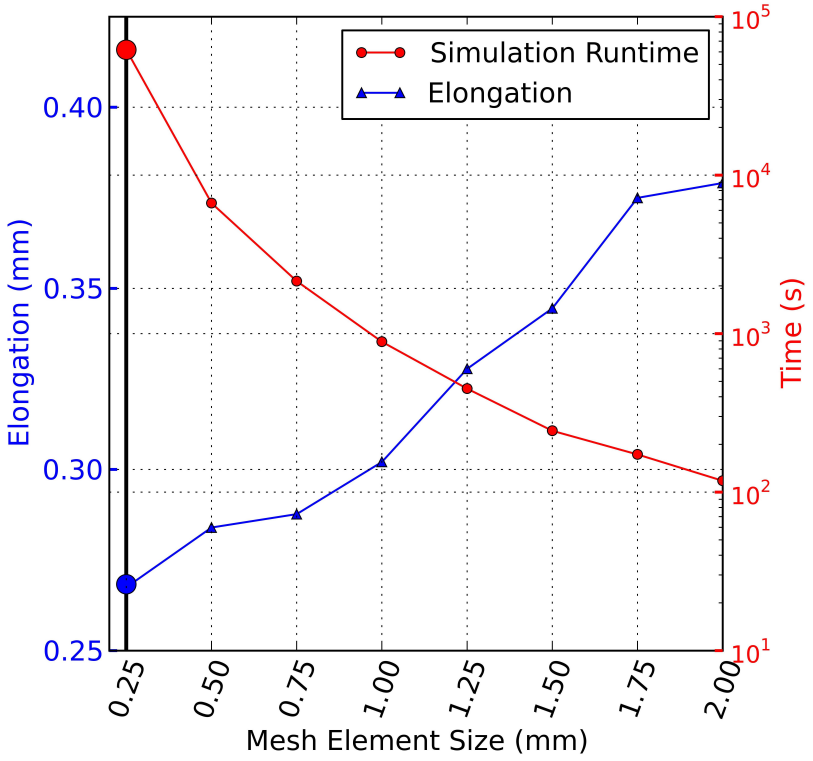

Figure 3.2: Flat Mylar convergence study

Table 3.2: Material properties of Mylar provided by DuPont Teijin Films[166] (MD = machine direction, TD = transverse direction)

Property	Direction	Typical Value	Unit
Tensile strength, ultimate	MD	196	MPa
	TD	235	MPa
Young's modulus (tension)	MD	4805	MPa
	TD	5001	MPa
Young's modulus (compression)		$2726 - 2834$	MPa
Density		0.00139	g/mm^2
Poisson's ratio		0.38	

using this mesh size would extend 0.2683 mm in length (x-direction) as seen in Figure 3.3.

Results of elongation from the flat Mylar FE analysis compare to theoretical results calculated using Equation 3.9 with a 1.76 % error. Theoretical results suggest

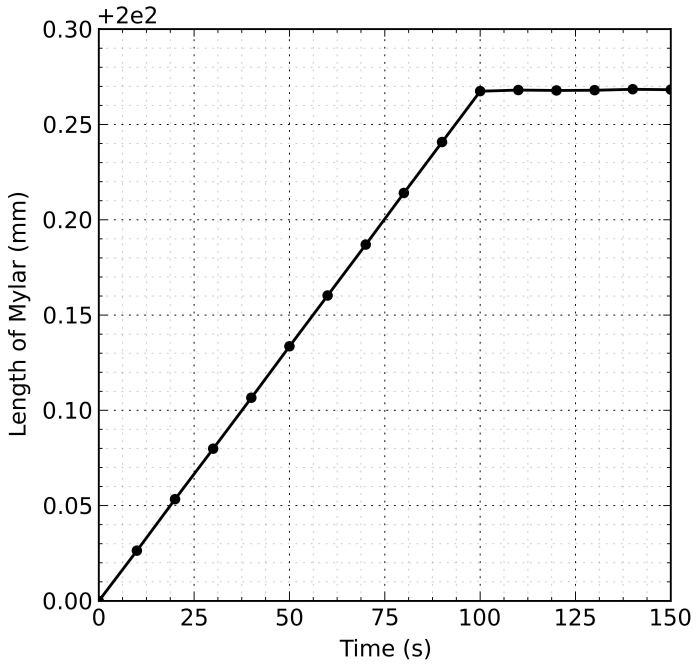

Figure 3.3: Elongation of Mylar under $0 - 10\,\mathrm{N}$ load

that elongation of this section of flat Mylar under a 10 N load would only experience a 0.273 mm elongation.

$$\Delta L = \frac{F L_0}{A_0 E} \tag{3.9}$$

where

ΔL = elongation (mm)
F = force exerted (N)
L_0 = original length (mm)
A_0 = original cross sectional area (mm)
E = Young's modulus (MPa)

The error accrued due to Mylar elongation will depend on both peak force exerted on the Mylar by the stent, as well as peak horizontal displacement of the slide during data collection. The force profile for this simulation uses a constant load application rate, therefore, the time at which peak experimental force occurs in modeled data can be determined by linear interpolation of results. The magnitude of modeled elongation at peak experimental force is found at this interpolated time value. Error induced by Mylar deformation is presented in Table 3.3 and is calculated as the difference between the peak distance moved by the linear slide and the elongation introduced

Table 3.3: Elongation error

Stent Diameter	Peak Force (N)	Slide Displacement (mm)	%Error
10 mm	7.60 ± 0.03	10.11 ± 0.01	2.72 ± 0.01
10 mm	7.60 ± 0.03	10.11 ± 0.01	2.01 ± 0.00
12 mm	8.56 ± 0.14	11.96 ± 0.00	1.96 ± 0.03
14 mm	8.37 ± 0.08	15.16 ± 0.01	1.48 ± 0.01
16 mm	8.18 ± 0.02	15.64 ± 0.00	1.40 ± 0.00
18 mm	7.42 ± 0.19	17.48 ± 0.00	1.14 ± 0.03
20 mm	7.44 ± 0.08	20.24 ± 0.00	0.98 ± 0.01
24 mm	6.42 ± 0.04	23.00 ± 0.01	0.75 ± 0.01

by Mylar deformation. At 10 N force, modeled results show the Mylar sheet reaching a peak stress of 16.91 MPa in the machine direction. This is 17.5 % of Mylar's yield stress of ∼96.5 MPa, consequently, plastic deformation is not likely.

As long as AR values are taken using the machine vision system of the radial extensometer instead of through implicit calculation, AR error due to Mylar elongation is entirely avoided. All experimental tests performed for these works use machine vision for AR calculation. Because each test performed with the radial extensometer is forced to achieve 50 % AR, Mylar elongation should not have any effect on experimental results.

3.4.2 90 Degree Mylar and Rigid Roller Contact

A second model, seen in Figure 3.4, was built to ensure effective contact between shaped sections of Mylar and roller supports. The roller is created as a stainless steel 316L rigid body and modeled using the "*MAT_RIGID" material model. The roller is modeled as a rigid body under the assumption that its deformation throughout the simulation is insignificant and will have a negligible effect on model results. Defining the roller as a rigid bodies will speed up simulation time by avoiding the calculation of unnecessary stress and strain results for the roller. Material values are taken from the MatWeb material property database and are shown in Table 3.4[176]. FE model material value inputs can be found in Appendix B.2. All Mylar on roller contacts are modeled as frictionless throughout these works. This assumption creates a reasonable

representation of the experimental setup, as the leading roller is bearing mounted.

Table 3.4: Material properties of an annealed, cold drawn stainless steel 316L bar[176]

Property	Typical Value	Unit
Tensile strength, ultimate	585	MPa
Tensile strength, yield	380	MPa
Young's modulus	193	GPa
Density	0.008	g/mm^2
Poisson's ratio	0.3	

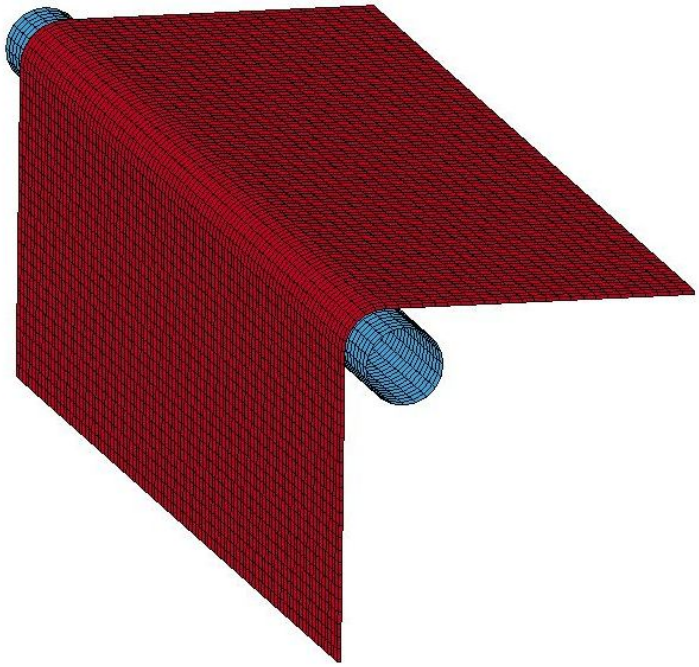

Figure 3.4: 90 ° Angle Mylar and rigid roller contact visualization

For the Mylar to roller contact definition, a penalty-based contact algorithm was employed using LS-DYNA's "*CONTACT_AUTOMATIC_SURFACE_TO _SURFACE" contact interface definition. In a penalty-based contact, penetration of contacting surfaces is eliminated by applying a force proportional to the penetration depth of any infiltrating surfaces[177]. This is in contrast to constraint-based

contacts where two contiguous surfaces are bound together, sharing nodes and avoid penetration or separation. This surface-to-surface card was selected over others due to the types of elements coming into contact, the Mylar shell surface and the rigid roller shell surface. An automatic contact was selected because it is less dependent on reliable contact orientation, improving contact stability[177, 178]. For a rigid body in any penalty-based contact, LS-DYNA advises that proper distribution of contact forces can be promoted by ensuring that contact surface node spacing of a rigid body be no coarser than the mesh of deformable parts which it comes into contact with. Because no stress or strain calculations are performed for a rigid body, refining the mesh of a rigid body has little effect on CPU requirements[177]. For these reasons, the rigid roller was modeled with the same mesh density as the Mylar sheet.

In order to ensure contacts don't fail during simulation, a comparison of contact data is performed. Figure 3.5 shows both a force transmission of 50 N and equal opposing forces between slave and master segments. Symmetry and consistency of slave and master y-contact force suggests the presence of a stable contact force.

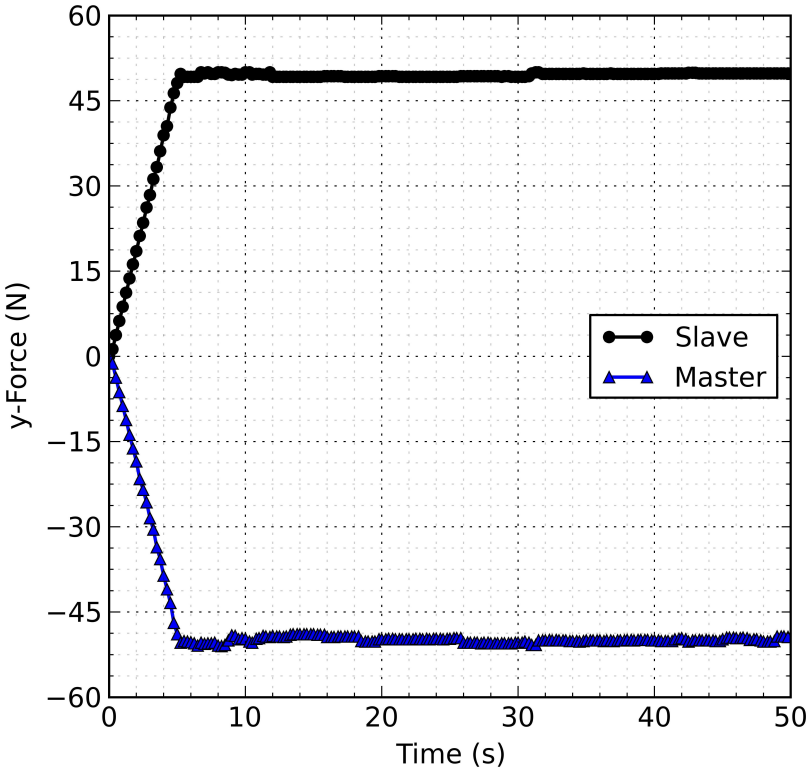

Figure 3.5: Angled x and y contact verification

3.4.3 Full System - Free Mylar; Rigid Rollers and Stent analog

Building upon the previous 90° Mylar simulation of Section 3.4.2, and to ensure the stability of multiple contacts before progressing to multiple deformable bodies, a rigid Tygon tubing stent analog was added to the simulation along with a second roller[179]. Figure 3.6 shows the fully meshed model used for this stage of simulation.

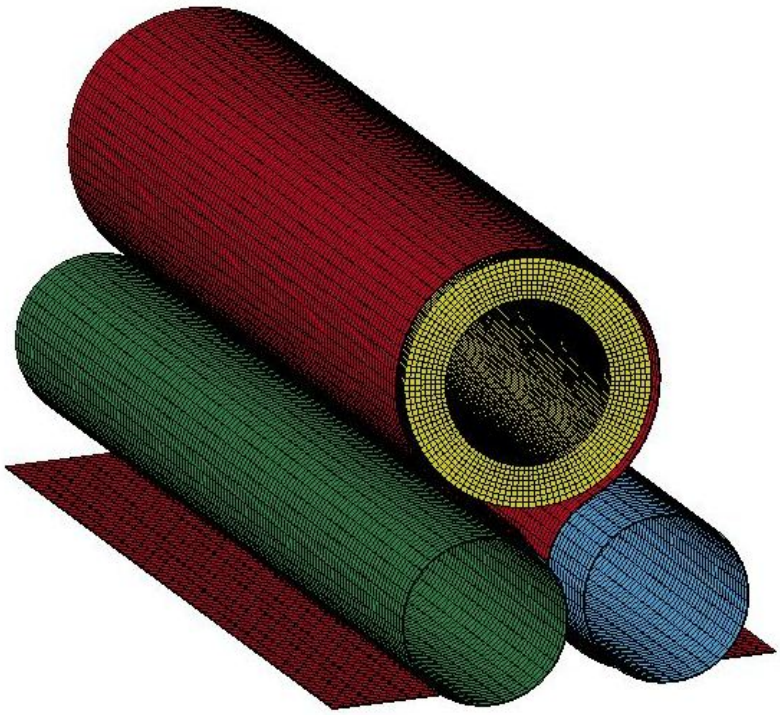

Figure 3.6: Full assembly using rigid Tygon tubing stent analog

Figure 3.7 compares the initial system configuration of this model to the fully constricted configuration. All system parts except for the Mylar were made rigid so changes in system performance due to the newly added stent analog and roller could be monitored with changes in Mylar mesh size. All contacts use the same definitions as those in Section 3.4.2. Comparing total Mylar displacement in the x-direction and time required for model completion, the converged curved Mylar mesh size was determined to be 0.5 mm (Figure 3.8). Observing Figure 3.9, contacts display equal and opposing forces between slave and master segments indicating stable contacts.

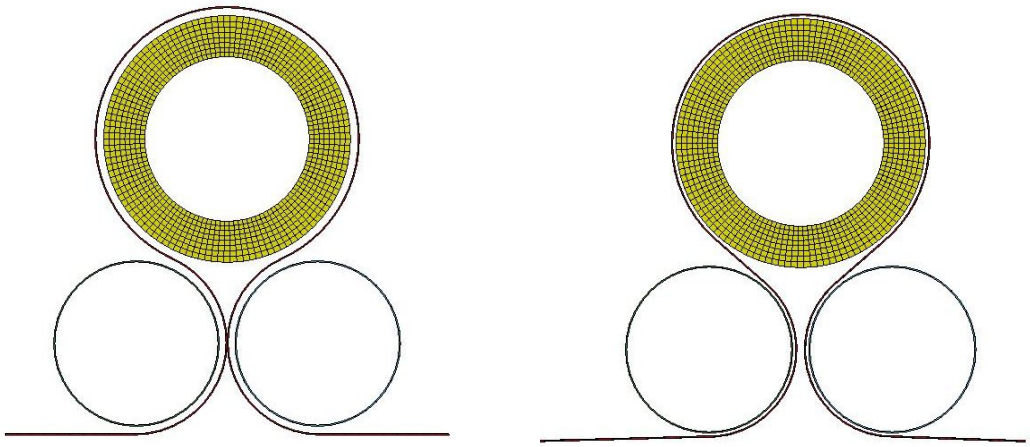

(a) Simulation start (original) **(b)** Fully constricted

Figure 3.7: Contact test for full system with rigid rollers, rigid stent analog and free Mylar

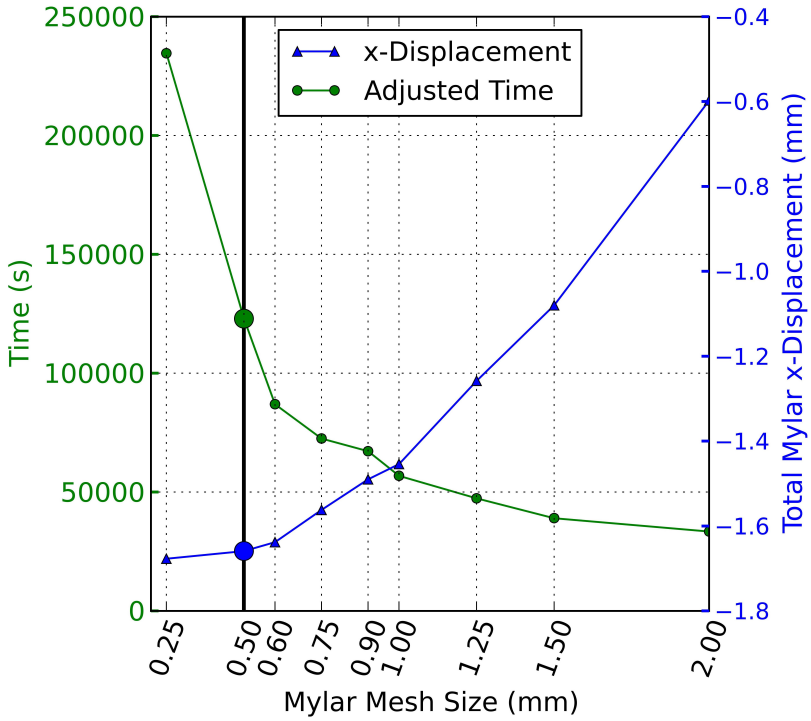

Figure 3.8: Convergence study for full system with rigid rollers, rigid stent analog and free Mylar

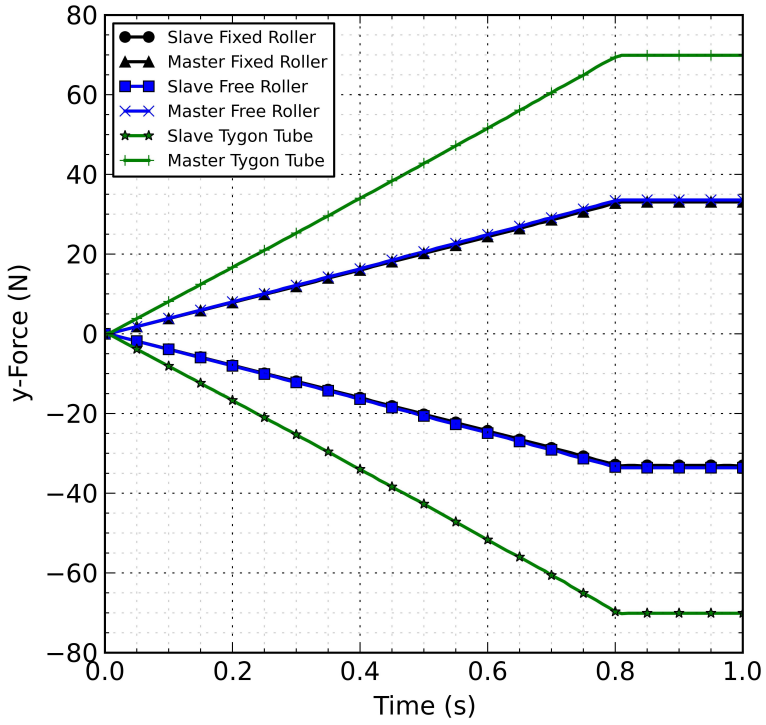

Figure 3.9: Full system; rigid rollers and stent with free Mylar, y-contact force

3.4.4 Full System - Rigid Rollers; Free Stent Analog and Mylar

The next step toward a complete system model is to change the material model of the stent analog from "*MAT_RIGID" to "*MAT_ELASTIC". This alteration will allow the stent analog to move freely and be deformed by the Mylar film during simulation.

Contact between Mylar and the non-rigid analog will include large deformation and non-ideal contact angles. Considering these circumstances, "*CONTACT_AUTOMATIC_SURFACE_TO_SURFACE" will not operate as effectively due to its preference for normal orientation of both contacting shell surface segments. Contact formulation is changed to "*CONTACT_AUTOMATIC_NODES_TO_SURFACE", which checks each slave node for penetration through the master surface and is not limited by contact surface orientation[177]. A soft contact algorithm is used to avoid contact failure due to large differences in Young's modulus between the Tygon tubing stent analog and Mylar film. Using the same criteria as in Sections 3.4.2 and 3.4.3, contact success can be shown by the symmetry of slave and master y-force values as seen in Figure 3.10.

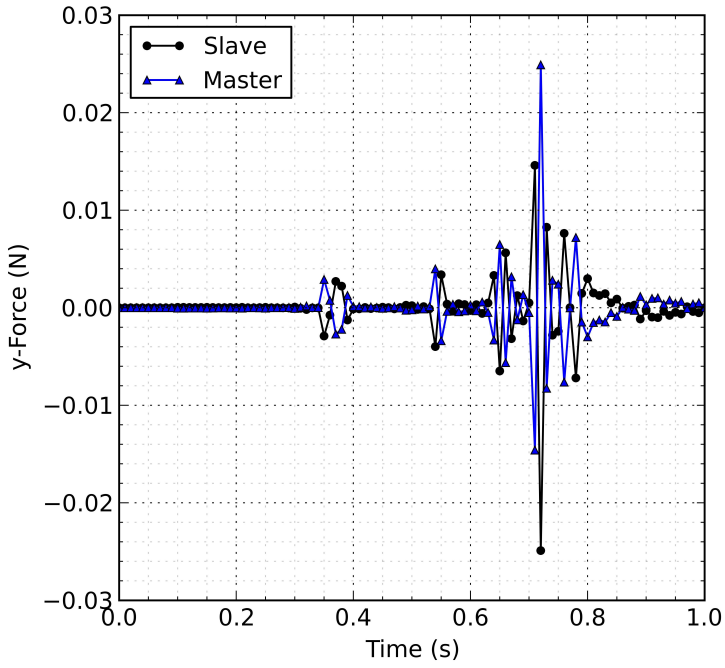

Figure 3.10: y-Contact force between Tygon tubing stent analog and Mylar film

A comparison of original and fully constricted model shapes can be seen in Figure 3.11. This deformation is caused in a similar fashion to previous model iterations, however, the Mylar film was moved by assigning a set displacement instead of a set force. This change was made in order to constrict the Tygon tubing regardless of the force required.

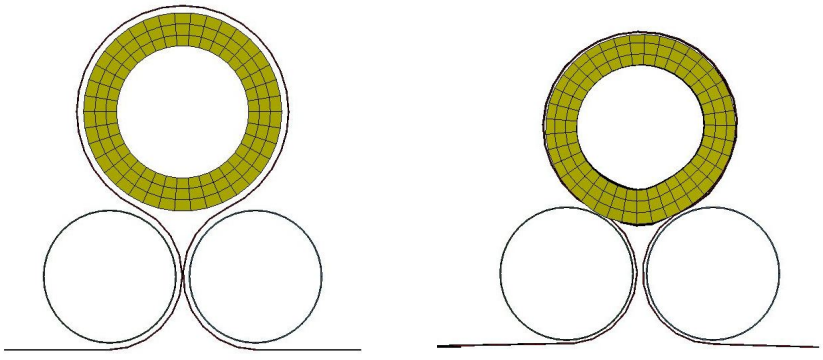

(a) Simulation start (original) **(b)** Fully constricted

Figure 3.11: Contact test on full system with rigid rollers; free stent analog and Mylar

3.4.5 Completed Simulation - Rigid Rollers; Free Stent and Mylar with Friction

Figure 3.12 shows a rendering of the final completed simulation. Several changes have been made since the previous iteration to achieve this completed model.

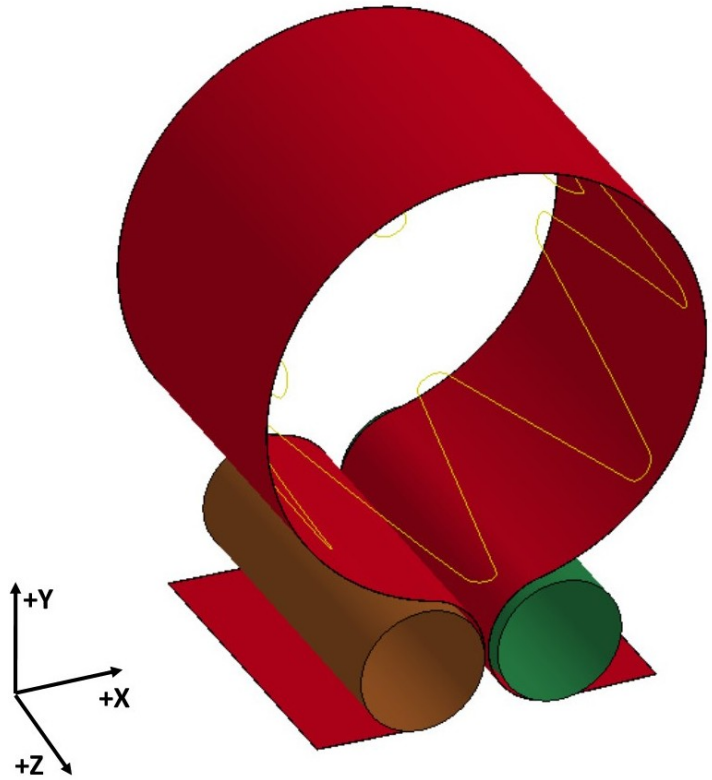

Figure 3.12: Final completed model - rigid rollers; free stent and Mylar with friction

First, the manner in which displacement was applied to the model was changed to more closely resemble that of the experimental setup. Instead of fixing the rollers and one edge of the Mylar like in previous iterations, the rollers and one free edge of the Mylar are moved a set distance in the +x-direction, while one edge of the Mylar remains constrained.

Next, the roller furthest in the -x direction was made free to rotate. As the Mylar mesh slides over the roller mesh during simulation; x, y and z penalty forces ensure no contact penetration occurs. Even though contact between Mylar and rollers is frictionless, tangential contact penalty forces were growing so large prior to the Mylar sliding over the roller that the contact was failing. Allowing the frictionless roller to

rotate eliminated both this buildup of contact penalty force and unintentional contact penetration.

The Tygon tubing stent analog from previous model iterations was used to develop an effective contact between the Mylar film and a deformable part. With an established effective contact, the stent analog was replaced with an uncovered, geometrically accurate replica of a 12 mm (20.35 mm uncovered, fully expanded diameter) Zenith z-stent. Results from chemical analysis in Section 5.2 confirm that Zenith z-stents are composed of stainless steel 316L. The new geometrically correct stent model uses the same stainless steel 316L elastic material model as the system rollers whose properties are defined in Table 3.4. An extra constraint was added to the stent to avoid movement in the z-direction throughout simulation. A node at the peak of each bend on the +z side of the stent was constrained to avoid motion in the z-direction. Only one side of the stent was constrained to ensure the stent could still extend in the z-direction during constriction.

Contact definition variables for slave and master penalty stiffness scaling factors as well as sliding interface penalty scaling factors were manipulated to achieve a stable contact between the significantly varying thicknesses and Young's moduli of Mylar and stainless steel. These values ensure that contact penetration does not occur throughout simulation while using penalty based contact algorithms. For the contact between stent and Mylar, the interface definition was changed from "*CONTACT_AUTOMATIC_NODES_TO_SURFACE" to "*CONTACT_NODES_TO_SURFACE" since removal of the Tygon stent analog in the previous model iteration. Because Mylar shell elements only need to check for contact penetration on one side throughout simulation and the direction of surface orientation is known, the Mylar to stent contact is changed to a non-automatic formulation to reduce simulation time[180]. "*CONTACT_NODES_TO_SURFACE" is effective for a beam to shell surface contact like that between the stent and Mylar[181]. This one-way contact checks each slave node (stent beam elements) for penetration through the master surface (Mylar shell elements)[177].

Along with updated Mylar to stainless steel contacts, a stent self-contact was introduced using "*CONTACT_AUTOMATIC_GENERAL" to ensure that during constriction the stent couldn't pass through itself. If beam elements from different

sections of the stent come close enough to touch each other during constriction, the ability for the stent to interact with itself is crucial to model accuracy.

The width of Mylar and rollers were shortened to better match the width of the stent. Previous Mylar and roller widths of 55 mm and 65 mm were altered to their new dimensions of 16.7 mm and 17.7 mm respectively. With a width of 16.21 mm (Table 5.1), the stent is still able to fit inside the Mylar loop throughout constriction and expansion. Shortening these dimensions cut a significant amount run-time from the simulation as a large number of elements could be removed from the system mesh.

To improve the accuracy of model results, geometry of the un-deformed Mylar was corrected. This correction ensured that during constriction and expansion the leading and trailing sections of the Mylar film remained parallel to the x-z plane. Geometry of the rollers was also adjusted to make certain that the outer diameter used by the LS-DYNA contact algorithm accurately represented the geometry of the rollers in the experimental setup.

A new technique to gather simulated force data in a similar fashion to that used by the radial extensometer experimental setup was introduced in this section. The "nodfor" database file was output during simulation, which allows forces registered by constrained nodes and nodes with prescribed motion to be output and plotted.

Finally, frictional effects were introduced to the model using the Coulomb friction constants. The static and dynamic coefficients of friction are both set equal to each other, eliminating dependence of the results on relative velocity of the surfaces in contact. An in depth explanation of coefficient selection can be found in Section 3.5.3. This constant will not only serve to introduce frictional effects into the simulation but also as a method of accounting for unknown sources of error during model fitting.

A significantly more dramatic result is noticed between the original and fully constricted models than in previous iterations. The geometrically accurate stent is able to deform radially far more than the previously used Tygon tubing analog. A comparison of fully expanded and fully constricted simulation states is shown in Figure 3.13.

The interaction between stent and Mylar can be visualized in a full system representation of von Mises stress in Figure 3.14. Interestingly, contact and force transfer between the stent and Mylar sheet during expansion seems to be limited to the legs of

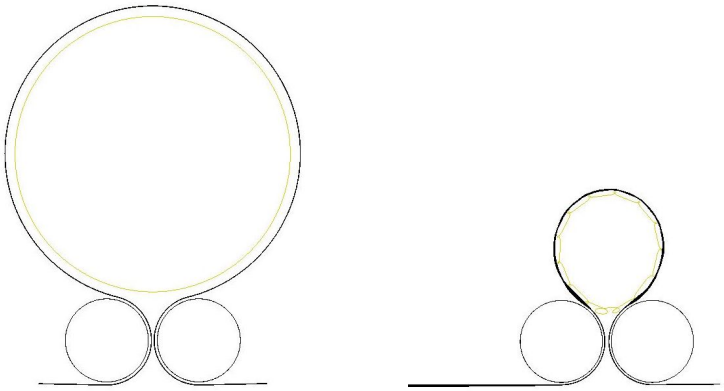

(a) Simulation start (original) **(b)** Fully constricted

Figure 3.13: Completed simulation constriction with rigid rollers; free stent and Mylar with friction

the stent as shown by areas of peak von Mises stress in this figure. It is very promising to see symmetrical loading around the Mylar for the points where each stent leg and the Mylar come into contact.

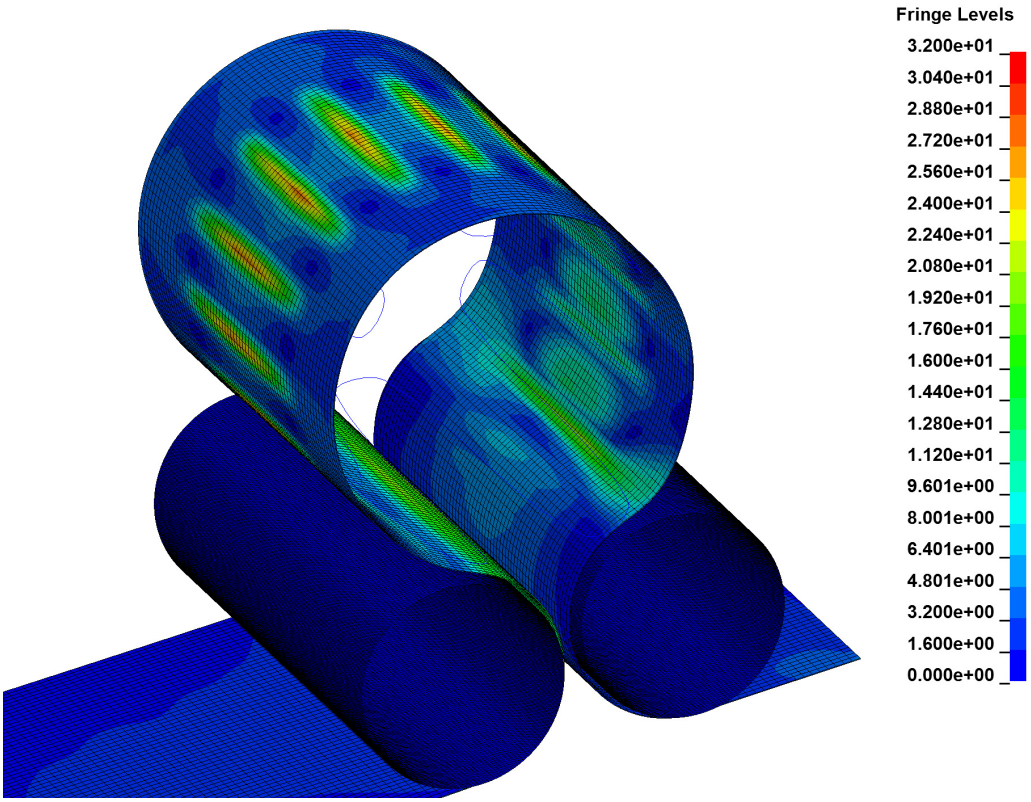

Figure 3.14: von Mises stress (MPa), full model at 157.5 s

3.5 Convergence Study

The final completed model requires a fully converged mesh and comparison to a real world data set to gain credibility. Demonstrating model convergence for this system is challenging because it contains three separate parts interacting with each other, introducing three degrees of freedom.

3.5.1 Geometrical Accuracy and Mesh Refinement

Geometrical refinement of the rollers has made it possible to remove one of the three degrees of freedom in this system. Rollers are modeled as rigid bodies which means there are no stress or strain values calculated for them during the simulation. According to LS-DYNA support documents on rigid body contacts, rigid bodies require a reasonably fine mesh which accurately captures the true geometry of the part[182]. Measuring the length of the tangential line between the flat edge created by meshing a circular shape, and the arc of the perfect circle being meshed is called a "sagitta" line. Altering roller mesh density has an impact on the height of the sagitta line, which becomes an excellent representation of geometric accuracy. Figure 3.15 shows that the roller mesh density of 0.1 mm used in the final model, accurately represents the circular shape being simulated.

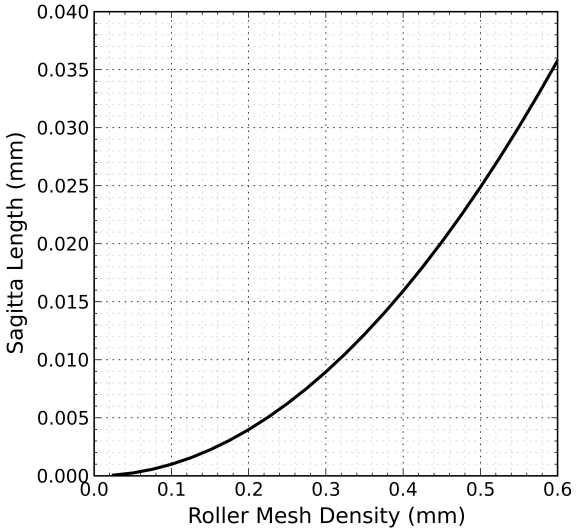

Figure 3.15: Separation error: a sagitta line drawn between the outer edge of the roller geometry and the mesh created to represent it

LS-DYNA recommends that rigid body node spacing be no coarser than the mesh of whatever deformable parts it comes into contact with[182]. In the final simulation, the roller mesh size is much smaller than that of the Mylar at 0.1 mm and 0.25 mm respectively. With geometric and mesh density errors minimized, the impact of roller mesh size should not have an impact on overall model convergence or contact stability.

3.5.2 Final Convergence

Two degrees of freedom remain, Mylar and stent mesh density, therefore, a two-dimensional convergence study is required to analyze the combined impact of these characteristics on overall model behavior. Convergence is analyzed using both model completion time (Figure 3.16) and peak simulated force (Figure 3.17).

The final converged mesh size selection is annotated in Figures 3.16 and 3.17 with the letter 'A'. Convergence occurs with a Mylar mesh density of 0.25 mm and a stent mesh density of 0.4 mm. The converged force value of this model is at the center of the convergence "bowl" in Figure 3.16 at the point which reaches furthest toward equilibrium. Examining the simulation time convergence for this same mesh size, point 'A' falls within the equilibrium region of Figure 3.17, just before a steep ramp up in simulation run-time which occurs with decreasing Mylar mesh density.

A correction was made prior to moving on to model fitting. The input value for the Young's modulus of Mylar was discovered to be incorrect and was corrected to 4805.26 MPa[166]. This will not impact the convergence study outcome, as the value was kept constant throughout the investigation.

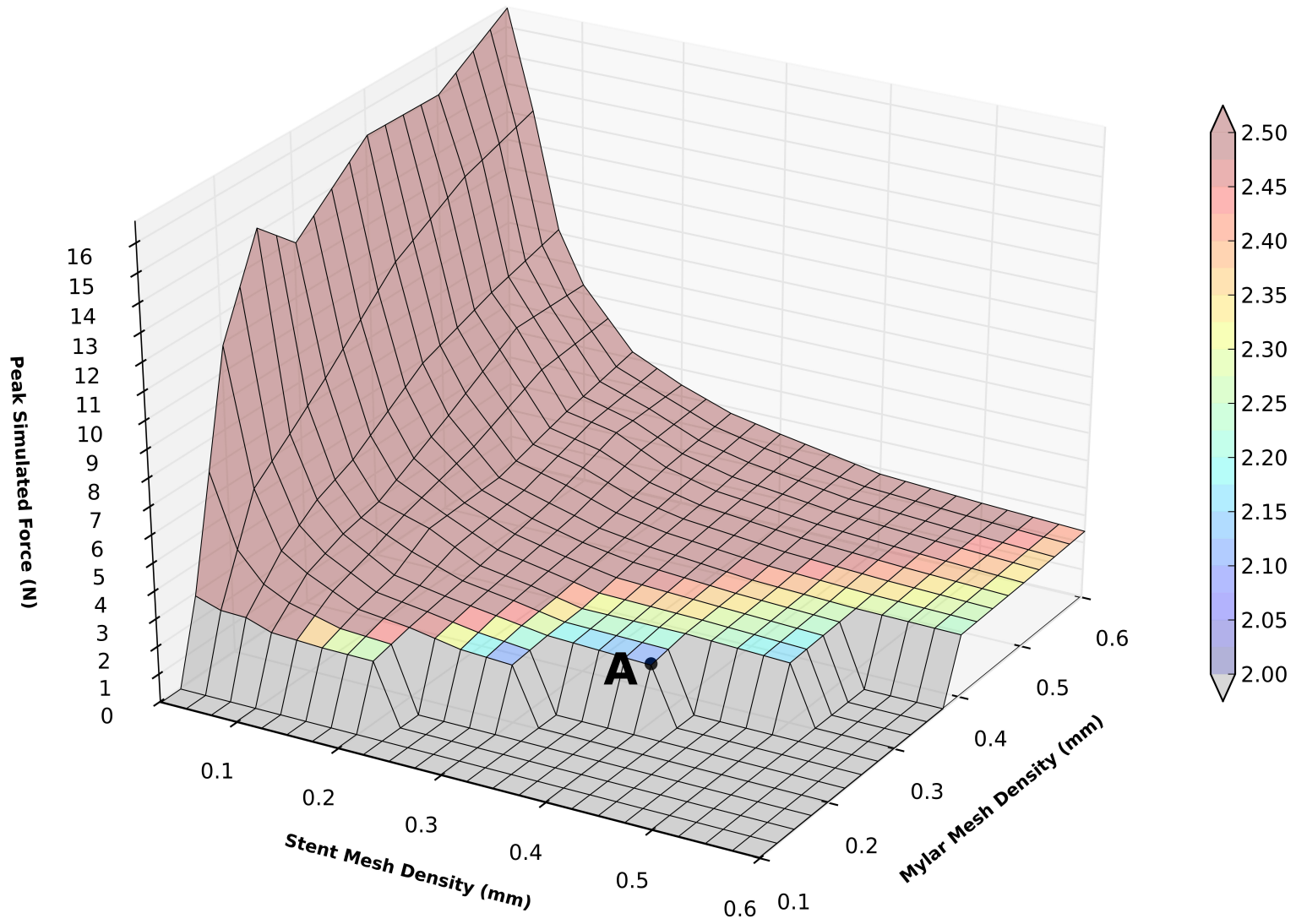

Figure 3.16: Mesh convergence with respect to peak force

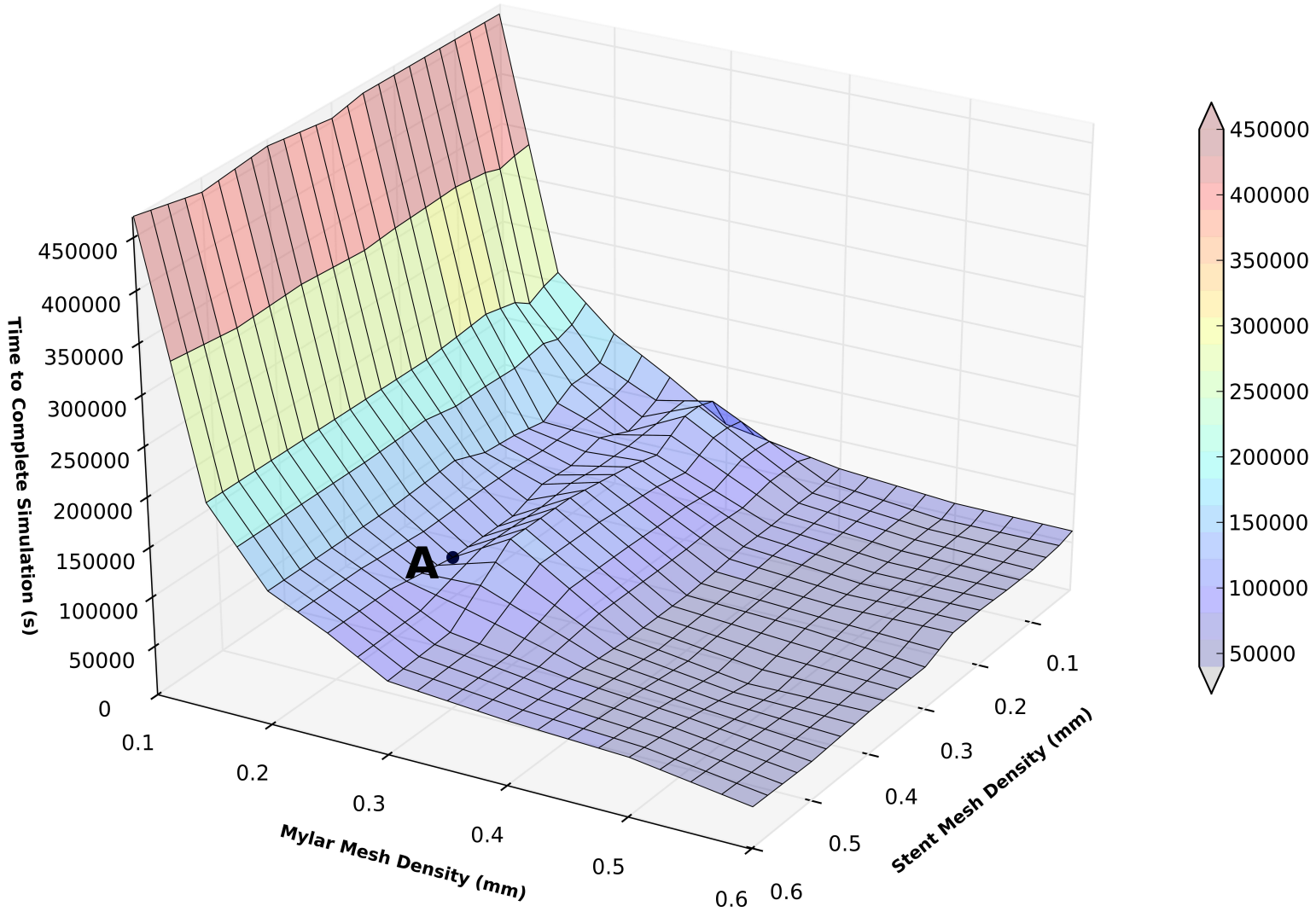

Figure 3.17: Mesh convergence with respect to simulation duration

3.5.3 Model Fit

As previously stated, because this model was designed to match the experimental setup of the radial extensometer, it is possible to fit the final converged simulation to experimental results. Experimental data used in this comparison is calculated in the same fashion as in Chapter 2.

Modeled and experimental data sets compare an uncovered 12 mm (uncovered diameter = 20.35 mm) stent being constricted to a diameter equal to that of a covered stent constricted to 50 % AR (final diameter = 8.49 mm). Because these data sets represent the same motion and mechanics, lining up known values for the center point (the point of peak constriction) of modeled and experimental data will give an accurate comparison of the two results.

The Coulomb friction constant is used as a fitting parameter to match modeled and experimental data as closely as possible. Static and dynamic Coulomb constant values are kept equal throughout model fitting; the effect of altering their values is demonstrated in Figure 3.18. In general, as the Coulomb constant grows, peak force will increase and force measured during expansion will decrease. A frictionless model may best match linear experimental results encountered following the initial force drop-off at the onset of expansion, however, to best match the entire force profile observed during stent expansion, a contact formulation including friction was used. Now that the convergence study is complete, the Coulomb constant value of 0.01 used throughout this investigation can be optimized to yield a better comparison between modeled and simulated results. Observation of the frictionless curve in Figure 3.18 reveals that friction is not solely responsible for force profile non-symmetry. Radial extensometer and stent mechanics may have a larger impact on collected force data than previously thought. Figure 3.18 demonstrates that friction has a large impact on the smoothness and linearity of the radial force profile during expansion.

Model fit success was determined using the coefficient of determination (r^2), standard error of the estimate (SE), mean absolute percent error (MAPE) and mean percent error (MPE) values calculated using Equations 3.10−3.13. As can be seen in Table 3.5, a Coulomb friction constant of 0.0025 best matches experimental data with an r^2 value of 0.953, a standard error of 0.086 N, a MAPE of 13.94 % and an MPE of 3.09 %. These results show a very good fit between experimental and modeled

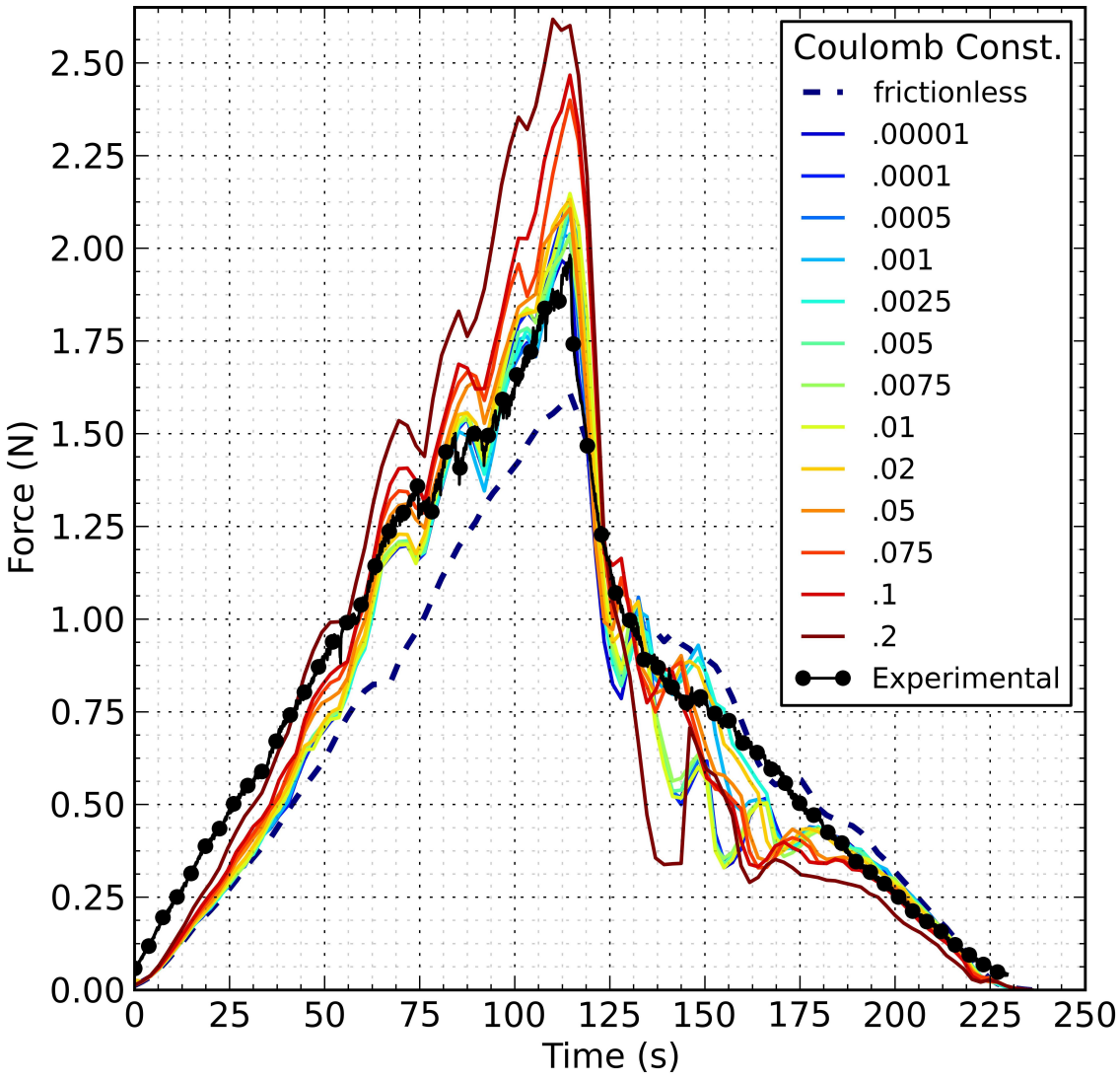

Figure 3.18: The impact on simulation results due to varying the Coulomb friction constants

results. An Coulomb friction constant of 0.0025 falls within the range used by Vad et al.[115], however, it is important to note they did not test stents as small as 12mm in diameter and the stents they were testing were of a different wire configuration. All tests used 4 CPU (central processing unit) cores and 500 million words of memory.

$$r^2 = 1 - \frac{\sum_{t=1}^{n} \left(Y_{1,t} - Y_{2,t}\right)^2}{\sum_{t=1}^{n} \left(Y_{1,t} - \bar{Y_1}\right)^2} \tag{3.10}$$

$$SE = \sqrt{\frac{\sum_{t=1}^{n} \left(Y_{1,t} - Y_{2,t}\right)^2}{n}} \tag{3.11}$$

$$MAPE = \frac{100}{n} \sum_{t=1}^{n} \left| \frac{Y_{1,t} - Y_{2,t}}{Y_{1,t}} \right| \tag{3.12}$$

$$MPE = \frac{100}{n} \sum_{t=1}^{n} \frac{Y_{1,t} - Y_{2,t}}{Y_{1,t}} \tag{3.13}$$

where

r^2 = coefficient of determination
$SE_{Estimate}$ = standard error of the estimate (N)
$MAPE$ = mean absolute percent error (%)
Y_1 = priginal force dataset (N)
$\bar{Y_1}$ = mean of force dataset (N)
Y_2 = model fit force dataset (N)
n = number of values in dataset

Referencing Table 3.5 and Figures 3.19(a) through 3.19(d), it is interesting to note that as friction rises above a Coulomb constant of 0.05, there is a rapid decline in coefficient of determination, peak simulated force and simulation run-time; while standard error rises significantly. Coulomb constant values above 0.05 are detrimental to simulation performance and should not be used.

Because modeled and experimental results are aligned for comparison using the peak value of constriction, any deviation from the ideal 50 % AR for either result will contribute to model fitting error.

A new set of experimental data was taken and adjustments to model inputs were made due to the discovery of errors in the linear velocity of modeled components and the peak AR of collected experimental results (Table 3.6). Experimental data sets did not reach target values for gross or covered AR (82.6 % and 50 % respectively). Because of this miscalculation, original experimental values for maximum gross and covered AR noted in Table 3.6 correspond to errors of 2.13% and 10.2% respectively when compared to target values.

Table 3.5: Model fitting results

Coulomb	CPU Time (s)	F_{Peak} (N)	r^2	SE (N)	MAPE (%)	MPE (%)
0.0	98638	1.61	0.967	0.072	15.20	-8.29
0.00001	92002	1.97	0.852	0.150	20.44	12.38
0.0001	91927	2.14	0.842	0.155	20.51	11.10
0.0005	93533	2.04	0.860	0.146	19.70	11.61
0.001	96466	2.10	0.914	0.114	16.01	3.76
0.0025	**98638**	**2.04**	**0.949**	**0.088**	**13.94**	**3.09**
0.005	93534	2.12	0.843	0.154	20.24	11.21
0.0075	95597	2.04	0.865	0.143	19.64	11.73
0.01	93155	2.15	0.811	0.169	20.48	11.28
0.02	97391	2.13	0.934	0.100	13.56	4.55
0.05	99542	2.11	0.919	0.111	15.92	11.52
0.075	81722	2.40	0.776	0.184	19.20	11.53
0.1	81794	2.47	0.750	0.195	20.74	13.42
0.2	81794	2.62	0.502	0.275	33.96	26.70

Table 3.6: First and second round model and experiment (±SD)

	Model 1	Model 2	Experiment 1	Experiment 2
Linear velocity (mm/s)	0.36	0.33	0.33	0.33
Gross reduction (%AR)	82.4	82.4	80.9 ± 1.1	82.7 ± 0.5
Covered reduction (%AR)	49.5	49.5	44.9 ± 3.0	50.2 ± 1.4

Measurement of AR for modeled data was performed using scaled images from LS-PrePost that were imported into SolidWorks. Results are accurate when compared to target values with a calculated deviation from 50 % AR for gross and covered AR of 0.2 % and 1.0 % respectively. Unfortunately, model linear velocity was off when compared to experimental settings by 8.48 %.

Both errors were corrected prior to a comparison of final fit model and experimental data. After correction, linear velocity of model and experimental systems were equivalent. Comparison of modeled and experimental values for gross and covered AR were 0.3 % and 1.4 % respectively. With these corrections, it is now possible to

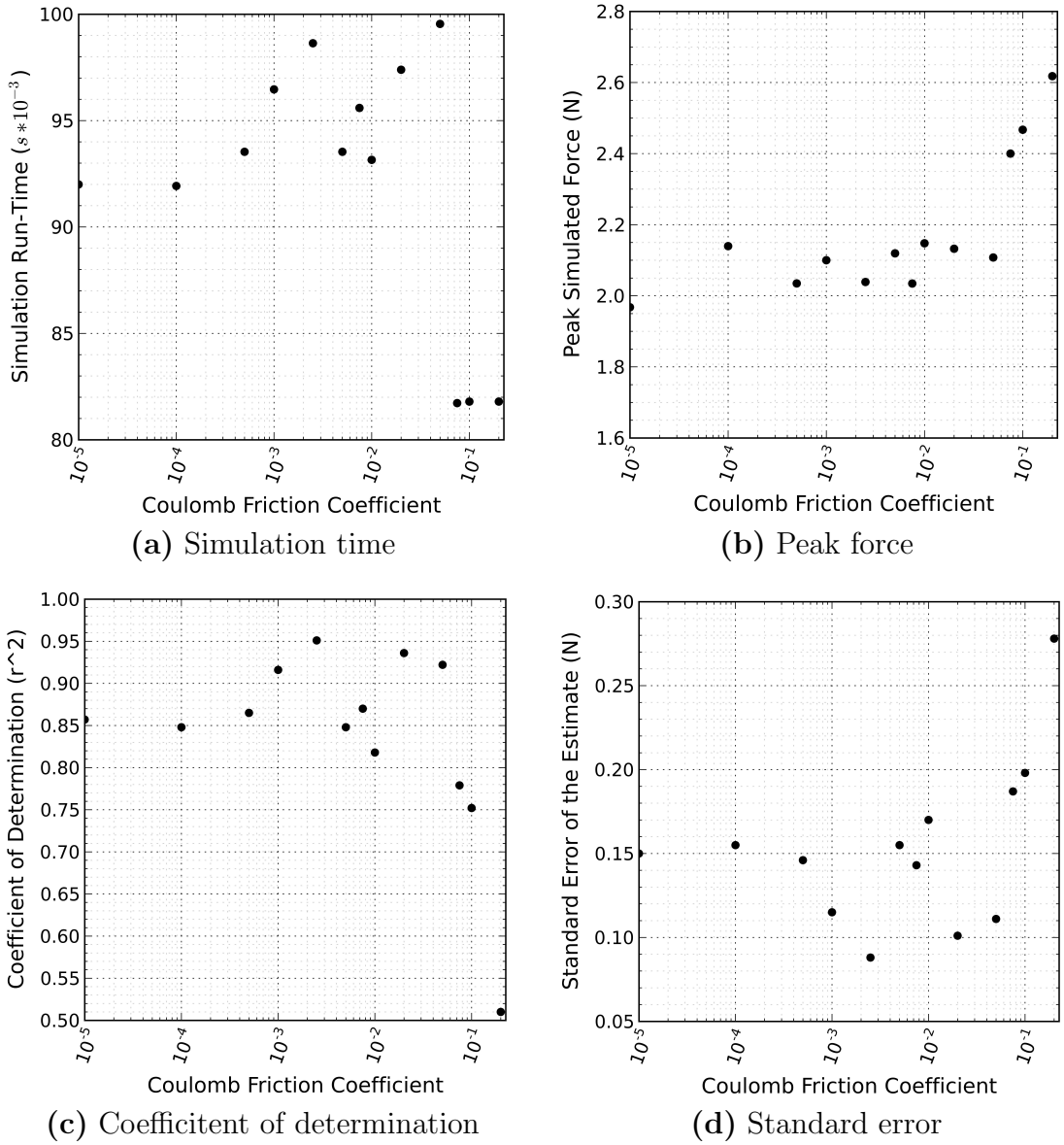

(a) Simulation time **(b)** Peak force

(c) Coefficitent of determination **(d)** Standard error

Figure 3.19: Results of model fitting friction analysis

be confident that the point of max constriction for both experimental and modeled data is lined up to within an acceptable margin of error prior to comparison.

Comparing corrected data to experimental data produces a slightly altered coefficient of determination of $r^2 = 0.946$, a standard error of 0.099 N, a MAPE of 11.69 % and an MPE of 1.69 %. For a Coulomb constant of 0.0025, these values still present the best fit compared to other results in Table 3.5. It is unlikely that re-running every model with new input for linear velocity will change the outcome of the model fit.

r^2 and standard error results for a Coulomb constant of 0.0025 demonstrate a good fit between model and experimental results. This validated model can now be used for analysis.

The final converged model, fit to experimental data with a coulomb constant of 0.0025 is presented in Figure 3.20. Modeled data is offset by 12.351 s to line up the point at which modeled and experimental data both reach max constriction. Enlarged results for the period of stent expansion only are shown in Figure 3.21.

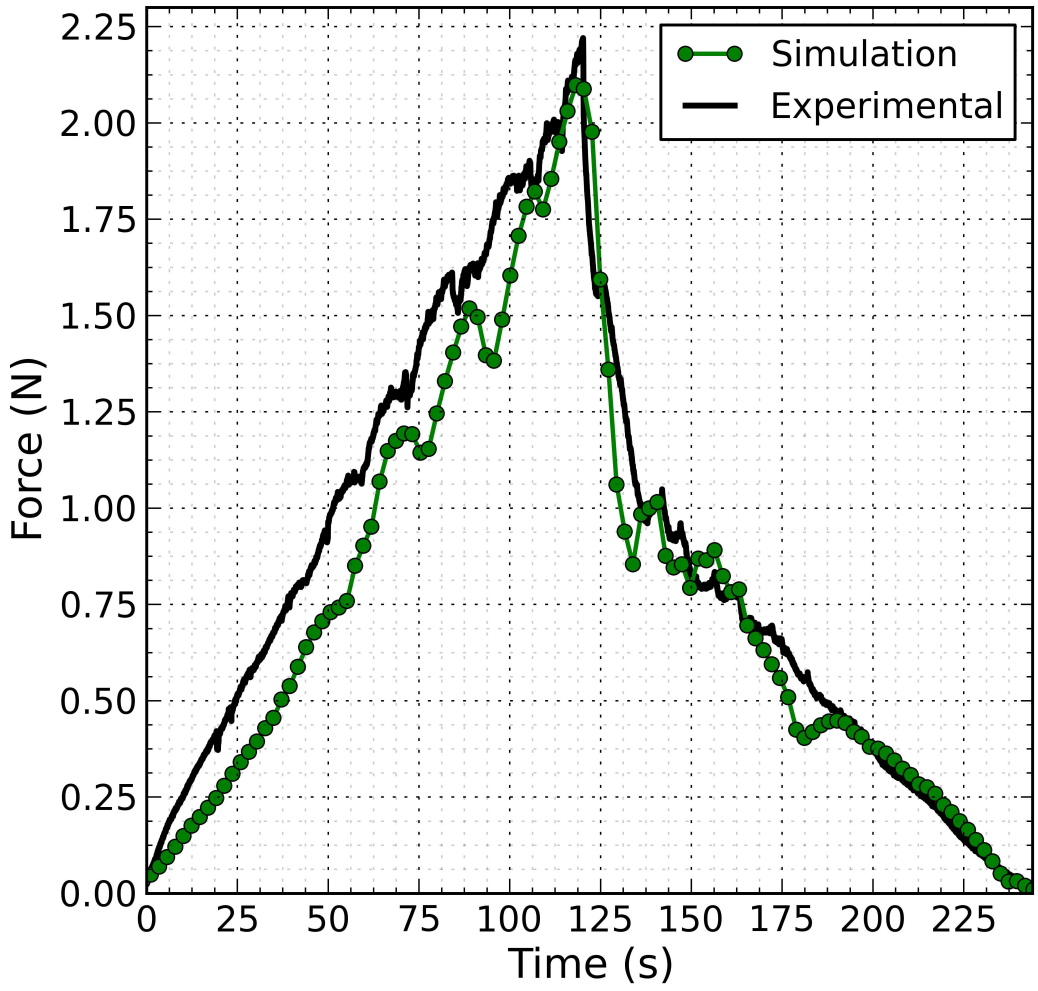

Figure 3.20: Completed model fit and comparison of full simulated and experimental data profile

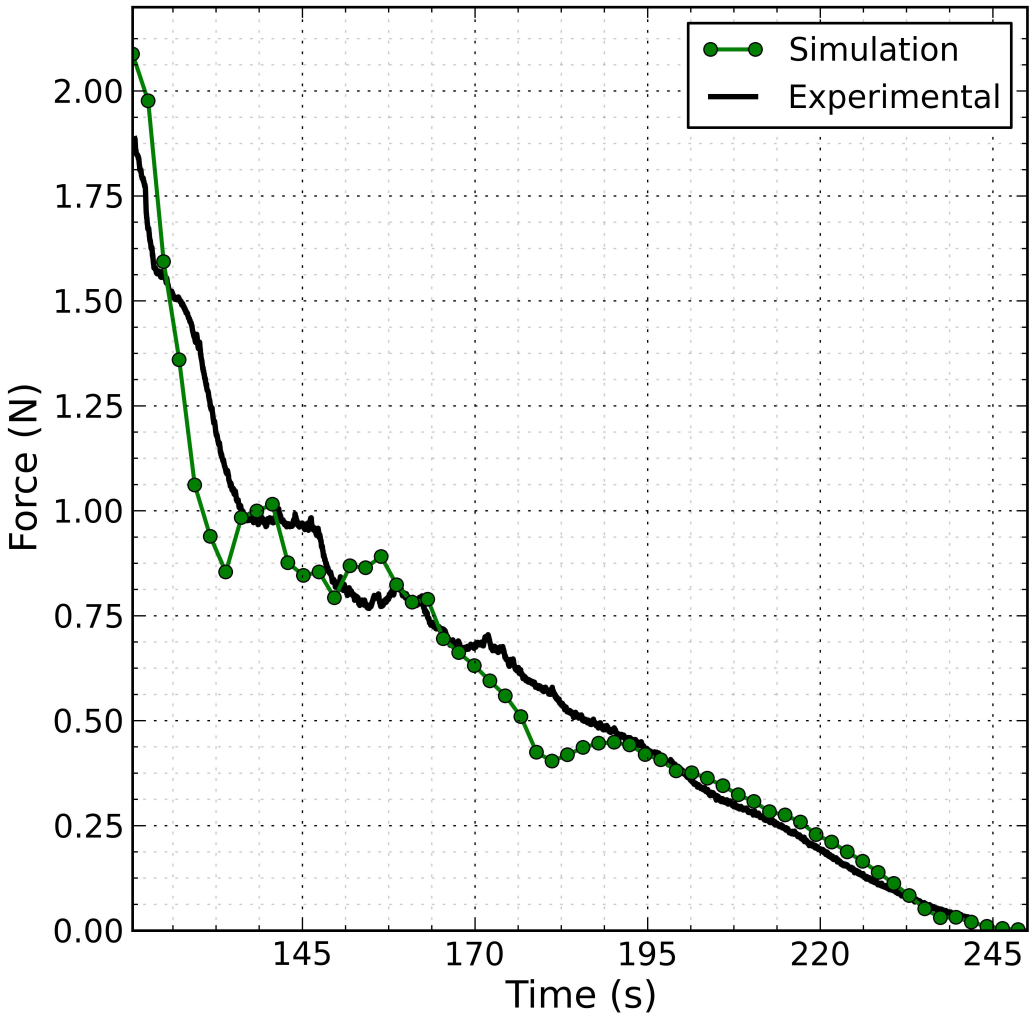

Figure 3.21: Completed model fit and comparison of simulated and experimental data during expansion only

Chapter 4

Supplemental Finite Element Investigations

With a completed model fit it is possible to draw some preliminary conclusions on the mechanical properties of self-expanding z-stents by examining the mechanisms responsible for radial force generation. Model analysis will also prove useful to understanding the impact of the radial extensometer on collected data.

In the future, adjustments to stent performance will be made based on patient specific requirements. Initial in-vivo modeling will introduce tools to examine the interaction between custom prosthetics and the vessel wall. Future iterations of this preliminary simulation could also both investigate the impact of varying haemodynamic drag loads on stent fixation as well as the likelihood of endoleak at different levels of oversize and AR.

4.1 Model Analysis

All analysis is performed in the local coordinate system using 's' (vertical orthogonal) and 't' (horizontal orthogonal) directions as demonstrated in Figure 4.1.

Examining results for bending moment in the t-direction, it is possible to extract data from a node in the center of a stent bend and leg to examine their individual contributions to overall model results. Figure 4.2 shows a significant difference between bend and leg t-bending moment profiles. The smooth, symmetric profile measured in the center of a stent leg that is not in contact with a roller, averaged with a t-bending moment profile from the center of one of its nearest bends reveals a curve of similar shape to the final model fit in Figure 3.20. Figure 4.2 is critical as it provides convincing evidence that the complete stent force profile is a combination of input from several different mechanical systems. Friction, t-bending , s-bending, torsion and the radial extensometer itself all play a roll in the shape of collected data. The sharp drop-off in t-bending moment data collected from the center of the stent

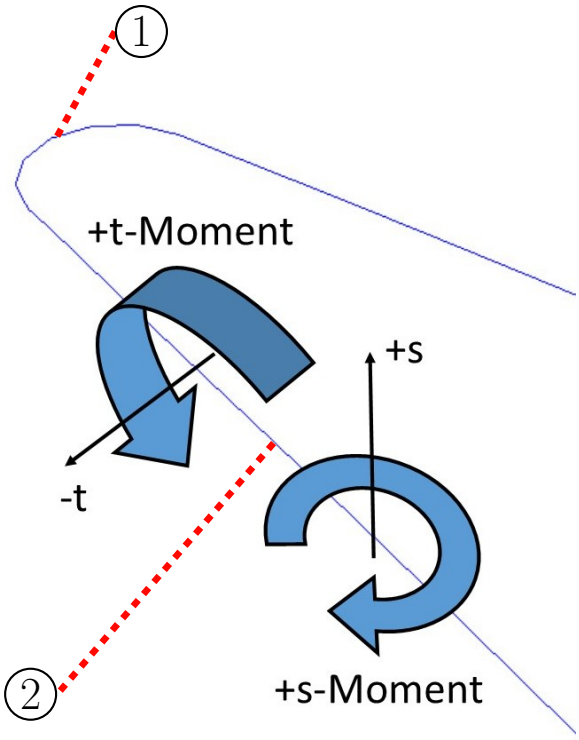

Figure 4.1: Coordinate system for model analysis - demonstrated on stent leg: 1 - center of bend, 2 - center of stent leg

bend provides insight into why the frictionless simulation radial force profile from Figure 3.18 did not produce symmetric results during constriction and expansion.

There is evidence that the origin of spikes and dips in data throughout the simulation is due primarily to stent legs passing over the radial extensometer's rollers. Figure 4.3(a) shows a filled outer profile for superimposed t-bending moment results of all stent legs that come into contact with rollers throughout testing. The stark contrast in shape between a non-contact stent leg and the contact leg t-bending moment outline demonstrates the impact that rollers have on modeled and experimental results. Figure 4.3(b) presents the same data set, however, all contact and non-contact t-bending moment values are averaged instead of showing the maximum profile of superimposed data sets. This figure demonstrates how well the peaks and troughs of contact leg and model fit data line up. It is clear that contact of stent legs and rollers has a visible impact on collected radial force data, which is significantly larger at higher levels of constriction as stent legs are pinched between and forced into the +x and -x rollers.

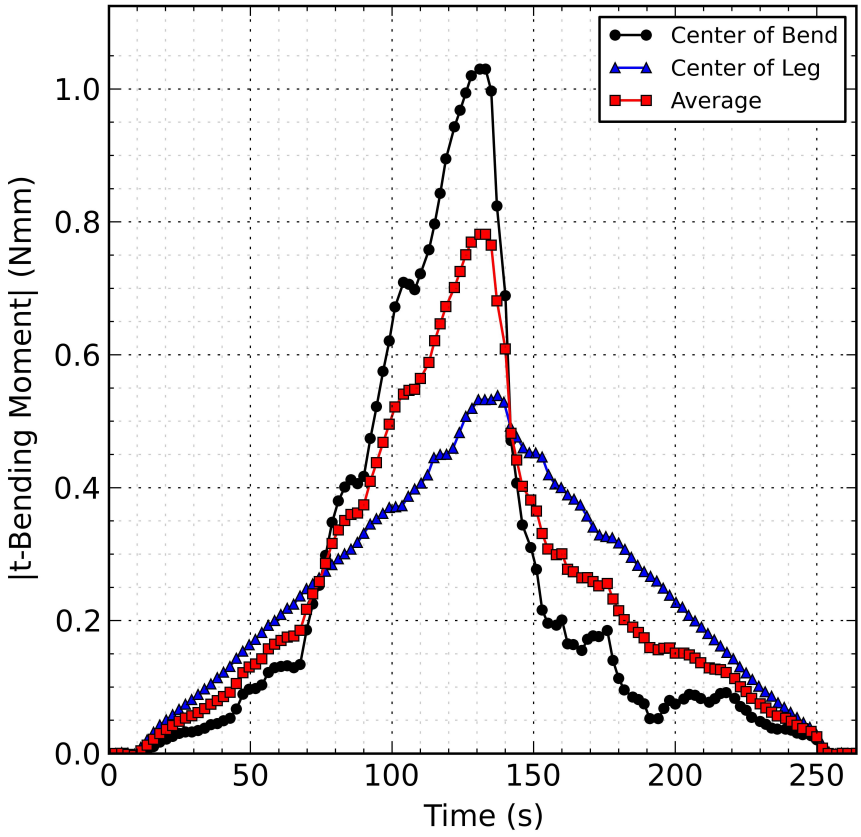

Figure 4.2: t-Bending moment comparison between stent leg and bend - not in contact with the rollers

Moving on to examine bending in the s-direction, Figure 4.4(a) demonstrates that there is a smooth, linear, symmetric increase and decrease of s-bending moment throughout testing at nodes centered in stent bends. There is no s-bending moment measured at nodes centered in the stent leg. Figure 4.4(b) shows the smooth, linear increase of s-moment bending from the center of a stent leg to the center of the nearest stent bend. The profile exhibited by Figure 4.4(b) is nearly identical to that which would be expected from a bending moment diagram for a cantilever beam, with a slight deviation near element number 18 as the nodes transition through the stent bend. It is interesting to note that each stent leg can be represented by two cantilever beams acting in opposite directions which start at neighboring stent bends and end in the middle of the stent leg.

Axial stress (Figure 4.5(a)) and s-bending moment (Figure 4.5(b)) have nearly identical profiles and distributions. Furthermore, both axial stress and s-bending also

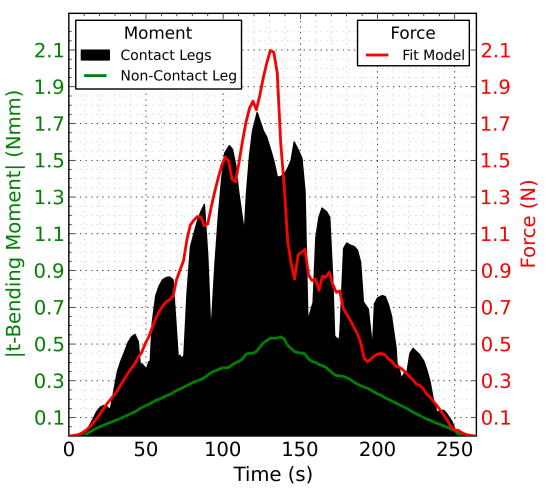

(a) Outline of superimposed t-bending moment profiles

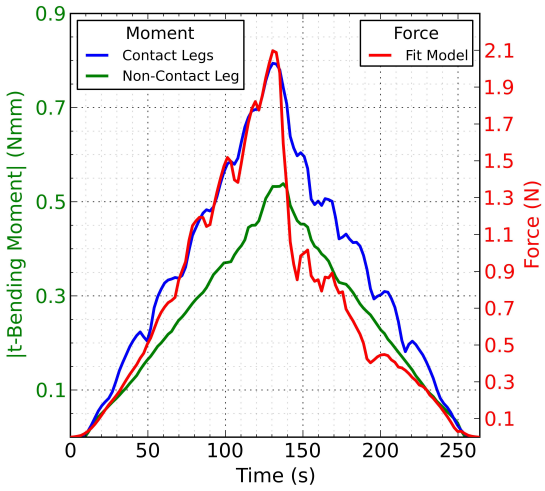

(b) t-Bending moment average

Figure 4.3: The impact of stent wire leg and roller contact on radial force results

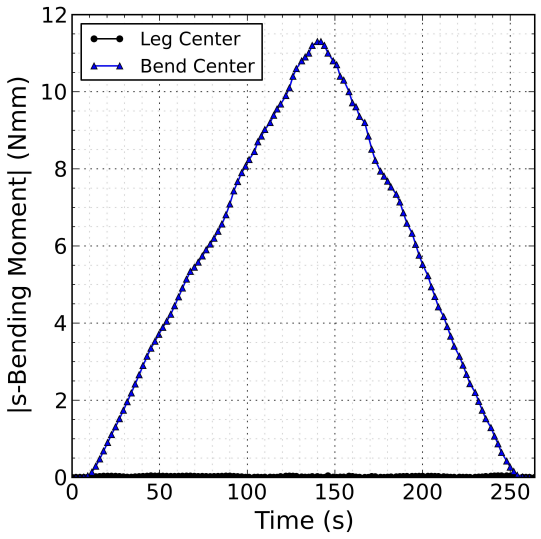

(a) s-Bending moment - center of bend vs. center of leg

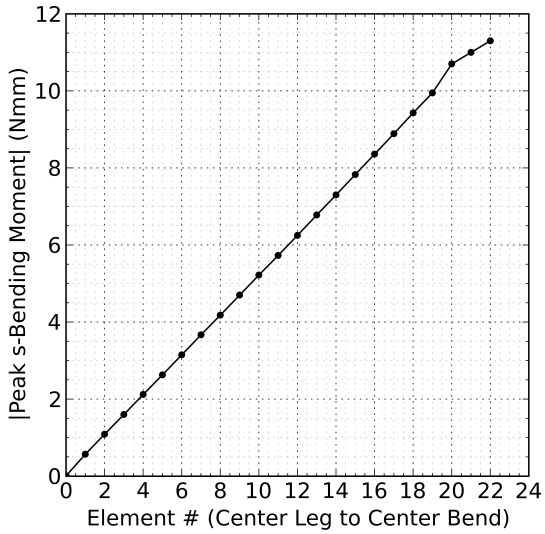

(b) s-Bending moment distribution at peak load from center leg (x= 0) to center bend (x= 22) (Nmm)

Figure 4.4: s-Bending moment - bend vs. leg

have zero values at the center of stent legs. Both profiles provide evidence that the large peak and sharp drop-off in force during the switch from constriction to expansion is caused by stent bends being pinched between the rollers of the experimental setup.

t-Bending moment results do not show the same contrast between pinched and unpinched bends.

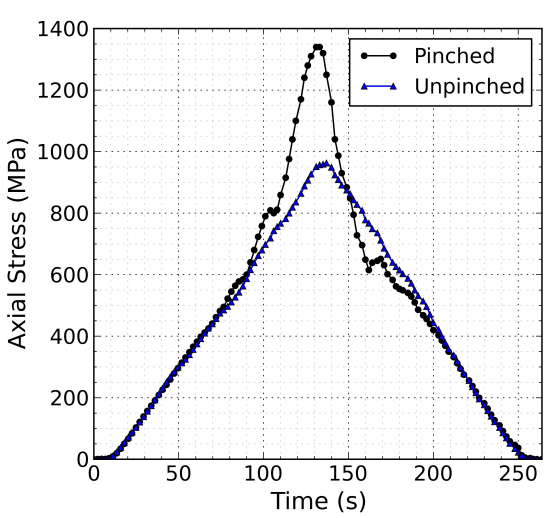

(a) Axial stress - center of bend

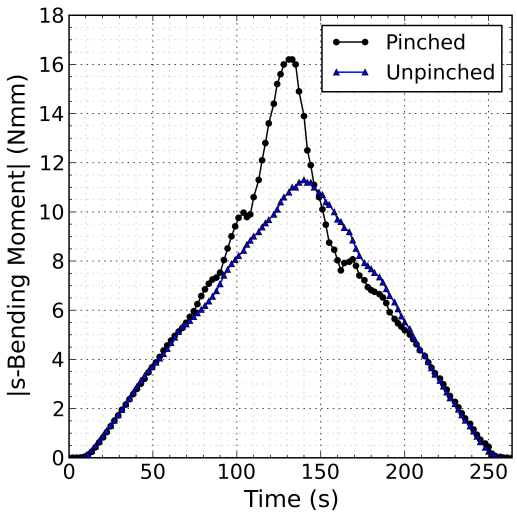

(b) s-Bending moment - center of bend

Figure 4.5: Comparison of axial stress and s-bending moment profiles

As was seen for s-bending moment, t-bending moment also produces a double cantilever-like reaction where two cantilevers, anchored in stent bends, meet in the center of the stent leg (Figure 4.6(a)). This bending moment causes the center of stent legs to bow out radially, explaining why the majority of arterial contact and force transfer is performed by stent legs, as shown in Figure 3.14.

Figures 4.7 and 4.6(b) show s and t-force distribution during expansion at 159.75 s through the simulation. At this point, the drop off in force following the switch from constriction to expansion has finished and stent force is linearly decreasing. The reaction portrayed in these figures is a good example of what could be expected during a smooth expansion. t-Force distribution shows connected stent legs pushing away from each other, while s-force distribution demonstrates an interesting zig-zag pattern of force distribution on alternating stent legs. s-Force and radial force present identical profiles, which Figure 4.7 shows is of negligible magnitude in bends and at a maximum in stent legs. This is in line with previous observations of the transfer of force between stent and Mylar as seen in Figure 3.14. With further analysis, s-force data will help develop an understanding of how radial force generated by the stent

and linear force measured by the radial extensometer force gauge relate to each other. Radial force data is crucial to developing an understanding of how stents interact with the vessel walls.

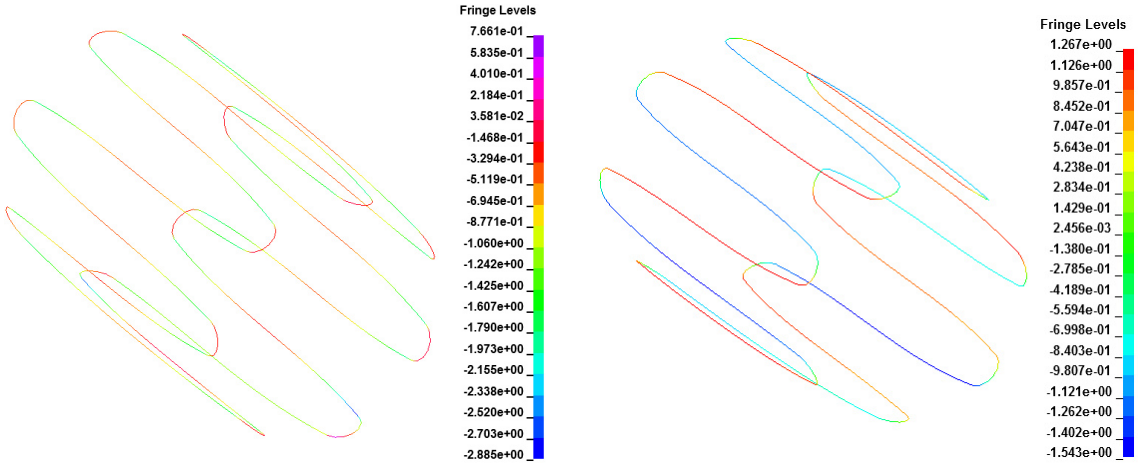

(a) t-Bending moment (Nmm) **(b)** t-Force (N)

Figure 4.6: t-Bending moment and force distributions during expansion at 159.75 s

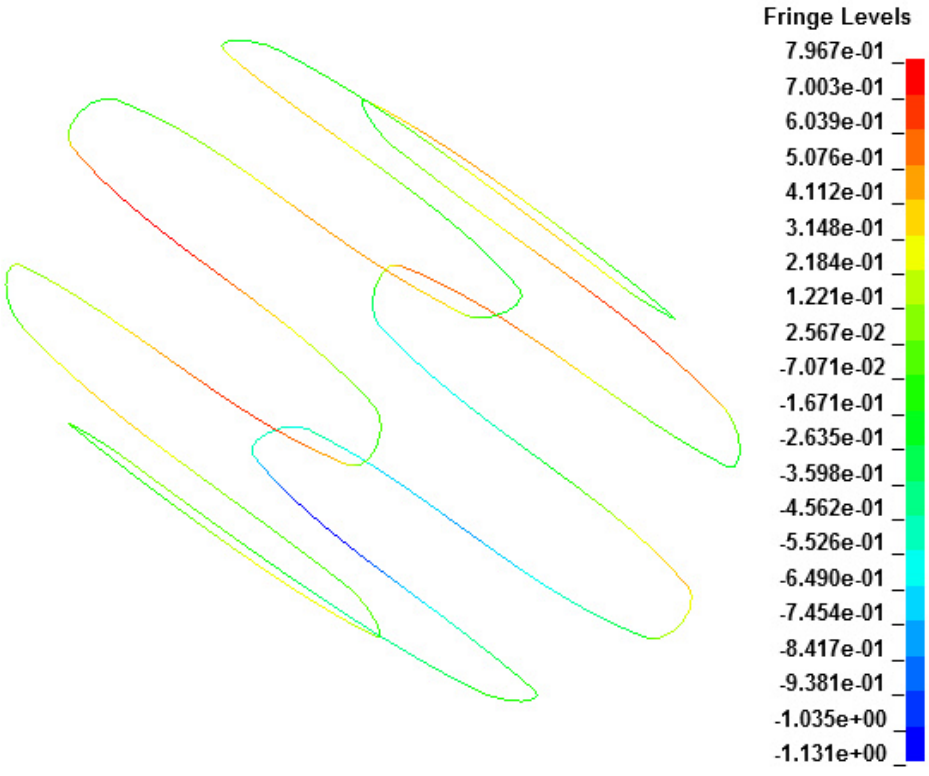

Figure 4.7: s-Force [RADIAL FORCE] during expansion at 159.75 s (N)

Regardless of where on the stent torsion is measured, there is an incredibly abrupt drop off in torsion and a slow period of controlled relaxation ("unwinding") following the change from constriction to expansion. Summing the magnitude of the torsional resultant for one entire leg, from the center of neighboring bends, Figure 4.8(a) provides a similar profile to the final model fit in Figure 3.20.

The direction of torsion alternates for each stent leg. The slope direction also makes an abrupt change at the peak of each bend with nearly identical but opposite profiles going down each adjoining leg. The nearly identical but opposite torsional resultant profiles from the center of two adjoining legs is shown in Figure 4.8(b). Both profiles displayed in Figure 4.8 provide more evidence as to the origin of the non-symmetrical radial force profile.

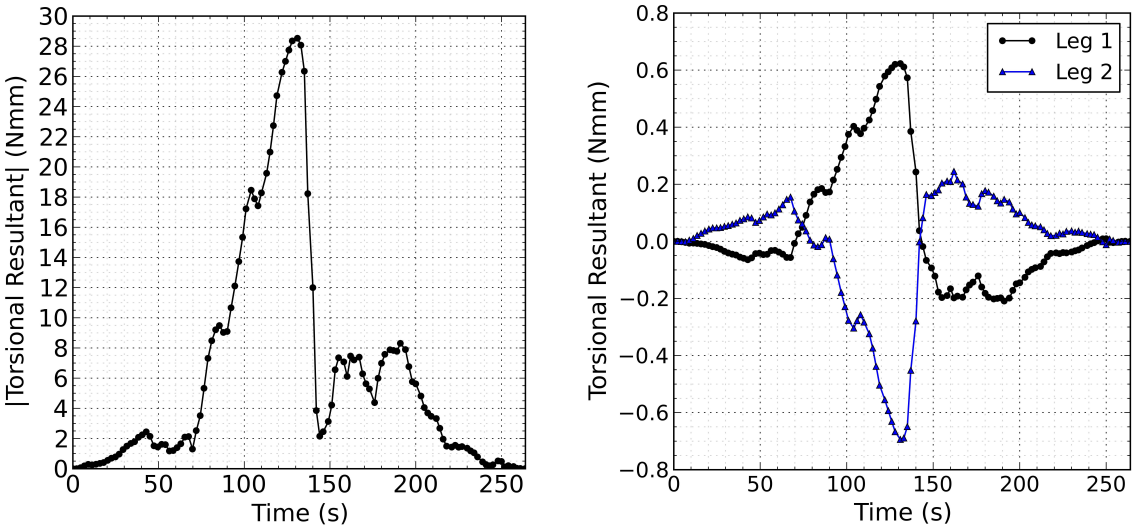

(a) Magnitude of summed torsional resultant for one entire leg, from the center of neighboring bends

(b) Torsion through out simulation measured at the center of adjoining legs

Figure 4.8: Torsion

Analysis of peak von Mises stress throughout constriction shows there is a significant chance of plastic deformation (Figure 4.9). Peak von Mises stress occurs at 130.5 s with a maximum value of 1418 MPa (true stress), which corresponds to the same time as the moment of peak axial stress. This peak stress value is well above the yield strength of annealed then cold drawn stainless steel 316L of 380 MPa[176]. During the first constriction of the stent, bends and a moderate length of stent leg

on either side, would undergo plastic deformation if they hadn't already been strain hardened during the manufacturing process. The FE model begins at a zero stress state, without any of the internal stresses that would be left over from stent manufacturing. This could potentially contribute error to simulated results. The peak von Mises stress encountered during stent constriction is still well below the fracture strength of stainless steel 316L of 2675 MPa (true stress)[183].

Interestingly, Figure 3.14 demonstrates that the point of highest deviatoric stress in the Mylar is found where stent legs make contact. However, Figure 4.9 shows that the point of highest deviatoric stress in the stent is in the bends.

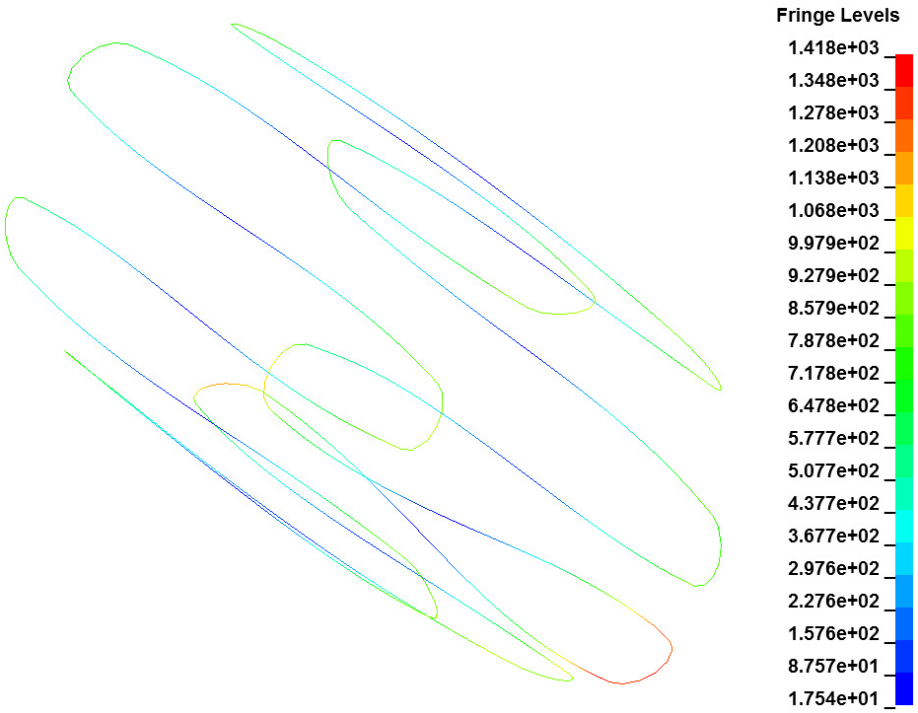

Figure 4.9: Visualization of peak von Mises stress at 130.5 s (MPa)

4.1.1 Free Body Analysis

A final analysis was performed to determine whether reaction forces experienced at both Mylar anchors were equal. Using the system present in Figure 3.12, the free-body diagram (FBD) in Figure 4.10 shows that T_1 and T_2 should display an equal result unless interfered with by friction. Figure 4.11 compares T_1 and T_2 and reveals the difference between them, labeled $F_{Unknown}$, which most likely represents

frictional effects. Magnitude of $F_{Unknown}$ changes direction following the switch from constriction to expansion, as would be expected for friction.

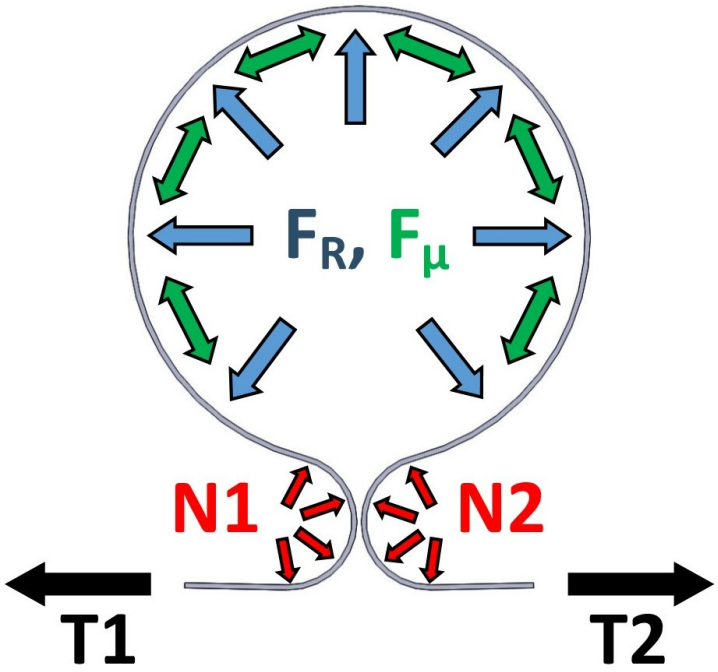

Figure 4.10: Free-body diagram of contributing reactions. F_R = radial force, F_μ = friction force (constriction and expansion), N_1/N_2 = normal roller forces, T_1/T_2 = Mylar tensile forces

Unrolling the FBD of Figure 4.10, a new FBD perspective (Figure 4.12) can be visualized to help understand $F_{Unknown}$ from figure 4.11. Assuming uniformly distributed loads, equal roller contact area and frictionless rollers, a value of $F_{Unknown}$ during constriction can be defined using the analysis performed from Equation 4.1 to 4.8.

Assuming static friction,

$$F_{\mu s} = \mu_s F_R \tag{4.1}$$

where

$F_{\mu s}$ = static friction force (N)
μ_s = static Coulomb friction constant
F_R = radial force (N)

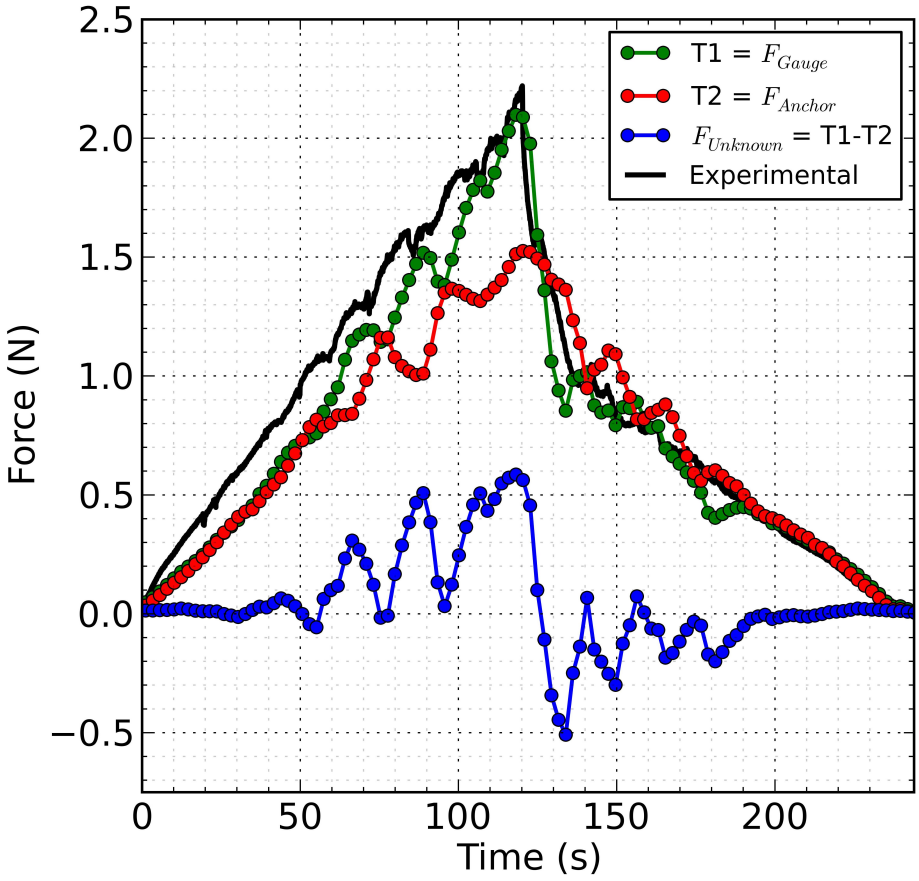

Figure 4.11: Comparison between force gauge and linear force data from the moving anchor

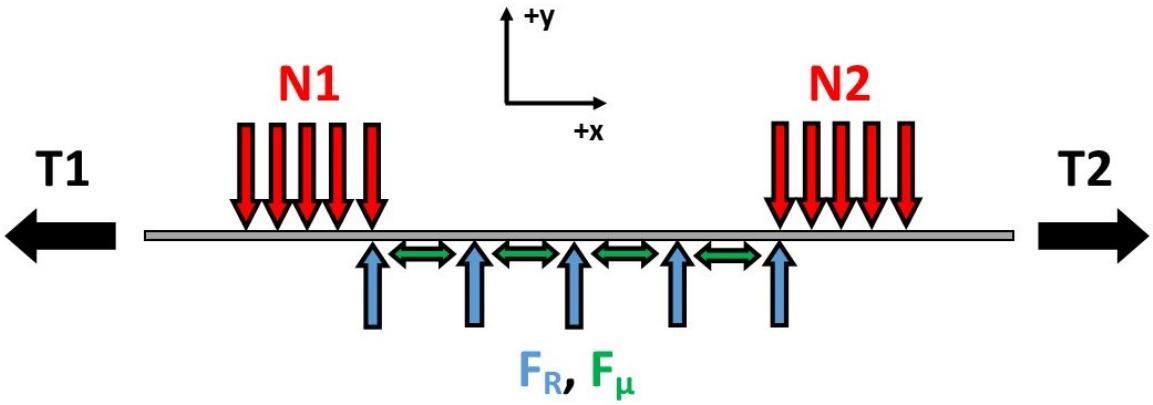

Figure 4.12: Unrolled free body diagram of contributing reactions. F_R = radial force, F_μ = friction force (constriction and expansion), N_1/N_2 = normal roller forces, T_1/T_2 = Mylar tensile forces

Equilibrium equations become

$$\sum F_x = 0 \tag{4.2}$$

$$T_1 = T_2 + F_{\mu s} \tag{4.3}$$

$$\sum F_y = 0 \tag{4.4}$$

$$F_R = N_1 + N_2 \tag{4.5}$$

where

F_x/F_y = x and y-component forces (N)
T_1/T_2 = Mylar tensile forces (N)
N_1/N_2 = normal roller forces (N)

Assuming a linear radial stiffness,

$$F_R = kAR \tag{4.6}$$

where

k = radial stiffness (N/mm^2)
AR = area reduction (%)

Substituting Equation 4.1 into 4.3,

$$T_1 = T_2 + \mu_s F_R \tag{4.7}$$

Finally, substituting Equation 4.6 into 4.7

$$T_1 = T_2 + \mu_s kAR \tag{4.8}$$

Solving for the $F_{Unknown}$ force profile from figure 4.11, Equation 4.8 becomes $F_{Unknown} = T_1 - T_2 = \mu_s kAR$.

In future stent wire simulations, in addition to altered material properties, alterations to wire cross section could be used to manipulate torsion, s-bending and t-bending moments. Developing the ability to predictably control these stent mechanics would enable new intelligent options for stent design.

Future work should analyze the method of conversion from radial force to linear force measured by the force gauge and how these two compare. An accurate representation of radial force is very important to understanding friction between the artery wall and stent, as well as for determining what radial force is needed for solid stent fixation. Having the ability to convert between the linear force read at the radial extensometer force gauge and the radial force exerted by the stent would enable the calculation of meaningful friction and radial force values that could be used for more precise simulation and improved stent-graft design.

4.2 In-Vivo Finite Element Model

Progress was made on an explicit model to simulate the interaction between a self-expanding endovascular stent and the arterial wall. A visual representation of these efforts can be seen in Figure 4.13.

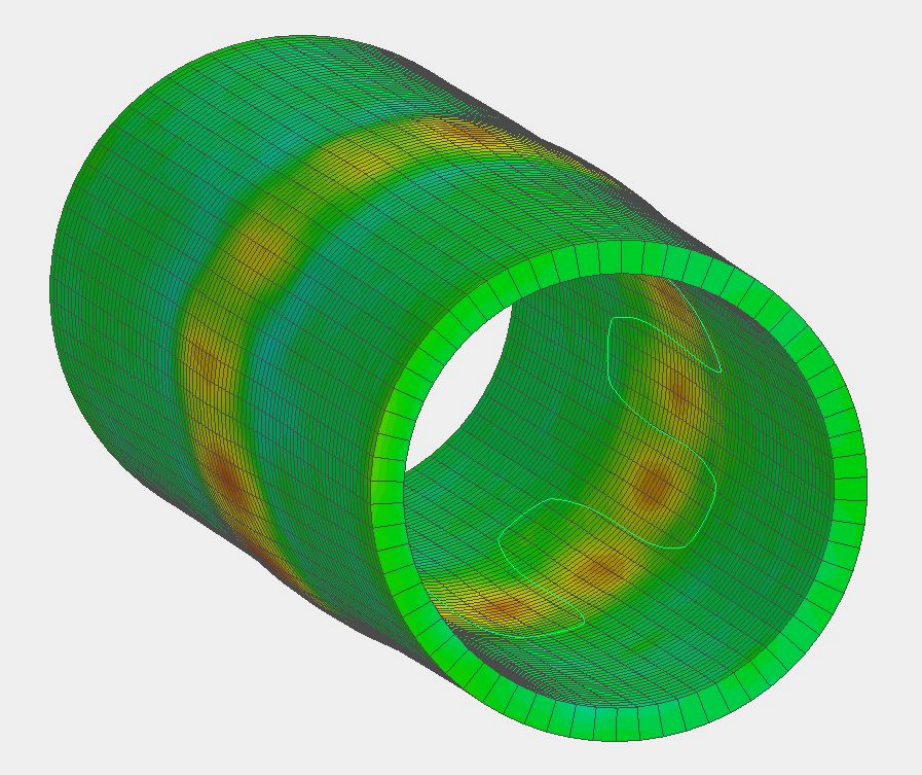

Figure 4.13: Simulated pressure created by a single self-expanding z-stent deployed in-vivo

The same stent used in the completed in-vitro simulation was used for in-vivo modeling. The uncovered 12 mm stent was first constricted inside of a simulated catheter. Once the stent was constricted enough to fit entirely inside of the simulated artery, the catheter mesh was made completely penetrable and the stent expanded inside of the artery. Once the stent came into contact with the artery wall, the simulation continued for a small period of time to help dampen shock and establish an equilibrium. A rendering of the initial model including the catheter as well as a final view of the simulation with stent and arterial wall in contact is shown in Figure 4.14.

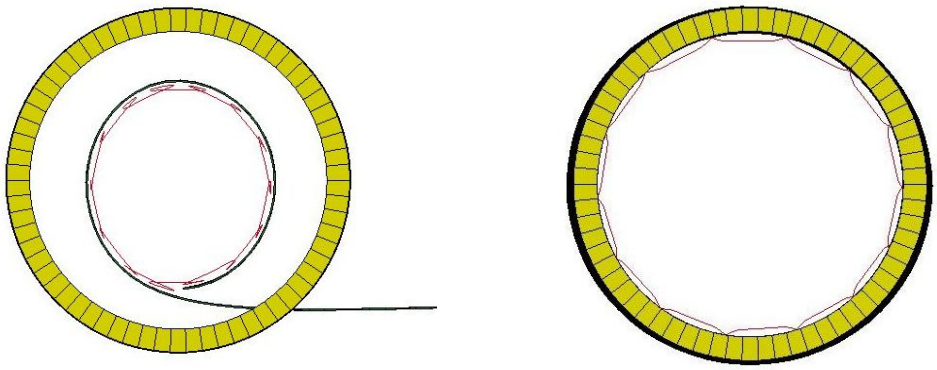

(a) Initial in-vivo **(b)** Expanded in-vivo

Figure 4.14: Initial and final rendering of in-vivo simulation

Arterial simulation made use of the "*MAT_SOFT_TISSUE" material model. Y.C. Fung's constants for the carotid artery of the rabbit were used as soft tissue hyper-elastic coefficients for this simulation[184]. Values for bulk modulus, mass density and stretch ratio were taken from literature published by Rudolf Bötticher on fluid structure interaction with "*MAT_SOFT_TISSUE"[185]. Arterial diameter and wall thickness were set to 10.5 mm and 0.75 mm respectively, as initial estimates of carotid artery dimensions. These values can be refined as the model is further developed.

To demonstrate successful interaction between stent and artery, internal energy of the stent was output in Figure 4.15. The initial ramp-up in internal energy corresponds to constriction of the stent inside the simulated catheter. At the point of peak

internal energy, the catheter is removed and the stent begins to freely expand. Soon after, internal energy stops dropping and eventually reaches an equilibrium signifying a successful contact between arterial wall and stent graft. Oscillations are due to the short model duration required for the explicit solver.

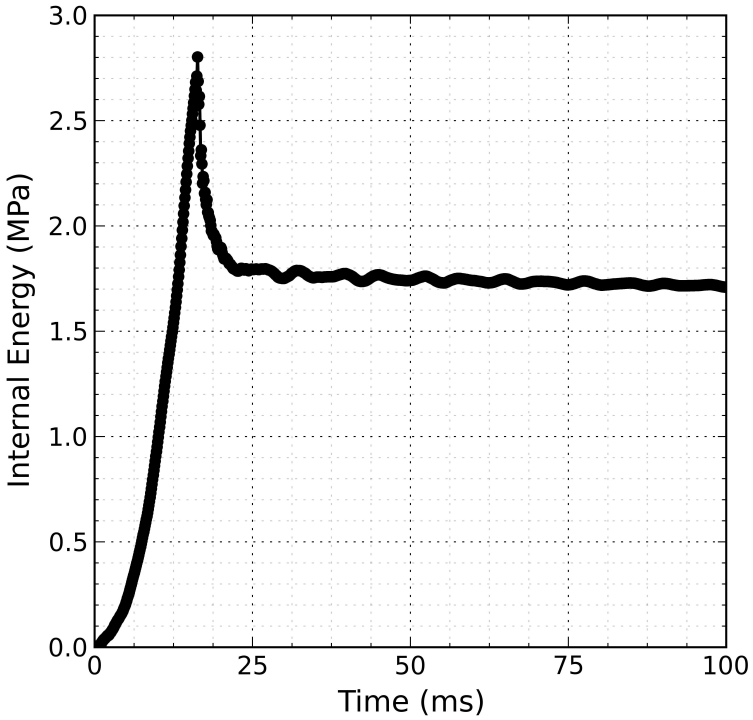

Figure 4.15: Internal energy trend of a self-expanding z-stent during expansion in-vivo

There is significant room for improvement of material values, geometry and other components of this model in the future. New iterations of this model would benefit from the addition of a graft to the stent in order to better simulate contact and friction between the two bodies. Ideally, once a stable contact has been achieved, fluids could be introduced to model drag force on the stent as well as stent radial force required to avoid migration and endoleak under different conditions.

Chapter 5

Stent Design and Manufacture

Along with the knowledge gained through FE modeling, future stent improvements requires an understanding of manufacturing techniques, materials and geometry of currently available technology. A catalog of existing Zenith z-stent dimensions was produced to both gather the information required to develop accurate manufacturing tools and to obtain baseline data against which custom stents could be compared. The same Logitech C920 webcam used in the radial extensometer was used to take pictures of the stents for cataloging on a 0.25 in (6.35 mm) graph paper background. The setup used for image collection is shown in Figure 5.1. Metallographic and chemical analysis of nitinol and stainless steel stent wires was performed to verify chemical composition as well as manufacturing and treatment processes used by industry. These efforts ensure stents developed for analysis are an accurate representation of currently available prosthetics.

Figure 5.1: Setup for precise stent measurement and cataloging

5.1 Stent Cataloging

Stents are placed flat on the graph paper background of the measurement apparatus shown in Figure 5.1, with one bend section flat on the paper's surface. Measurements are taken in the stent's x-z plane. The ruled background of the photography setup was used to provide a scale to dimension pictures taken by the camera. Figure 5.2 itemizes presented dimensions for further explanation.

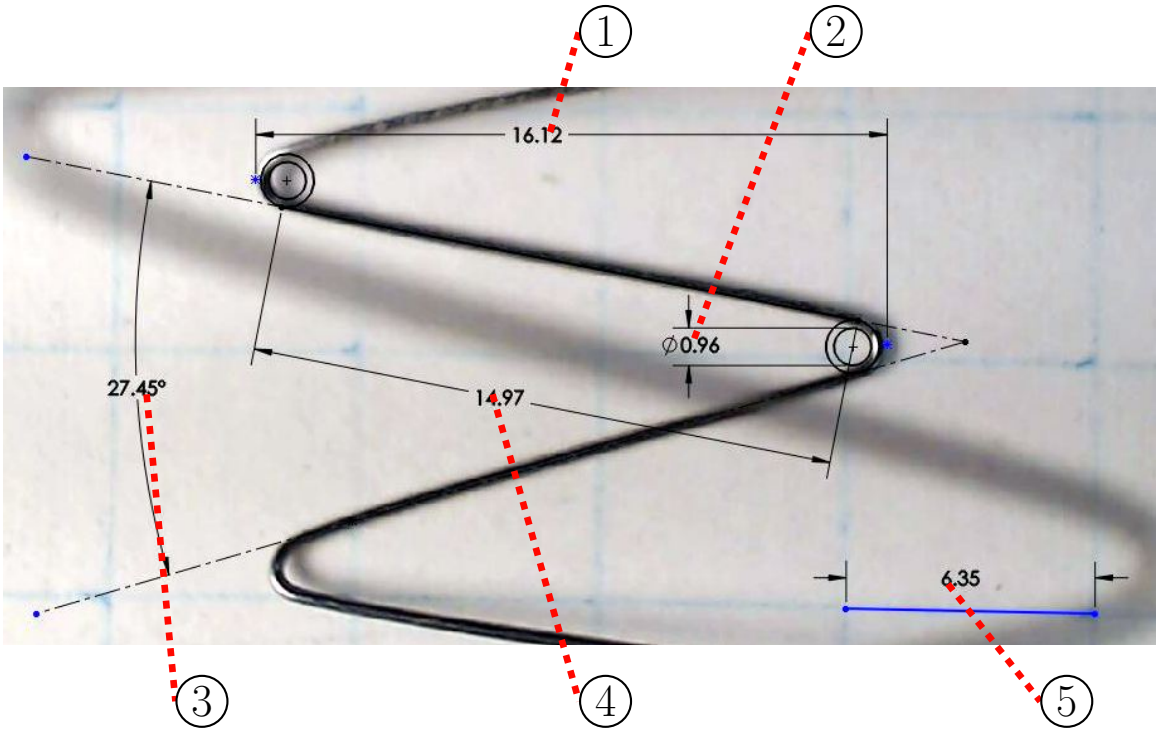

Figure 5.2: Measure of stent characteristics, x-z plane

(1) **Stent width**: Measured from bend peak to peak.

(2) **Bend radius**: Measured from the inside edge of each bend. Bend radius was measured from the inside edge to give a consistent point of comparison as well as to indicate the size of bend post used during the manufacturing process.

(3) **Bend angle**: Measured through the center of adjoining stent wire legs.

(4) **Leg length**: Measured from the center of two neighboring bend radius circles.

(5) **Image sizing**: The stent is placed on a backdrop of 6.35 mm graph paper. This known value is used to dimension the image from pixels to millimeters for extraction of image geometry.

Stents of all sizes are catalogued in Table 5.1 to gather information relevant to their mechanical design and function. Refining the stent design parameters examined by others: bend angle, leg length, bend diameter and wire diameter were collected as the four base characteristics influencing stent performance and the production of force[139, 147, 137, 1]. Other characteristics needed to fully catalogue stent geometry were also compiled. In figure 5.1, "[c]overed diameter stated" varies from "[c]overed diameter measured" because the stated diameter is rounded for labeling purposes by the manufacturer. Bend diameter and wire diameter values are based off of manufacturer's specifications and do not vary by a significant amount.

Table 5.1: Stent catalogue (±SD, 1/32 in = 0.79 mm)

Covered diameter stated (mm)	10	12	14	16	18
Covered diameter measured (mm)	11.45 ± 0.05	12.37 ± 0.09	14.59 ± 0.13	16.78 ± 0.05	18.16 ± 1.74
Uncovered diameter (mm)	16.90 ± 0.24	20.35 ± 0.25	24.04 ± 0.13	24.53 ± 0.32	26.92 ± 0.30
Bend angle (°)	23.00 ± 2.40	25.98 ± 1.10	27.31 ± 2.77	26.78 ± 0.92	28.15 ± 0.26
Stent width (mm)	16.41 ± 0.09	16.21 ± 0.05	16.03 ± 0.08	16.05 ± 0.01	16.19 ± 0.02
Leg length (mm)	15.40 ± 0.21	15.42 ± 0.25	15.28 ± 0.06	15.14 ± 0.18	15.24 ± 0.26
Bend diameter	1/32 in	1/32 in	1/32 in	1/32 in	1/32 in
Wire diameter (mm)	0.40	0.40	0.40	0.40	0.40
Bends per side	7	7	8	9	9

Covered stent diameter stated (mm)	20	24	30	34	42
Covered diameter measured (mm)	20.55 ± 0.22	24.30 ± 0.21	29.73 ± 0.28	34.30 ± 0.20	41.66 ± 0.20
Uncovered diameter (mm)	28.98 ± 0.63	28.30 ± 0.16	35.63 ± 0.25	46.59 ± 0.13	51.01 ± 0.30
Bend angle (°)	26.96 ± 1.41	26.83 ± 0.74	25.88 ± 1.03	26.54 ± 0.64	26.52 ± 1.19
Stent width (mm)	16.08 ± 0.04	16.15 ± 0.12	16.13 ± 0.04	21.04 ± 0.08	20.79 ± 0.22
Leg length (mm)	15.41 ± 0.19	15.50 ± 0.18	15.12 ± 0.30	19.99 ± 0.28	19.71 ± 0.14
Bend diameter	1/32 in	1/32 in	1.00 mm	1.00 mm	1.00 mm
Wire diameter (mm)	0.40	0.40	0.45	0.50	0.50
Bends per side	10.00	10.00	12.00	12.00	14.00

5.2 Metallographic and Chemical Analysis

Stent materials used by industry were analyzed to ensure FE models from Chapter 3 use accurate parameters, and that properties of in house manufactured stents are comparable to those produced by industry. Original FDA documents from 2003 as well as patents for the Zenith self-expanding stent-graft do not indicate the material used in the manufacture of the z-stent wires[186, 187, 188, 189]. However, the Summary of Safety and Effectiveness Data document submitted to the FDA in 2012 for the Zenith fenestrated AAA endovascular graft and alignment stent confirms that stainless steel 316L is used in the manufacture of Zenith self-expanding z-stents[190].

Metallographic analysis was performed to reinforce knowledge of stent material alloy type and to investigate manufacturing processes that may have been used. Metallographic analysis was completed in four steps:

1. **Figure 5.3(a)**: Stainless steel 316L and nitinol (nickel titanium) stent legs are cut into small sections and mounted in bakelite (a thermosetting resin) using the Struers (Ballerup, Denmark) CitoPress-1. Stent wire sections are mounted both axially and longitudinally.

2. **Figure 5.3(b)**: Mounted samples are finely polished using the Struers Tegramin-20. Prior to polishing, a stronger abrasive is used to grind 50 % of the way through longitudinally mounted samples. Fully polished samples are shown in Figure 5.3(c).

3. **Figure 5.3(d)**: Polished samples are analyzed before and after etching at a variety of magnifications using a standard high power microscope with a connected digital vision system. Kalling's reagent 2, the suggested etchant for stainless steels, was far too powerful, causing significant corrosion and pitting after only a brief moment of contact with the mounted samples[191]. Aqua Regia was selected as a final suitable etchant. Three, ten second rounds of etching were performed with a series of pictures taken after each one.

4. **Figure 5.3(f)**: Following the first round of etching, the scanning electron microscope (SEM) (Figure 5.3(e)) was used to further investigate grain structure, however, grain structure was better revealed in images taken using the standard

(a) Mount wires tangentially and axially

(b) Polish samples for initial analysis

(c) Mounted wire samples

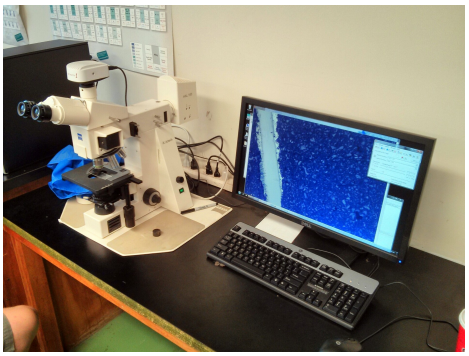

(d) Analyze microstructure and texture

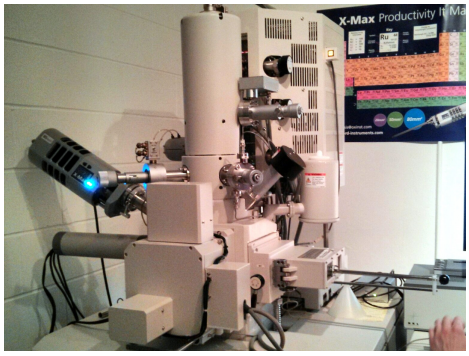

(e) Etch and analyze using the SEM and EDS

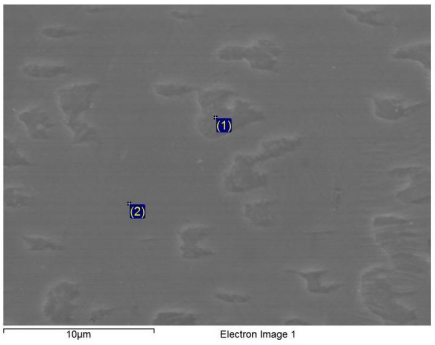

(f) SEM image during EDS analysis at 10 µm

Figure 5.3: Microstructure and texture analysis process

microscope. Energy-dispersive x-ray spectroscopy (EDS) was used to analyze the chemical composition of both stainless steel 316L and nitinol stents.

A weak magnetism was discovered in the stainless steel 316L stent wire used in Zenith stents. This is interesting because annealed stainless steel 316L is primarily

composed of an austenitic face-centered-cubic (FCC) non-magnetic crystal structure with a small amount of body-centered-cubic (BCC) ferrite that did not convert to austenite due to the relatively low nickel content in stainless steel 316L. The amount of ferrite in annealed stainless steel 316L is not enough to instill notable magnetism in this material. There must be a secondary process and crystal structure present which is causing this magnetism.

Different balances of elements present in stainless steel will push and pull the phase of the metal between ferrite, austenite and martensite. Chromium, molybdenum, silicon and niobium are ferrite stabilizing. Nickel, manganese and carbon are austenite stabilizing[192]. Martensite, a magnetic, body-centered-tetragonal (BCT) crystal structure found in Fe-Ni alloys, can be formed by either heat treating austenite with low nickel equivalent (the combined effect of all austenite stabilizing elements) or by high shear strain imbued upon austenite during a cold-working (drawing) process[193].

Wire used in stainless steel 316L Zenith z-stents displays a strong longitudinal texture (Figure 5.4). Narrow cross-sections of these long, narrow grains can be seen in the axial transection of stent wire in Figure 5.5. Zenith stent wire must have been subjected to the high strain of a cold-working process to develop these narrow, elongated grains parallel to the direction of extrusion[193]. The use of this manufacturing process explains the origin of magnetism discovered in the Zenith stent graft; the strength of magnetism is related to the proportion of delta-ferrite and martensite present in stainless steel 316L wire.

Cold working stent wire and the associated increase in martensite not only affects magnetism but also causes work hardening of the stainless steel due to an increased dislocation density and transformation from soft FCC austenite to hard, highly-strained BCT martensite[194].

Finally, using low-carbon stainless steel 316L with a carbon content below 0.35 % helps avoid precipitation of carbon along grain boundaries. Avoiding carbon precipitation will fend off cementite (iron carbide) and chromium carbide production, conserving stores of chromium in the stainless steel 316L grain boundaries. Chromium stores are required to produce a protective chromium oxide layer on the wire surface, therefore, using a low-carbon stainless steel improves the corrosion resistance of

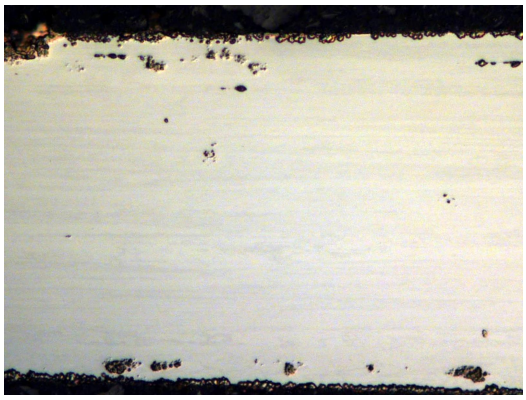

(a) Longitudinal grain texture at 500x

(b) Longitudinal grain texture at 1000x

Figure 5.4: Stainless steel 316L stent wire microstructure and texture

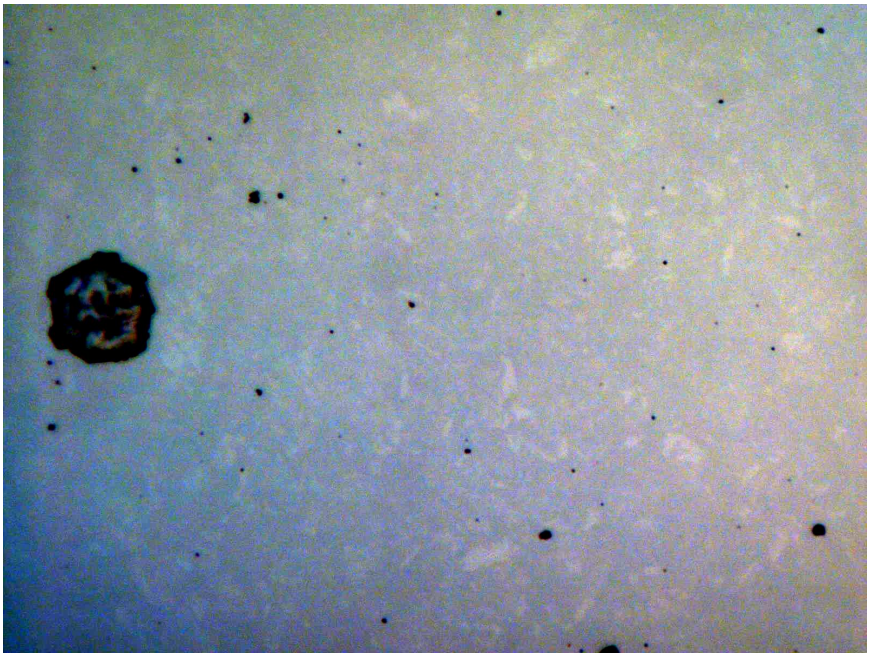

Figure 5.5: Stainless steel 316L stent wire axial texture

stents[195].

Changes in material properties due to the wire drawing process will have an impact on the performance of stainless steel stents. Manipulating the martensite content in wires used for stent manufacture could be a possible way of manipulating the characteristics of future stainless steel stents.

Although both Cook (Zenith) stainless steel 316L and Medtronic (Talent) nitinol z-stents were analyzed, the focus of this work falls solely on the performance of those manufactured with stainless steel 316L. Although it may not possess the shape memory alloy material properties of nitinol, it can easily be brazed, welded and heat treated making it much easier to work with. Stainless steel 316L stents have shown less corrosion and embrittlement when compared to their nitinol counterparts, due to leaching of nickel out of the nickel-titanium alloy[196, 146]. However, nitinol z-stents are able to avoid high material stresses through austenite to martensite transformation, remaining more compliant due to martensite's lower Young's modulus; while plasticity may occur in those manufactured using stainless steel 316L[27, 130]. A longitudinal cross section of nitinol used in the Talent stent at room temperature is shown in Figure 5.6. Grains of austenite and martensite are visible running parallel to the wire direction.

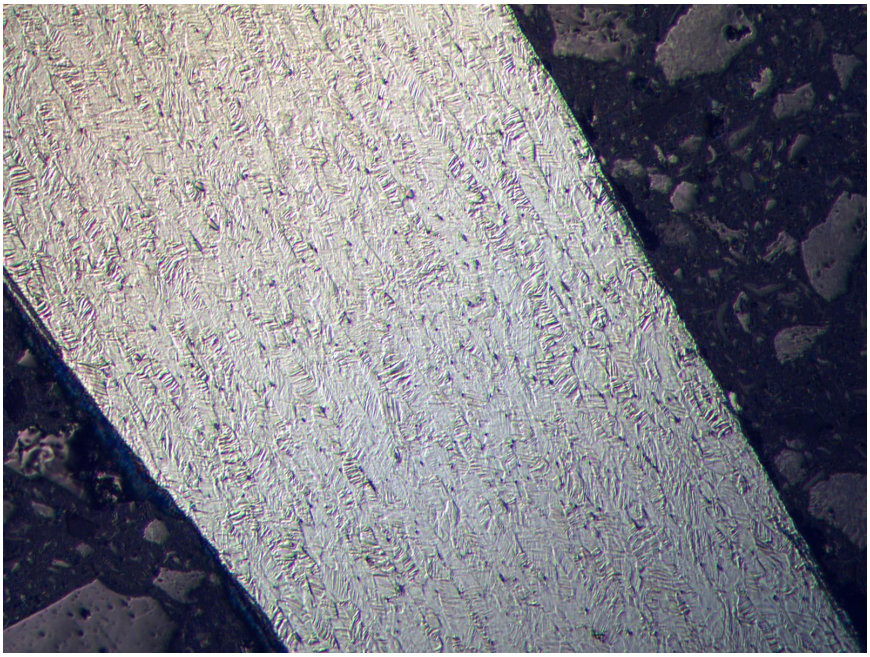

Figure 5.6: NiTi grain structure at 500x

Results from chemical analysis of stent sections using EDM are presented in Tables 5.2 and 5.3. Stainless Steel 316L and Nitinol composition was successfully validated with data presented by the American Society for Testing and Materials. Chemical

components which contributed less than 0.1 % by weight to overall material composition were not picked up by EDM.

Table 5.2: Verification of material composition for stainless steel 316L sample[197]

Element	Weight %	Atomic %	Book Value (Weight %)	% Difference
Si	0.72	1.41	0.750	4.00
Cr	18.88	19.94	16.0 – 18.0	4.89
Mn	1.46	1.46	2.000	27.00
Fe	69.94	68.78	62.045 – 69.005	1.35
Ni	9.00	8.42	10.0 – 14.0	10.00
C	DNR	DNR	0.030	N/A
P	DNR	DNR	0.045	N/A
S	DNR	DNR	0.030	N/A
Mb	DNR	DNR	2.0 – 3.0	N/A
N	DNR	DNR	0.100	N/A

Table 5.3: Verification of material composition for Ni-Ti sample[198]

Element	Weight %	Atomic %	Book Value (Weight %)	% Difference
Ti	42.87	47.92	42.75 – 45.50	0.00
Ni	57.13	52.08	54.50 – 57.00	0.23
C	DNR	DNR	0.050 MAX	N/A
Co	DNR	DNR	0.050 MAX	N/A
Cu	DNR	DNR	0.010 MAX	N/A
Cr	DNR	DNR	0.010 MAX	N/A
H	DNR	DNR	0.005 MAX	N/A
Fe	DNR	DNR	0.050 MAX	N/A
Nb	DNR	DNR	0.025 MAX	N/A
N + O	DNR	DNR	0.050 MAX	N/A

5.3 Jig Design and Manufacture

Several different attempts were made at designing and rapid prototyping a mechanism that could be used to precisely and reliably manufacture z-stents.

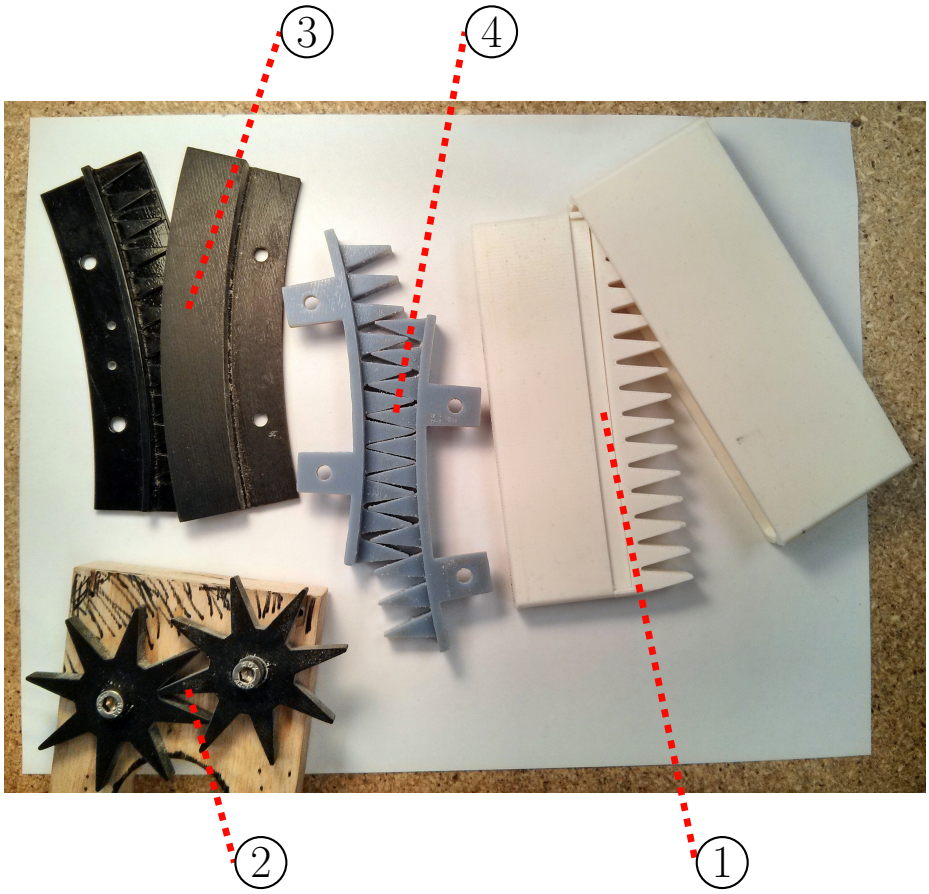

Figure 5.7: Stent bender design iterations

The following design iterations are labeled in Figure 5.7:

(1) **Crimping bender**: This system was printed with a Stratysis, Dimension (Rehovot, Israel) fused deposition modeling machine. Unfortunately, the layered deposition method is inherently weak where layers of material have fused together. During the crimping process, as the stent wire was drawn into the crimping apparatus, the stent wire would split layers of fused plastic and cut through the bending jig. Unfortunately, even altering the orientation of layer deposition was not enough to compensate for the low strength of ABS plastic

used by this printer. Had this bending process worked, this apparatus was designed with interchangeable crimping jaws of varying profiles that could easily be swapped to bend an entire stent reliably and consistently in one motion.

② **First iteration feed through bender**: Learning from the difficulties encountered using fused deposition to manufacture wire benders, a Stratysis Objet ultraviolet (UV) cured photopolymer printer was used for manufacturing. The layer thickness is much finer on this machine (0.33 mm vs. 0.028 mm) creating a far more dense part with better layer bonding. Instead of being able to bend an entire stent in one motion, this iteration of wire bender was designed to continuously bent stent wire. This machine was successful in bending wire into a precise, repeatable shape. Unfortunately, the bend angle created with the small bending wheels used in this device was too large and could not be reduced without either increasing the radius of the wheel or adjusting the leg length of the stent to an inappropriate size.

③ **Second iteration feed through bender (low angle)**: Building upon the first feed through bender, this second iteration device increases the radius of bending wheel in order to decrease the bend angle of manufactured stents. This iteration included flat shields on either side of the bending teeth to keep the wire in place during bending. Unfortunately, crimping teeth were made too narrow and once forces reached a certain limit (usually after the engagement of $1-2$ teeth) wire would not feed properly between the two jaws, slipping out of the machine (Figure 5.8).

④ **Third iteration feed through bender (low angle, wide contact surface)**: In this new design, side shields were removed and teeth were made significantly wider. A center groove was added to guide wire through crimping teeth during bending. Unfortunately, using a large radius wheel means that during bending the wire must be drawn through several teeth. The force required to draw wire into the apparatus during bending chipped and broke teeth, destroying the device. The feed through bender was abandoned after this iteration.

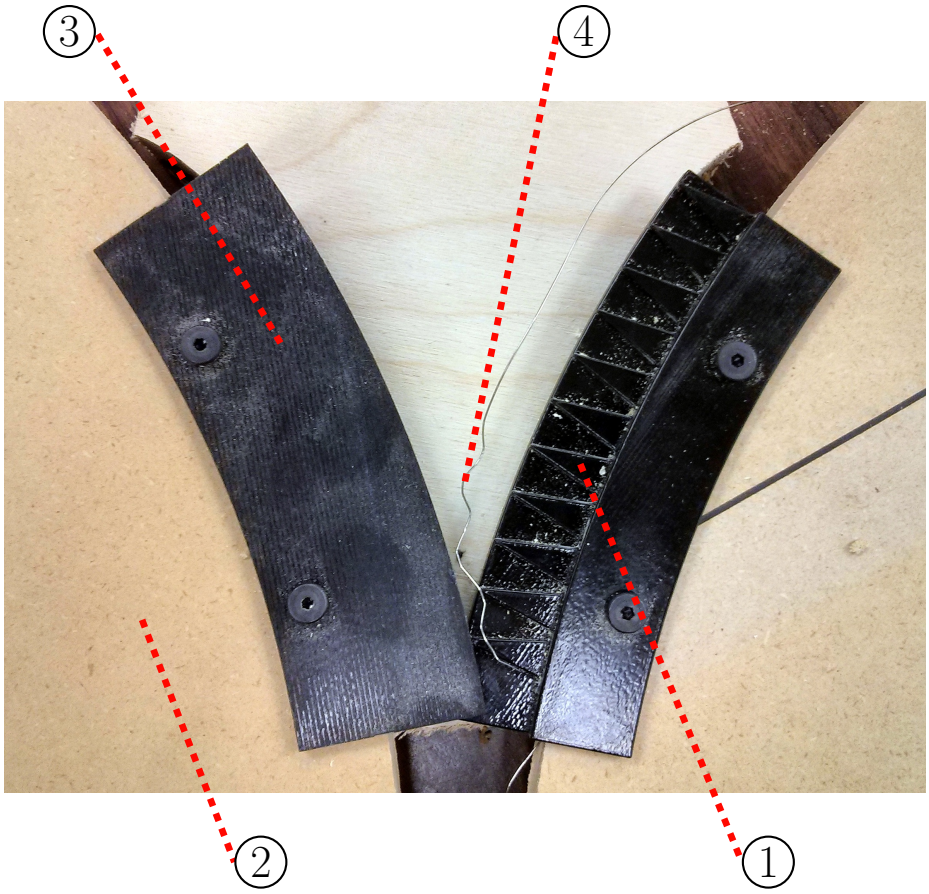

Figure 5.8: Second iteration feed through bender (low angle) showing failed attempt due to slipped wire: 1 - bending teeth, 2 - wheel for mounting bender, 3 - flat bending shield, 4 - stent wire

5.3.1 Final Jig Design

The final iteration of the stent bending apparatus was designed with several features in mind. Ease of manufacturing (i.e. bending an entire stent in one motion) was substituted in favor of functionality. It was designed as a manual, single bend jig which requires several uses to complete a single stent (Figure 5.9). A second generation of these benders were printed with clear material using the Stratasys Objet to ease the positioning of stents as well as the bending process itself (Figure 5.10). All CAD drawings for this final generation of benders can be found in Appendix F.

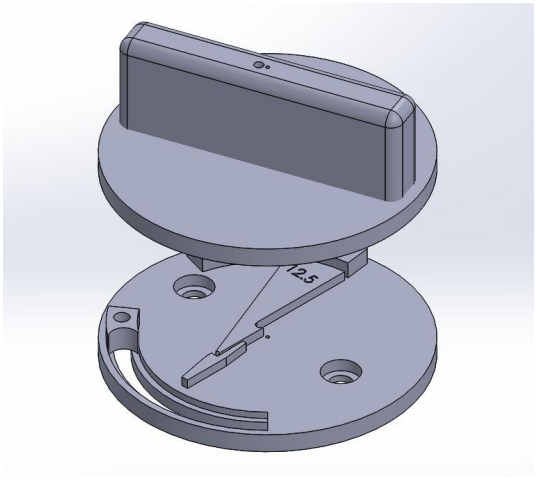

(a) Final CAD rendering of stent wire bending jig

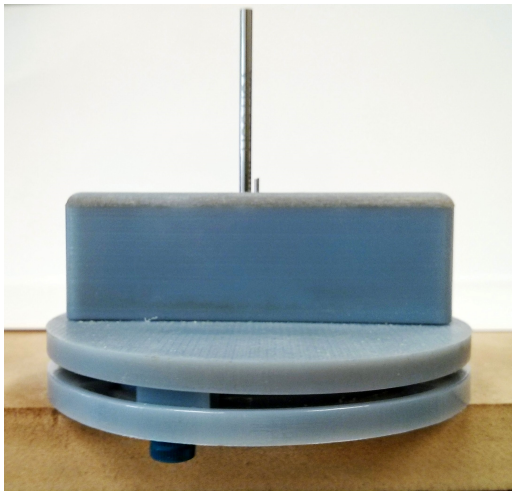

(b) Completed stent wire bending jig–in use

Figure 5.9: Completed stent wire bending jig

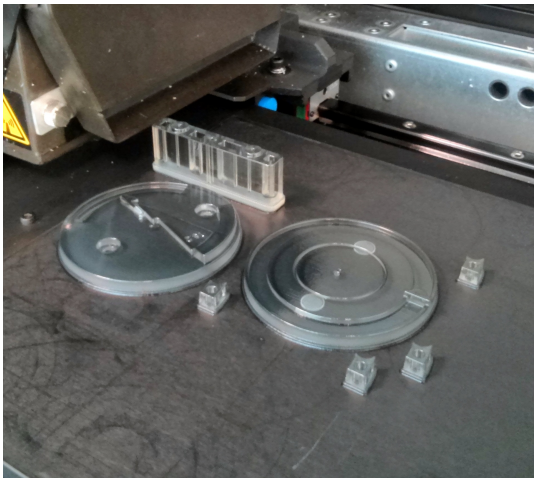

(a) three-dimensional printing of clear wire bending jig

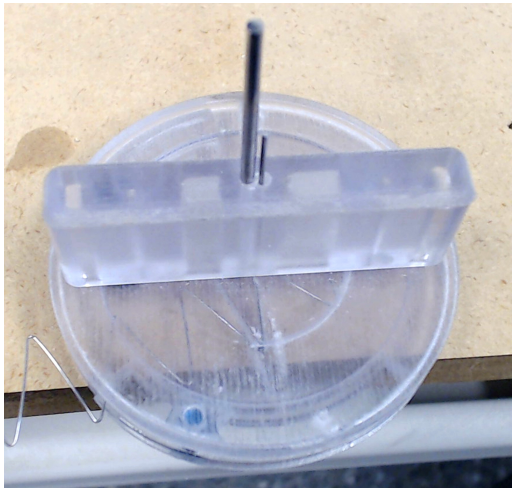

(b) Clear stent wire bending jig–in use

Figure 5.10: Completed clear stent wire bending jig

Referring to Figure 5.11, enumerated design features of the final stent bending jig are as follows:

(1) The lower bending jig plate of the bending jig (Appendix F, page 210) is fixed to a firm surface using $10-32\text{x}1/2\,\text{in}$ low profile socket head machine screws.

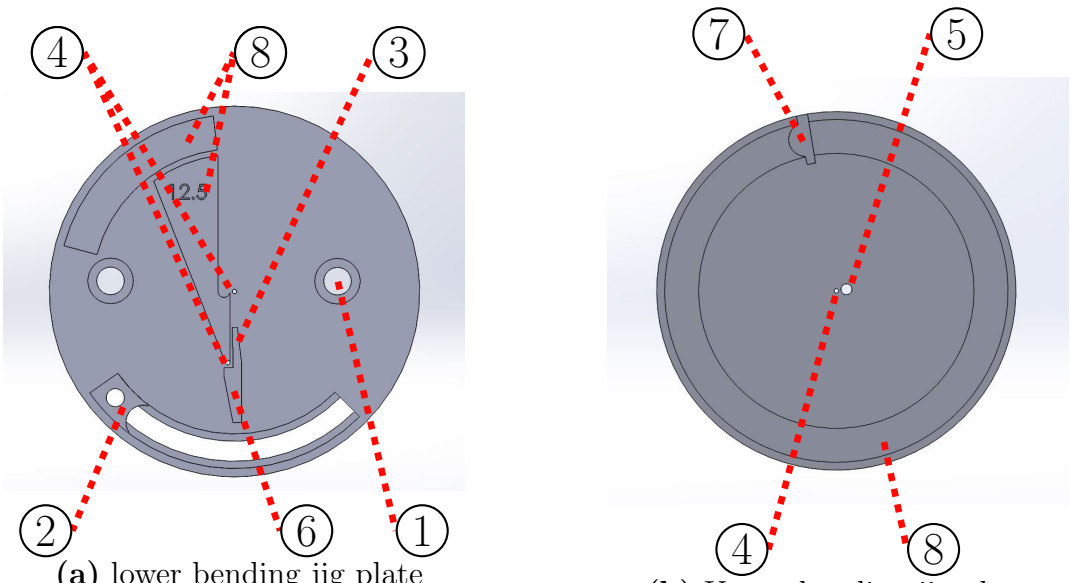

(a) lower bending jig plate

(b) Upper bending jig plate

Figure 5.11: Final stent wire bending jig

(2) Bend angle is adjusted using a stopper (Appendix F, page 212) which can be precisely positioned using the angular placement tool (Appendix F, page 213) shown in Figure 5.12(a).

(3) A lip built into a raised section of the jig base plate allows wire legs to be clipped into the jig, securing sections of wire before bending.

(4) Two 1/32 in bending posts are used. One fixed to the lower plate near the outside edge of the jig to hold the wire in place during bending, ensuring a precise leg length; another which is fixed to the upper bending jig plate (Appendix F, page 209) in the center of the bending jig, which the wire is bent around.

(5) A thicker 2 mm post is fixed to the upper plate and positioned on the outside of the center bend post. The stent wire fits between the two posts which are fixed to the top plate. This gap between the 2 mm and 1/32 in bend posts can be seen in the center of Figure 5.11(b). The larger 2 mm outer post bends the wire around the center bend post.

(6) A section of the lower plate is raised starting one wire diameter beneath the outermost bending post. This prevents the stent wire from moving during the

bending process. This ridge also provides a firm landmark for wire placement during setup.

(7) A bumper on the top plate hits against the stopper (enumerated value 2 in Figure 5.11(a)) on the bottom plate, ensuring stent wires can be bent to a repeatable angle. To avoid pinching the stent wire between bumpers on the top and bottom plates, the bumper on the top plate remains in front of the stent wire during bending.

(8) Stability and control of the jig is promoted with two raised platforms on the lower plate and a trough on the upper plate. The inner most raised platform of the lower plate rests on the top plate during bending, providing a stable contact during the bending process. The outer most raised platform is higher than the inner platform. This section fits inside of the trough on the upper plate keeping the upper and lower sections aligned during bending as well as providing more surface area for added stability.

A handle is connected to the backside of the jig top plate (Figure 5.11(b)) using two threshold fit pegs. Proper tolerancing is critical to jig functionality. Following some experimentation on how printed component tolerances interact, a diametral tolerance of 0.006 in was employed for freely moving parts such as the bend angle stopper, socket head screw counter sinks and radial alignment slot. Tight fitting parts such as the handle attachment plugs and all posts associated with bending use a zero tolerance fit.

5.4 Stent Manufacture

Stents are manufactured using a jig that has been manufactured and set up to achieve an appropriate leg length, wire diameter and bend radius in the final product. The only stent characteristic which is adjustable on each jig is the bend angle. There are four main steps in stent manufacture:

1. **Figure 5.12(a)**: The angle of bend is set using an angular placement tool. The bend stopper is secured using a $6-32$x1/4 screw fastened from the underside of the lower jig plate.

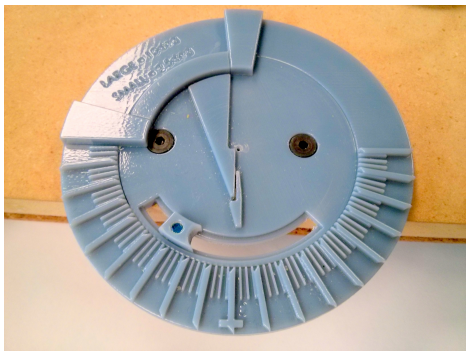

(a) Set bend angle using angle tool

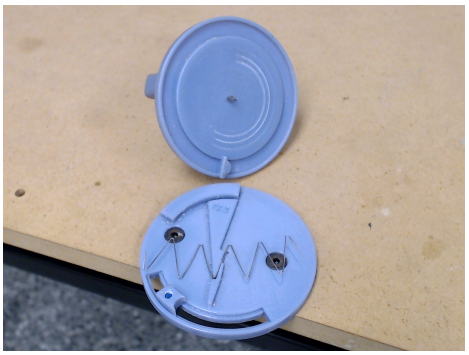

(b) Bend stent wire

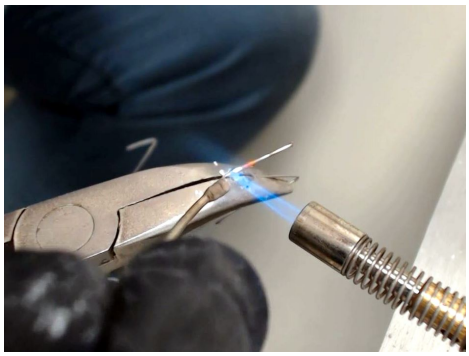

(c) Braze first side of wire

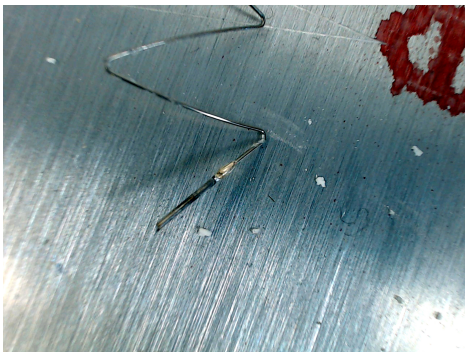

(d) Completed first braze

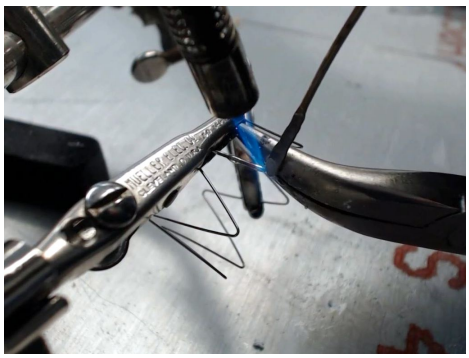

(e) Braze second side of wire

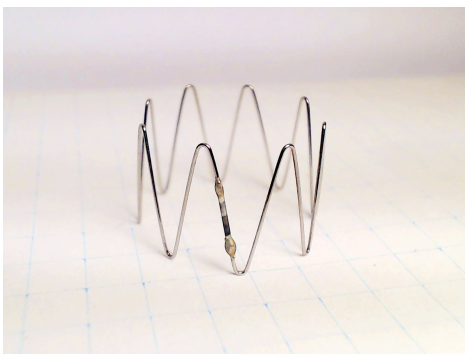

(f) Completed stent

Figure 5.12: Custom stent manufacturing process

2. **Figure 5.12(b)**: Repeated bends are made until the desired number has been achieved. If coiled wire is used, the wire should be flipped to point upward for one bend and downward for another, to ensure the completed stent is flat and straight.

3. **Figure 5.12(c)**: One side of the bent stent wire is brazed inside of a section

of 22 gauge, 316 stainless steel hypodermic tubing (inner diameter = $0.016\,in$, outer diameter = $0.028\,in$) using pliers as a heat sink. Care must be taken not to accidentally heat the stent wire above its recrystallization temperature; annealing the stent wire will remove its spring temper and make the wire unsuitable for use in a self-expanding stent. A completed first braze is shown in Figure 5.12(d).

4. **Figure 5.12(e)**: The second braze is made in the same way as the first, however, the stent must be supported in a position identical to that of its final state. The pliers are again used as a heat sink to avoid overheating the wire. A finished stent should maintain a circular shape with identical bends and minimal excess filler metal. A completed stent is shown in Figure 5.12(f).

Manufactured stents are checked for accuracy with the same apparatus used to catalogue industry stents in Section 5.1. Dimensional accuracy is verified prior to using lab manufactured stents for analysis.

5.5 Discussion

Analysis of materials and manufacturing processes for Zenith z-stents has improved the accuracy of stents manufactured for experimental analysis making them more comparable to those available through industry. The wire bending jig was designed to manufacture small, repeatable batches of customizable z-stents. However, it is more than likely that industry uses automated wire bending and brazing techniques to achieve a more repeatable, precise end product. Stents manufactured with bending jigs are inspected prior to experimental use to ensure analogy with their industrial counterpart. Brazing will be the major source of error for stents manufactured using the wire bending jig. Brazed joints produced by unskilled hands may be suitable for testing but they are not as uniform as their industrial counterpart and their strength cannot be guaranteed. No stent manufactured using the bending jig has broken due to a failed brazed joint.

With the ability to design and manufacture custom stents for analysis. Next steps will focus on manufacturing stents in order to gather information on their mechanical properties. This information will be used in cooperation with information gathered

during FE analysis to investigate a method of predicting z-stent force generation for patient-specific stent geometries.

Chapter 6

Stent Design Parameters and Radial Force Prediction

This chapter investigates the relationship between stent geometry and radial force generation. Results from this analysis are used to create a preliminary software for predicting radial force generated by self-expanding z-stents in patient specific scenarios.

6.1 Stent Characteristic Study Methodology

Several stents were manufactured using stainless steel 316L spring tempered steel. Leg length, bend angle, wire diameter and bend radius (the four criteria established in Chapter 2 as being crucial to radial force development) were altered and radial force generation data was collected for all stent iterations. Stents were manufactured and measured using techniques described in Chapter 5. Table 6.1 shows all nine stents manufactured for use in this experiment. The "baseline" stent is a laboratory manufactured copy of the Cook (Zenith) 14 mm self-expanding z-stent.

Stent characteristic data was collected using the radial extensometer introduced in Chapter 2, employing the method outlined in Appendix C. At least three sets of data were collected for each stent configuration to ensure a baseline sample size for meaningful statistics. A second ++wire diameter stent was manufactured to verify irregular behavior encountered during testing of the first. Data analysis was performed slightly differently than in previous chapters: instead of setting AR with the first test trial and running others to the same displacement, AR data is collected for every trial.

Force data is collected at 1612 Hz as explained in Section 2.2.2, however, the maximum possible frame rate of images collected by the Logitech C920 webcam while monitoring stent radius hovers around 30 Hz. With this difference and variability of sample rates, the time stamp for these two sets of data do not line up. In order to plot these two variables against each other, a common time stamp had to be established.

Table 6.1: Stent characteristic catalog (±SD, 1/32 in = 0.79 mm, 1/16 in = 1.59 mm)

	Baseline 14 mm	++Wire Diameter	+Wire Diameter	+Leg Length	−Leg Length
Uncovered stent diameter (mm)	24.02 ± 0.08	24.49 ± 0.24	24.28 ± 0.04	24.84 ± 0.15	19.70 ± 0.29
Bend angle (°)	28.68 ± 3.02	27.01 ± 1.00	26.71 ± 1.00	27.05 ± 1.43	25.73 ± 1.93
Stent width (mm)	16.00 ± 0.08	16.08 ± 0.03	16.14 ± 0.06	18.28 ± 0.16	13.48 ± 0.04
Leg length (mm)	15.32 ± 0.20	14.82 ± 0.52	15.13 ± 0.66	17.42 ± 0.74	12.27 ± 0.47
Bend diameter	1/32 in	1/32 in	1/32 in	1/32 in	1/32 in
Wire diameter (mm)	0.40	0.50	0.45	0.40	0.40
Bends per side	8	8	8	8	8

	++Bend Diameter	+Bend Diameter	+Bend Angle	−Bend Angle
Uncovered stent diameter (mm)	24.38 ± 0.04	24.53 ± 0.05	26.76 ± 0.07	17.960 ± 0.250
Bend angle (°)	26.47 ± 1.41	26.49 ± 0.85	32.67 ± 3.59	19.44 ± 2.19
Stent width (mm)	16.48 ± 0.04	16.22 ± 0.09	15.71 ± 0.12	16.32 ± 0.06
Leg length (mm)	15.14 ± 0.41	15.05 ± 0.15	14.82 ± 0.36	15.11 ± 0.27
Bend diameter (mm)	1/16 in	1.00 mm	1/32 in	1/32 in
Wire diameter (mm)	0.40	0.40	0.40	0.40
Bends per side	8	8	8	8

AR values were up-sampled to match the time stamp and data rate of force data using LabVIEW's built-in "interpolate 1D" VI.

Force and AR are both independent, non-monotonically increasing variables which are dependent on time stamp values. Averaging multiple data sets collected for each stent characteristic becomes difficult because time stamps, peak AR and therefore the number of sample points do not match between individual runs. Data sets cannot simply be lined up and averaged like with the previous method. In order to average force values from different unique data sets, each set must be interpolated against a consistent range of AR values. This consistent AR range will become a dependent variable against which averaged force values can be plotted.

Because AR and force values are not monotonically increasing, a classic linear interpolation cannot be used to line up values between data sets due to the fact that certain values may repeat. To address this issue, data sets are aligned for plotting using two-dimensional grid interpolation. The built-in Python function "scipy.interpolate.griddata()" performs this task using original force and AR, as well as the new consistant monotonically increasing AR range as input. Following a two-dimensional interpolation, a new one-dimensional monotonically increasing array of interpolated force values is output.

Force data can now be averaged and is filtered as explained in Section 2.2.2. Filtering was performed after averaging to preserve characteristics of the original data as much as possible.

Data is plotted in two manners: "Full data" refers to the actual AR that each 14 mm uncovered stent encounters during testing, while "Scaled to 14 mm covered" indicates that only the region in the uncovered stent's full AR data set that corresponds to the $0 - 50\,\%$ AR region for a covered 14 mm stent is shown. AR values for the uncovered stent are converted to represent AR values of the covered 14 mm stent using Equation 6.1.

$$\%AR_c = 100\left[1 - \left(\frac{2\sqrt{\left(\frac{100-\%AR_o}{100}\right)\left(\pi\frac{D_o}{2}\right)^2}}{\pi D_c}\right)^2\right] \tag{6.1}$$

where

$\%AR_c$ = covered area reduction (%)
$\%AR_o$ = original area reduction (%)
D_c = unconstricted covered stent diameter (mm)
D_o = unconstricted uncovered stent diameter (mm)

Curve fitting was used to show the trends plots that may have irregular profiles. Polynomial and exponential regression were compared because curve profiles share characteristics that could be matched by either method. Linear regression of original and fit data was used to calculate an r^2 value for each type using Equation 3.10. Because the data trend possesses a single inflection point, a polynomial fit should be selected using Equation 6.2, where $n - 2 \geq$ # of inflection points (n = polynomial order)[199]. With a single inflection point present in results, a cubic fit should be adequate; results in Table 6.2 show that this method achieves a reasonable fit. Although the r^2 value increases with higher order, there is no need to overfit the data, as this will cause other problems to arise such as a wavy fit. All r^2 values were calculated using Equation 3.10, whose results were identical to output produced by Python's linear regression function "scipy.stats.linregress()". An exponential fit was calculated using formula 6.3 and is very comparable to polynomial results.

$$y = a_0 + a_1x + a_2x^2 + a_3x^3 + ... + a_nx^n \tag{6.2}$$

$$y = a * \exp(-bx) - c \tag{6.3}$$

where

a, b, c = regression coefficients
y = y-value input (N)
x = x-value input (%OA)

Increasing wire diameter did not produce as large an increase in separation of force profiles as expected. In the case of ++wire diameter, nine independent sets of data from two unique stents were collected and averaged to ensure results were not

Table 6.2: Wire diameter - r^2 values for different curve fitting methods

	Exponential	1^{st} order	2^{nd} order	**3^{rd} order**
Labmade	0.9235	0.8437	0.9015	**0.9379**
++Wire diameter	0.9630	0.8911	0.9508	**0.9681**
+Wire diameter	0.9874	0.9231	0.9794	**0.9905**

	4^{th} order	5^{th} order	6^{th} order
Labmade	0.9705	0.9911	0.9932
++Wire diameter	0.9803	0.9899	0.9959
+Wire diameter	0.9948	0.9968	0.9971

erroneous. Figure 6.1 presents results for altered wire diameter plotted with a cubic polynomial fit whose r^2 value is given in Table 6.2.

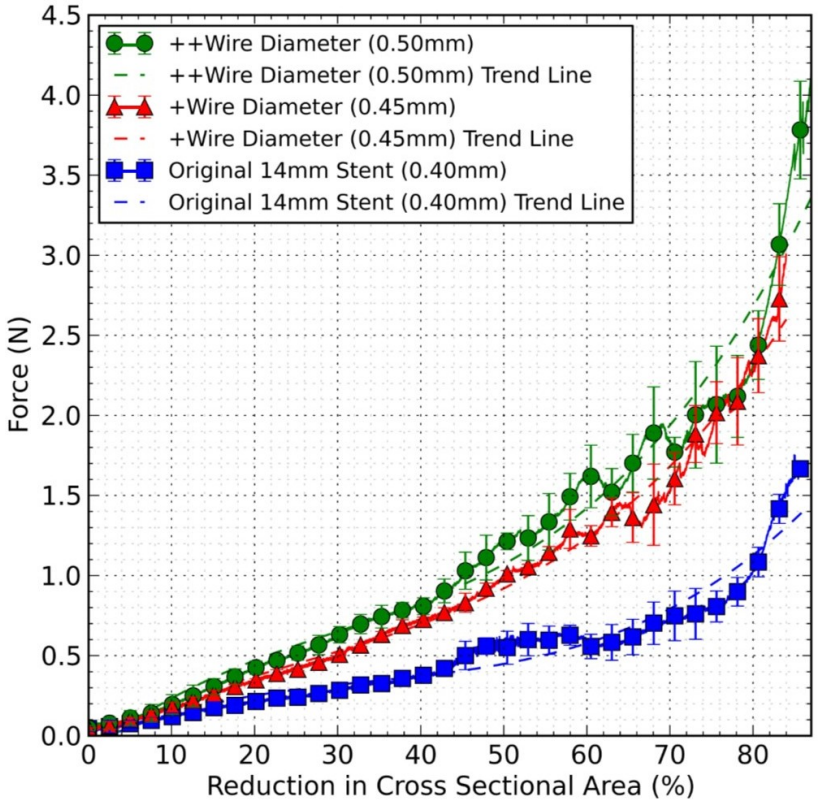

(a) Wire diameter - full data - polynomial fit

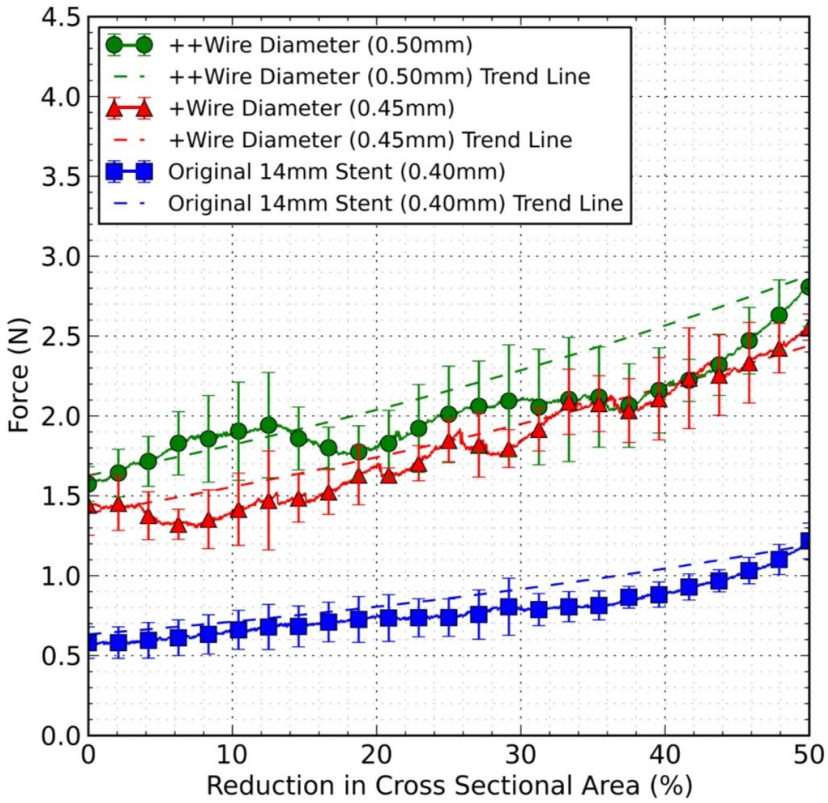

(b) Wire diameter - scaled to 14 mm covered - polynomial fit

Figure 6.1: Results of altered wire diameter with polynomial fit

6.2 Stent Characteristic Study Results

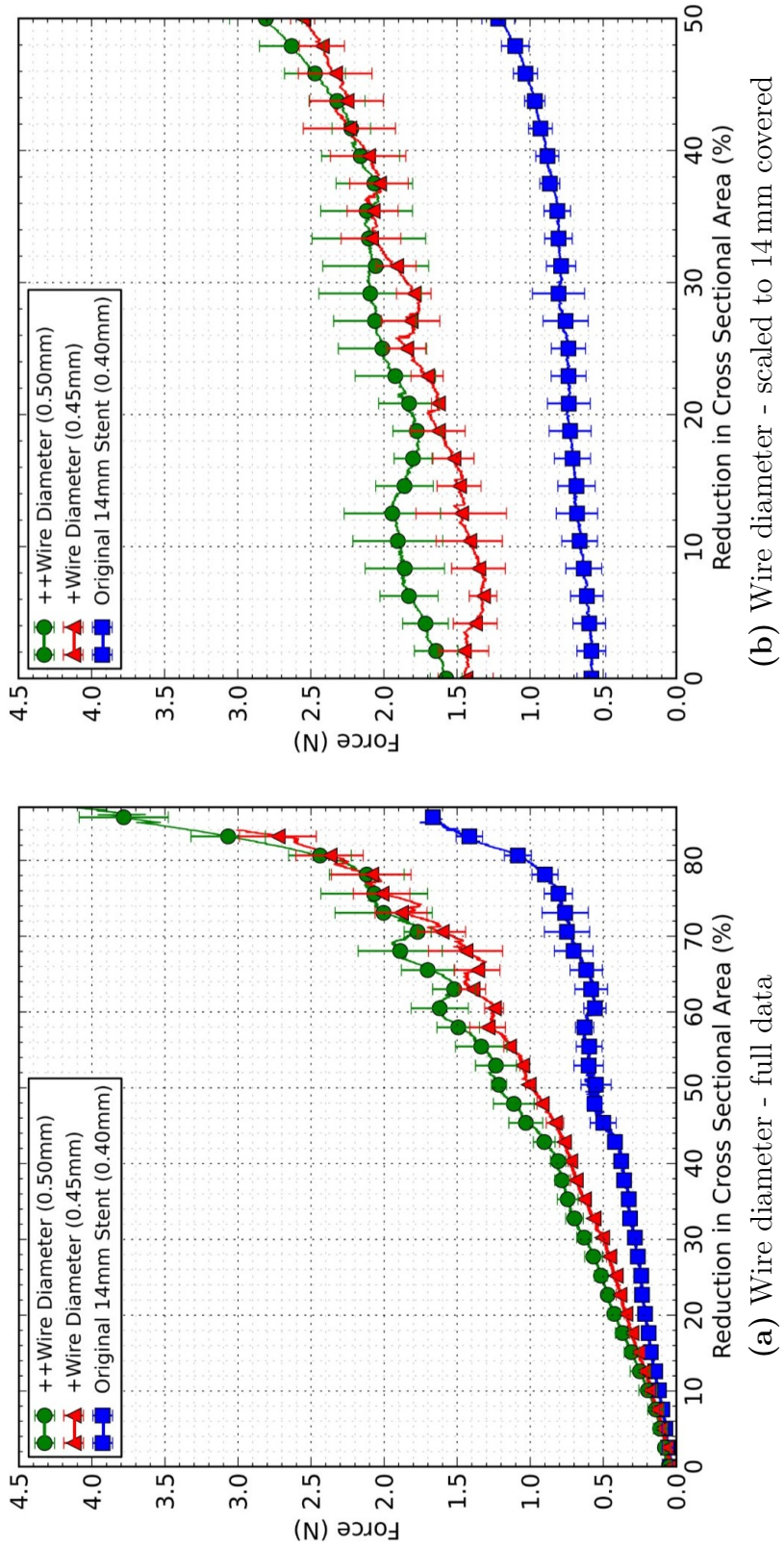

(a) Wire diameter - full data

(b) Wire diameter - scaled to 14 mm covered

Figure 6.2: Effect of altering wire diameter

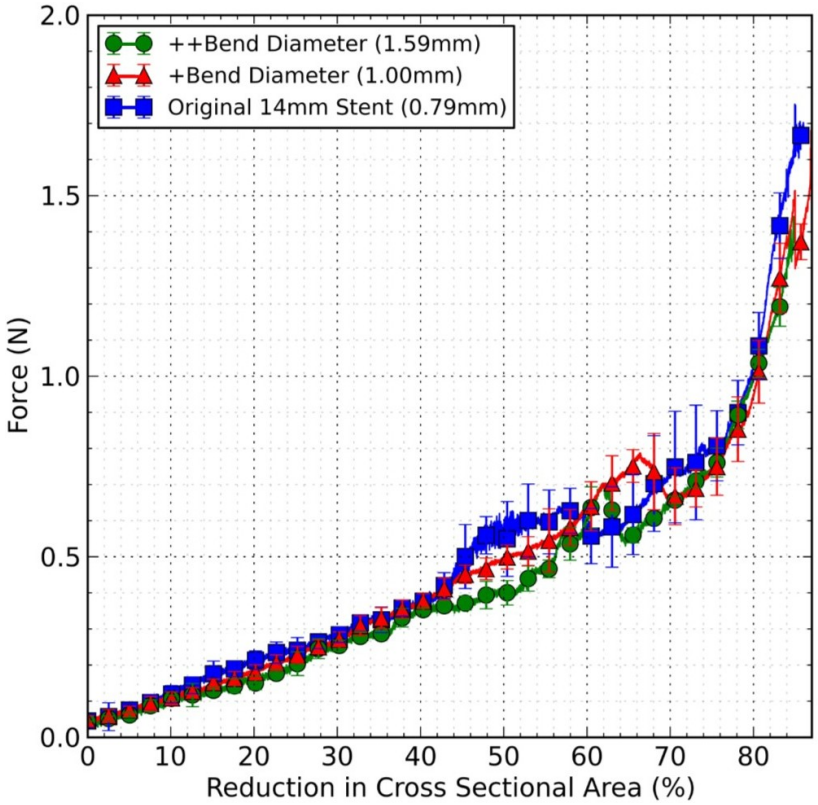

(a) Bend diameter - full data

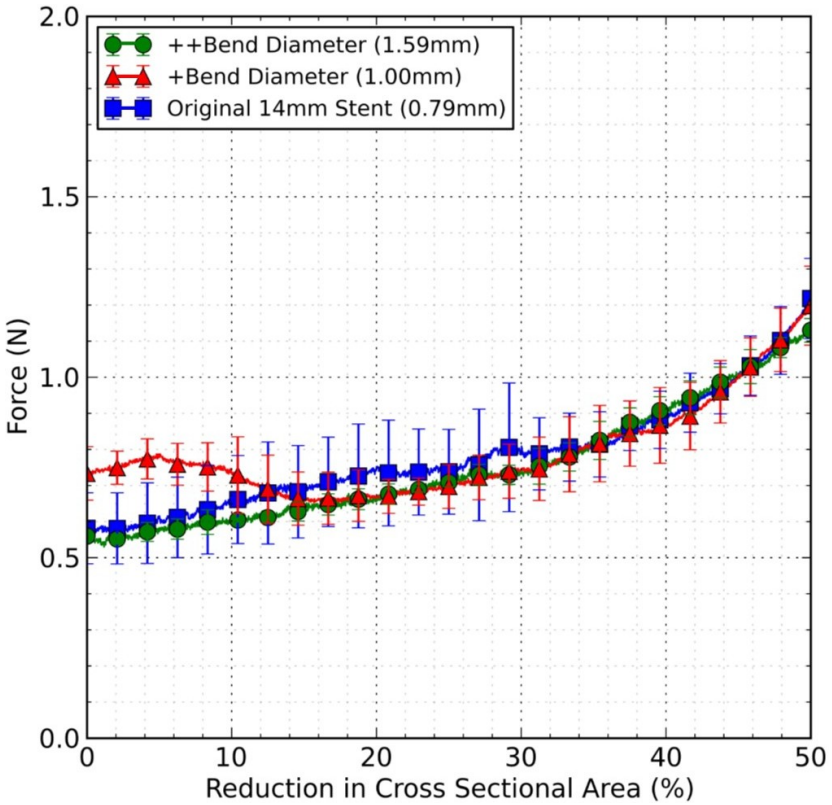

(b) Bend diameter - scaled to 14 mm covered

Figure 6.3: Effect of altering bend radius

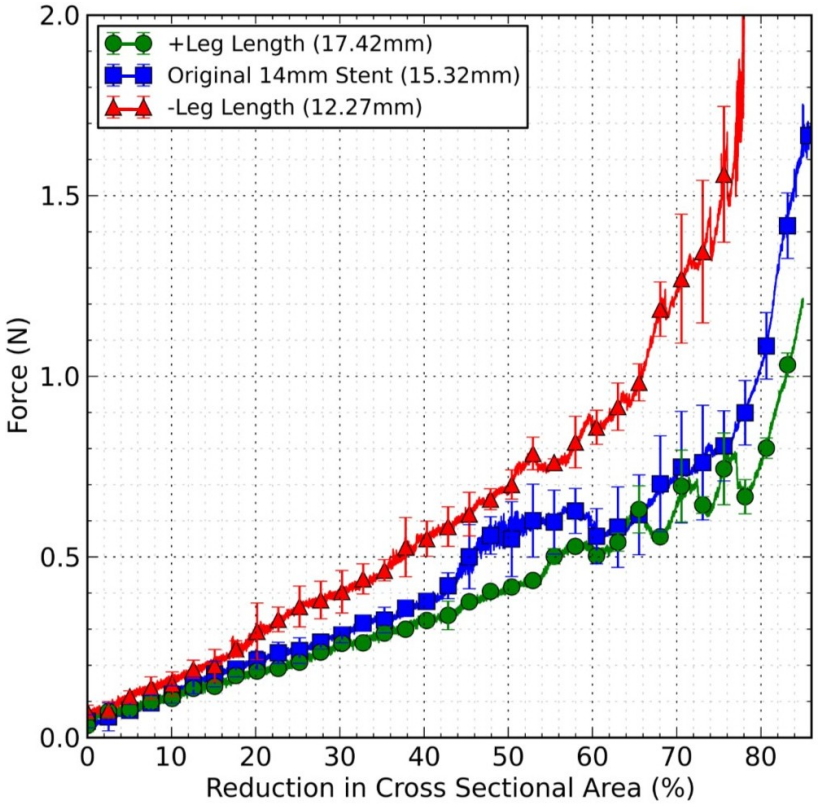

(a) Leg length - full data

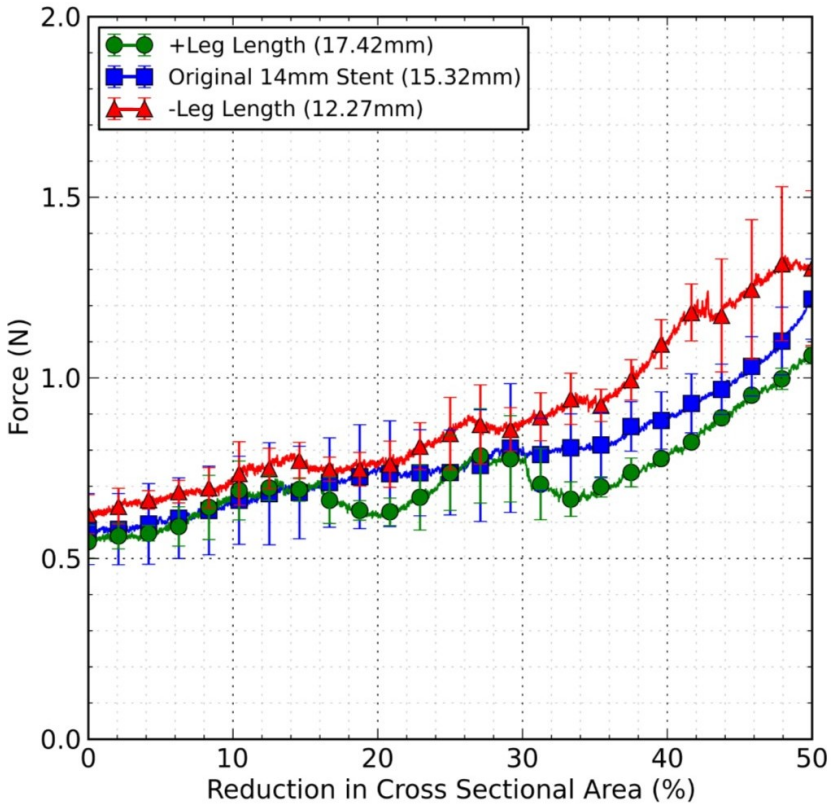

(b) Leg length - scaled to 14 mm covered

Figure 6.4: Effect of altering leg length

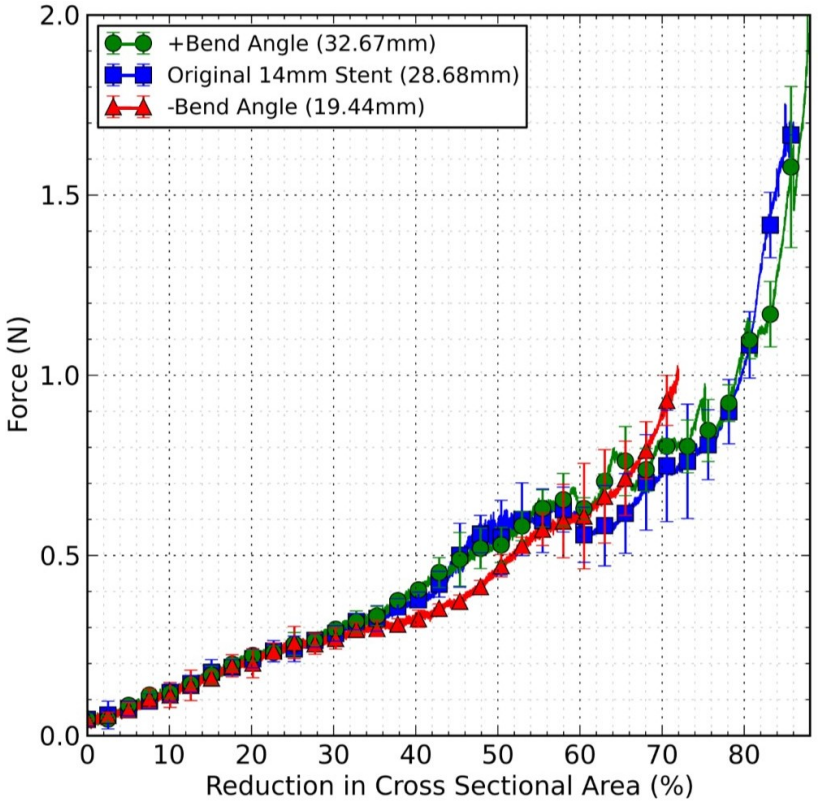

(a) Bend angle - full data

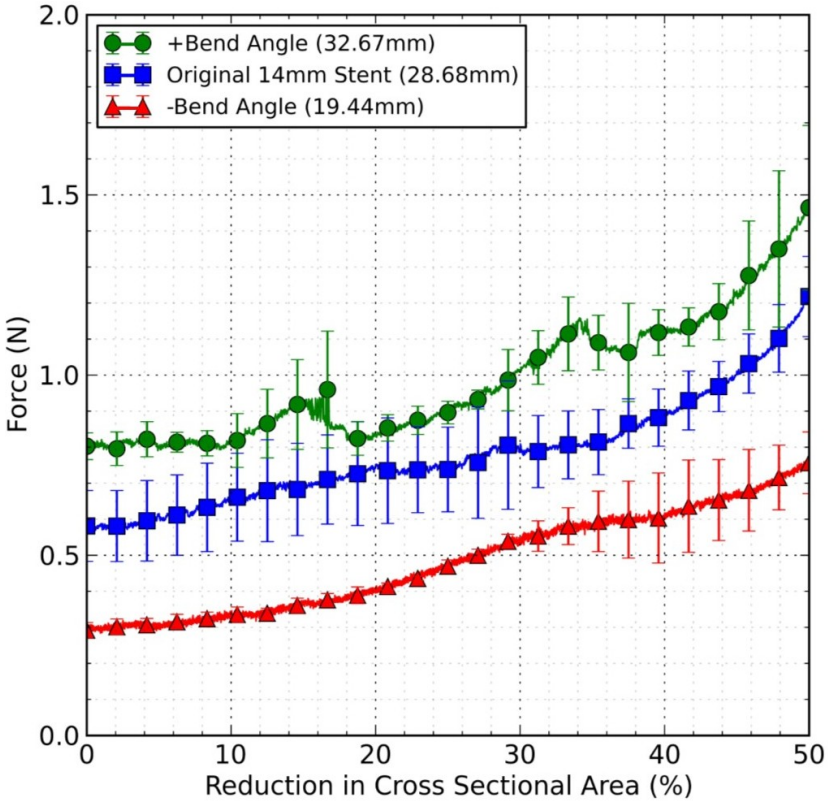

(b) Bend angle - scaled to 14 mm covered

Figure 6.5: Effect of altering bend angle

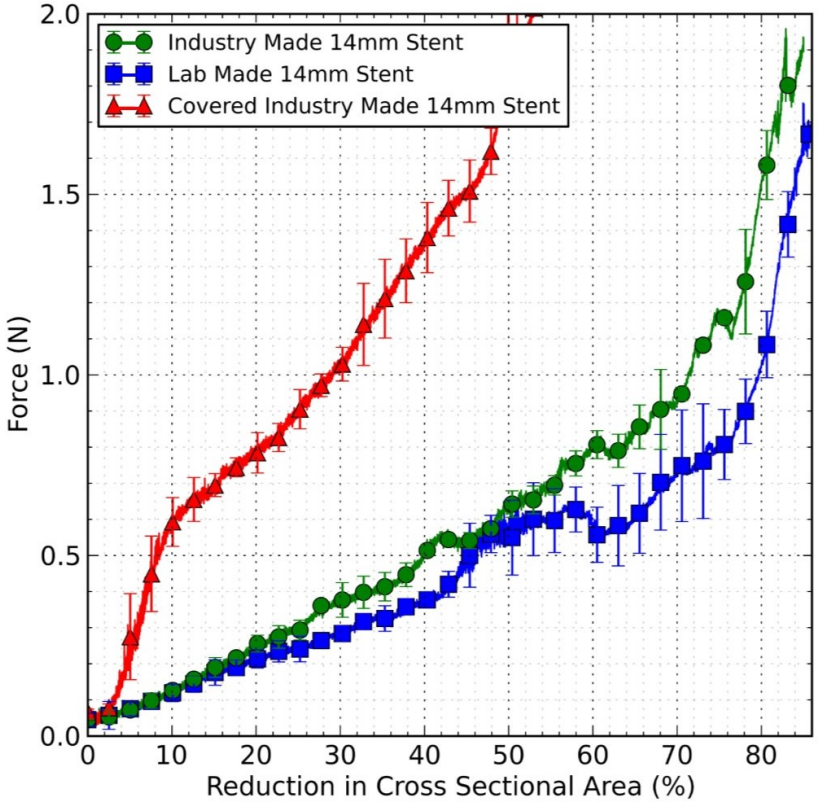

(a) Comparison - full data

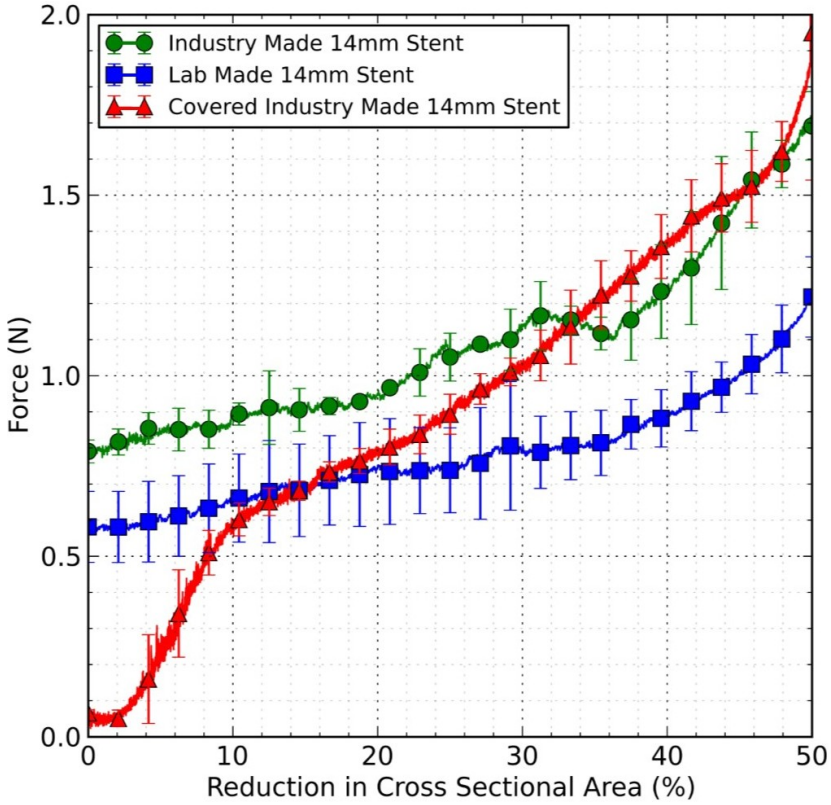

(b) Comparison - scaled to 14 mm covered

Figure 6.6: Comparison of lab, industry and covered stents

6.3 Radial Force Prediction Software

The GUI for software that was developed to use stent characteristic study results for radial force prediction is shown in Figure 6.7. Python code for this program can be found in Appendix G.

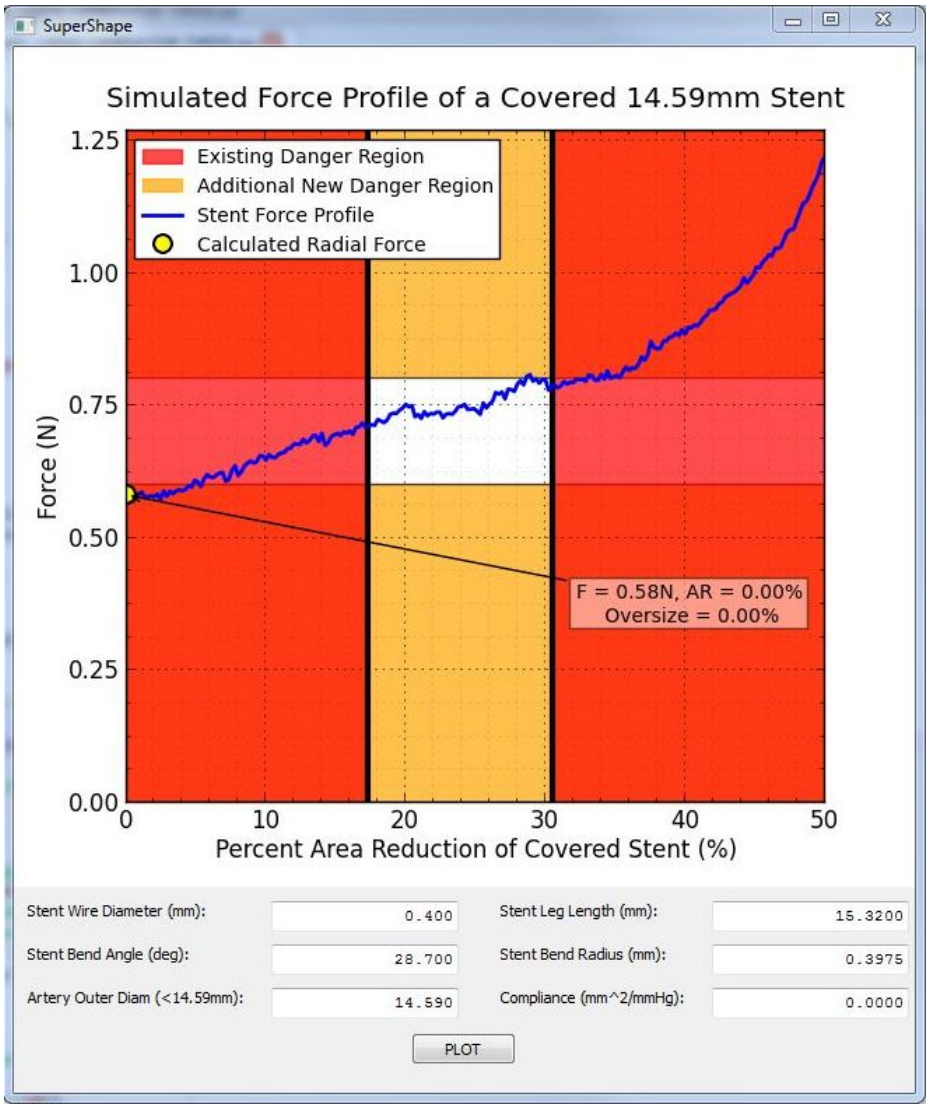

Figure 6.7: Radial force prediction software

This program is run in two stages. An initial run takes in all stent characteristic files and averages individual trials for each characteristic in the same manner explained in Section 6.1. These overall characteristic results are dumped into a temporary file to avoid having to repeat this computationally intensive step for every

alteration in program input. Using this temporary file reduced profile rendering time from $\sim$796 s to $\sim$1 s.

Two steps go into simulating an expected stent radial force profile. First, using Python's "numpy.polyfit()" least squares polynomial function from Python, a linear fit is created to correlate the three different sets of averaged stent characteristic data at each AR interval. A linear fit is assumed because there are not enough trials for each design parameter to draw conclusions on their order. The user input value for each design parameter was used to interpolate predicted values from polynomial functions for each interval of AR.

The final simulated stent force profile is calculated with the algorithm presented in Equations 6.4−6.8, which combines the contribution of each user input stent design parameter.

$$wd_{effect} = wd_{force} - original \tag{6.4}$$

$$ll_{effect} = ll_{force} - original \tag{6.5}$$

$$ba_{effect} = ba_{force} - original \tag{6.6}$$

$$br_{effect} = br_{force} - original \tag{6.7}$$

$$simulated = original + (wd + ll + ba + br)_{effect} \tag{6.8}$$

where

wd = wire diameter (mm)
ll = leg length (mm)
ba = bend angle (°)
br = bend radius (mm)

There are two separate danger regions outlined in Figure 6.7. The area labeled "Existing Danger Region" shows the current rule of thumb values for AAA stent-graft oversize compared to the outer arterial diameter of $10 - 20\,\%$. This corresponds to an AR range of $17.36 - 30.56\,\%$. Figure 6.6(b) demonstrates that oversizing greater than $10\,\%$ avoids the sudden drop-off in radial force below $10\,\%$ AR for a covered stent-graft.

The region labeled "Additional New Danger Region" is a secondary area intended to be used in tandem with existing limits. General limits based on oversizing alone do not adjust to account for the wide range of radial forces produced by different

brands and sizes of stents at the same AR. The additional new radial force region could be used as a more precise design criteria, varying based on individual stent, vessel and patient requirements. The "Additional New Danger Region" range shown in Figure 6.7 is an approximation; refined values will minimize vessel remodeling while ensuring adequate stent-graft fixation. Further research on vessel mechanics and the interaction between prosthesis and vessel walls is required to fully define this new range.

Figure 6.8 demonstrates the impact of entering patient specific characteristics for arterial diameter and compliance on the baseline results shown in Figure 6.7. Figure 6.8(a) shows the predicted radial force for a patient with an outer arterial diameter of 12.5 mm without any compensation for compliance. While the results shown in Figure 6.8(b) demonstrate the reduction in oversize and AR when an arterial compliance of 0.2 mm^2/mmHg is included in the prediction.

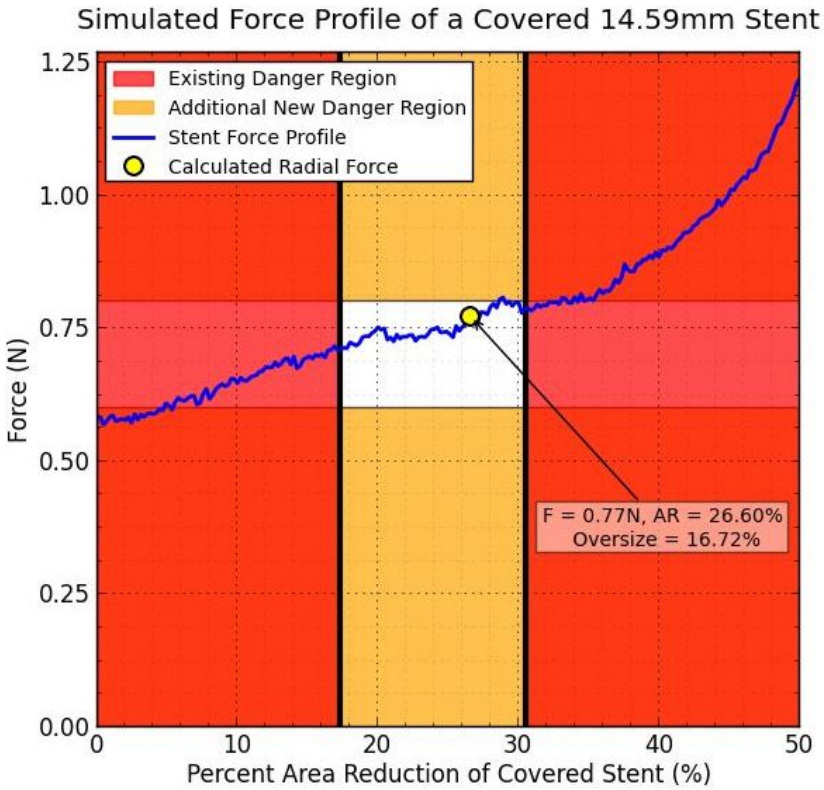

(a) Compliance = $0.0\,\mathrm{mm}^2/\mathrm{mmHg}$

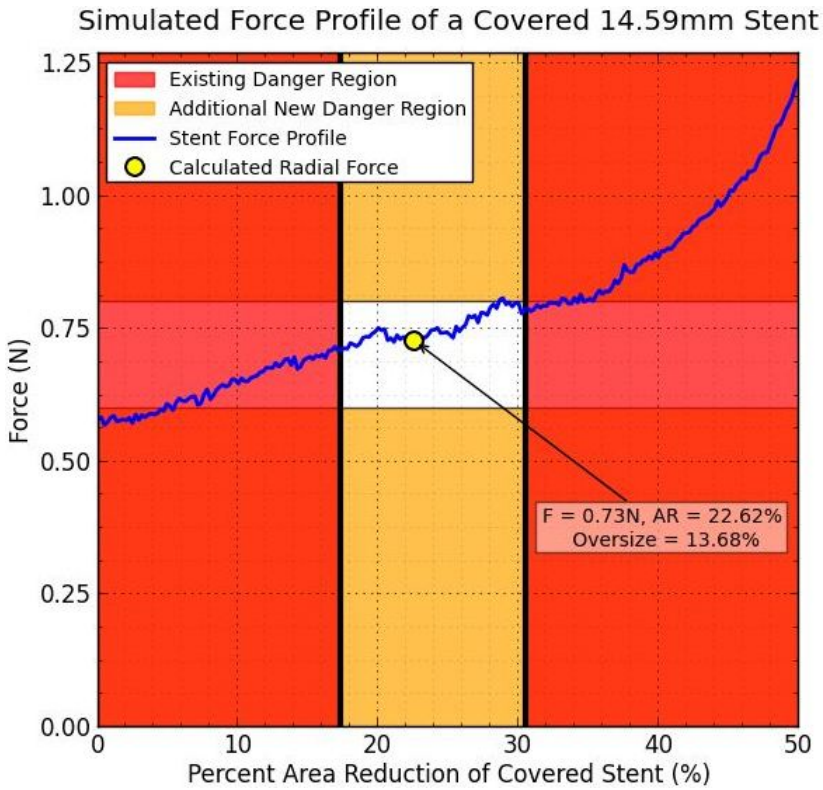

(b) Compliance = $0.2\,\mathrm{mm}^2/\mathrm{mmHg}$

Figure 6.8: The effect of compliance on the simulated radial force profile for a 14.59 mm stent expanded inside an artery with an outer diameter of 12.5 mm

Using the four stent design parameter input boxes in the simulation software (wire diameter, leg length, bend angle and bend radius) the user can alter the output stent force profile shown in Figure 6.8. Once this profile falls inside the safe region, patient specific characteristics can be added to ensure their vales wont shift radial force into either danger area. Patient specific input includes outer artery diameter, which must be below the original covered stent diameter of 14.59 mm, as well as arterial compliance measured in $mm^2/mmHg$. The effect of arterial compliance on simulated radial force is calculated using Equations 6.9 to 6.12. The change in area due to compliance from Equation 6.12 is subtracted from the original unaffected AR value giving a new AR value for the simulated compliant artery. This new AR value and its associated radial force value from the original force profile become the new x and y-simulated output respectively.

$$P = \frac{F_R}{SA_{STENT}} * 7500.616 \tag{6.9}$$

$$C_{AC} = Compliance * P \tag{6.10}$$

$$OA = \pi \left(\frac{D_{CO}}{2} \right)^2 \tag{6.11}$$

$$\Delta A_C = \frac{C_{AC}}{OA} * 100 \tag{6.12}$$

where

D_{CO} = covered original diameter (mm)
P = pressure (mmHg)
SA_{STENT} = stent surface area (mm^2)
C_{AC} = compliance area change (mm^2)
OA = original area (mm^2)
ΔA_C = change in area due to compliance (mm^2)

6.4 Discussion

Results presented in Figures 6.2 through 6.5 demonstrate the impact of each stent design parameter on overall radial force generation. Table 6.3 presents results for standard error of the estimate and t-values, which were calculated using Equations

3.11 and 6.15, to evaluate the hypotheses presented in Equations 6.13 and 6.14. p-Values are calculated to evaluate whether the alternative hypothesis is statistically significant. Results show that the only stent characteristic not to achieve statistical significance is "+bend radius"; it's trend line has a 13.4 % chance of replicating the original 14 mm stent, baseline trend.

These results agree with earlier investigations by Snowhill et al. in 2001, whose results showed that manipulating leg length and wire gauge had the largest impact on radial force. They elaborated that radial force is maximized with increasing wire diameter and number of bends; as well as when leg length is equal to vessel diameter for stents with $5-7$ bends. They found a parabolic relationship between radial force and leg length for z-stents[137].

$$H_0 = \mu_1 = \mu_2 \tag{6.13}$$

$$H_A = \mu_1 \neq \mu_2 \parallel \mu_1 > \mu_2 \parallel \mu_1 < \mu_2 \tag{6.14}$$

where

$$\begin{aligned} H_0 &= \text{null hypothesis} \\ H_A &= \text{alternative hypothesis} \\ \mu_1 &= \text{first dataset mean (N)} \\ \mu_2 &= \text{second dataset mean (N)} \end{aligned}$$

$$t_{test} = \frac{\bar{Y_2} - \bar{Y_1}}{\sqrt{\frac{S_1^2}{n_1} + \frac{S_2^2}{n_2}}} \tag{6.15}$$

where

$$\begin{aligned} Y_1 &= \text{original force dataset (N)} \\ S_1^2 &= \text{standard deviation of original dataset (N)} \\ Y_2 &= \text{altered characteristic force dataset (N)} \\ S_2^2 &= \text{standard deviation of altered dataset (N)} \\ \bar{Y_1}, \bar{Y_2} &= \text{mean of forces (N)} \\ t_{test} &= \text{t-test value} \\ n_1, n_2 &= \text{number of values in dataset} \end{aligned}$$

There is much room for expansion of this software. This program currently predicts radial force for different design parameter iterations of the 14 mm stent. To make this software compatible with larger diameter stents, a full range of design parameter profiles would have to be created for each stent diameter. In the future, a

Table 6.3: Standard error, t-test and p-values for different stent characteristic changes (SError units match those of the column heading)

	+Wire Diameter	++Wire Diameter	+Bend Radius	++Bend Radius
SError	1.05	1.25	0.07	0.04
t-Test	-102.732	-139.469	-1.501	3.926
p-Value	0.000	0.000	0.134	0.000

	−Bend Angle	+Bend Angle	−Leg Length	+Leg Length
SError	0.30	0.21	0.12	0.07
t-Test	39.826	-25.718	-12.992	8.054
p-Value	0.000	0.000	0.000	0.000

software that could take in patient arterial dimensions and compliance alone, while calculating the design parameters required to achieve a target radial force would be the most useful and revolutionary. Future iterations could use these results to select stents from a catalog of available models or to suggest manufacture of a specific stent geometry.

Chapter 7

Conclusion

Although self-expanding endovascular z-stents have been used for several years in the management of aneurysmal arterial disease, it has not previously been possible to characterize their mechanics. The objective of this work was not only to develop investigative tools intended for use in rectifying a deficient understanding of stent mechanics but also to characterize the impact of altering stent design parameters on overall stent performance. Results from this analysis were used to predict stent performance based on both varied stent geometry and patient specific arterial diameter and compliance.

A novel radial extensometer and modern data acquisition system were developed to both improve the quality of data being collected for stent radial force characterization as well as to standardize the method of data collection for future works. This system was sized appropriately for loading forces that could be expected from available stent-grafts. As an improvement over previous experimental methods, a machine vision system was added to not only eliminate error from Mylar deformation but also to reduce error due to manual calculation by explicitly calculating AR in real-time throughout testing. Through analysis of the orientation of stent brazed joints, it became evident that brazed stent connections have an impact on the symmetry of radial force distribution. Orientation of stents and positioning of the brazed connection during implantation will have an impact on the interaction between stent and arterial wall, especially if multiple stents are used in the same prosthetic. A final investigation confirmed results presented by Johnston et al. explaining that the force applied by stents placed in an end-to-end configuration was equivalent to the sum of forces applied by individual stents[1]. Testing of a single stent with and without a graft covering showed that the woven polyester graft had very little impact on radial force results above 10 % AR.

Results initially presented by Johnston et al. regarding a discrepancy between

stent diameter and radial force generation have been verified, clearly demonstrating that smaller stent diameters exhibit higher radial force than larger diameter stents across the entire range of AR values that may be encountered following implantation[1]. Considering that drag force rises along with arterial diameter, it is logical that radial force exerted by stent-grafts should also increase with diameter up to a certain limit intended to avoid vessel remodeling.

A converged FE model of the radial extensometer testing a 12 mm stent was developed to analyze stent mechanics and provide a tool for future stent development. Validation of the converged radial force profile during expansion provided a good fit attaining an r^2 of 0.946, a standard error of 0.099 N, a MAPE of 11.69 % and a MPE of 1.69 % when compared to experimental results. Adoption of the validated FE model and radial extensometer by others will establish a consistant platform for both comparison of results and cataloging the performance of existing prosthetics.

Analysis of the completed FE model provides evidence that the non-symmetric force profile created through comparison of results during constriction and expansion is not solely due to frictional effects. Simulation results show that both interaction between the stent and radial extensometer rollers as well as stent mechanics have an impact on radial force generation. The effect of torsion, s-bending and t-bending moments during stent expansion combine to create the collected radial force profile. The radial extensometer influences collected data through several means including the interaction between stent legs and radial extensometer rollers; pinching of the stent between radial extensometer rollers; as well as friction between the Mylar and stent.

Developing the ability to manufacture new stents required the investigation of current stent metallurgy and manufacturing techniques using SEM and EDS. This confirmed the use of stainless steel 316L and a wire drawing manufacturing process. Using this knowledge and an analysis of currently available stent geometries, a small batch stent manufacturing process was developed to produce exact and altered replicas of a 14 mm Cook (Zenith) z-stent. Several stents with variations of the four main design criteria (leg length, wire diameter, bend diameter and bend angle) were fabricated to perform a parametric study on their individual impact on radial force generation. The performance of these altered stent geometries were analyzed using

the newly developed radial extensometer. Results showed that the only design parameter not to have a statistically significant impact on radial force generation was a lesser increased in bend diameter (1.00 mm vs. the original 0.794 mm [1/32 in]), however a larger variation of this parameter (1.588 mm [1/16 in]) was statistically significant.

Using results from the design parameter analysis, software was developed to predict radial force generation for 14 mm stents with any combination of the four investigated parameters. Patient specific values for inner arterial diameter and compliance alter results to show how a specific stent geometry would perform. Developing the ability to manipulate the fixation (radial) force to an ideal value for each individual stent and patient instead of relying on $10 - 20\,\%$ oversize as a guideline will improve the precision of EVAR, enabling the expansion of possible stent-graft uses to more sensitive pathologies such as vena cava stenosis and aortic dissection.

7.1 Recommendations and Future Work

Each component analyzed in these works has the potential to be expanded upon. In the case of the radial extensometer, altering the program from positional control (linear slide displacement) to a system controlled by an input value for AR would greatly simplify data collection. This would ensure each test constricts to a desired AR instead of having to redo trials that do not achieve the correct AR due to inaccurate input for linear slide displacement. Future iterations of the radial extensometer could be expanded to include the ability to manipulate temperature and humidity in order to observe their effect on stent expansion and radial force. It could be useful to develop the ability to more closely simulate conditions that would be encountered in-vivo in the experimental setup.

Further analysis of FE model results should reveal more information regarding the connection between radial force generation and force values collected from the linear force gauge. Establishing a range of force gauge values that correspond to ideal in-vivo radial forces would be an important step in the development of mechanically correct stents, however this would require further development of the in-vivo stent expansion model.

The FE model should be used to both fully characterize the mechanisms behind radial force generation and to resolve the individual contributions of torsion, s-bending and t-bending moments on radial force generation. The effect of altered stent geometry, wire cross-section, materials, type of wire connection (potentially seamless) or even a non-uniform wire diameter are all possible ways that stent mechanics could be altered. Developing a methodology to predictably alter torsion, s-bending and t-bending moments would facilitate the design of stents based on mechanical understanding instead of prediction. Stents developed using the FE model could then be manufactured and tested in the radial extensometer to verify their performance.

Stent force prediction software is currently only available for 14 mm stents. To expand this program's functionality, future work should focus on collecting design parameter data for other stent diameters. Ideally, future iterations of this software could take in patient arterial dimensions and compliance alone, calculating design parameters required to achieve a target radial force. The program could use these results to select a stent from a catalog of available models or suggest the manufacturing of a specific geometry. Medical professionals and patients would benefit from a software which improves prosthetic selection for each case.

The theory and tools developed in this work can be used to further investigate and improve the performance of available prosthetics, enhancing patient care and widening potential applications of endovascular devices to more sensitive procedures. Increasing both the number of possible applications for stent-grafts as well as the use of EVAR over OSR will increase the demand for prosthetics, expanding the available market for manufacturers. Advancements in the understanding of stent mechanics will bolster progress toward the design of stent grafts that reduce incidence of migration, endoleak and rupture.

References

[1] CliftonR. Johnston et al. "The Mechanical Properties of Endovascular Stents: An In Vitro Assessment". English. In: *Cardiovascular Engineering* 10 (3 2010), pp. 128–135. ISSN: 1567-8822. DOI: 10.1007/s10558-010-9097-9. URL: http://dx.doi.org/10.1007/s10558-010-9097-9.

[2] C. Shu et al. "Endovascular Repair of Complicated Acute Type-B Aortic Dissection with Stentgraft: Early and Mid-term Results". In: *European Journal of Vascular and Endovascular Surgery* 42.4 (2011), pp. 448–453. ISSN: 1078-5884. DOI: http://dx.doi.org/10.1016/j.ejvs.2011.05.013. URL: http://www.sciencedirect.com/science/article/pii/S1078588411003236.

[3] Warren Swee and Michael D Dake. "Endovascular management of thoracic dissections". In: *Circulation* 117.11 (2008), pp. 1460–1473.

[4] Ryan Jean-Baptiste, DavidM. Williams, and JosephJ. Gemmete. "Successful Treatment of Superior Vena Cava Rupture with Placement of a Covered Stent: A Report of Two Cases". English. In: *CardioVascular and Interventional Radiology* 34.3 (2011), pp. 667–671. ISSN: 0174-1551. DOI: 10.1007/s00270-011-0128-8. URL: http://dx.doi.org/10.1007/s00270-011-0128-8.

[5] S. Dendo et al. "Severe obstruction of the superior vena cava caused by tumor invasion recanalization using a PTFE-covered Z stent". English. In: *Journal of Cardiovascular Surgery* 43.2 (Apr. 2002), pp. 287–90. URL: http://ezproxy.library.dal.ca/login?url=http://search.proquest.com/docview/224420110?accountid=10406.

[6] Z. Li and C. Kleinstreuer. "Analysis of biomechanical factors affecting stent-graft migration in an abdominal aortic aneurysm model". In: *Journal of Biomechanics* 39.12 (2006), pp. 2264–2273. ISSN: 0021-9290. DOI:

http://dx.doi.org/10.1016/j.jbiomech.2005.07.010. URL: http://www.sciencedirect.com/science/article/pii/S0021929005003453.

[7] Mital Desai et al. "AAA Stent-Grafts: Past Problems and Future Prospects". English. In: *Annals of Biomedical Engineering* 38 (4 2010), pp. 1259–1275. ISSN: 0090-6964. DOI: 10.1007/s10439-010-9953-1. URL: http://dx.doi.org/10.1007/s10439-010-9953-1.

[8] Hope G. Alcorn et al. "Risk Factors for Abdominal Aortic Aneurysms in Older Adults Enrolled in the Cardiovascular Health Study". In: *Arteriosclerosis, Thrombosis, and Vascular Biology* 16 (1996), pp. 963–970. DOI: 10.1161/01.ATV.16.8.963. URL: http://atvb.ahajournals.org/content/16/8/963.full.

[9] National Institute for Health and Care Excellence. *NICE technology appraisal guidance [TA167]. Clinical need and practice*. Feb. 2009. URL: http://www.nice.org.uk/guidance/TA167/chapter/2-Clinical-need-and-practice (visited on 05/11/2015).

[10] L. Joseph Melton III et al. "Changing Incidence of Abdominal Aortic Aneurysms: A Population-Based Study". In: *American Journal of Epidemiology* 120.3 (1984), pp. 379–386. URL: http://aje.oxfordjournals.org/content/120/3/379.full.pdf+html.

[11] Martin P. Nevitt, David J. Ballard, and John W. Hallett. "Prognosis of Abdominal Aortic Aneurysms". In: *New England Journal of Medicine* 321.15 (1989). PMID: 2674715, pp. 1009–1014. DOI: 10.1056/NEJM198910123211504. eprint: http://dx.doi.org/10.1056/NEJM198910123211504. URL: http://dx.doi.org/10.1056/NEJM198910123211504.

[12] C. J. H. Ingoldby, R. Wujanto, and J. E. Mitchell. "Impact of vascular surgery on community mortality from ruptured aortic aneurysms". In: *British Journal of Surgery* 73.7 (1986), pp. 551–553. ISSN: 1365-2168. DOI: 10.1002/bjs.1800730711. URL: http://dx.doi.org/10.1002/bjs.1800730711.

[13] J. EARLE JR. M.D. ESTES. "Abdominal Aortic Aneurysm: A Study of One Hundred and Two Cases". In: *Circulation* 2 (2 Aug. 1950), pp. 258–264. URL: http://ovidsp.ovid.com/ovidweb.cgi?T=JS&CSC=Y&NEWS=N&PAGE=fulltext&D=ovfta&AN=00003017-195008000-00013.

[14] D. Emeiuck M.D. Szilacyi et al. "Contribution of Abdominal Aortic Aneurysmectomy to Prolongation of Life". In: *Annals of Surgery* 164 (4 Oct. 1966), pp. 678–699. URL: http://ovidsp.ovid.com/ovidweb.cgi?T=JS&CSC=Y&NEWS=N&PAGE=fulltext&D=ovfta&AN=00000658-196610000-00014.

[15] C Dubost, M Allary, and N Oeconomos. "Resection of an aneurysm of the abdominal aorta: reestablishment of the continuity by a preserved human arterial graft, with result after five months". In: *A.M.A. archives of surgery* 64 (3 1952), pp. 405–408. DOI: 10.1001/archsurg.1952.01260010419018. URL: http://archsurg.jamanetwork.com/article.aspx?articleid=550230.

[16] Stefano Bonardelli et al. "Risk factors for immediate results and long-term survival following elective open surgery for AAA.Statistical analysis of 1111 consecutively-treated patients". In: *Annali Italiani Di Chirurgia* 78 (4 Aug. 2007), pp. 265–276.

[17] Simon Rinckenbach et al. "Current Outcome of Elective Open Repair for Infrarenal Abdominal Aortic Aneurysm". In: *Annals of Vascular Surgery* 8 (6 2004), pp. 704–709. URL: http://link.springer.com/article/10.1007/s10016-004-0114-6.

[18] Calvin B. Ernst. "Abdominal Aortic Aneurysm". In: *New England Journal of Medicine* 328.16 (1993). PMID: 8455684, pp. 1167–1172. DOI: 10.1056/NEJM199304223281607. eprint: http://dx.doi.org/10.1056/NEJM199304223281607. URL: http://dx.doi.org/10.1056/NEJM199304223281607.

[19] Peter L. Faries et al. "Stent graft treatment for abdominal aortic aneurysm repair: recent developments in therapy". In: *Current Opinion in Cardiology* 19 (6 Nov. 2004), pp. 551–557. ISSN: 0268-4705.

[20] CHARLES T. DOTTER and MELVIN P. JUDKINS. "Transluminal Treatment of Arteriosclerotic Obstruction: Description of a New Technic and a Preliminary Report of Its Application". In: *Circulation* 30.5 (1964), pp. 654–670. DOI: 10.1161/01.CIR.30.5.654. eprint: http://circ.ahajournals.org/content/30/5/654.full.pdf+html. URL: http://circ.ahajournals.org/content/30/5/654.abstract.

[21] Charles Dotter. "Transluminally-placed Coilspring Endarterial Tube Grafts: Long-term Patency in Canine Popliteal Artery". In: *Investigative Radiology* 4 (5 1969), pp. 329–332. ISSN: 0020-9996. URL: http://ovidsp.ovid.com/ovidweb.cgi?T=JS&PAGE=reference&D=ovfta&NEWS=N&AN=00004424-196909000-00008.

[22] JulioC. Palmaz. "Intravascular stenting: from basic research to clinical application". English. In: *CardioVascular and Interventional Radiology* 15.5 (1992), pp. 279–284. ISSN: 0174-1551. DOI: 10.1007/BF02733951. URL: http://dx.doi.org/10.1007/BF02733951.

[23] NL Volodos et al. "A self-fixing synthetic blood vessel endoprosthesis". In: *Vestnik khirurgii imeni II Grekova* 137.11 (1986), p. 123.

[24] H.M. Lazarus. *Intraluminal graft device, system and method*. US Patent 4,787,899. Nov. 1988. URL: http://www.google.com/patents/US4787899.

[25] Alexander Balko et al. "Transfemoral placement of intraluminal polyurethane prosthesis for abdominal aortic aneurysm". In: *Journal of Surgical Research* 40.4 (1986), pp. 305–309. ISSN: 0022-4804. DOI: http://dx.doi.org/10.1016/0022-4804(86)90191-5. URL: http://www.sciencedirect.com/science/article/pii/0022480486901915.

[26] Frank J. Criado. "EVAR at 20: The Unfolding of a Revolutionary New Technique that Changed Everything". In: *Journal of Endovascular Therapy* 17.6 (2010), pp. 789–796. DOI: 10.1583/10-3291.1. eprint: http://jet.sagepub.com/content/17/6/789.full.pdf+html. URL: http://jet.sagepub.com/content/17/6/789.short.

[27] T. W. Duerig, D. E. Tolomeo, and M. Wholey. "An overview of superelastic stent design". In: *Minimally Invasive Therapy and Allied Technologies* 9.3-4 (2000), pp. 235–246. DOI: 10.1080/13645700009169654. eprint: http://dx.doi.org/10.1080/13645700009169654. URL: http://dx.doi.org/10.1080/13645700009169654.

[28] Ole Martin Pedersen, Aslak Aslaksen, and Harald Vik-Mo. "Ultrasound measurement of the luminal diameter of the abdominal aorta and iliac arteries in patients without vascular disease". In: *Journal of Vascular Surgery* 17.3 (1993), pp. 596–601. ISSN: 0741-5214. DOI: http://dx.doi.org/10.1016/0741-5214(93)90161-E. URL: http://www.sciencedirect.com/science/article/pii/074152149390161E.

[29] David W. Feigal Jr. MD. MPH. *FDA Public Health Notification: Problems with Endovascular Grafts for Treatment of Abdominal Aortic Aneurysm (AAA)*. U.S. Food and Drug Administration. Apr. 2001. URL: http://www.fda.gov/MedicalDevices/Safety/AlertsandNotices/PublicHealthNotifications/ucm062191.htm (visited on 05/15/2015).

[30] Anahita Dua et al. "Epidemiology of aortic aneurysm repair in the United States from 2000 to 2010". In: *Journal of Vascular Surgery* 59.6 (2014), pp. 1512–1517. ISSN: 0741-5214. DOI: http://dx.doi.org/10.1016/j.jvs.2014.01.007. URL: http://www.sciencedirect.com/science/article/pii/S0741521414001025.

[31] Frank J. Criado MD. FACS. FSVM. *The EVAR Landscape in 2011. A status report on AAA therapy.* Endovascular Today, Bryn Mawr Communications II, LLC. Mar. 2011. URL: http://evtoday.com/2011/03/the-evar-landscape-in-2011/ (visited on 05/20/2015).

[32] Endovascular Today. *AAA MAIN BODY GRAFTS. Buyer's Guide.* Bryn Mawr Communications II, LLC. URL: http://bmctoday.net/evtoday/buyersguide/2013/chart.asp?id=aaa_main_body_grafts_us (visited on 05/15/2015).

[33] Eanas S. Yassa MD. and Joseph V. Lombardi MD. *Infrarenal EVAR Technology Review*. Bryn Mawr Communications II, LLC. Mar. 2012. URL: http://evtoday.com/pdfs/et0312_F9_Lombardi.pdf (visited on 05/20/2015).

[34] Endovascular Today. *2015 BUYER'S GUIDE. AAA MAIN BODY GRAFTS*. Bryn Mawr Communications II, LLC. 2015. URL: http://evtoday.com/buyers-guide/2015-europe/chart.asp?id=aaa_main_body_grafts_EU (visited on 05/23/2015).

[35] Barry R. Liden. *Edwards Lifesciences to Discontinue Lifepath AAA Program*. Edwards Lifesciences. Apr. 6, 2004. URL: http://www.edwards.com/newsroom/Pages/nr20040406.aspx (visited on 05/23/2015).

[36] Boston Scientific. *Guidant to Discontinue Product for Treating Abdominal Aortic Aneurysms*. Boston Scientific. June 26, 2003. URL: http://news.bostonscientific.com/index.php?s=24913&item=22025 (visited on 05/23/2015).

[37] U.S. Food and Drug Administration. *EXCLUDER Bifurcated Endoprosthesis - P020004*. U.S. Food and Drug Administration. Nov. 2, 2002. URL: http://www.fda.gov/MedicalDevices/ProductsandMedicalProcedures/DeviceApprovalsandClearances/Recently-ApprovedDevices/ucm083074.htm (visited on 05/20/2015).

[38] U.S. Food and Drug Administration. *Zenith AAA Endovascular Graft - P020018*. U.S. Food and Drug Administration. May 23, 2003. URL: http://www.fda.gov/MedicalDevices/ProductsandMedicalProcedures/DeviceApprovalsandClearances/Recently-ApprovedDevices/ucm082436.htm (visited on 05/20/2015).

[39] U.S. Food and Drug Administration. *Endologix PowerLink System - P040002*. U.S. Food and Drug Administration. Oct. 29, 2004. URL: http://www.fda.gov/MedicalDevices/ProductsandMedicalProcedures/DeviceApprovalsandClearances/Recently-ApprovedDevices/ucm080664.htm (visited on 05/20/2015).

[40] Joan Brown. "Anaconda AAA Stent Graft System". In: *Vascular Voice* 5 (2 Sept. 2010), p. 2. URL: http://www.michiganvascularcenter.com/newsletter_images/1369166152.pdf.

[41] Endovascular Today. *Milestones*. Bryn Mawr Communications II, LLC. June 6, 2014. URL: http://www.jotec.com/english/unternehmen-meilensteine.pml (visited on 05/23/2015).

[42] Dominique B. Buck et al. "Endovascular treatment of abdominal aortic aneurysms". In: *Nat Rev Cardiol* 11 (2 Feb. 2014), pp. 112–123. URL: http://dx.doi.org/10.1038/nrcardio.2013.196.

[43] Acquire Media. *Endologix Announces FDA Approval of AFX Endovascular AAA System. New EVAR Device to be Introduced at the Annual Meeting of the Society for Vascular Surgery*. Endologix, Inc. June 15, 2011. URL: http://investor.endologix.com/releasedetail.cfm?ReleaseID=584985 (visited on 05/20/2015).

[44] Endovascular Today. *Bolton Medical Gains CE Mark for Treovance Abdominal Stent Graft With Navitel Delivery System*. Bryn Mawr Communications II, LLC. Mar. 1, 2013. URL: http://evtoday.com/2013/02/supplement/ce-mark-approved-for-the-bolton-medical-treovance-abdominal-stent-graft-with-navitel-delivery-system (visited on 05/20/2015).

[45] Vascular News. *Incraft AAA Stent Graft System*. BIBA Medical. Oct. 15, 2014. URL: http://www.vascularnews.com/vn-featured-products/vascular-news---featured-products/incraft-aaa-stent-graft-system (visited on 05/23/2015).

[46] P. Mangell et al. "Are self-expanding stents superior to balloon-expanded in dilating aortas? An experimental study in pigs". In: *European Journal of Vascular and Endovascular Surgery* 12.3 (1996), pp. 287–294. ISSN: 1078-5884. DOI: http://dx.doi.org/10.1016/S1078-5884(96)80246-2.

URL: http://www.sciencedirect.com/science/article/pii/S1078588496802462.

[47] Geert Willem H. Schurink et al. "Stent attachment site-related endoleakage after stent graft treatment: An in vitro study of the effects of graft size, stent type, and atherosclerotic wall changes". In: *Journal of Vascular Surgery* 30.4 (1999), pp. 658–667. ISSN: 0741-5214. DOI: http://dx.doi.org/10.1016/S0741-5214(99)70105-9. URL: http://www.sciencedirect.com/science/article/pii/S0741521499701059.

[48] Stephan H. Duda et al. "Physical Properties of Endovascular Stents: An Experimental Comparison". In: *Journal of Vascular and Interventional Radiology* 11.5 (2000), pp. 645–654. ISSN: 1051-0443. DOI: 10.1016/S1051-0443(07)61620-0. URL: http://www.sciencedirect.com/science/article/pii/S1051044307616200.

[49] Robert Hopkins et al. "Effects of study design and trends for EVAR versus OSR". In: *Vascular Health and Risk Management* 4 (5 Oct. 2008), pp. 1011–1022. URL: http://www.ncbi.nlm.nih.gov/pmc/articles/PMC2605334/.

[50] Ruth L. Bush et al. "Open Versus Endovascular Abdominal Aortic Aneurysm Repair in VA Hospitals". In: *Journal of the American College of Surgeons* 202.4 (2006), pp. 577–587. ISSN: 1072-7515. DOI: 10.1016/j.jamcollsurg.2006.01.005. URL: http://www.sciencedirect.com/science/article/pii/S1072751506000433.

[51] D. Stoeckel, C. Bonsignore, and S. Duda. "A survey of stent designs." In: *Minimally Invasive Therapy and Allied Technologies* 11.4 (2002), pp. 137–147. ISSN: 13645706. URL: http://ezproxy.library.dal.ca/login?url=http://search.ebscohost.com/login.aspx?direct=true&db=aph&AN=11557635&site=ehost-live.

[52] Andres Schanzer and Louis Messina. "Two Decades of Endovascular Abdominal Aortic Aneurysm Repair: Enormous Progress With Serious Lessons Learned". In: *Journal of the American Heart Association* 1.3 (2012). DOI: 10.1161/JAHA.111.000075. eprint:

http://jaha.ahajournals.org/content/1/3/e000075.full.pdf+html. URL: http://jaha.ahajournals.org/content/1/3/e000075.short.

[53] Zhonghua Li and Clement Kleinstreuer. "Blood flow and structure interactions in a stented abdominal aortic aneurysm model". In: *Medical Engineering and Physics* 27.5 (2005), pp. 369–382. ISSN: 1350-4533. DOI: http://dx.doi.org/10.1016/j.medengphy.2004.12.003. URL: http://www.sciencedirect.com/science/article/pii/S1350453305000032.

[54] Geoffrey H. White, Weiyun Yu, and James May. "'Endoleak'-A Proposed New Terminology to Describe Incomplete Aneurysm Exclusion by an Endoluminal Graft". In: *Journal of Endovascular Surgery* 3.1 (1996). PMID: 8991758, pp. 124–125. DOI: 10.1583/1074-6218(1996)003<0124b:>2.0.CO;2. eprint: http://dx.doi.org/10.1583/1074-6218(1996)003<0124b:>2.0.CO;2. URL: http://dx.doi.org/10.1583/1074-6218(1996)003%3C0124b:%3E2.0.CO;2.

[55] Geoffrey H. White et al. "Endoleak as a Complication of Endoluminal Grafting of Abdominal Aortic Aneurysms: Classification, Incidence, Diagnosis,and Management". In: *Journal of Endovascular Surgery* 4.2 (1997). PMID: 9185003, pp. 152–168. DOI: 10.1583/1074-6218(1997)004<0152:EAACOE>2.0.CO;2. eprint: http://dx.doi.org/10.1583/1074-6218(1997)004<0152:EAACOE>2.0.CO;2. URL: http://dx.doi.org/10.1583/1074-6218(1997)004%3C0152:EAACOE%3E2.0.CO;2.

[56] Thorsten A. Bley et al. "Endovascular Abdominal Aortic Aneurysm Repair: Nonenhanced Volumetric CT for Follow-up". In: *Radiology* 253.1 (2009). PMID: 19703867, pp. 253–262. DOI: 10.1148/radiol.2531082093. eprint: http://dx.doi.org/10.1148/radiol.2531082093. URL: http://dx.doi.org/10.1148/radiol.2531082093.

[57] Andres Schanzer et al. "Predictors of Abdominal Aortic Aneurysm Sac Enlargement After Endovascular Repair". In: *Circulation* 123.24 (2011), pp. 2848–2855. DOI: 10.1161/CIRCULATIONAHA.110.014902. eprint:

http://circ.ahajournals.org/content/123/24/2848.full.pdf+html. URL: http://circ.ahajournals.org/content/123/24/2848.abstract.

[58] Donald T. Baril et al. "Endovascular Stent-Graft Repair of Failed Endovascular Abdominal Aortic Aneurysm Repair". In: *Annals of Vascular Surgery* 22 (1 Jan. 2008), pp. 30–36. URL: https://www.clinicalkey.com/#!/content/playContent/1-s2.0-S0890509607003561.

[59] Christopher K. Zarins et al. "AneuRx stent graft versus open surgical repair of abdominal aortic aneurysms: Multicenter prospective clinical trial". In: *Journal of Vascular Surgery* 29.2 (1999), pp. 292–308. ISSN: 0741-5214. DOI: http://dx.doi.org/10.1016/S0741-5214(99)70382-4. URL: http://www.sciencedirect.com/science/article/pii/S0741521499703824.

[60] J. Buth et al. "Endoleaks during follow-up after endovascular repair of abdominal aortic aneurysm: Are they all dangerous?" English. In: *Journal of Cardiovascular Surgery* 44.4 (Aug. 2003), pp. 559–66. URL: http://ezproxy.library.dal.ca/login?url=http://search.proquest.com/docview/224415526?accountid=10406.

[61] Wesley S. Moore, Robert B. Rutherford, and EVT Investigators. "Transfemoral endovascular repair of abdominal aortic aneurysm: Results of the North American {EVT} phase 1 trial". In: *Journal of Vascular Surgery* 23.4 (1996), pp. 543–553. ISSN: 0741-5214. DOI: http://dx.doi.org/10.1016/S0741-5214(96)80032-2. URL: http://www.sciencedirect.com/science/article/pii/S0741521496800322.

[62] Daniel M. Mandziak et al. "Outcome of endoleak following endoluminal abdominal aortic aneurysm repair". In: *ANZ Journal of Surgery* 74.12 (2004), pp. 1039–1042. ISSN: 1445-2197. DOI: 10.1111/j.1445-1433.2004.03263.x. URL: http://dx.doi.org/10.1111/j.1445-1433.2004.03263.x.

[63] W.Charles Sternbergh III et al. "Influence of endograft oversizing on device migration, endoleak, aneurysm shrinkage, and aortic neck dilation: results from the zenith multicenter trial". In: *Journal of Vascular Surgery* 39.1 (2004), pp. 20–26. ISSN: 0741-5214. DOI:

http://dx.doi.org/10.1016/j.jvs.2003.09.022. URL: http://www.sciencedirect.com/science/article/pii/S0741521403013855.

[64] Jeffrey P. Carpenter. "Midterm results of the multicenter trial of the Powerlink bifurcated system for endovascular aortic aneurysm repair". In: *Journal of Vascular Surgery* 40.5 (2004), pp. 849–859. ISSN: 0741-5214. DOI: http://dx.doi.org/10.1016/j.jvs.2004.08.051. URL: http://www.sciencedirect.com/science/article/pii/S0741521404011462.

[65] Jeffrey P Carpenter et al. "Multicenter pivotal trial results of the Lifepath System for endovascular aortic aneurysm repair". In: *Journal of Vascular Surgery* 39.1 (2004), pp. 34–42. ISSN: 0741-5214. DOI: http://dx.doi.org/10.1016/j.jvs.2003.10.036. URL: http://www.sciencedirect.com/science/article/pii/S0741521403015131.

[66] Elliot L. Chaikof et al. "Reporting standards for endovascular aortic aneurysm repair". In: *Journal of Vascular Surgery* 35.5 (2002), pp. 1048–1060. ISSN: 0741-5214. DOI: http://dx.doi.org/10.1067/mva.2002.123763. URL: http://www.sciencedirect.com/science/article/pii/S0741521402923864.

[67] Jonathan R. Boyle et al. "Pragmatic Minimum Reporting Standards for Endovascular Abdominal Aortic Aneurysm Repair". In: *Journal of Endovascular Therapy* 18.3 (2011), pp. 263–271. DOI: 10.1583/11-3473.1. eprint: http://jet.sagepub.com/content/18/3/263.full.pdf+html. URL: http://jet.sagepub.com/content/18/3/263.short.

[68] I.E. Steingruber et al. "Technical and clinical success of infrarenal endovascular abdominal aortic aneurysm repair: A 10-year single-center experience". In: *European Journal of Radiology* 59.3 (2006). ¡ce:title¿Uncommon Traumatic Injuries¡/ce:title¿, pp. 384–392. ISSN: 0720-048X. DOI: 10.1016/j.ejrad.2006.04.002. URL: http://www.sciencedirect.com/science/article/pii/S0720048X06001264.

[69] Naoki Toya et al. "Endotension following endovascular aneurysm repair". In: *Vascular Medicine* 13.4 (2008), pp. 305–311.

[70] David C. Brewster et al. “Initial experience with endovascular aneurysm repair: Comparison of early results with outcome of conventional open repair”. In: *Journal of Vascular Surgery* 27.6 (1998), pp. 992–1005. ISSN: 0741-5214. DOI: http://dx.doi.org/10.1016/S0741-5214(98)70002-3. URL: http://www.sciencedirect.com/science/article/pii/S0741521498700023.

[71] Jeffrey J. Siracuse et al. “Comparative safety of endovascular and open surgical repair of abdominal aortic aneurysms in low-risk male patients”. In: *Journal of Vascular Surgery* 60.5 (2014), pp. 1154–1158. ISSN: 0741-5214. DOI: http://dx.doi.org/10.1016/j.jvs.2014.05.018. URL: http://www.sciencedirect.com/science/article/pii/S0741521414009999.

[72] Paul D. Hayes et al. “Cost-Effectiveness Analysis of Endovascular versus Open Surgical Repair of Acute Abdominal Aortic Aneurysms Based on Worldwide Experience”. In: *Journal of Endovascular Therapy* 17.2 (2010), pp. 174–182. DOI: 10.1583/09-2941.1. eprint: http://jet.sagepub.com/content/17/2/174.full.pdf+html. URL: http://jet.sagepub.com/content/17/2/174.abstract.

[73] Krassi Ivancev et al. “Abdominal Aortic Aneurysms: Experience With the Ivancev-Malmö Endovascular System for Aortomonoiliac Stent-Grafts”. In: *Journal of Endovascular Surgery* 4.3 (1997). PMID: 9291049, pp. 242–251. DOI: 10.1583/1074-6218(1997)004<0242:AAAEWT>2.0.CO;2. eprint: http://dx.doi.org/10.1583/1074-6218(1997)004<0242:AAAEWT>2.0.CO;2. URL: http://dx.doi.org/10.1583/1074-6218(1997)004%3C0242:AAAEWT%3E2.0.CO;2.

[74] Umar Sadat et al. “Endovascular vs open repair of acute abdominal aortic aneurysms-A systematic review and meta-analysis”. In: *Journal of Vascular Surgery* 48.1 (2008), pp. 227–236. ISSN: 0741-5214. DOI: http://dx.doi.org/10.1016/j.jvs.2007.11.028. URL: http://www.sciencedirect.com/science/article/pii/S0741521407017818.

[75] P. W. Stather et al. “Systematic review and meta-analysis of the early and late outcomes of open and endovascular repair of abdominal aortic

aneurysm." In: *British Journal of Surgery* 100.7 (2013), pp. 863–872. ISSN: 00071323. URL: http://ezproxy.library.dal.ca/login?url=http://search.ebscohost.com/login.aspx?direct=true&db=aph&AN=87405788&site=ehost-live.

[76] Sherif Sultan and Niamh Hynes. "Clinical Efficacy and Cost per Quality-Adjusted Life Years of Pararenal Endovascular Aortic Aneurysm Repair Compared With Open Surgical Repair". In: *Journal of Endovascular Therapy* 18.2 (2011), pp. 181–196. DOI: 10.1583/10-3072.1. eprint: http://jet.sagepub.com/content/18/2/181.full.pdf+html. URL: http://jet.sagepub.com/content/18/2/181.abstract.

[77] Konstantinos G. Moulakakis et al. "Conversion to Open Repair after Endografting for Abdominal Aortic Aneurysm: A Review of Causes, Incidence, Results, and Surgical Techniques of Reconstruction". In: *Journal of Endovascular Therapy* 17.6 (2010), pp. 694–702. DOI: 10.1583/1545-1550-17.6.694. eprint: http://jet.sagepub.com/content/17/6/694.full.pdf+html. URL: http://jet.sagepub.com/content/17/6/694.abstract.

[78] David C Brewster et al. "Long-term Outcomes After Endovascular Abdominal Aortic Aneurysm Repair: The First Decade". In: *Annals of Surgery* 244 (3 Sept. 2006), pp. 426–438. DOI: 10.1097/01.sla.0000234893.88045.dc. URL: http://www.ncbi.nlm.nih.gov/pmc/articles/PMC1856532/.

[79] Philip Joseph. "Long-term outcome of open or endovascular repair of abdominal aortic aneurysm: The DREAM Study Group. The New England Journal of Medicine 2010; 362: 1881-1889". In: *Vascular Medicine* 15.6 (2010), pp. 515–516. DOI: 10.1177/1358863X10391839. eprint: http://vmj.sagepub.com/content/15/6/515.full.pdf+html. URL: http://vmj.sagepub.com/content/15/6/515.abstract.

[80] Juan Carlos Parodi et al. "Intra-aneurysmal pressure after incomplete endovascular exclusion". In: *Journal of Vascular Surgery* 34.5 (2001), pp. 909–914. ISSN: 0741-5214. DOI:

http://dx.doi.org/10.1067/mva.2001.119038. URL: http://www.sciencedirect.com/science/article/pii/S0741521401891461.

[81] Eleftherios S. Xenos et al. "Distribution of Sac Pressure in an Experimental Aneurysm Model after Endovascular Repair: The Effect of Endoleak Types I and II". In: *Journal of Endovascular Therapy* 10.3 (2003), pp. 516–523. DOI: 10.1177/152660280301000317. eprint: http://jet.sagepub.com/content/10/3/516.full.pdf+html. URL: http://jet.sagepub.com/content/10/3/516.abstract.

[82] J.W. Hinnen et al. "Aneurysm Sac Pressure after EVAR: The Role of Endoleak". In: *European Journal of Vascular and Endovascular Surgery* 34.4 (2007), pp. 432–441. ISSN: 1078-5884. DOI: http://dx.doi.org/10.1016/j.ejvs.2007.05.022. URL: http://www.sciencedirect.com/science/article/pii/S1078588407003991.

[83] N Chakfé et al. "Influence of the Textile Structure on the Degradation of Explanted Aortic Endoprostheses". In: *European Journal of Vascular and Endovascular Surgery* 27.1 (2004), pp. 33–41. ISSN: 1078-5884. DOI: http://dx.doi.org/10.1016/S1078-5884(03)00341-1. URL: http://www.sciencedirect.com/science/article/pii/S1078588403003411.

[84] Christopher K Zarins et al. "Explant analysis of AneuRx stent grafts: relationship between structural findings and clinical outcome". In: *Journal of Vascular Surgery* 40.1 (2004), pp. 1–11. ISSN: 0741-5214. DOI: http://dx.doi.org/10.1016/j.jvs.2004.03.008. URL: http://www.sciencedirect.com/science/article/pii/S0741521404003726.

[85] F.J.V. Schl osser et al. "Aneurysm Rupture after EVAR: Can the Ultimate Failure be Predicted?" In: *European Journal of Vascular and Endovascular Surgery* 37.1 (2009), pp. 15–22. ISSN: 1078-5884. DOI: http://dx.doi.org/10.1016/j.ejvs.2008.10.011. URL: http://www.sciencedirect.com/science/article/pii/S1078588408005480.

[86] Peter L. Harris et al. "Incidence and risk factors of late rupture, conversion, and death after endovascular repair of infrarenal aortic aneurysms: The {EUROSTAR} experience". In: *Journal of Vascular Surgery* 32.4 (2000),

pp. 739–749. ISSN: 0741-5214. DOI: http://dx.doi.org/10.1067/mva.2000.109990. URL: http://www.sciencedirect.com/science/article/pii/S0741521400093605.

[87] Timothy A.M. Chuter. "Stent-graft design: the good, the bad and the ugly". In: *Cardiovascular Surgery* 10.1 (2002), pp. 7–13. ISSN: 0967-2109. DOI: http://dx.doi.org/10.1016/S0967-2109(01)00120-X. URL: http://www.sciencedirect.com/science/article/pii/S096721090100120X.

[88] T J Corbett, A Callanan, and T M McGloughlin. "In vitro measurement of the axial migration force on the proximal end of a bifurcated abdominal aortic aneurysm stent-graft model". In: *Proceedings of the Institution of Mechanical Engineers, Part H: Journal of Engineering in Medicine* 225.4 (2011), pp. 401–409. DOI: 10.1177/09544119JEIM748. eprint: http://pih.sagepub.com/content/225/4/401.full.pdf+html. URL: http://pih.sagepub.com/content/225/4/401.abstract.

[89] Timothy J. Corbett et al. "A Review of the in Vivo and in Vitro Biomechanical Behavior and Performance of Postoperative Abdominal Aortic Aneurysms and Implanted Stent-Grafts". In: *Journal of Endovascular Therapy* 15.4 (2008), pp. 468–484. DOI: 10.1583/08-2370.1. eprint: http://jet.sagepub.com/content/15/4/468.full.pdf+html. URL: http://jet.sagepub.com/content/15/4/468.abstract.

[90] E. Civilini et al. "Delayed Upstream Migration of an Iliac Stent". In: *European Journal of Vascular and Endovascular Surgery* 34.2 (2007), pp. 214–216. ISSN: 1078-5884. DOI: http://dx.doi.org/10.1016/j.ejvs.2007.04.004. URL: http://www.sciencedirect.com/science/article/pii/S1078588407002699.

[91] Y. C. Chan et al. "Large infra-renal abdominal aortic aneurysms: endovascular vs. open repair - single centre experience". In: *International Journal of Clinical Practice* 61.3 (2007), pp. 373–378. ISSN: 1742-1241. DOI: 10.1111/j.1742-1241.2006.01032.x. URL: http://dx.doi.org/10.1111/j.1742-1241.2006.01032.x.

[92] Joost A. van Herwaarden et al. “Long-Term Single-Center Results with AneuRx Endografts for Endovascular Abdominal Aortic Aneurysm Repair”. In: *Journal of Endovascular Therapy* 14.3 (2007), pp. 307–317. DOI: 10.1583/06-1993.1. eprint: http://jet.sagepub.com/content/14/3/307.full.pdf+html. URL: http://jet.sagepub.com/content/14/3/307.abstract.

[93] Timothy Resch et al. “Distal Migration of Stent-Grafts after Endovascular Repair of Abdominal Aortic Aneurysms”. In: *Journal of Vascular and Interventional Radiology* 10.3 (1999), pp. 257–264. ISSN: 1051-0443. DOI: http://dx.doi.org/10.1016/S1051-0443(99)70027-8. URL: http://www.sciencedirect.com/science/article/pii/S1051044399700278.

[94] Irwin V. Mohan et al. “Factors and Forces Influencing Stent-Graft Migration after Endovascular Aortic Aneurysm Repair”. In: *Journal of Endovascular Therapy* 9.6 (2002), pp. 748–755. DOI: 10.1177/152660280200900606. eprint: http://jet.sagepub.com/content/9/6/748.full.pdf+html. URL: http://jet.sagepub.com/content/9/6/748.abstract.

[95] Roy K. Greenberg et al. “An update of the Zenith endovascular graft for abdominal aortic aneurysms: Initial implantation and mid-term follow-up data”. In: *Journal of Vascular Surgery* 33.2, Part B (2001), pp. 157–164. ISSN: 0741-5214. DOI: http://dx.doi.org/10.1067/mva.2001.111683. URL: http://www.sciencedirect.com/science/article/pii/S0741521401612424.

[96] III Conners Michael S. et al. “Endograft migration one to four years after endovascular abdominal aortic aneurysm repair with the AneuRx device: A cautionary note”. In: *Journal of Vascular Surgery* 36 (3 2002), pp. 476–484. DOI: 10.1067/mva.2002.126561. URL: http://dx.doi.org/10.1067/mva.2002.126561 (visited on 05/15/2015).

[97] James T. Lee MD et al. “Stent-Graft Migration Following Endovascular Repair of Aneurysms With Large Proximal Necks: Anatomical Risk Factors and Long-term Sequelae”. In: *Journal of Endovascular Therapy* 9 (5 2002), pp. 652–64. DOI: 10.1177/152660280200900517.

[98] Piergiorgio Cao et al. "Device migration after endoluminal abdominal aortic aneurysm repair: Analysis of 113 cases with a minimum follow-up period of 2 years". In: *Journal of Vascular Surgery* 35.2 (2002), pp. 229–235. ISSN: 0741-5214. DOI: http://dx.doi.org/10.1067/mva.2002.120045. URL: http://www.sciencedirect.com/science/article/pii/S0741521402073342.

[99] Zhonghua Li. "Computational Analyses and Simulations of Fluid-structure Interactions Applied to Stented Abdominal Aortic Aneurysms". PhD. North Carolina State University, June 2005. URL: http://www.lib.ncsu.edu/resolver/1840.16/4965.

[100] Christopher K Zarins et al. "Stent graft migration after endovascular aneurysm repair: importance of proximal fixation". In: *Journal of Vascular Surgery* 38.6 (2003), pp. 1264–1272. ISSN: 0741-5214. DOI: http://dx.doi.org/10.1016/S0741-5214(03)00946-7. URL: http://www.sciencedirect.com/science/article/pii/S0741521403009467.

[101] Martin Malina et al. "Endovascular AAA Exclusion: Will Stents With Hooks and Barbs Prevent Stent-Graft Migration?" In: *Journal of Endovascular Surgery* 5.4 (1998), pp. 310–317. DOI: 10.1583/1074-6218(1998)005<0310:EAEWSW>2.0.CO;2. URL: http://dx.doi.org/10.1583/1074-6218(1998)005%3C0310:EAEWSW%3E2.0.CO;2.

[102] I.V. Mohan, R.J.F. Laheij, and P.L. Harris. "Risk Factors for Endoleak and the Evidence for Stent-graft Oversizing in Patients Undergoing Endovascular Aneurysm Repair". In: *European Journal of Vascular and Endovascular Surgery* 21.4 (2001), pp. 344–349. ISSN: 1078-5884. DOI: http://dx.doi.org/10.1053/ejvs.2000.1341. URL: http://www.sciencedirect.com/science/article/pii/S1078588400913418.

[103] Anne Amblard et al. "Analysis of type I endoleaks in a stented abdominal aortic aneurysm". In: *Medical Engineering & Physics* 31.1 (2009), pp. 27–33. ISSN: 1350-4533. DOI:

http://dx.doi.org/10.1016/j.medengphy.2008.03.005. URL: http://www.sciencedirect.com/science/article/pii/S1350453308000453.

[104] David Roy et al. "A Literature Review of the Numerical Analysis of Abdominal Aortic Aneurysms Treated with Endovascular Stent Grafts". In: *Computational and Mathematical Methods in Medicine* 2012 (Sept. 2012), pp. 1–16. ISSN: 1748-670X. DOI: 10.1155/2012/820389. URL: http://www.ncbi.nlm.nih.gov/pmc/articles/PMC3445816/.

[105] J. van Prehn et al. "Oversizing of Aortic Stent Grafts for Abdominal Aneurysm Repair: A Systematic Review of the Benefits and Risks". In: *European Journal of Vascular and Endovascular Surgery* 38.1 (2009), pp. 42–53. ISSN: 1078-5884. DOI: http://dx.doi.org/10.1016/j.ejvs.2009.03.025. URL: http://www.sciencedirect.com/science/article/pii/S1078588409001762.

[106] C Alberto Figueroa et al. "A Computational Framework for Fluid-Solid-Growth Modeling in Cardiovascular Simulations". In: *Computer methods in applied mechanics and engineering* 198 (45-46 Sept. 2009), pp. 3583–3602. ISSN: 0045-7825. URL: http://www.ncbi.nlm.nih.gov/pmc/articles/PMC2770883/.

[107] Sergio M. Sampaio et al. "Aortic Neck Dilation after Endovascular Abdominal Aortic Aneurysm Repair: Should Oversizing Be Blamed?" In: *Annals of Vascular Surgery* 20.3 (2006), pp. 338–345. ISSN: 0890-5096. DOI: http://dx.doi.org/10.1007/s10016-006-9067-2. URL: http://www.sciencedirect.com/science/article/pii/S0890509606613642.

[108] Timothy J. Corbett et al. "An Improved Methodology for Investigating the Parameters Influencing Migration Resistance of Abdominal Aortic Stent-Grafts". In: *Journal of Endovascular Therapy* 17.1 (2010), pp. 95–107. DOI: 10.1583/09-2920.1. eprint: http://jet.sagepub.com/content/17/1/95.full.pdf+html. URL: http://jet.sagepub.com/content/17/1/95.abstract.

[109] Kurt Liffman et al. "Analytical Modeling and Numerical Simulation of Forces in an Endoluminal Graft". In: *Journal of Endovascular Therapy* 8.4

(2001), pp. 358–371. DOI: 10.1177/152660280100800405. eprint: http://jet.sagepub.com/content/8/4/358.full.pdf+html. URL: http://jet.sagepub.com/content/8/4/358.abstract.

[110] L. Morris et al. "A mathematical model to predict the in vivo pulsatile drag forces acting on bifurcated stent grafts used in endovascular treatment of abdominal aortic aneurysms (AAA)". In: *Journal of Biomechanics* 37.7 (2004), pp. 1087–1095. ISSN: 0021-9290. DOI: http://dx.doi.org/10.1016/j.jbiomech.2003.11.014. URL: http://www.sciencedirect.com/science/article/pii/S0021929003004263.

[111] D.S. Molony et al. "A Computational Study of the Magnitude and Direction of Migration Forces in Patient-specific Abdominal Aortic Aneurysm Stent-Grafts". In: *European Journal of Vascular and Endovascular Surgery* 40.3 (2010), pp. 332–339. ISSN: 1078-5884. DOI: http://dx.doi.org/10.1016/j.ejvs.2010.06.001. URL: http://www.sciencedirect.com/science/article/pii/S1078588410003461.

[112] T Resch et al. "The Impact of Stent Design on Proximal Stent-graft Fixation in the Abdominal Aorta: an Experimental Study". In: *European Journal of Vascular and Endovascular Surgery* 20.2 (2000), pp. 190–195. ISSN: 1078-5884. DOI: http://dx.doi.org/10.1053/ejvs.1999.0991. URL: http://www.sciencedirect.com/science/article/pii/S1078588499909917.

[113] S.M Volodos et al. "Factors Affecting the Displacement Force Exerted on a Stent Graft after AAA Repair-An In vitro Study". In: *European Journal of Vascular and Endovascular Surgery* 26.6 (2003), pp. 596–601. ISSN: 1078-5884. DOI: http://dx.doi.org/10.1016/j.ejvs.2003.08.002. URL: http://www.sciencedirect.com/science/article/pii/S1078588403004374.

[114] W.Charles Sternbergh III et al. "Aortic neck angulation predicts adverse outcome with endovascular abdominal aortic aneurysm repair". In: *Journal of Vascular Surgery* 35.3 (2002), pp. 482–486. ISSN: 0741-5214. DOI: http://dx.doi.org/10.1067/mva.2002.119506. URL: http://www.sciencedirect.com/science/article/pii/S0741521402166055.

[115] Vad S et al. “Determination of coefficient of friction for self-expanding stent-grafts”. In: *Journal of biomechanical engineering* 132.12 (2010), p. 121007. URL: http://europepmc.org/abstract/MED/21142321.

[116] Wei Wu et al. “Delivery and release of nitinol stent in carotid artery and their interactions: A finite element analysis”. In: *Journal of Biomechanics* 40.13 (2007), pp. 3034–3040. ISSN: 0021-9290. DOI: http://dx.doi.org/10.1016/j.jbiomech.2007.02.024. URL: http://www.sciencedirect.com/science/article/pii/S0021929007001145.

[117] Francesco Migliavacca et al. “Stainless and shape memory alloy coronary stents: a computational study on the interaction with the vascular wall”. English. In: *Biomechanics and Modeling in Mechanobiology* 2.4 (2004), pp. 205–217. ISSN: 1617-7959. DOI: 10.1007/s10237-004-0039-6. URL: http://dx.doi.org/10.1007/s10237-004-0039-6.

[118] Michele Conti. “Finite element analysis of self-expanding braided wirestent”. Belgium: Ghent University, 2007. URL: http://www-2.unipv.it/compmech/dissertations/conti.pdf.

[119] Anamika Prasad et al. “A computational framework for investigating the positional stability of aortic endografts”. English. In: *Biomechanics and Modeling in Mechanobiology* 12.5 (2013), pp. 869–887. ISSN: 1617-7959. DOI: 10.1007/s10237-012-0450-3. URL: http://dx.doi.org/10.1007/s10237-012-0450-3.

[120] Barry J. Doyle, John Killion, and Anthony Callanan. “Use of the photoelastic method and finite element analysis in the assessment of wall strain in abdominal aortic aneurysm models”. In: *Journal of Biomechanics* 45.10 (2012), pp. 1759–1768. ISSN: 0021-9290. DOI: http://dx.doi.org/10.1016/j.jbiomech.2012.05.004. URL: http://www.sciencedirect.com/science/article/pii/S0021929012002667.

[121] L. Speelman et al. “Initial stress and nonlinear material behavior in patient-specific {AAA} wall stress analysis”. In: *Journal of Biomechanics* 42.11 (2009), pp. 1713–1719. ISSN: 0021-9290. DOI:

http://dx.doi.org/10.1016/j.jbiomech.2009.04.020. URL: http://www.sciencedirect.com/science/article/pii/S0021929009002206.

[122] MARK FILLINGER. "The Long-Term Relationship of Wall Stress to the Natural History of Abdominal Aortic Aneurysms (Finite Element Analysis and Other Methods)". In: *Annals of the New York Academy of Sciences* 1085.1 (2006), pp. 22–28. ISSN: 1749-6632. DOI: 10.1196/annals.1383.037. URL: http://dx.doi.org/10.1196/annals.1383.037.

[123] A.K Venkatasubramaniam et al. "A Comparative Study of Aortic Wall Stress Using Finite Element Analysis for Ruptured and Non-ruptured Abdominal Aortic Aneurysms". In: *European Journal of Vascular and Endovascular Surgery* 28.2 (2004), pp. 168–176. ISSN: 1078-5884. DOI: http://dx.doi.org/10.1016/j.ejvs.2004.03.029. URL: http://www.sciencedirect.com/science/article/pii/S1078588404001789.

[124] M.L. Raghavan et al. "Wall stress distribution on three-dimensionally reconstructed models of human abdominal aortic aneurysm". In: *Journal of Vascular Surgery* 31.4 (2000), pp. 760–769. ISSN: 0741-5214. DOI: http://dx.doi.org/10.1067/mva.2000.103971. URL: http://www.sciencedirect.com/science/article/pii/S074152140064421X.

[125] Jonathan P Vande Geest et al. "The Effects of Anisotropy on the Stress Analyses of Patient-Specific Abdominal Aortic Aneurysms". In: *Annals of biomedical engineering* 36 (6 June 2008), pp. 921–932. ISSN: 0090-6964. DOI: 10.1007/s10439-008-9490-3. URL: http://www.ncbi.nlm.nih.gov/pmc/articles/PMC2674610/.

[126] Barry J. Doyle et al. "Identification of rupture locations in patient-specific abdominal aortic aneurysms using experimental and computational techniques". In: *Journal of Biomechanics* 43.7 (2010), pp. 1408–1416. ISSN: 0021-9290. DOI: http://dx.doi.org/10.1016/j.jbiomech.2009.09.057. URL: http://www.sciencedirect.com/science/article/pii/S0021929010000187.

[127] Ethan O. Kung et al. "In Vitro Validation of Finite-Element Model of AAA Hemodynamics Incorporating Realistic Outlet Boundary Conditions". In:

Journal of Biomechanical Engineering 133 (4 Feb. 2011), p. 041003. ISSN: 0148-0731. URL: http://dx.doi.org/10.1115/1.4003526.

[128] David S Molony et al. "Fluid-structure interaction of a patient-specific abdominal aortic aneurysm treated with an endovascular stent-graft". In: *Biomed Eng Online* 8 (2009), p. 24. URL: http://www.ncbi.nlm.nih.gov/pmc/articles/PMC2764714/.

[129] David S. Molony et al. "Geometrical Enhancements for Abdominal Aortic Stent-Grafts". In: *Journal of Endovascular Therapy* 15.5 (2008), pp. 518–529. DOI: 10.1583/08-2388.1. eprint: http://jet.sagepub.com/content/15/5/518.full.pdf+html. URL: http://jet.sagepub.com/content/15/5/518.abstract.

[130] Nicolas Demanget et al. "Computational comparison of the bending behavior of aortic stent-grafts". In: *Journal of the Mechanical Behavior of Biomedical Materials* 5.1 (2012), pp. 272–282. ISSN: 1751-6161. DOI: 10.1016/j.jmbbm.2011.09.006. URL: http://www.sciencedirect.com/science/article/pii/S1751616111002402.

[131] Nicolas Demanget et al. "Severe Bending of Two Aortic Stent-Grafts: An Experimental and Numerical Mechanical Analysis". English. In: *Annals of Biomedical Engineering* 40.12 (2012), pp. 2674–2686. ISSN: 0090-6964. DOI: 10.1007/s10439-012-0618-0. URL: http://dx.doi.org/10.1007/s10439-012-0618-0.

[132] Nicolas Demanget et al. "Finite element analysis of the mechanical performances of 8 marketed aortic stent-grafts". In: *Journal of Endovascular Therapy* 20.4 (2013), pp. 523–535.

[133] Shijia Zhao, Linxia Gu, and Stacey R. Froemming. "Finite Element Analysis of the Implantation of a Self-Expanding Stent: Impact of Lesion Calcification". In: *Journal of Medical Devices* 6 (2 Apr. 2012), p. 021001. ISSN: 1932-6181. URL: http://dx.doi.org/10.1115/1.4006357.

[134] Dorothy B. Abel et al. "Preclinical testing for aortic endovascular grafts: Results of a Food and Drug Administration workshop". In: *Journal of Vascular Surgery* 35.5 (2002), pp. 1022–1028. ISSN: 0741-5214. DOI:

http://dx.doi.org/10.1067/mva.2002.123762. URL: http://www.sciencedirect.com/science/article/pii/S0741521402141292.

[135] Christopher K. Zarins and Charles A. Taylor. "Endovascular Device Design in the Future: Transformation from Trial and Error to Computational Design". In: *Journal of Endovascular Therapy* 16.1 suppl (2009), pp. 12–21. DOI: 10.1583/08-2640.1. eprint: http://jet.sagepub.com/content/16/1_suppl/12.full.pdf+html. URL: http://jet.sagepub.com/content/16/1_suppl/12.abstract.

[136] R. Wang and K. Ravi-Chandar. "Mechanical Response of a Metallic Aortic Stent—Part II: A Beam-on-Elastic Foundation Model". In: *Journal of Applied Mechanics* 71.5 (2004), pp. 706–712. DOI: 10.1115/1.1782912. URL: http://link.aip.org/link/?AMJ/71/706/1.

[137] Patrick B. Snowhill et al. "Characterization of Radial Forces in Z Stents". In: *Investigative Radiology* 36 (9 Sept. 2001), pp. 521–530. ISSN: 0020-9996. URL: http://journals.lww.com/investigativeradiology/pages/articleviewer.aspx?year=2001&issue=09000&article=00004&type=abstract.

[138] C. Kleinstreuer et al. "Computational mechanics of Nitinol stent grafts". In: *Journal of Biomechanics* 41.11 (2008), pp. 2370–2378. ISSN: 0021-9290. DOI: 10.1016/j.jbiomech.2008.05.032. URL: http://www.sciencedirect.com/science/article/pii/S0021929008002777.

[139] B. FALLONE, S. WALLACE, and C. GIANTURCO. "Elastic Characteristics of the Self-expanding Metallic Stents". In: *Investigative Radiology* 23 (5 1988), pp. 370–376. ISSN: 0020-9996. URL: http://ovidsp.ovid.com/ovidweb.cgi?T=JS&PAGE=reference&D=ovfta&NEWS=N&AN=00004424-198805000-00008.

[140] Dorothy B. Abel et al. "Evolution and Future of Preclinical Testing for Endovascular Grafts". In: *Journal of Endovascular Therapy* 13.5 (2006), pp. 649–659. DOI: 10.1583/06-1872.1. eprint: http://jet.sagepub.com/content/13/5/649.full.pdf+html. URL: http://jet.sagepub.com/content/13/5/649.abstract.

[141] F. Nematzadeh and S.K. Sadrnezhaad. "Effects of material properties on mechanical performance of Nitinol stent designed for femoral artery: Finite element analysis". In: *Scientia Iranica* 19.6 (2012), pp. 1564–1571. ISSN: 1026-3098. DOI: http://dx.doi.org/10.1016/j.scient.2012.10.024. URL: http://www.sciencedirect.com/science/article/pii/S1026309812002350.

[142] F. Nematzadeh and S.K. Sadrnezhaad. "Effects of Crimping on Mechanical Performance of Nitinol Stent Designed for Femoral Artery: Finite Element Analysis". English. In: *Journal of Materials Engineering and Performance* 22.11 (2013), pp. 3228–3236. ISSN: 1059-9495. DOI: 10.1007/s11665-013-0635-7. URL: http://dx.doi.org/10.1007/s11665-013-0635-7.

[143] S. De Bock et al. "Filling the void: A coalescent numerical and experimental technique to determine aortic stent graft mechanics". In: *Journal of Biomechanics* 46.14 (2013), pp. 2477–2482. ISSN: 0021-9290. DOI: http://dx.doi.org/10.1016/j.jbiomech.2013.07.010. URL: http://www.sciencedirect.com/science/article/pii/S0021929013003357.

[144] U.S. Food and Drug Administration. *Guidance for Industry and FDA Staff - Non-Clinical Engineering Tests and Recommended Labeling for Intravascular Stents and Associated Delivery Systems*. U.S. Food and Drug Administration. Apr. 18, 2010. URL: http://www.fda.gov/RegulatoryInformation/Guidances/ucm071863.htm (visited on 05/25/2015).

[145] Fritz Flueckiger et al. "Strength, Elasticity, and Plasticity of Expandable Metal Stents: In Vitro Studies with Three Types of Stress". In: *Journal of Vascular and Interventional Radiology* 5.5 (1994), pp. 745–750. ISSN: 1051-0443. DOI: 10.1016/S1051-0443(94)71594-3. URL: http://www.sciencedirect.com/science/article/pii/S1051044394715943.

[146] Abul Hasan Muhammad Bashar et al. "Mechanical Properties of Various Z-Stent Designs: An Endovascular Stent-Grafting Perspective". In: *Artificial Organs* 27.8 (2003), pp. 714–721. ISSN: 1525-1594. DOI:

10.1046/j.1525-1594.2003.06995.x. URL: http://dx.doi.org/10.1046/j.1525-1594.2003.06995.x.

[147] S Sawada et al. "Study of the physical properties of expandable metallic stents". In: *Radiation medicine* 9.6 (1990), pp. 213–216.

[148] C. MAULI AGRAWAL and HOWARD G. CLARK. "Deformation Characteristics of a Bioabsorbable Intravascular Stent". In: *Investigative Radiology* 27 (12 1992), pp. 1020–1024. ISSN: 0020-9996. URL: http://journals.lww.com/investigativeradiology/Fulltext/1992/12000/Deformation_Characteristics_of_a_Bioabsorbable.7.aspx.

[149] Steven V. Lossef et al. "Comparison of Mechanical Deformation Properties of Metallic Stents with Use of Stress-Strain Analysis". In: *Journal of Vascular and Interventional Radiology* 5.2 (1994), pp. 341–349. ISSN: 1051-0443. DOI: http://dx.doi.org/10.1016/S1051-0443(94)71499-8. URL: http://www.sciencedirect.com/science/article/pii/S1051044394714998.

[150] JohnF. Dyet et al. "Mechanical properties of metallic stents: How do these properties influence the choice of stent for specific lesions?" English. In: *CardioVascular and Interventional Radiology* 23.1 (2000), pp. 47–54. ISSN: 0174-1551. DOI: 10.1007/s002709910007. URL: http://dx.doi.org/10.1007/s002709910007.

[151] Joel L. Berry et al. "A Method to Evaluate the Elastic Behavior of Vascular Stents". In: *Journal of Vascular and Interventional Radiology* 7.3 (1996), pp. 381–385. ISSN: 1051-0443. DOI: http://dx.doi.org/10.1016/S1051-0443(96)72875-0. URL: http://www.sciencedirect.com/science/article/pii/S1051044396728750.

[152] Stephan C. Schrader and Rafael Beyar. "Evaluation of the compressive mechanical properties of endoluminal metal stents". In: *Catheterization and Cardiovascular Diagnosis* 44.2 (1998), pp. 179–187. ISSN: 1097-0304. DOI: 10.1002/(SICI)1097-0304(199806)44:2<179::AID-CCD11>3.0.CO;2-I. URL: http://dx.doi.org/10.1002/(SICI)1097-0304(199806)44:2%3C179::AID-CCD11%3E3.0.CO;2-I.

[153] Renjun Wang and Krishnaswamy Ravi-Chandar. "Mechanical response of a metallic aortic stent". In: *Pressure-diameter relashionship. Submitted to Journal of Applied Mechanics* (2001).

[154] Yasuhiro Shobayashi et al. "Mechanical design of an intracranial stent for treating cerebral aneurysms". In: *Medical Engineering and Physics* 32.9 (2010), pp. 1015–1024. ISSN: 1350-4533. DOI: 10.1016/j.medengphy.2010.07.002. URL: http://www.sciencedirect.com/science/article/pii/S135045331000144X.

[155] Michiel T. Voûte et al. "Radial Force Measurements in Carotid Stents: Influence of Stent Design and Length of the Lesion". In: *Journal of Vascular and Interventional Radiology* 22 (5 May 2011), pp. 661–666. URL: https://www.clinicalkey.com/#!/content/playContent/1-s2.0-S105104431100580X.

[156] Dierk Vorwerk et al. "Neointima formation following arterial placement of self-expanding stents of different radial force: Experimental results". English. In: *CardioVascular and Interventional Radiology* 17.1 (1994), pp. 27–32. ISSN: 0174-1551. DOI: 10.1007/BF01102068. URL: http://dx.doi.org/10.1007/BF01102068.

[157] Machine Solutions Inc. *Radial Expansion Force Testing Equipment*. 2012. URL: http://www.machinesolutions.com/Medical-Device-Performance-Testing/Testing-Equipment/Radial-Expansion-Force-Testing-Equipment-RX550-650.htm (visited on 05/29/2015).

[158] *Motorized Linear Slide, 150 mm travel, RS-232 plus manual control. Detailed Specs*. Zaber Technologies Inc. 2015. URL: http://zaber.com/products/product_detail.php?detail=T-LSR150A#tabs (visited on 03/12/2015).

[159] *Miniature Low Profile Tension Link Load Cells, Metric Ranges, 19 to 25 mm Height. LCM703 Specifications*. Omega Environmental. 2015. URL: http://www.omega.ca/shop/pptsc.asp?ref=LCM703 (visited on 03/12/2015).

[160] *Logitech HD Pro Webcam C920. Specifications*. Logitech. 2015. URL: http://www.logitech.com/en-us/product/hd-pro-webcam-c920?crid=34 (visited on 03/12/2015).

[161] *Software/Binary Labview Driver*. Zaber. 2015. URL: http://www.zaber.com/wiki/Software/Binary_Labview_Driver (visited on 03/05/2015).

[162] *python(x,y). Scientific-oriented Python Distribution based on Qt and Spyder*. Version 2.7.9.0. 2015. URL: http://www.logitech.com/en-us/product/hd-pro-webcam-c920?crid=34 (visited on 03/18/2015).

[163] *Motorized Linear Slide. 150 mm travel, RS-232 plus manual control*. Zaber. URL: zaber.com/products/product_detail.php?detail=T-LSR150A (visited on 08/08/2014).

[164] *RS-232 Communications Protocol*. Zaber. URL: http://www.zaber.com/wiki/T-Series/RS-232_Communications_Protocol/motion_products (visited on 03/05/2015).

[165] *LCM703 Series Load Cell*. Omega. 2014. URL: http://www.omega.ca/shop/pptsc.asp?ref=LCM703 (visited on 09/15/2014).

[166] *Mylar Physical-Thermal Properties*. DuPont Teijin Films. URL: http://usa.dupontteijinfilms.com/informationcenter/downloads/Physical_And_Thermal_Properties.pdf (visited on 01/20/2014).

[167] DuPont. *DuPont Teijin Films Mylar D804 Polyester Film, 92 Gauge*. MatWeb. URL: http://www.matweb.com/search/datasheet.aspx?matguid=f1c55ecb497a4c8aaf08634aae8a0536&ckck=1 (visited on 08/17/2015).

[168] Walt Kester. *ADC Architectures III: Sigma-Delta ADC Basics*. Maxim Integrated. URL: http://www.analog.com/static/imported-files/tutorials/MT-022.pdf (visited on 01/25/2014).

[169] *NI9237 Operating Instructions and Specifications*. National Instruments. URL: http://www.ni.com/pdf/manuals/374186e.pdf (visited on 01/20/2014).

[170] *SolidWorks*. Dassault Systems. URL: www.solidworks.com (visited on 09/16/2014).

[171] *HyperMesh*. Altair. URL: www.altairhyperworks.com/Product,7,HyperMesh.aspx (visited on 11/19/2014).

[172] *LS-DYNA*. Livermore Software Technology Corporation. URL: www.lstc.com/products/ls-dyna (visited on 11/19/2014).

[173] *LS-PrePost*. Livermore Software Technology Corporation. URL: www.lstc.com/products/ls-prepost (visited on 11/19/2014).

[174] *2-D Meshing*. Altair. URL: http://training.altairuniversity.com/modeling/meshing-2/meshing/ (visited on 02/08/2015).

[175] Paul Kinney. ""CleanUp: Improving Quadrilateral Finite Element Meshes"". In: (). URL: www.cs.berkely.edu/~jrs/meshpapers/Kinney.pdf.

[176] *316L Stainless Steel*. MatWeb, LLC. URL: http://matweb.com/search/DataSheet.aspx?MatGUID=c02b8c0ae42e459a872553e0ebfab648&ckck=1 (visited on 04/07/2015).

[177] *Contact modeling in LS-DYNA*. Livermore Software Technology Corporation. URL: http://www.dynasupport.com/tutorial/ls-dyna-users-guide/contact-modeling-in-ls-dyna (visited on 02/13/2015).

[178] *Contact Overview*. Livermore Software Technology Corporation. URL: http://www.dynasupport.com/howtos/contact/contact-overview (visited on 02/13/2015).

[179] *Sain-Gobain NortonTygonHigh-Purity*. MatWeb, LLC. URL: matweb.com/search/DataSheet.aspx?MatGUID=ffe16576dab942b2ab1fd04b2658b93f (visited on 04/07/2015).

[180] LS-DYNA Support. *Contact types*. 2001. URL: http://www.dynasupport.com/tutorial/contact-modeling-in-ls-dyna/contact-types (visited on 05/30/2015).

[181] LS-DYNA Support. *How can I handle contact between beams and shells?* URL: http://www.dynasupport.com/faq/contact/how-can-i-handle-contact-between-beams-and-shells (visited on 05/30/2015).

[182] *Rigid body contact*. Livermore Software Technology Corporation. URL: http://www.dynasupport.com/tutorial/contact-modeling-in-ls-dyna/rigid-body-contact (visited on 01/12/2015).

[183] R.K. Blandford et al. "Tensile Stress-Strain Results for 304L and 316L Stainless Steel Plate at Temperature". In: *2007 ASME Pressure Vessels and Piping Division Conference*. Idaho National Laboratory. San Antonio, Texas, July 2007.

[184] Y.C. Fung. "Biomechanics. Mechanical Properties of Living Tissues". In: New York: Springer-Verlag, 1993. Chap. 8.6, pp. 345–346. ISBN: 978-1-4757-2257-4. DOI: 10.1007/978-1-4757-2257-4.

[185] Rudolf Bötticher and TMB GmbH. "Fluid Structure Interaction with *MAT_SOFT_TISSUE and EFG Elements". In: 5th European LS-DYNA Users Conference. 2005. URL: http://www.dynalook.com/european-conf-2005/Boetticher.pdf.

[186] W.A. Cook et al. "Stent graft with improved proximal end". WO Patent App. PCT/US2003/026,042. Mar. 2004. URL: https://www.google.com/patents/WO2004017866A1?cl=en.

[187] T.A. Osborne and S.E. Eells. "Stent graft repair device". CA Patent 2,562,463. Mar. 2014. URL: https://www.google.com/patents/CA2562463C?cl=en.

[188] T.A. Osborne. "Composite stent graft". US Patent 8,343,204. Jan. 2013. URL: https://www.google.com/patents/US8343204.

[189] U.S. Food and Drug Administration. *Summary of Safety and Effectiveness Data. Zenith AAA Endovascular Graft with the H&L-B One-Shot Introduction System*. U.S. Food and Drug Administration. 2003. URL: http://www.accessdata.fda.gov/cdrh_docs/pdf2/P020018b.pdf (visited on 05/29/2015).

[190] U.S. Food and Drug Administration. *Summary of Safety and Effectiveness Data. Zenith Fenestrated AAA Endovascular Graft and Zenith Alignment Stent*. U.S. Food and Drug Administration. 2003. URL: http://www.accessdata.fda.gov/cdrh_docs/pdf2/P020018S040b.pdf (visited on 05/29/2015).

[191] Günter Petzow and Veronica Carle. *Metallographic Etching. Techniques for Metallography Ceramography Plastography*. Trans. by Uta Harnisch. 2nd ed. Metals Part, Ohio: ASM International, 1999. Chap. 1.9.10, p. 100. ISBN: 0-87171-633-4. DOI: TN60.7.P4713.

[192] F. C. Hull. "Delta Ferrite and Martnesite Formation in Stainless Steels". In: *Welding Journal* 52.5 (1973), p. 193. URL: http://www.aws.org/wj/supplement/WJ_1973_05_s193.pdf.

[193] William F. Hosford. *Pysical Metallurgy*. 2nd ed. Taylor & Francis Group, CRC Press, 2010. Chap. 11.11, pp. 140, 169, 174–175. ISBN: 978-1-4398-1360-7. DOI: TN690.H845.

[194] John D Verhoeven. *Steel metallurgy for the non-metallurgist*. ASM International, 2007. URL: https://northtexas.asminternational.org/content/ASM/StoreFiles/05214G_Frontmatter.pdf.

[195] John C. Tverberg. *The Role of Alloying elements on the Fabricability of Austenitic Stainless Steel*. Mukwonago, Wisconsin: CSI Designs, Metals and Materials Consulting Engineers. URL: http://www.csidesigns.com/tech/fabtech.pdf.

[196] Carsten Heintz et al. "Corroded Nitinol Wires in Explanted Aortic Endografts: An Important Mechanism of Failure?" In: *Journal of Endovascular Therapy* 8.3 (2001), pp. 248–253. DOI: 10.1177/152660280100800303. eprint:

http://jet.sagepub.com/content/8/3/248.full.pdf+html. URL: http://jet.sagepub.com/content/8/3/248.abstract.

[197] ASTM International. *A240A240M-15a. Standard Specification for Chromium and Chromium-Nickel Stainless Steel Plate, Sheet, and Strip for Pressure Vessels and for General Applications*. ASTM International. West Conshohocken, PA, 2015, p. 3. URL: http://compass.astm.org/download/A240A240M.17960.pdf.

[198] ASTM International. *F2063-12. Standard Specification for Wrought Nickel-Titanium Shape Memory Alloys for Medical Devices and Surgical Implants*. ASTM International. West Conshohocken, PA, 2015, p. 3. URL: http://compass.astm.org/download/F2063.31587.pdf.

[199] Gurley. *Numerical Methods Lecture 5 - Curve Fitting Techniques*. CGN 3421. Indian Institute of Technology Delhi. URL: http://web.iitd.ac.in/~pmvs/courses/mel705/curvefitting.pdf%5Ctexttt%7B%EF%BF%BD%EF%BF%BD%EF%BF%BD%7D (visited on 03/01/2015).

[200] AndrewM. Walker et al. "In vitro post-stenotic flow quantification and validation using echo particle image velocimetry (Echo PIV)". English. In: *Experiments in Fluids* 55.10, 1821 (2014). ISSN: 0723-4864. DOI: 10.1007/s00348-014-1821-6. URL: http://dx.doi.org/10.1007/s00348-014-1821-6.

[201] *T-LSR Quick Command Reference*. Zaber. URL: http://www.zaber.com/wiki/Manuals/T-LSR#Quick_Command_Reference (visited on 03/05/2015).

Appendix A

PIV Vision System

A particle counting algorithm was developed as a contribution to a publication by Walker et al. entitled "In vitro post-stenotic flow quantification and validation using echo particle image velocimetry (Echo PIV)"[200].

A.1 Methodology

To characterize a fluid velocity profile captured using echo particle image velocimetry (PIV), a particle density histogram was created by analyzing multiple images of particle seeded flow. Using LabVIEW IMAQ, these images were edited to improve particle counting accuracy before separating a flow region into several subsections (histogram bins) and counting particles inside of them.

A low pass filter is performed on collected images to reduce background noise and improve image contrast of available bitmap (BMP) images. Next, a morphological filter was applied to enlarge smaller particles ensuring they wouldn't be lost during further processing. Some particles may touch after their shape is altered, therefore, the image is passed through the "IMAQ Separation" VI, which separates touching particles by eroding any small isthmuses that may have developed between them. After passing the image through a user defined brightness, contrast and gamma (BCG) filter, thresholding is performed to create a binary black and white image and equalization is used to increase contrast and particle boundary visibility. This edited image is cropped to the desired output shape (Figure A.2) and divided into histogram bin subsections. The particles in each of these bins are counted using the "IMAQ Count Objects 2" VI (Figure A.3). Bin values are averaged across all images and output as a histogram for particle distribution visualization. Once all images have been analyzed, count data for each image and each bin is output to a text file for post-processing. If desired, a last step in image processing locates the center of each particle and replaces

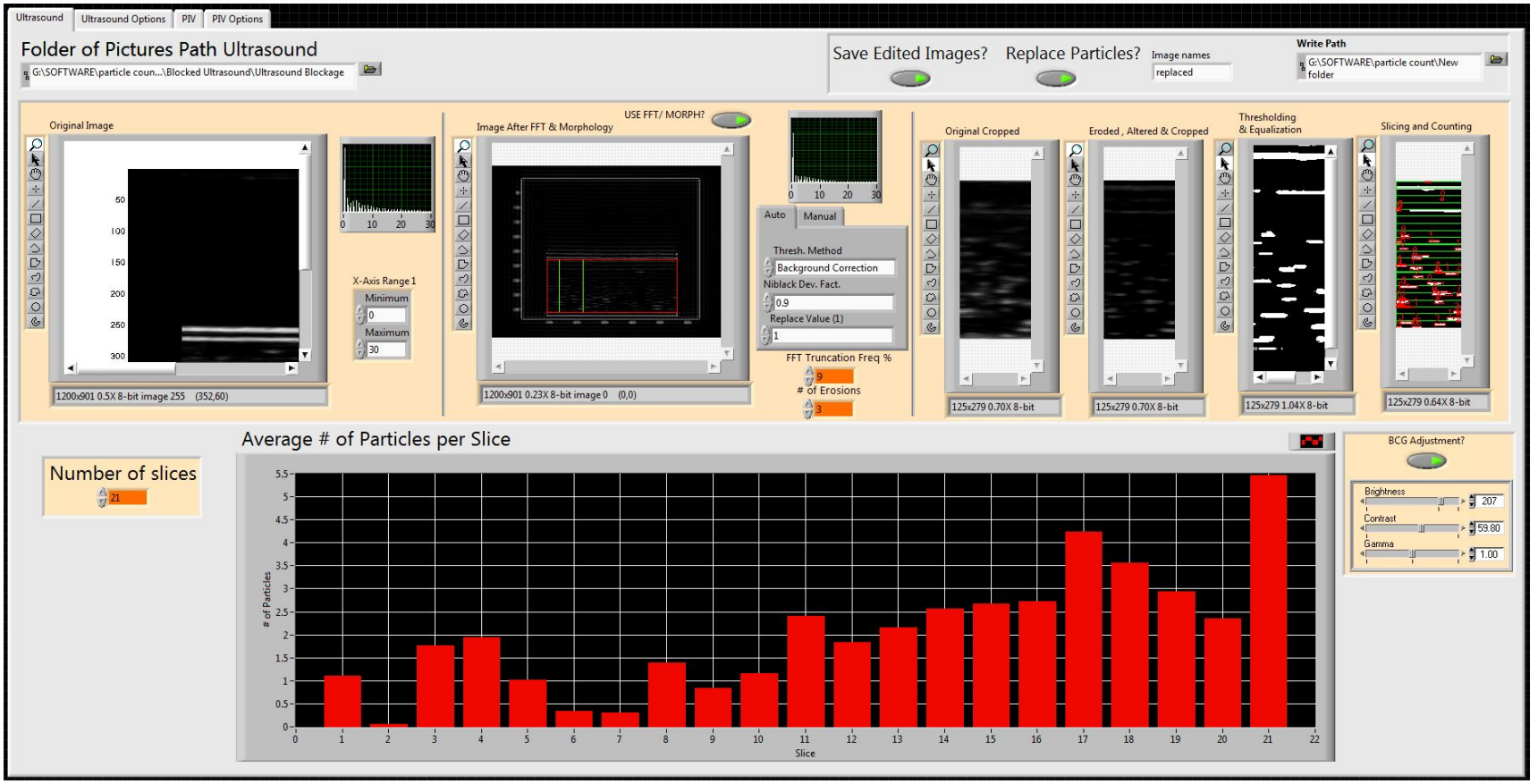

Figure A.1: Console for PIV vision editing

all particles with equally sized white circles. This ideal output with identical circular particles provides a much clearer image for further analysis (Figure A.4). The complete LabVIEW GUI is shown in Figure A.1.

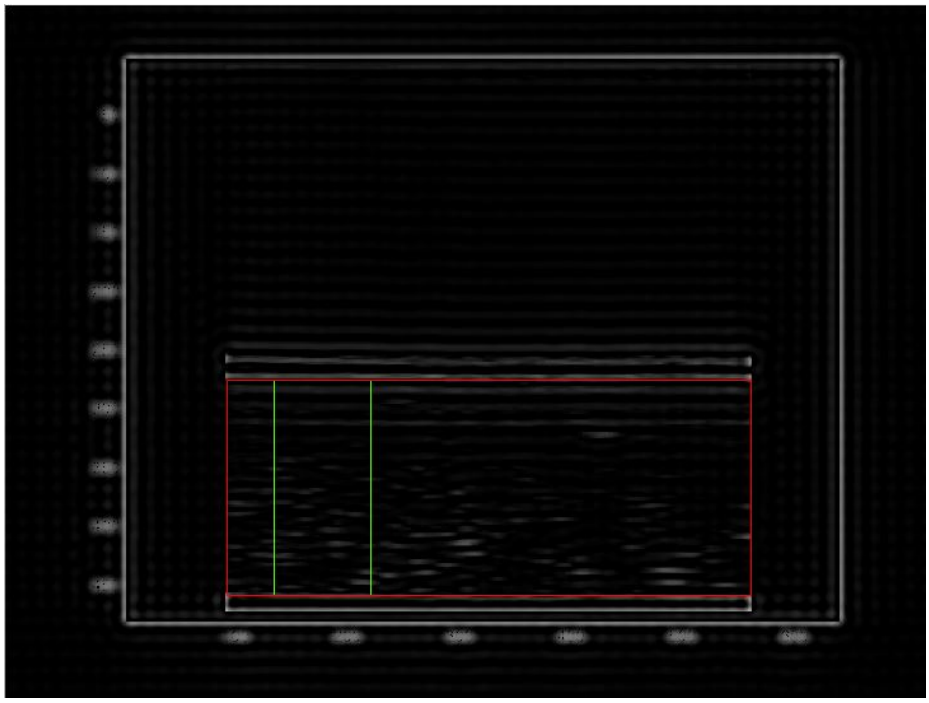

Figure A.2: Cropping (red) and counting (green) regions of interest

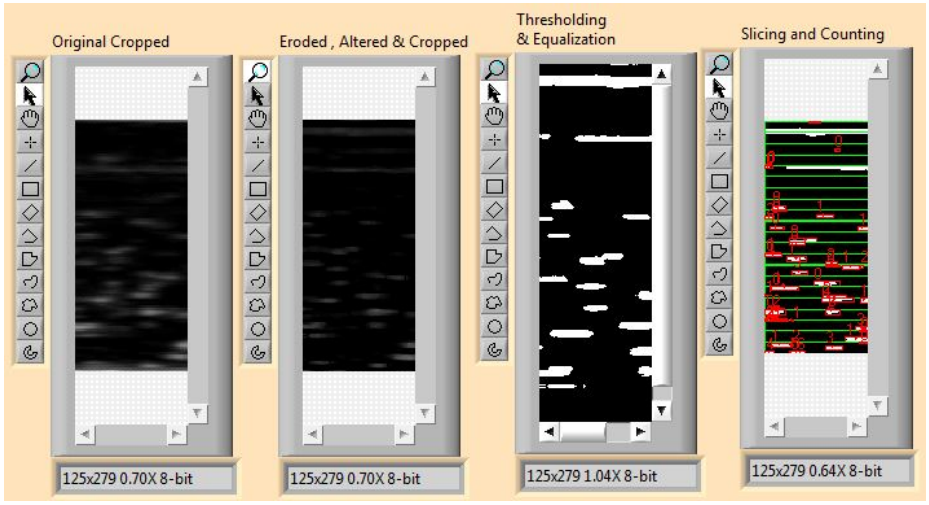

Figure A.3: Ultrasound image editing steps

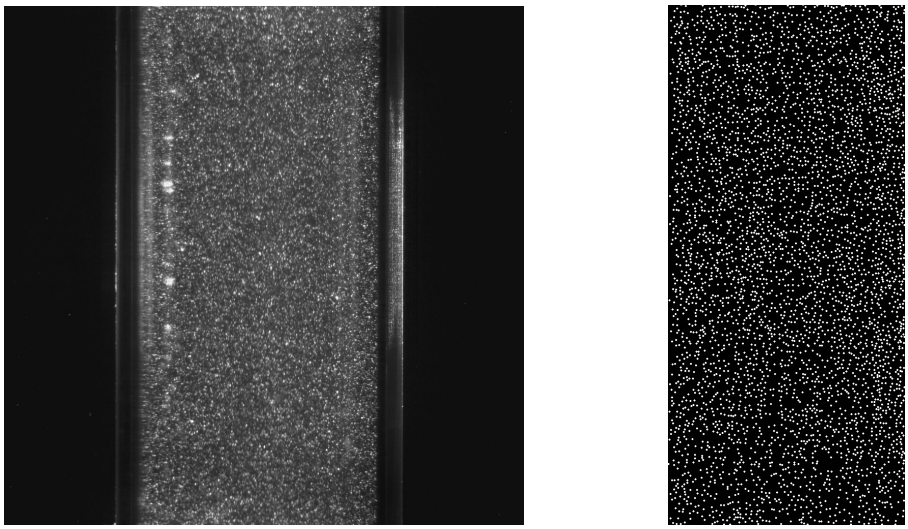

(a) Original PIV Image

(b) Edited PIV image with replaced particles

Figure A.4: Comparison of original PIV image and PIV image with replaced particles

A.2 Program Operation

To operate this program the following steps should be taken:

1. Select "Ultrasound" or "PIV" depending on the type of input images available.
2. Select a location for "Folder of Pictures Path", as well as a "Write Path" for edited pictures and raw data.
3. Files must be in BMP format numbered incrementally starting at 1.
4. Under the "Options" tab, the cropping boundaries for the region of interest and full boundary should be input.
5. Saving options such as folder and file name can be input in the top left corner of this tab.
6. In the main program, ultrasound or PIV tab, select whether edited images should be saved and whether particles should be replaced.
7. Input the "Number of Slices" desired for image and histogram binning.

8. Run the program.

Any other settings available in this program can be adjusted to manipulate the output. However, these extra settings are not required to successfully operate this software.

Appendix B

FEA code

B.1 Main Body

```
$$$$$$$$$$$$$$$$$$$$$$$$$$$$$$$$$$$$$$$$$$$$$$$$$$$$$$$$$$$$$$$$$$$$$$$$$$$$$$$$
$                                                                              $
$ CONFIDENTIAL & PROPREITARY                                                   $
$                                                                              $
$ Use in any form is restricted to JOEL SCOTT or his delegates.               $
$                                                                              $
$$$$$$$$$$$$$$$$$$$$$$$$$$$$$$$$$$$$$$$$$$$$$$$$$$$$$$$$$$$$$$$$$$$$$$$$$$$$$$$$
$
$ Units
$---+----1----+----2----+----3----+----4----+----5----+----6----+----7----+----8
$   LENGTH      MASS      TIME     FORCE    STRESS    ENERGY     POWER   DENSITY
$     [mm]       [g]      [ms]       [N]     [MPa]    [N-mm]       [W]   [kg/m3]
$
$
*KEYWORD_ID
$---+----1----+----2----+----3----+----4----+----5----+----6----+----7----+----8
$            PROJECT                NUM                                    STAGE
FULL                SYSTEM              MAT ELASTIC
$
$
$---+----1----+----2----+----3----+----4----+----5----+----6----+----7----+----8
$                                                                              $
$                          PARAMETER DEFINITIONS                               $
$                                                                              $
$---+----1----+----2----+----3----+----4----+----5----+----6----+----7----+----8
*PARAMETER
$---+----1----+----2----+----3----+----4----+----5----+----6----+----7----+----8
$    PRMR1      VAL1     PRMR2      VAL2     PRMR3      VAL3     PRMR4      VAL4
R ENDTIM   +263636.4R HLDTIM   +131818.0R DTOUT      +2250.0R MAXDISP       43.5
$    PRMR5      VAL5     PRMR6      VAL6     PRMR7      VAL7     PRMR8      VAL8
R LOAD     -0.892857R FRIC        +0.000R SFACT         1.00
$
$
*TITLE
mylar
$
$
$---+----1----+----2----+----3----+----4----+----5----+----6----+----7----+----8
$                                                                              $
$                                 CONTROL CARD                                 $
$                                                                              $
```

```
$---+----1----+----2----+----3----+----4----+----5----+----6----+----7----+----8
$*CONTROL_TIMESTEP
$---+----1----+----2----+----3----+----4----+----5----+----6----+----7----+----8
$   DTINIT    TSSFAC      ISDO    TSLIMT     DT2MS      LCTM     ERODE     MS1ST
$         0       0.9         0       0.0       0.0         0         0         1
$---+----1----+----2
$   DT2MSF   DT2MSLC
$
*CONTROL_OUTPUT
$---+----1----+----2----+----3----+----4----+----5----+----6----+----7----+----8
$    NPOPT    NEECHO    NREFUP    IACCOP     OPIFS    IPNINT    IKEDIT    IFLUSH
                                                                            20
$---+----1----+----2----+----3----+----4----+----5----+----6----+----7----+----8
$    IPRTF    IERODE     TET10    MSGMAX    IPCURV      GMDT   IP1DBLT      EOCS

$
$
*CONTROL_PARALLEL
$---+----1----+----2----+----3----+----4----+----5----+----6----+----7----+----8
$     NCPU    NUMRHS     CONST      PARA
         8         0         1         1
$
*CONTROL_TERMINATION
$---+----1----+----2----+----3----+----4----+----5
$   ENDTIM    ENDCYC     DTMIN    ENDENG    ENDMAS
&ENDTIM            0       0.0       0.0       0.0
$
*CONTROL_IMPLICIT_GENERAL
$---+----1----+----2----+----3----+----4----+----5----+----6----+----7----+----8
$   imflag       dt0    IMFORM      NSBS       IGS     CNSTN      FORM    ZERO_V
         1    2250.0
$
*CONTROL_IMPLICIT_SOLUTION
$---+----1----+----2----+----3----+----4----+----5----+----6----+----7----+----8
$  nlsolvr    ilimit    maxref     dctol     ectol     rctol     lstol    abstol
        12         1     99999      0.01     0.001              9999.0   1.0e-10
$---+----1----+----2----+----3----+----4----+----5----+----6----+----7----+----8
$    dnorm   divflag     istif   nlprint    nlnorm   d3itctl     cpchk
         1                             2         1       101         1
$---+----1----+----2----+----3----+----4----+----5----+----6----+----7----+----8
$   arcctl    arcdir    arclen    arcmth    arcdmp    arcpsi    arcalf    arctim
                                      1         1
$---+----1----+----2----+----3----+----4----+----5----+----6----+----7----+----8
$    lsmtd     lsdir      irad      srad      awgt      sred
         5         4         1         0
$
*CONTROL_IMPLICIT_SOLVER
$---+----1----+----2----+----3----+----4----+----5----+----6----+----7----+----8
$   lsolvr   prntflg    negeig     order      drcm    drcprm  au-tospc  au-totol
         5
$
$---+----1----+----2----+----3----+----4----+----5----+----6----+----7----+----8
$   lcpack    mtxdmp
```

```
95
96  $
97  *CONTROL_IMPLICIT_AUTO
98  $---+----1----+----2----+----3----+----4----+----5----+----6----+----7----+----8
99  $    iauto    iteopt    itewin     dtmin     dtmax     dtexp     kfail    kcycle
100          1         1         1    2250.0    2250.0
101 $
102 *CONTROL_IMPLICIT_DYNAMICS
103 $---+----1----+----2----+----3----+----4----+----5----+----6----+----7----+----8
104 $    imass     gamma      beta    TDYBIR    TDYDTH    TDYBUR     IRATE
105          0      0.50      0.25                                      2
106 $
107 *CONTROL_CONTACT
108 $---+----1----+----2----+----3----+----4----+----5----+----6----+----7----+----8
109 $   SLSFAC    RWPNAL    ISLCHK    SHLTHK    PENOPT    THKCHG     ORIEN    ENMASS
110     0.0001      -1.0         2         2         1
111 $---+----1----+----2----+----3----+----4----+----5----+----6----+----7----+----8
112 $   USRSTR    USRFRC     NSBCS    INTERM     XPENE     SSTHK      ECDT   TIEDPRJ
113
114 $---+----1----+----2----+----3----+----4----+----5----+----6----+----7----+----8
115 $    SFRIC     DFRIC       EDC       VFC        TH     TH_SF    PEN_SF
116
117 $---+----1----+----2----+----3----+----4----+----5----+----6----+----7----+----8
118 $   IGNORE    FRCENG   SKIORWG    OUTSEG   SPOTSTP   SPOTDEL
119                   1
120 $---+----1----+----2----+----3----+----4----+----5----+----6----+----7----+----8
121 $     ISYM    NSEROD    RWGAPS    RWGDTH     RWKSF      ICOV    SWRADF    ITHOFF
122
123 $---+----1----+----2----+----3----+----4----+----5----+----6----+----7----+----8
124 $   SHLEDG    PSTIFF    ITHCNT    TDCNOF     FTALL             SHLTRW
125
126 $
127 *CONTROL_RIGID
128 $---+----1----+----2----+----3----+----4----+----5----+----6----+----7----+----8
129 $      LMF      JNTF    ORTHMD     PARTM    SPARSE    METALF    PLOTEL     RBSMS
130          1         1
131 $
132 *CONTROL_SHELL
133 $---+----1----+----2----+----3----+----4----+----5----+----6----+----7----+----8
134 $   WRPANG     ESORT     IRNXX    ISTUPD    THEORY       BWC     MITER      PROJ
135
136 $---+----1----+----2----+----3----+----4----+----5----+----6----+----7----+----8
137 $  ROTASCL    INTGRD    LAMSHT    CSTYP6    THSHEL
138
139 $---+----1----+----2----+----3----+----4----+----5----+----6----+----7----+----8
140 $   PSTUPD   SIDT4TU     CNTCO    ITSFLG    IRQUAD
141
142 $---+----1----+----2----+----3----+----4----+----5----+----6----+----7----+----8
143 $   NFAIL1    NFAIL4   PSNFAIL    KEEPCS     DELFR   DRCPSID    DRCPRM
144          2         2
145 $
146 $
147 $*CONTROL_IMPLICIT_STABILIZATION
```

```
$---+----1----+----2----+----3----+----4----+----5----+----6----+----7----+----8
$      ias     scale    tstart      tend
$         1     0.001
$
$*DAMPING_FREQUENCY_RANGE
$---+----1----+----2----+----3----+----4----+----5----+----6----+----7----+----8
$    CDAMP      FLOW     FHIGH      PSID   (blank)    PIDREL
$       .02+2.000E-20+2.000E-18         6
$
$
$*CONTROL_IMPLICIT_EIGENVALUE
$---+----1----+----2----+----3----+----4----+----5----+----6----+----7----+----8
$     NEIG    CENTER     LFLAG    LFTEND     RFLAG    RHTEND    EIGMTH    SHFSCL
$        10
$---+----1----+----2----+----3----+----4----+----5----+----6----+----7----+----8
$   ISOLID     IBEAM    ISHELL   ITSHELL    MSTRES    EVDUMP
$
$
$*PART_MODES
$---+----1----+----2----+----3----+----4----+----5----+----6----+----7----+----8
$      PID      NMFB      FORM     ANSID    FORMAT    KMFLAG     NUPDF    SIGREC
$
$
*CONTROL_ENERGY
$---+----1----+----2----+----3----+----4
$     HGEN      RWEN    SLNTEN     RYLEN
         1         2         2         2
$
$
$*CONTROL_HOURGLASS
$---+----1----+----2
$      IHQ        QH
$         4        .1
$
$
$---+----1----+----2----+----3----+----4----+----5----+----6----+----7----+----8
$                                                                             $
$                        DATABASE CONTROL FOR BINARY                          $
$                                                                             $
$---+----1----+----2----+----3----+----4----+----5----+----6----+----7----+----8
*DATABASE_BINARY_D3PLOT
$---+----1----+----2----+----3----+----4
$  DT/CYCL      LCDT      BEAM     NPLTC
&DTOUT             0         0         0
$---+----1
$    IOOPT
         0
$
$
$
*DATABASE_BINARY_RUNRSF
$---+----1----+----2----+----3----+----4----+----5----+----6----+----7----+----8
$  DT/CYCL   LCDT/NR      BEAM     NPLTC    PSETID
```

```
         1         1
$
*DATABASE_EXTENT_BINARY
$---+----1----+----2----+----3----+----4----+----5----+----6----+----7----+----8
$    NEIPH     NEIPS    MAXINT    STRFLG    SIGFLG    EPSFLG    RLTFLG    ENGFLG

$---+----1----+----2----+----3----+----4----+----5----+----6----+----7----+----8
$   CMPFLG    IEVERP    BEAMIP     DCOMP      SHGE     STSSZ    N3THDT   IALEMAT
                              4
$---+----1----+----2----+----3----+----4----+----5----+----6----+----7----+----8
$  NINTSLF   PKP_SEN      SCLP     HYDRO     MSSCL     THERM    INTOUT    NODOUT
                    1
$---+----1----+----2----+----3----+----4----+----5----+----6----+----7----+----8
$     DTDT    RESPLT     NEIPB
                    1
$
$
*DATABASE_BINARY_INTFOR
$---+----1----+----2----+----3----+----4----+----5----+----6----+----7----+----8
$  DT/CYCL   LCDT/NR      BEAM     NPLTC    PSETID
         1         1
$
$
*DATABASE_EXTENT_INTFOR
$---+----1----+----2----+----3----+----4----+----5----+----6----+----7----+----8
$    NGLBV     NVELO    NPRESU    NSHEAR     NFORC     NGAPC     NFAIL    IEVERF

$
$
*DATABASE_GLSTAT
$---+----1----+----2----+----3----+----4----+----5----+----6----+----7----+----8
$       DT    BINARY      LCUR     IOOPT   OPTION1   OPTION2   OPTION3   OPTION4
    &DTOUT         1
$
$
*DATABASE_RWFORC
$---+----1----+----2----+----3----+----4----+----5----+----6----+----7----+----8
$       DT    BINARY      LCUR     IOOPT   OPTION1   OPTION2   OPTION3   OPTION4
    &DTOUT         1
$
$
*DATABASE_SLEOUT
$---+----1----+----2----+----3----+----4----+----5----+----6----+----7----+----8
$       DT    BINARY      LCUR     IOOPT   OPTION1   OPTION2   OPTION3   OPTION4
    &DTOUT         1
$
$
*DATABASE_MATSUM
$---+----1----+----2----+----3----+----4----+----5----+----6----+----7----+----8
$       DT    BINARY      LCUR     IOOPT   OPTION1   OPTION2   OPTION3   OPTION4
    &DTOUT         1
$
$
```

```
*DATABASE_RCFORC
$---+----1----+----2----+----3----+----4----+----5----+----6----+----7----+----8
$       DT    BINARY      LCUR     IOOPT   OPTION1   OPTION2   OPTION3   OPTION4
    &DTOUT         1
$
$
*DATABASE_NODFOR
$---+----1----+----2----+----3----+----4----+----5----+----6----+----7----+----8
$       DT    BINARY      LCUR     IOOPT   OPTION1   OPTION2   OPTION3   OPTION4
    &DTOUT         1
$
$
*DATABASE_NODOUT
$---+----1----+----2----+----3----+----4----+----5----+----6----+----7----+----8
$       DT    BINARY      LCUR     IOOPT   OPTION1   OPTION2   OPTION3   OPTION4
    &DTOUT         1                        &DTOUT
$
$
*DATABASE_SPCFORC
$---+----1----+----2----+----3----+----4----+----5----+----6----+----7----+----8
$       DT    BINARY      LCUR     IOOPT   OPTION1   OPTION2   OPTION3   OPTION4
    &DTOUT         1
$
$
*DATABASE_SWFORC
$---+----1----+----2----+----3----+----4----+----5----+----6----+----7----+----8
$       DT    BINARY      LCUR     IOOPT   OPTION1   OPTION2   OPTION3   OPTION4
    &DTOUT         1
$
$
*DATABASE_BNDOUT
$---+----1----+----2----+----3----+----4----+----5----+----6----+----7----+----8
$       DT    BINARY      LCUR     IOOPT   OPTION1   OPTION2   OPTION3   OPTION4
    &DTOUT         1
$
$
*DATABASE_NODAL_FORCE_GROUP
$---+----1----+----2----+----3----+----4----+----5----+----6
$     NSID       CID
         1
$
$
*DATABASE_NODAL_FORCE_GROUP
$---+----1----+----2----+----3----+----4----+----5----+----6
$     NSID       CID
         2
$
$
$---+----1----+----2----+----3----+----4----+----5----+----6----+----7----+----8
$                                                                             $
$                                PART CARDS                                   $
$                                                                             $
$---+----1----+----2----+----3----+----4----+----5----+----6----+----7----+----8
```

```
$
*INCLUDE
$ Import material database
matdef.k
$
$
*INCLUDE
$ Import mesh of all parts
12mm stent.mesh
$
$
*INCLUDE
$ Import mylar part
mylar.part
$
$
*INCLUDE
$ Import roller part
roller.part
$
$
*INCLUDE
$ Import stent part
stent.part
$
$
$---+----1----+----2----+----3----+----4----+----5----+----6----+----7----+----8
$                                                                             $
$                              BOUNDARY SPC CARDS                             $
$                                                                             $
$---+----1----+----2----+----3----+----4----+----5----+----6----+----7----+----8
$
*BOUNDARY_SPC_SET_ID
$       ID                                                            HEADING
         1                                                          FIXanchor
$---+----1----+----2----+----3----+----4----+----5----+----6----+----7----+----8
$     nsid       cid      dofx      dofy      dofz      dofrx     dofry    dofrz
         2         0         1         1         1         1         1         1
$
$
*BOUNDARY_SPC_SET_ID
$       ID                                                            HEADING
         2                                                 MYLAR CONSTRAINT  LOAD
$---+----1----+----2----+----3----+----4----+----5----+----6----+----7----+----8
$     nsid       cid      dofx      dofy      dofz      dofrx     dofry    dofrz
         6         0         0         1         1         1         1         1
$
$
*BOUNDARY_SPC_SET_ID
$       ID                                                            HEADING
         3                                                          FIXSTENTZ
$---+----1----+----2----+----3----+----4----+----5----+----6----+----7----+----8
$     nsid       cid      dofx      dofy      dofz      dofrx     dofry    dofrz
```

```
         4         0         0         0         1         0         0         0
$
$
$*BOUNDARY_SPC_SET_ID
$       ID                                                              HEADING
$         5                                                            FIXMylar1
$---+----1----+----2----+----3----+----4----+----5----+----6----+----7----+----8
$     nsid       cid      dofx      dofy      dofz     dofrx     dofry     dofrz
$         7         0         0         0         1         1         1         0
$
$
$*BOUNDARY_SPC_SET_ID
$       ID                                                              HEADING
$         6                                                            FIXMylar1
$---+----1----+----2----+----3----+----4----+----5----+----6----+----7----+----8
$     nsid       cid      dofx      dofy      dofz     dofrx     dofry     dofrz
$         8         0         0         0         1         0         0         0
$
$
*BOUNDARY_SPC_SET_ID
$       ID                                                              HEADING
         7                                                            FIXMylar1
$---+----1----+----2----+----3----+----4----+----5----+----6----+----7----+----8
$     nsid       cid      dofx      dofy      dofz     dofrx     dofry     dofrz
         9         0         0         0         1         0         0         0
$
$---+----1----+----2----+----3----+----4----+----5----+----6----+----7----+----8
$                                                                             $
$                          MOTION/DYNAMICS CARDS                              $
$                                                                             $
$---+----1----+----2----+----3----+----4----+----5----+----6----+----7----+----8
*BOUNDARY_PRESCRIBED_MOTION_SET_ID
$---+----1----+----+----+----+----+----+----+----+----+----+----+----+----+----2
$       ID                                                              HEADING
         1                                                          Mylar Edge
$---+----1----+----2----+----3----+----4----+----5----+----6----+----7----+----8
$      SID       DOF       VAD      LCID        SF       VID     DEATH     BIRTH
         1         1         2         1         1
$
$
*BOUNDARY_PRESCRIBED_MOTION_NODE_ID
$---+----1----+----+----+----+----+----+----+----+----+----+----+----+----+----2
$       ID                                                              HEADING
         1                                                       Trailing Roller
$---+----1----+----2----+----3----+----4----+----5----+----6----+----7----+----8
$      SID       DOF       VAD      LCID        SF       VID     DEATH     BIRTH
    701322         1         2         1         1
$
$
*BOUNDARY_PRESCRIBED_MOTION_NODE_ID
$---+----1----+----+----+----+----+----+----+----+----+----+----+----+----+----2
$       ID                                                              HEADING
         1                                                        Leading Roller
```

```
$---+----1----+----2----+----3----+----4----+----5----+----6----+----7----+----8
$      SID       DOF       VAD      LCID        SF       VID     DEATH     BIRTH
    735856         1         2         1         1
$
$
$*LOAD_BODY_Y
$---+----1----+----2----+----3----+----4----+----5----+----6----+----7----+----8
$     LCID        SF    lciddr        xc        yc        zc
$         2   0.00981
$---+----1----+----2----+----3----+----4----+----5----+----6----+----7----+----8
$     PSID
$         3
$
$
$---+----1----+----2----+----3----+----4----+----5----+----6----+----7----+----8
$                                                                              $
$                              LOAD CURVE CARDS                                $
$                                                                              $
$---+----1----+----2----+----3----+----4----+----5----+----6----+----7----+----8
$
$
*DEFINE_CURVE
$---+----1----+----2----+----3----+----4----+----5----+----6----+----7
$     LCID      SIDR       SFA       SFO      OFFA      OFFO    DATTYP
         1         0      +1.0      +1.0       0.0       0.0         0
$---+----1----+----2----+----3----+----4
$            XVALUES             YVALUES
           +0.000E+00          +0.000E+00
&HLDTIM                          &MAXDISP
&ENDTIM                         +0.000E+00
$
$
$*DEFINE_CURVE
$---+----1----+----2----+----3----+----4----+----5----+----6----+----7
$     LCID      SIDR       SFA       SFO      OFFA      OFFO    DATTYP
$         2         0      +1.0      +1.0       0.0       0.0         0
$
$---+----1----+----2----+----3----+----4
$           abscissa            ordinate
$          +0.000E+00          +1.000E+00
$&ENDTIM                       +1.000E+00
$
$$$$$$$$$$$$$$$$$$$$$$$$$$$$$$$$$$$$$$$$$$$$$$$$$$$$$$$$$$$$$$$$$$$$$$$$$$$$$$$
$---+----1----+----2----+----3----+----4----+----5----+----6----+----7----+----8
$                                                                              $
$                               CONTACT CARDS                                  $
$                                                                              $
$---+----1----+----2----+----3----+----4----+----5----+----6----+----7----+----8
$*CONTACT_2D_AUTOMATIC_NODES_TO_SURFACE_TITLE
*CONTACT_AUTOMATIC_SURFACE_TO_SURFACE_TITLE
$---+----1----+----+----+----+----+----+----+----+----+----+----+----+----+----2
$      CID                                                             HEADING
         1                                                 FIXED Mylar roller
```

```
$---+----1----+----2----+----3----+----4----+----5----+----6----+----7----+----8
$     SIDS      MIDS     SFACT      FREQ        FS        FD        DC
$     SSID      MSID     SSTYP     MSTYP    SBOXID    MBOXID       SPR       MPR
$        6         7                                                 1         1
         1         5         3         3                             1         1
$---+----1----+----2----+----3----+----4----+----5----+----6----+----7----+----8
$   TBIRTH    TDEATH       SOS       SOM       NDS       NDM       COF      INIT
$       FS        FD        DC        VC       VDC    PENCHK        BT        DT
$                                                                     1
$---+----1----+----2----+----3----+----4----+----5----+----6----+----7----+----8
$       VC       VDC       IPF     SLIDE    ISTIFF   TIEDGAP
$      SFS       SFM       SST       MST      SFST      SFMT       FSF       VSF
$                                      1         2
       5.0       5.0
$---+----1----+----2----+----3----+----4----+----5----+----6----+----7----+----8
$     SOFT    SOFSCL    LCIDAB    MAXPAR     SBOPT     DEPTH     BSORT    FRCFRQ
$         2                                     4         1
$---+----1----+----2----+----3----+----4----+----5----+----6----+----7----+----8
$   PENMAX    THKOPT    SHLTHK     SNLOG      ISYM     I2D3D    SLDTHK    SLDSTF
$       0.1
$---+----1----+----2----+----3----+----4----+----5----+----6----+----7----+----8
$     IGAP    IGNORE   DPR-FAC    DTSTIF                       FLANGL   CID_RCF
         2
$
$
$---+----1----+----2----+----3----+----4----+----5----+----6----+----7----+----8
*CONTACT_AUTOMATIC_SURFACE_TO_SURFACE_TITLE
$---+----1----+----+----+----+----+----+----+----+----+----+----+----+----+----2
$      CID                                                              HEADING
         2                                                  FREE Mylar roller
$---+----1----+----2----+----3----+----4----+----5----+----6----+----7----+----8
$     SSID      MSID     SSTYP     MSTYP    SBOXID    MBOXID       SPR       MPR
         1         3         3         3                             1         1
$---+----1----+----2----+----3----+----4----+----5----+----6----+----7----+----8
$       FS        FD        DC        VC       VDC    PENCHK        BT        DT
$---+----1----+----2----+----3----+----4----+----5----+----6----+----7----+----8
$      SFS       SFM       SST       MST      SFST      SFMT       FSF       VSF
       5.0       5.0
$---+----1----+----2----+----3----+----4----+----5----+----6----+----7----+----8
$     SOFT    SOFSCL    LCIDAB    MAXPAR     SBOPT     DEPTH     BSORT    FRCFRQ
$---+----1----+----2----+----3----+----4----+----5----+----6----+----7----+----8
$   PENMAX    THKOPT    SHLTHK     SNLOG      ISYM     I2D3D    SLDTHK    SLDSTF
$---+----1----+----2----+----3----+----4----+----5----+----6----+----7----+----8
$     IGAP    IGNORE   DPR-FAC    DTSTIF                       FLANGL   CID_RCF
         2
$
$
```

```
$---+----1----+----2----+----3----+----4----+----5----+----6----+----7----+----8
*CONTACT_NODES_TO_SURFACE_ID
$---+----1----+----+----+----+----+----+----+----+----+----+----+----+----+----2
$      CID                                                              HEADING
          4                                                               STENT
$---+----1----+----2----+----3----+----4----+----5----+----6----+----7----+----8
$     SSID      MSID     SSTYP     MSTYP    SBOXID    MBOXID       SPR       MPR
          4         1         3         3                              1         1
$---+----1----+----2----+----3----+----4----+----5----+----6----+----7----+----8
$       FS        FD        DC        VC       VDC    PENCHK        BT        DT
    0.0025    0.0025                               10
$---+----1----+----2----+----3----+----4----+----5----+----6----+----7----+----8
$      SFS       SFM       SST       MST      SFST      SFMT       FSF       VSF
                 10.0
$---+----1----+----2----+----3----+----4----+----5----+----6----+----7----+----8
$     SOFT    SOFSCL    LCIDAB    MAXPAR     SBOPT     DEPTH     BSORT    FRCFRQ

$---+----1----+----2----+----3----+----4----+----5----+----6----+----7----+----8
$   PENMAX    THKOPT    SHLTHK     SNLOG      ISYM     I2D3D    SLDTHK    SLDSTF

$---+----1----+----2----+----3----+----4----+----5----+----6----+----7----+----8
$     IGAP    IGNORE   DPR-FAC    DTSTIF                         FLANGL   CID_RCF
          2
$---+----1----+----2----+----3----+----4----+----5----+----6----+----7----+----8
$    Q2TRI    DTPCHK     SFNBR    FNLSCL    DNLSCL      TCSO    TIEDID    SHLEDG

$
$
$---+----1----+----2----+----3----+----4----+----5----+----6----+----7----+----8
*CONTACT_AUTOMATIC_GENERAL_ID
$---+----1----+----+----+----+----+----+----+----+----+----+----+----+----+----2
$      CID                                                              HEADING
          5                                                           STENTSELF
$---+----1----+----2----+----3----+----4----+----5----+----6----+----7----+----8
$     SSID      MSID     SSTYP     MSTYP    SBOXID    MBOXID       SPR       MPR
          4                   3                                        1         1
$---+----1----+----2----+----3----+----4----+----5----+----6----+----7----+----8
$       FS        FD        DC        VC       VDC    PENCHK        BT        DT

$---+----1----+----2----+----3----+----4----+----5----+----6----+----7----+----8
$      SFS       SFM       SST       MST      SFST      SFMT       FSF       VSF

$---+----1----+----2----+----3----+----4----+----5----+----6----+----7----+----8
$     SOFT    SOFSCL    LCIDAB    MAXPAR     SBOPT     DEPTH     BSORT    FRCFRQ

$---+----1----+----2----+----3----+----4----+----5----+----6----+----7----+----8
$   PENMAX    THKOPT    SHLTHK     SNLOG      ISYM     I2D3D    SLDTHK    SLDSTF

$---+----1----+----2----+----3----+----4----+----5----+----6----+----7----+----8
$     IGAP    IGNORE   DPR-FAC    DTSTIF                         FLANGL   CID_RCF
          2
$
$
```

```
$
*SET_PART
$---+----1----+----2----+----3----+----4----+----5----+----6----+----7----+----8
$      sid
         8
$---+----1----+----2----+----3----+----4----+----5----+----6----+----7----+----8
$     pid1      pid2      pid3      pid4
         4
$
$
*SET_PART
$---+----1----+----2----+----3----+----4----+----5----+----6----+----7----+----8
$      sid
         6
$---+----1----+----2----+----3----+----4----+----5----+----6----+----7----+----8
$     pid1      pid2      pid3      pid4
         1
$
$
$
*SET_PART
$---+----1----+----2----+----3----+----4----+----5----+----6----+----7----+----8
$      sid
         7
$---+----1----+----2----+----3----+----4----+----5----+----6----+----7----+----8
$     pid1      pid2      pid3      pid4
         5
$
*END
```

B.2 Materials

```
$$$$$$$$$$$$$$$$$$$$$$$$$$$$$$$$$$$$$$$$$$$$$$$$$$$$$$$$$$$$$$$$$$$$$$$$$$$$$$$$
$                                                                              $
$ CONFIDENTIAL & PROPREITARY                                                   $
$                                                                              $
$ Use in any form is restricted to JOEL SCOTT or his delegates.                $
$                                                                              $
$$$$$$$$$$$$$$$$$$$$$$$$$$$$$$$$$$$$$$$$$$$$$$$$$$$$$$$$$$$$$$$$$$$$$$$$$$$$$$$$
$
$
*MAT_ELASTIC_TITLE
$---+----1
$  HEADING
MYLAR
$---+----1----+----2----+----3----+----4----+----5----+----6----+----7
$      MID        RO         E        PR        DA        DB         K
$#     mid        ro         e        pr        da        db  not used
         1   0.00139 4805.2585    0.3800         0         0     0.000

$
$
*MAT_RIGID_TITLE
$---+----1
$  HEADING
ROLLER,FIXED
$---+----1----+----2----+----3----+----4----+----5----+----6----+----7----+----8
$      MID        RO         E        PR         N    COUPLE         M     ALIAS
$#     mid        ro         e        pr         n    couple         m     alias
         2     0.008 1.9300E+5  0.300000     0.000     0.000     0.000
$---+----1----+----2----+----3
$      CMO      CON1      CON2
$#     cmo      con1      con2
       1.0         5         4
$---+----1----+----2----+----3----+----4----+----5----+----6
$   LCO/A1        A2        A3        V1        V2        V3
$# lco or a1        a2        a3        v1        v2        v3
     0.000     0.000     0.000     0.000     0.000     0.000
$
$
*MAT_ELASTIC_TITLE
$---+----1
$  HEADING
STENT
$---+----1----+----2----+----3----+----4----+----5----+----6----+----7
$      MID        RO         E        PR        DA        DB         K
$#     mid        ro         e        pr        da        db  not used
         3     0.008  193000.0  0.300000         0         0         0
$
$
*END
```

B.3 Part1 - Mylar Sheet

```
$$$$$$$$$$$$$$$$$$$$$$$$$$$$$$$$$$$$$$$$$$$$$$$$$$$$$$$$$$$$$$$$$$$$$$$$$$$$$$$$
$                                                                              $
$ CONFIDENTIAL & PROPREITARY                                                   $
$                                                                              $
$ Use in any form is restricted to JOEL SCOTT or his delegates.                $
$                                                                              $
$$$$$$$$$$$$$$$$$$$$$$$$$$$$$$$$$$$$$$$$$$$$$$$$$$$$$$$$$$$$$$$$$$$$$$$$$$$$$$$$
$
*KEYWORD
$
$
$---+----1----+----2----+----3----+----4----+----5----+----6----+----7----+----8
$                                                                              $
$                                PART KEYWORDS                                 $
$                                                                              $
$---+----1----+----2----+----3----+----4----+----5----+----6----+----7----+----8
*PART
$---+----1
$  HEADING
MYLAR
$---+----1----+----2----+----3----+----4----+----5----+----6----+----7----+----8
$      PID     SECID       MID     EOSID      HGID      GRAV    ADPOPT      TMID
         1         1         1         0         0         0         0         0
$
$
$---+----1----+----2----+----3----+----4----+----5----+----6----+----7----+----8
$                                                                              $
$                              SECTION KEYWORDS                                $
$                                                                              $
$---+----1----+----2----+----3----+----4----+----5----+----6----+----7----+----8
*SECTION_SHELL
$---+----1
$  HEADING
$ SOLID
$---+----1----+----2----+----3----+----4----+----5----+----6----+----7----+----8
$    SECID    ELFORM      SHRF       NIP     PROPT   QR/IRID     ICOMP     SETYP
         1        16
$       t1        t2        t3        t4      nloc     marea      idof    edgset
    0.0254    0.0254    0.0254    0.0254                             3
$
*END
```

B.4 Part2 - Rollers

```
$$$$$$$$$$$$$$$$$$$$$$$$$$$$$$$$$$$$$$$$$$$$$$$$$$$$$$$$$$$$$$$$$$$$$$$$$$$$$$$$
$                                                                              $
$ CONFIDENTIAL & PROPREITARY                                                   $
$                                                                              $
$ Use in any form is restricted to Dr. Darrel A. Doman or his delegates.       $
$                                                                              $
$$$$$$$$$$$$$$$$$$$$$$$$$$$$$$$$$$$$$$$$$$$$$$$$$$$$$$$$$$$$$$$$$$$$$$$$$$$$$$$$
$
*KEYWORD
$
$
$---+----1----+----2----+----3----+----4----+----5----+----6----+----7----+----8
$                                                                              $
$                                PART KEYWORDS                                 $
$                                                                              $
$---+----1----+----2----+----3----+----4----+----5----+----6----+----7----+----8
*PART
$---+----1
$  HEADING
fixROLLER
$---+----1----+----2----+----3----+----4----+----5----+----6----+----7----+----8
$      PID     SECID       MID     EOSID      HGID      GRAV    ADPOPT      TMID
         5         2         2
$
$
*PART
$---+----1
$  HEADING
freeROLLER
$---+----1----+----2----+----3----+----4----+----5----+----6----+----7----+----8
$      PID     SECID       MID     EOSID      HGID      GRAV    ADPOPT      TMID
         3         2         2
$
$
$---+----1----+----2----+----3----+----4----+----5----+----6----+----7----+----8
$                                                                              $
$                              SECTION KEYWORDS                                $
$                                                                              $
$---+----1----+----2----+----3----+----4----+----5----+----6----+----7----+----8
*SECTION_SHELL
$---+----1
$  HEADING
$ SOLID
$---+----1----+----2----+----3----+----4----+----5----+----6----+----7----+----8
$    SECID    ELFORM      SHRF       NIP     PROPT   QR/IRID     ICOMP     SETYP
         2        16
$       t1        t2        t3        t4      nloc     marea      idof   edgeset
     0.325     0.325     0.325     0.325                             3
$
*END
```

B.5 Part3 - Stent

```
$$$$$$$$$$$$$$$$$$$$$$$$$$$$$$$$$$$$$$$$$$$$$$$$$$$$$$$$$$$$$$$$$$$$$$$$$$$$$$$$
$                                                                              $
$ CONFIDENTIAL & PROPREITARY                                                   $
$                                                                              $
$ Use in any form is restricted to JOEL SCOTT or his delegates.                $
$                                                                              $
$$$$$$$$$$$$$$$$$$$$$$$$$$$$$$$$$$$$$$$$$$$$$$$$$$$$$$$$$$$$$$$$$$$$$$$$$$$$$$$$
$
*KEYWORD
$
$
$---+----1----+----2----+----3----+----4----+----5----+----6----+----7----+----8
$                                                                              $
$                                PART KEYWORDS                                 $
$                                                                              $
$---+----1----+----2----+----3----+----4----+----5----+----6----+----7----+----8
*PART
$---+----1
$  HEADING
STENT
$---+----1----+----2----+----3----+----4----+----5----+----6----+----7----+----8
$      PID     SECID       MID     EOSID      HGID      GRAV    ADPOPT      TMID
         4         3         3         0         0         0         0         0
$
$
$---+----1----+----2----+----3----+----4----+----5----+----6----+----7----+----8
$                                                                              $
$                              SECTION KEYWORDS                                $
$                                                                              $
$---+----1----+----2----+----3----+----4----+----5----+----6----+----7----+----8
*SECTION_BEAM
$---+----1
$  HEADING
$ BEAM
$---+----1----+----2----+----3----+----4----+----5----+----6----+----7----+----8
$    SECID    ELFORM      SHRF   QR/IRID       CST     SCOOR       NSM
         3         1                 2.0       1.0       0.0
$---+----1----+----2----+----3----+----4----+----5----+----6----+----7----+----8
$        A       ISS       ITT         J        SA       IST
$   0.12566 0.0012566 0.0012566 0.0025133  0.113097
$---+----1----+----2----+----3----+----4----+----5----+----6----+----7----+----8
$      TS1       TS2       TT1       TT2     NSLOC     NTLOC
       0.4       0.4       0.0       0.0       0.0       0.0
$---+----1----+----2----+----3----+----4----+----5----+----6----+----7----+----8
$    STYPE        D1        D2        D3        D4        D5        D6
$SECTION_08
$
*END
```

Appendix C

Radial Extensometer Instructions

The following instruction set discusses in detail the process of setting up, operating and visualizing data collected by the radial extensometer.

C.1 Zero Force Calibration

The Force gauge was calibrated at several increments as described in Chapter 2.6 . The zero force increment must be re-calibrated often to ensure accurate data, and general calibration of the force gauge should be performed:

- If any part of the apparatus is disassembled.
- If there has been a change in lab conditions, especially temperature.
- Before each series of tests is performed.

To calibrate the force gauge:

1. Follow steps 1 through 8 to set up the force gauge but do not put a stent in the system.
2. Ensure the Mylar has some slack in it and is not pulling on the force gauge.
3. Open "Force Calibration.vi" and select a folder and file name for your calibration files (Figure C.1). This folder will be created in the same directory as the force calibration program and files will be labeled incrementally automatically. The software for this program was adapted from an example included with the LabVIEW distribution.
4. The default run-time of 10 s is appropriate and the sampling rate will automatically defaut to 1612 Hz, which is the minimum value possible on the NI9237 DAQ card.

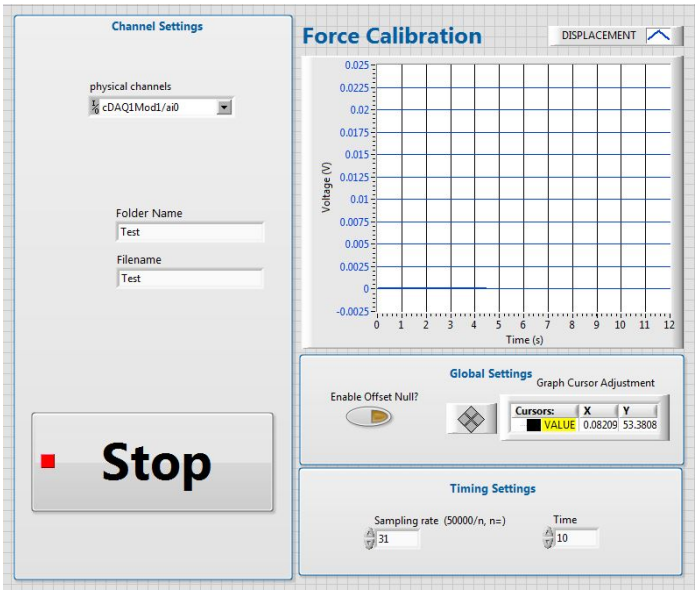

Figure C.1: Radial extensometer force gauge calibration software

5. Ensure nothing is in contact with the slide and run the "Force Calibration.vi" program.

6. Once the program has finished running for ten seconds. Move the slide away from the force gauge and then back to a position which minimizes any force that may be transferred from the Mylar to the Force gauge. This will reset the apparatus so we can take another sample of zero force data with a newly repositioned slide.

7. Repeat steps 5 through 6 four more times.

8. Now that all calibration data has been collected, open the "Calibration.py" program and change the file names in the code to match those created by "Force Calibration.vi".

9. Run the Python calibration program and write down the printed calibration results. These values are entered in the DAQ program as explained in Section C.2.

The program "Calibration.py" performs a bandstop filter at 60 Hz on all data to avoid any EMR interference. A Butterworth filter is also used at 20 Hz to reduce

noise. The program then calculates the average of all data sets and outputs the average voltage and standard deviation.

The linear slide is calibrated through homing, which is explained in its operating instructions. The webcam does not need to be calibrated as the values it records are dimensionless, however, ensure it is centered and pointing straight down the middle of the stent.

C.2 Operation

1. Ensure Mylar is not connected to the force gauge and that the slide is obstruction free.

2. Turn on and home the slide. Use the manual adjustment knob located on the end of the slide to translate the platform all the way toward the motor. Following homing, move slide 2/3 of the way toward the force gauge.

3. Remove L-shaped bracket from the linear slide plate by removing the three $1/4 - 20$x$3/8$ in hex cap screws from the base of the bracket (Figure C.2).

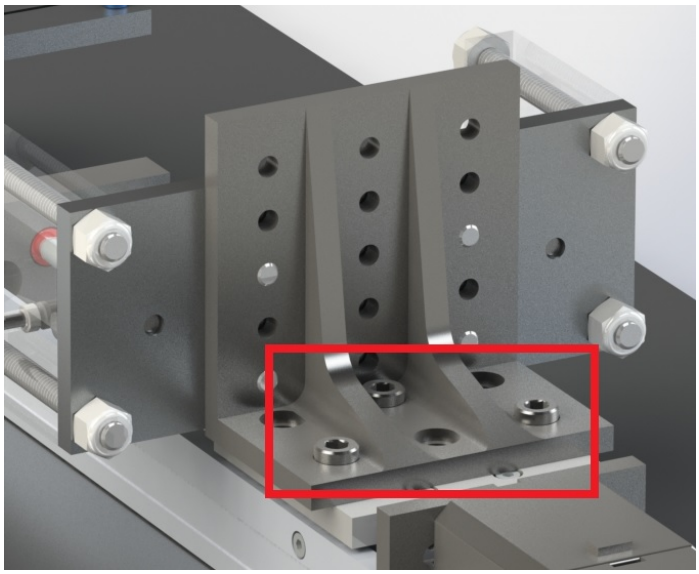

Figure C.2: Radial extensometer l-bracket removal

4. Remove the moving Mylar anchor (Appendix D, page 197) from the moving base plate shown in Appendix D on page 196, by removing the 2, $1/4 - 20$x$3/8$ in

socket cap screws (Figure C.3). There is a shim between these parts.

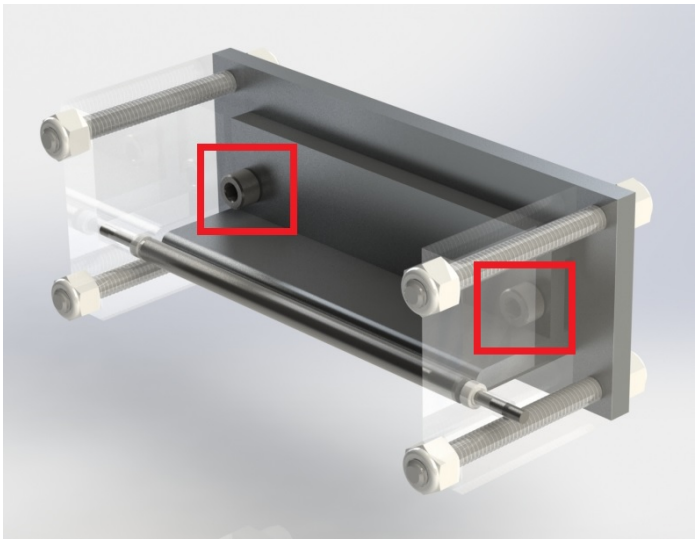

Figure C.3: Radial extensometer moving anchor removal

5. Turn the moving Mylar anchor upside down and put screws through both of the holes in this part in the direction shown in Figure C.4. Select a laser cut section of 0.0254 mm Mylar and thread the 1/4 in holes in the Mylar over the screws. The rest of the Mylar sheet should point toward the corner of the 'L'-shaped moving Mylar anchor. Next, thread the holes in the shim over the screw ends, sandwiching the Mylar between the moving Mylar anchor and the shim. Screw this assembly back onto the moving base plate as seen in Figure C.3. Pull very gently down on the Mylar to ensure it remains centered while tightening the moving Mylar anchor to the moving base plate. Reattach this assembly back onto the linear slide as was explained in 3.

6. Thread the Mylar up between the roller and moving Mylar anchor, then back through the same gap, creating a loop. Stents will be tested by placing them in this loop, ensure the Mylar doesn't fall back through the gap in the next few steps.

7. Remove the top component of the stationary Mylar anchor (Appendix D, page 201). Leave the screws protruding through the top stationary Mylar anchor and thread the holes in the loose end of the Mylar over these screws.

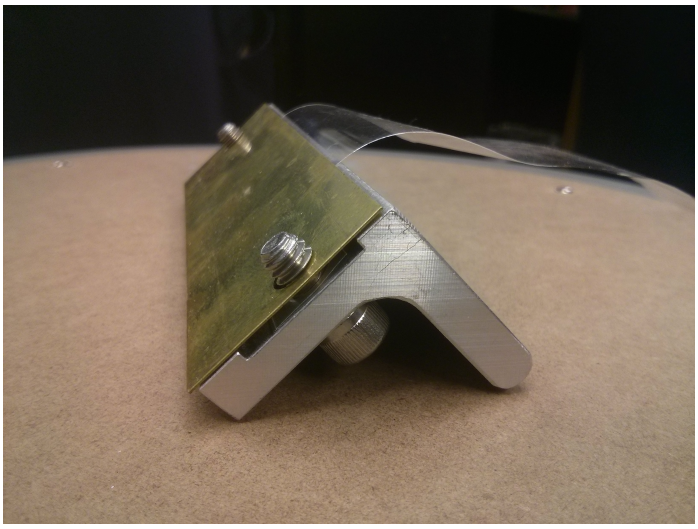

Figure C.4: Radial extensometer moving anchor Mylar attachment

8. Align the screws protruding through the top stationary Mylar anchor with the holes in the bottom stationary Mylar anchor. After ensuring there is no tension on the Mylar and that it is inline with the base plate anchor, tighten the screws, sandwiching the Mylar between the top and bottom stationary anchors. See Figure 2.1 for reference.

    - Ensure that the Mylar is aligned on the edges of the roller and moving Mylar anchor edge, on the front and back of the gap between them where the Mylar is doubled over.
    - Ensure both the force gauge and its associated clamp are parallel to the experiment base plate.
    - Avoid overtightening the force gauge mounting screw. This may have an effect on results.

9. Insert the stent into the Mylar loop with its brazed joints facing downward and manually move the slide to tighten the Mylar around the stent. Observe and adjust Mylar alignment. Ends of the roller that protrude through the acrylic roller supports (Appendix D, pages 198 and 199) can be used to adjust Mylar alignment.

10. Attach the webcam to the testing apparatus using the cantilever beam setup

seen in Figure 2.1. The camera should be pointing down the center of the stent being tested.

11. Calculate the required slide displacement in microsteps using the program entitled "Calculator.xlsx" (Figure C.5). The diameter of fully deployed covered and uncovered stents, as well as desired AR of the covered stent must be known. This displacement represents the number of microsteps required, rounded to the nearest integer, to constrict the uncovered stent to an AR that matches the value input for a covered stent.

Required Displacement		
Area Reduction Required	50	%
Diameter of fully deployed covered stent	14	mm
Displacement Required	12.88211658	mm
Microsteps Required	129860.0462	microsteps
Final Diameter	9.899494937	mm

Second Stent for Solving Comparative Reductions		
Area Reduction Required	83.67346939	%
Diameter of fully deployed uncovered stent	24.5	mm
Displacement Required	45.86883945	mm
Microsteps Required	462387.4944	microsteps
Final Diameter	9.899494937	mm

Figure C.5: Radial extensometer displacement calculator

12. Input the desired slide displacement into "Motion Control.csv" (Figure C.6) and save the file. Commands 21 and 23 seen in Figure C.6 call instructions "Move Relative" and "Stop" respectively [201]. Device number '0' refers to the communication (COM) port value connected to the linear slide.

Device Number	Command	Value
0	21	-462387
0	21	462387
0	23	0

Figure C.6: Radial extensometer motion control

- Commands issued in the motion control file will move the slide the same distance in both directions. The stent will first be constricted by moving the slide away from the force gauge by $-462\,387$ microsteps (45.87 mm),

then expanded by moving the slide toward the force gauge by the same interval. These motions will induce an area reduction of 50 % as was calculated with the displacement calculator (Figure C.5).

13. Ensure the force gauge and webcam are connected properly to the computer.

14. The main DAQ software "Joel Scott - Stent Analysis DAQ 5.0.vi" is used to control data collection and uses the motion control file that was just manipulated as an input. Open this file.

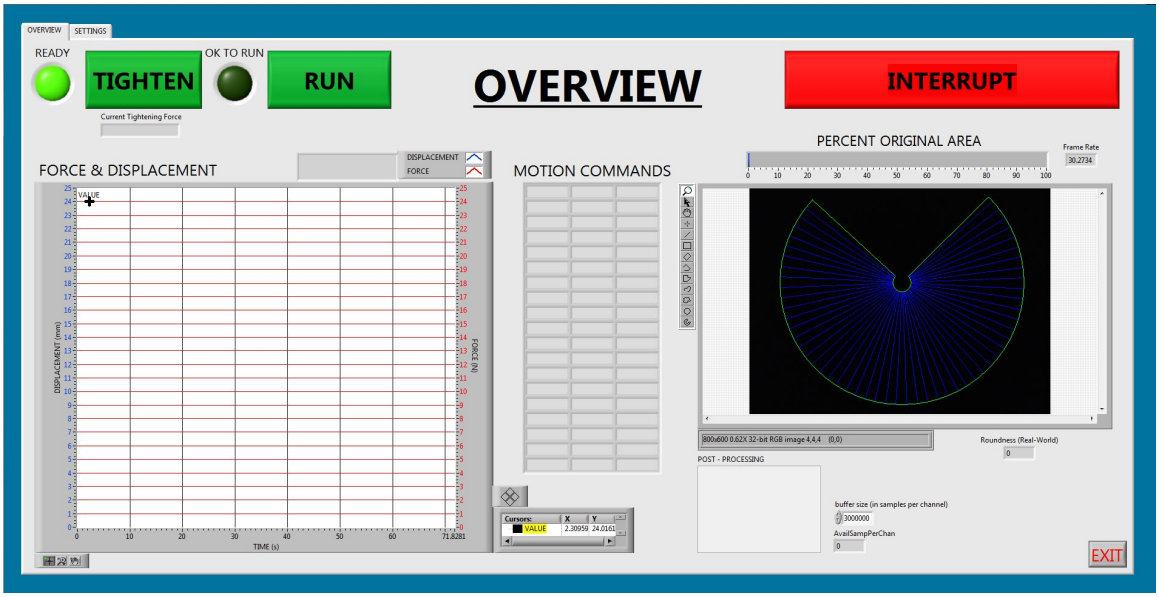

Figure C.7: Radial extensometer DAQ graphical user interface (GUI)

15. In "Joel Scott - Stent Analysis DAQ 5.0.vi", scroll down to reveal extra settings. This area is used to set more advanced settings than can be accessed from the main area.

16. File saving options can be found under the first tab. "Filename", will set the name for data, video and plot files created during each run of the DAQ software. If several tests are performed consecutively, incremental numbers will automatically be added to the end of this name. There is no need to change the file name after each test. Changing the file name will reset this concatenated value to zero. "Folder Name" will set the name of the folder that files will

be saved in. If the folder doesn't already exist, it will be created in the same directory as "Joel Scott - Stent Analysis DAQ 5.0.vi". By default, files are given a date and integer value as a name and saved in the folder labeled "Test Logs". Select a file and folder name.

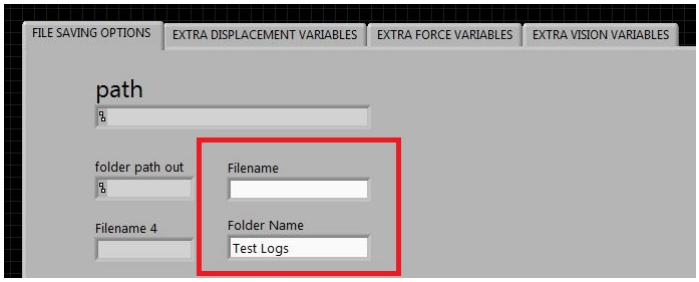

Figure C.8: Radial extensometer DAQ file saving options

17. Force data collection variables and calibration results can be set under the "Extra Force Variables" tab (Figure C.9).

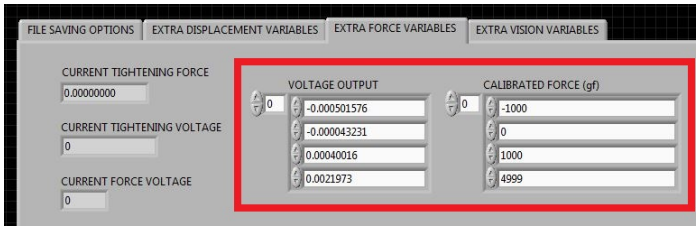

Figure C.9: Radial extensometer DAQ force options

18. Advanced vision and displacement variables can also be adjusted under their respective tabs in this section. Default values are optimized.

19. Select the "Settings" tab. There are only three variables that should have to be adjusted: "Rebound Force", "Base Force" and "Filename" (Figure C.10). Aside from "Filename", which tells the program where the motion control file can be found, these values set up the "tighten" feature seen in the top left of the main screen in the LabVIEW DAQ program (Figure C.7). When the tighten button is selected, the linear slide will begin moving away from the force gauge, tightening the Mylar around the stent. The value selected for "Rebound Force"

will cause the slide to stop moving and change directions when the force gauge reads this value. This step pre-tensions the Mylar, removing any slack from the system to avoid any differences in experimental setup between test runs or stents of different shapes and sizes. The value of rebound force should be set such that a guaranteed contact has happened between the stent and Mylar. This value is better off too high than too low. Once the linear slide has changed directions, it continues moving toward the force gauge, loosening the Mylar around the stent until the force gauge reads the value set for "Base Force". The "Base Force" value should be set at a point where there will be no force offset applied to the system but where the stent is still fully in contact with the Mylar. Rebound and base forces should be tuned to the point that there is no delay before OA data decreases at the beginning of each test.

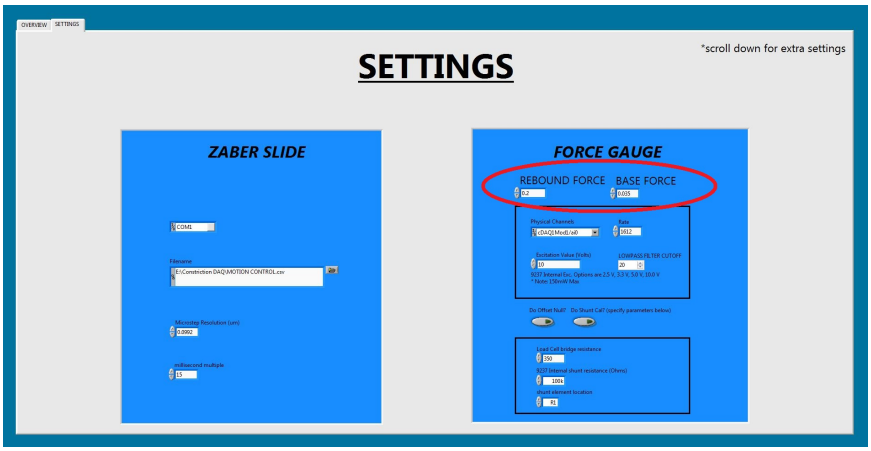

Figure C.10: Radial extensometer DAQ base and rebound force settings

20. Return to the main tab labeled "Overview" and select "Tighten" to begin the test. The Mylar will tighten around the stent as expected, then loosen to the set base force.

    - Once this tightening step is completed, double check that the starting point is appropriate, if not, stop the test and return to step 19.
    - The base and rebound forces should remain unchanged throughout all repetitive tests of the same stent.

21. After tightening is complete, center the webcam so it is looking down the barrel of the stent and ensure the Mylar is still straight.

22. Select "Run" to perform test.

    - It is important to note that the "Interrupt" button will not stop the test dead in its tracks. The slide must complete it's full command before stopping. Ensure the slide path is clear before starting the test. As a last resort, pull out the power cable to immediately stop the test.

23. Allow the test and Python script to run to completion and for plotted data to appear on the screen. Subsequent tests can only be started once the Python plot window, which appears following data analysis, is closed.

24. Once all tests have been performed, ensure that the Mylar is disconnected from the force gauge to protect the apparatus from damage. Disconnect the slide and NI cDAQ-9178 power and store all stents in their appropriately labeled drawers to avoid loss or mislabeling.

25. It is possible to re-plot any files that were created by LabVIEW and Python. The "Plot multiple files.py" program can be used to analyze, display and compare multiple runs of data at the same time. Plots are fully customizable.

Appendix D

Radial Extensometer Drawings

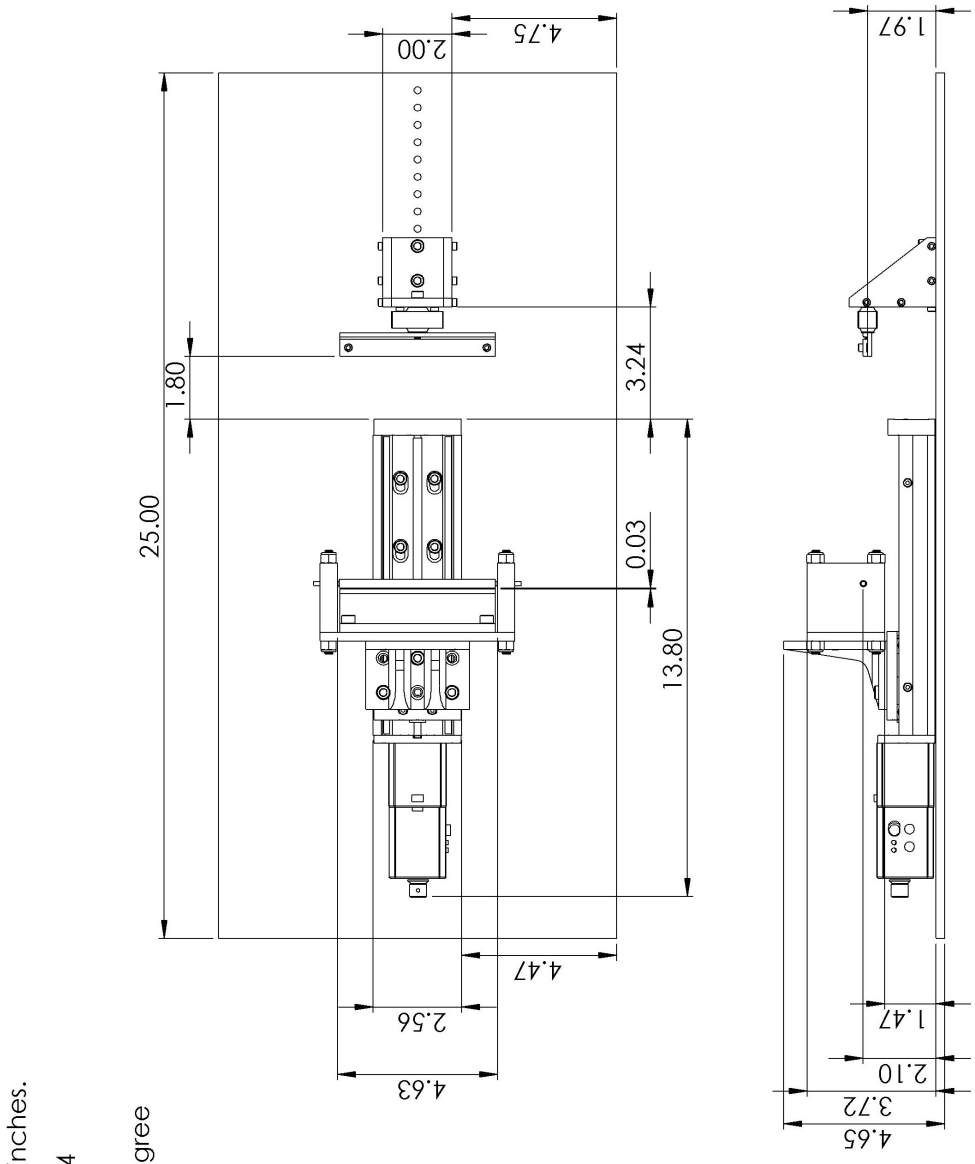

FULL SYSTEM - GENERAL DIMENSIONS

JOEL SCOTT - (902)-579-5922
DATE: Thursday, Nov 15, 2012
SCALE **1:5**, QUANTITY: 1

Dimensions are in inches.
Toperances:
Fractions = +/- 1/64
x.xx = +/- .01
x.xxx = +/- .005
Angle = +/- 1/2 degree

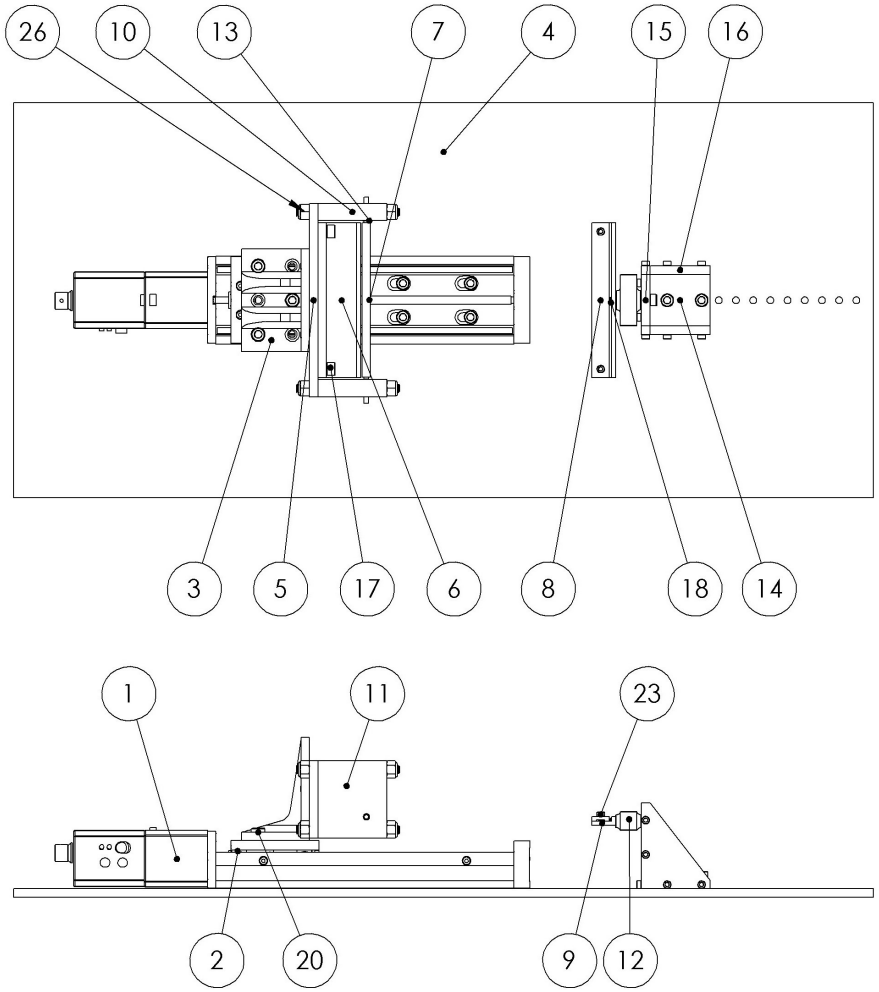

ITEM NO.	PART NAME	QTY.
1	T-LSR150A Linear Slide	1
3	AB90E - 90 Degree Mount	1
4	System Base	1
5	Moving Base Plate	1
6	Moving Mylar Anchor	1
7	Roller	1
8	Stationary Mylar Anchor - Top	1
9	Stationary Mylar Anchor - Bottom	1
10	acrylic support right	1
11	acrylic support left	1
12	50N - Force Transducer	1
13	.125" ID x .25" OD Extended Inner Ring Bearing	2
14	Stationary Mount - Bottom	1
15	Stationary Mount - Front	1
16	Stationary Mount - Sides	2
17	1/4"-10 x 7/16" Socket Head Cap Screw	4
18	M5-0.8 x 10mm Set Screw	1
19	M5-0.8 x 12mm Socket Head Cap Screw	1
20	M6-1.0 x 8mm Socket Head Cap Screw	3
21	1/4"-20 x 7/16" Socket Head Cap Screw	8
22	6-32 x 1/2" Socket Head Cap Screw	10
23	6-32 x 1/4" Socket Head Cap Screw	2
24	1/4"-20 x 3/8" Short Head Socket Head Cap Screw	4
25	1/4" x 3" threaded rod	4
26	1/4" lock nut	8

JOEL SCOTT - (902)-579-5922
DATE: Thursday, Nov 15, 2012
SCALE **1:4** QUANTITY: 1

STATIONARY ANCHOR - BOTTOM

Dimensions are in inches.
Toperances:
Fractions = +/- 1/64
x.xx = +/- .01
x.xxx = +/- .005
Angle = +/- 1/2 degree

NOTE: 1. Stock material is 12" in width. Please trim deformed edges to obtain 11.5" part width.
2. Please ensure that the two sets of tapped holes are in line. The right hand holes should be centered between the two rows of left hand holes.

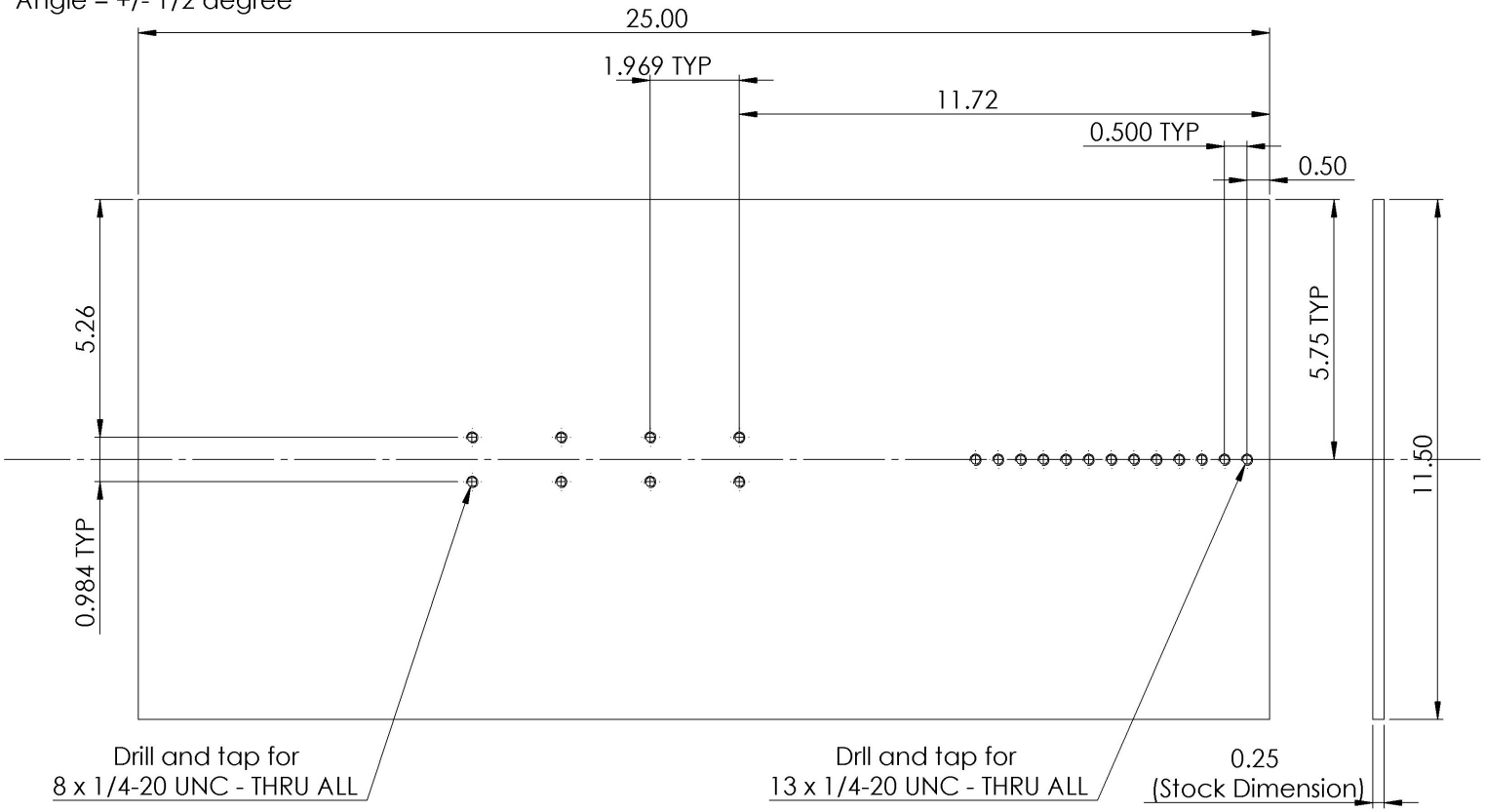

JOEL SCOTT - (902)-579-5922
MATERIAL: Aluminum 5052 - H32 (1/4" Sheet)
DATE: Thursday, Nov 15, 2012
SCALE **1:3**, QUANTITY: 1

SYSTEM BASE

Dimensions are in inches.
Toperances:
Fractions = +/- 1/64
x.xx = +/- .01
x.xxx = +/- .005
Angle = +/- 1/2 degree

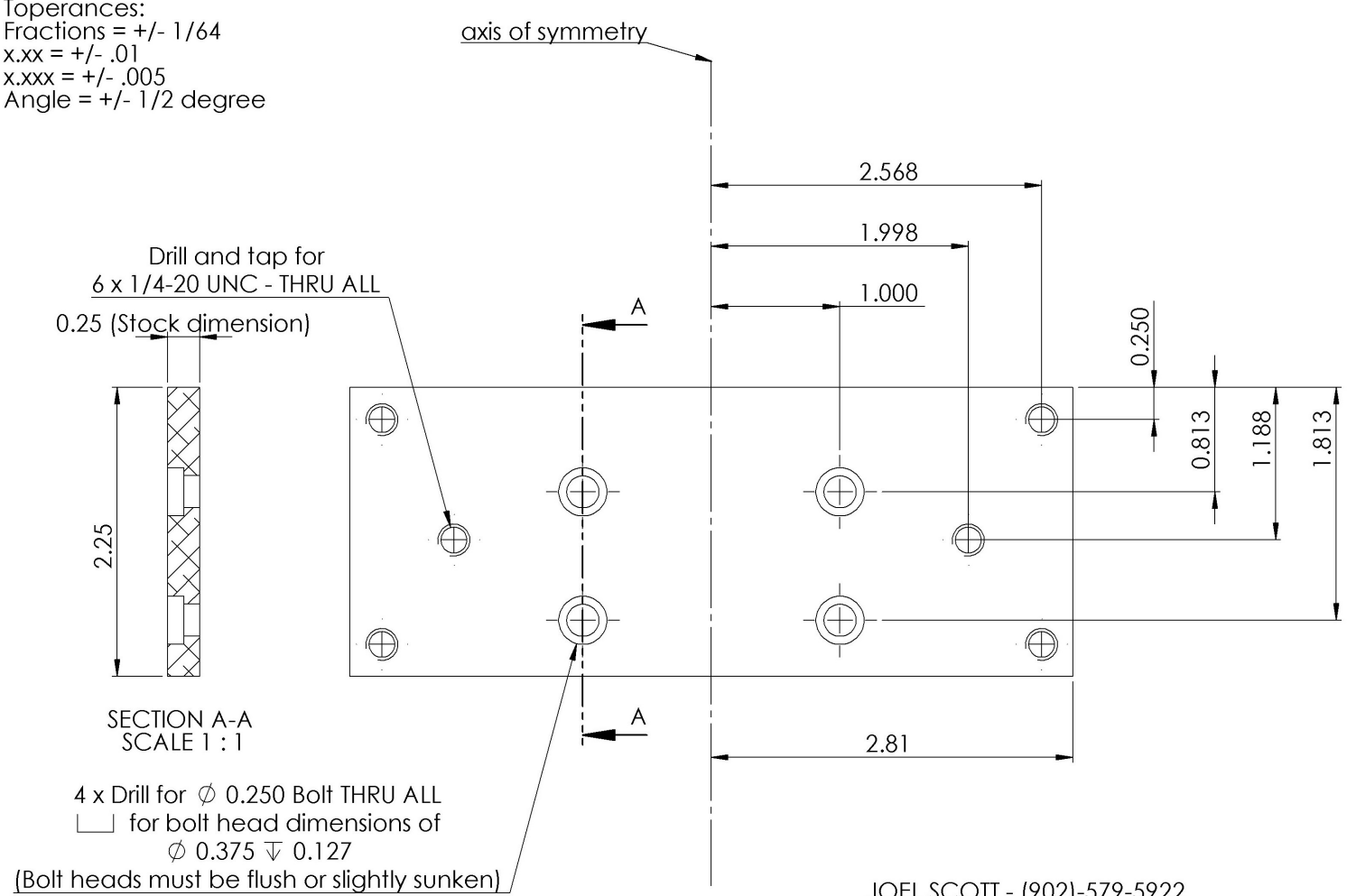

JOEL SCOTT - (902)-579-5922
MATERIAL: Aluminum 5052 - H32 (1/4" Sheet)
DATE: Thursday, Nov 15, 2012
SCALE 1:1, QUANTITY: 1

MOVING BASE PLATE

Dimensions are in inches.
Toperances:
Fractions = +/- 1/64
x.xx = +/- .01
x.xxx = +/- .005
Angle = +/- 1/2 degree

NOTE: Gap between rounded edge of this part and the roller must be larger than 0.025". Current dimensions allow for a gap of 0.031"

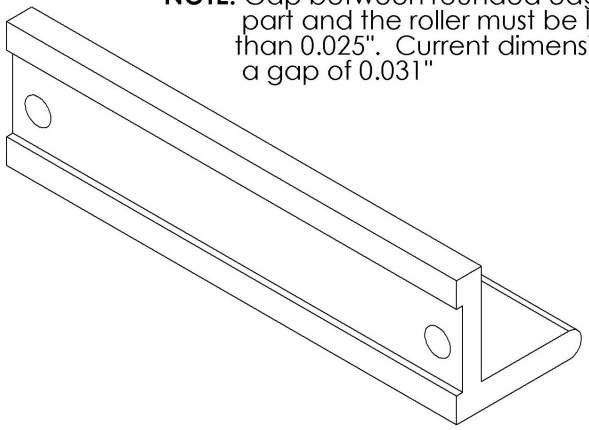

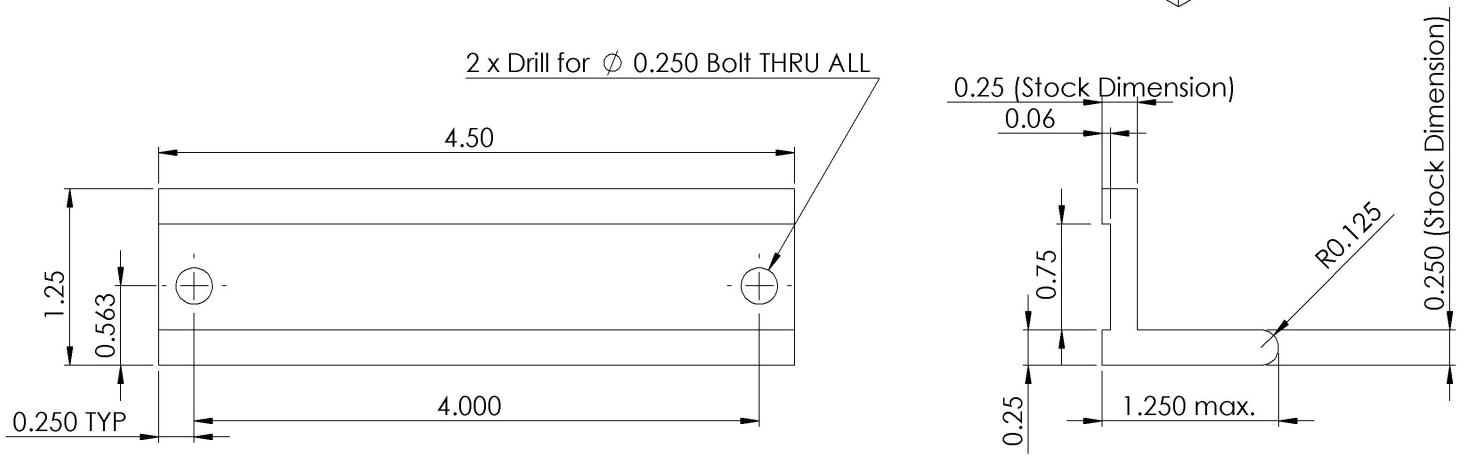

JOEL SCOTT - (902)-579-5922
MATERIAL: Aluminum 6061-T6 Angle (1/4" x 1-1/2" x 1-1/2")
DATE: Thursday, Nov 15, 2012
SCALE 1:1, QUANTITY: 1

MOVING MYLAR ANCHOR

Dimensions are in inches.
Toperances:
Fractions = +/- 1/64
x.xx = +/- .01
x.xxx = +/- .005
Angle = +/- 1/2 degree

NOTE: x & y dimensions for bearing sear along "C" plane should be precise to ensure alignment of bearings accross gap between left and right roller supports.

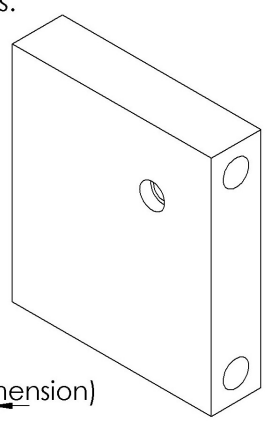

Drill for ∅ 0.188 THRU
BEARING FIT: Bearing dimensions are:
∅ 0.250" ↧ 0.109"
ALIGNS WITH BEARING IN "ROLLER SUPPORT - RIGHT"

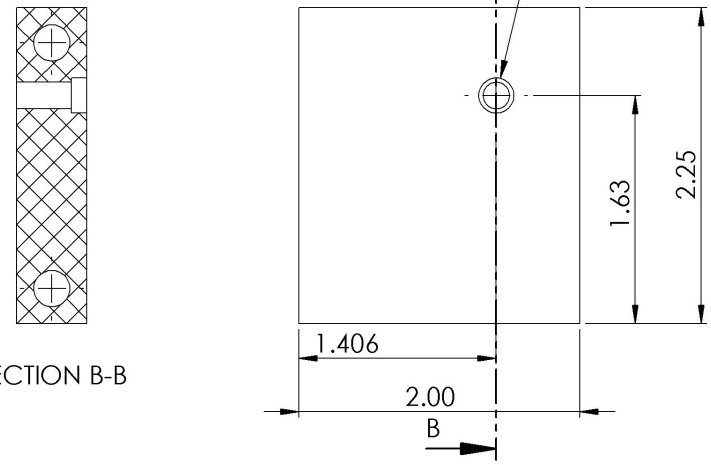

SECTION B-B

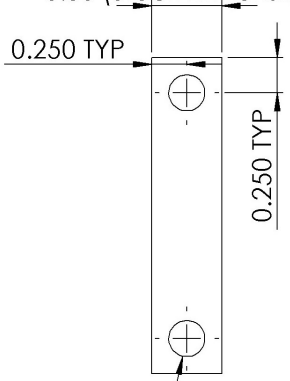

2 x Drill For ∅ 0.250 Bolt THRU

JOEL SCOTT - (902)-579-5922
MATERIAL: Acrylic
DATE: Thursday, Nov 15, 2012
SCALE 1:1, QUANTITY: 1

ROLLER SUPPORT - LEFT

Dimensions are in inches.
Toperances:
Fractions = +/- 1/64
x.xx = +/- .01
x.xxx = +/- .005
Angle = +/- 1/2 degree

NOTE: x & y dimensions for bearing sear along "C" plane should be precise to ensure alignment of bearings accross gap between left and right roller supports.

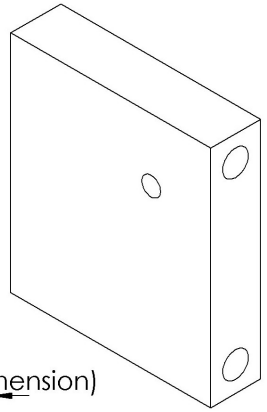

Drill for ∅ 0.188 THRU
BEARING FIT: Bearing dimensions are:
∅ 0.250" ⇩ 0.109"
ALIGNS WITH BEARING IN "ROLLER SUPPORT - RIGHT"

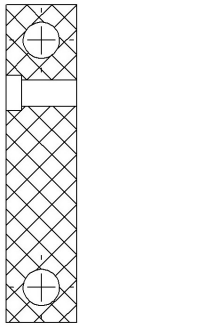

SECTION C-C

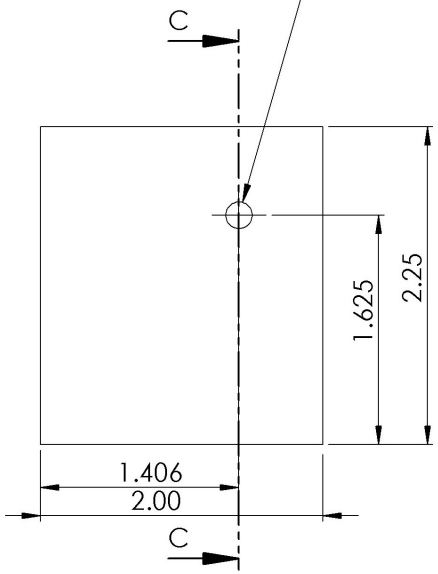

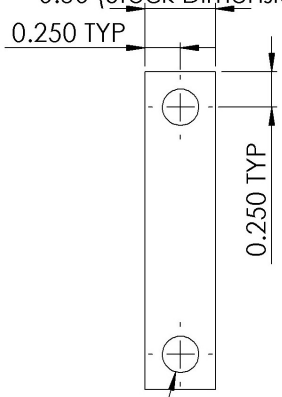

2 x Drill for ∅ 0.250 Bolt THRU

JOEL SCOTT - (902)-579-5922
MATERIAL: Acrylic
DATE: Thursday, Nov 15, 2012
SCALE 1:1, QUANTITY: 1

ROLLER SUPPORT - RIGHT

Dimensions are in inches.
Toperances:
Fractions = +/- 1/64
x.xx = +/- .01
x.xxx = +/- .005
Angle = +/- 1/2 degree

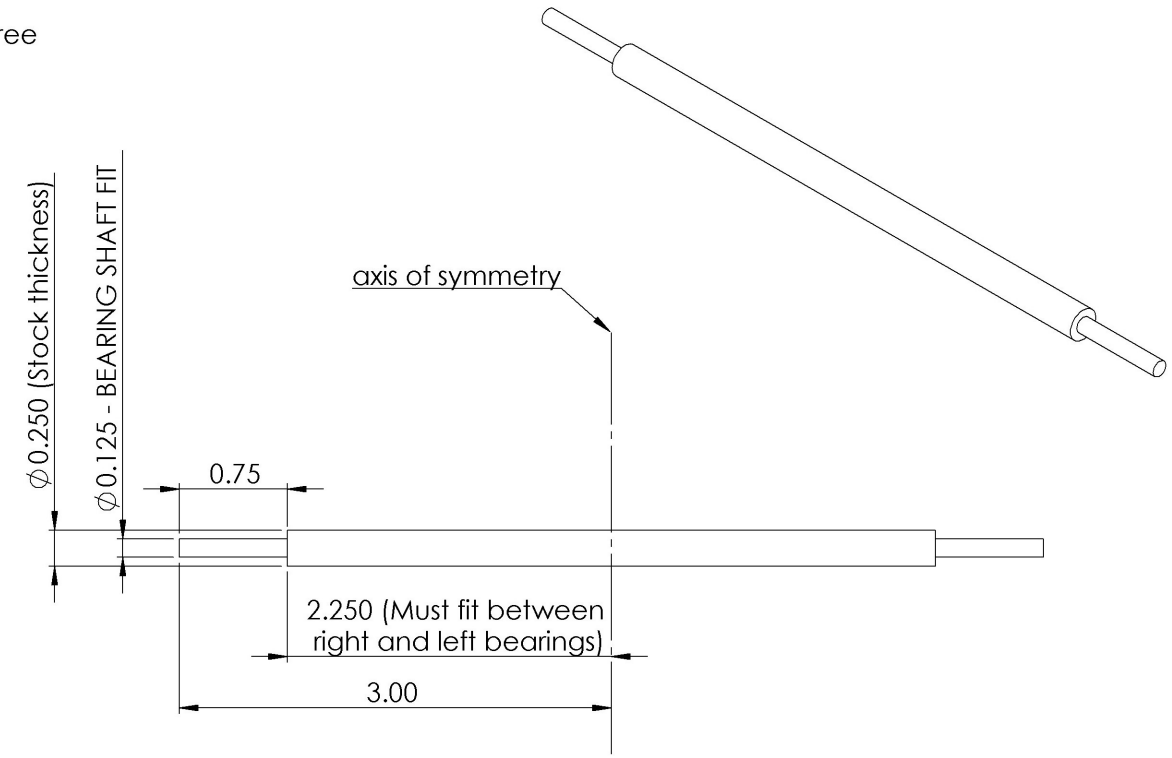

JOEL SCOTT - (902)-579-5922
MATERIAL: Stainless Steel 316
DATE: Thursday, Nov 15, 2012
SCALE 1:1, QUANTITY: 1

ROLLER

Dimensions are in inches.
Toperances:
Fractions = +/- 1/64
x.xx = +/- .01
x.xxx = +/- .005
Angle = +/- 1/2 degree

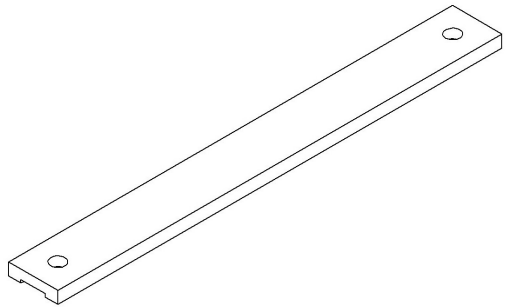

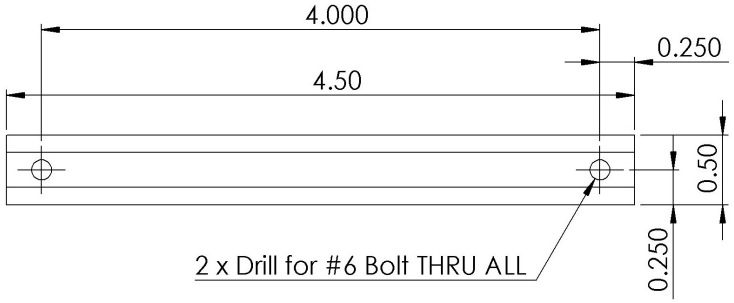

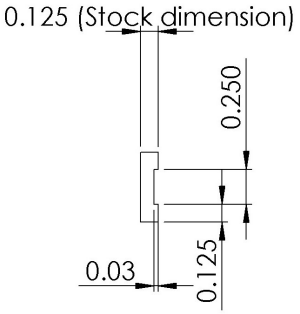

JOEL SCOTT - (902)-579-5922
MATERIAL: Aluminum angle 6061 - T6 (1/8" x 1-1/2" x 1-1/2")
DATE: Thursday, Nov 15, 2012
SCALE 1:1, QUANTITY: 1

STATIONARY MYLAR ANCHOR - TOP

Dimensions are in inches.
Toperances:
Fractions = +/- 1/64
x.xx = +/- .01
x.xxx = +/- .005
Angle = +/- 1/2 degree

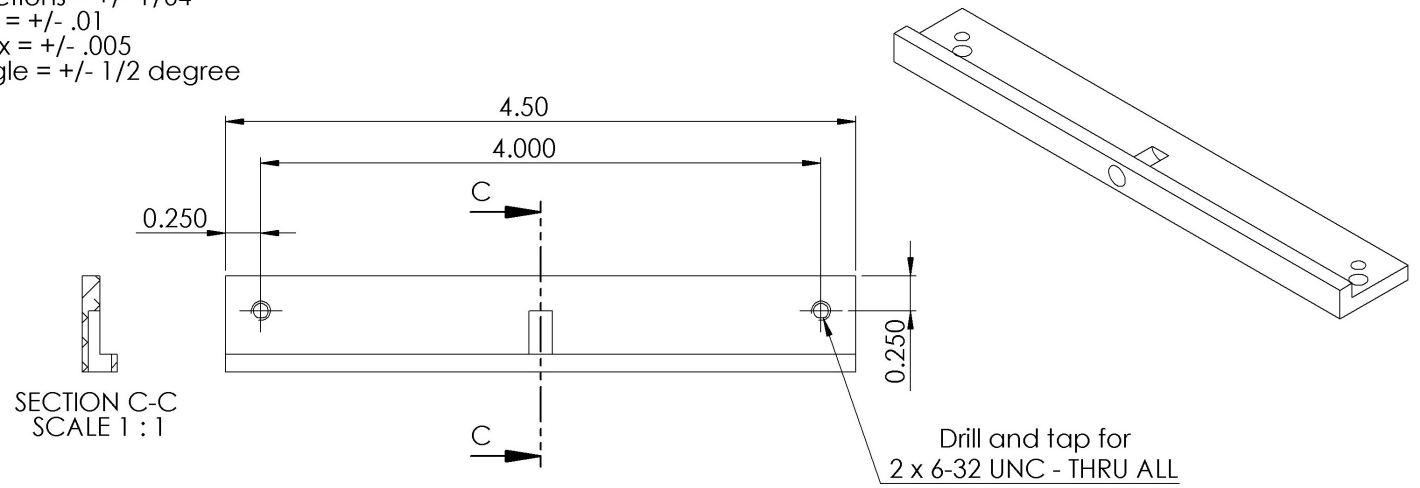

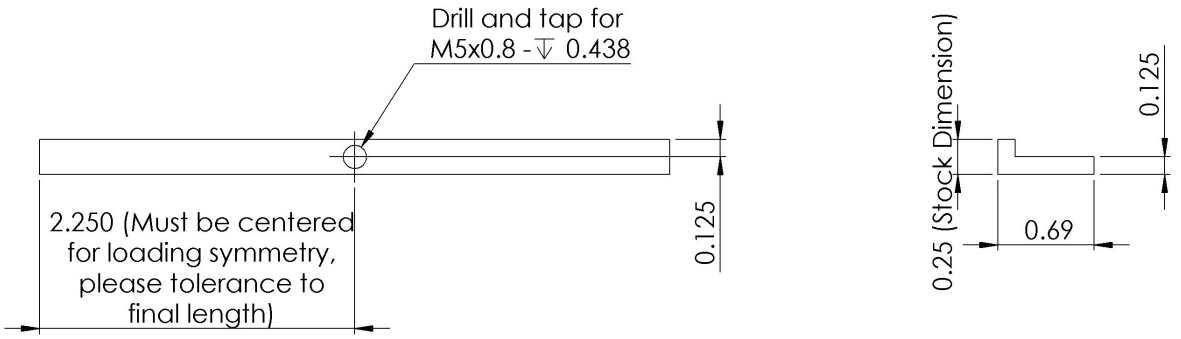

JOEL SCOTT - (902)-579-5922
MATERIAL: Aluminum 5052 - H32 Sheet
DATE: Thursday, Nov 15, 2012
SCALE 1:1, QUANTITY: 1

STATIONARY MYLAR ANCHOR - BOTTOM

Dimensions are in inches.
Toperances:
Fractions = +/- 1/64
x.xx = +/- .01
x.xxx = +/- .005
Angle = +/- 1/2 degree

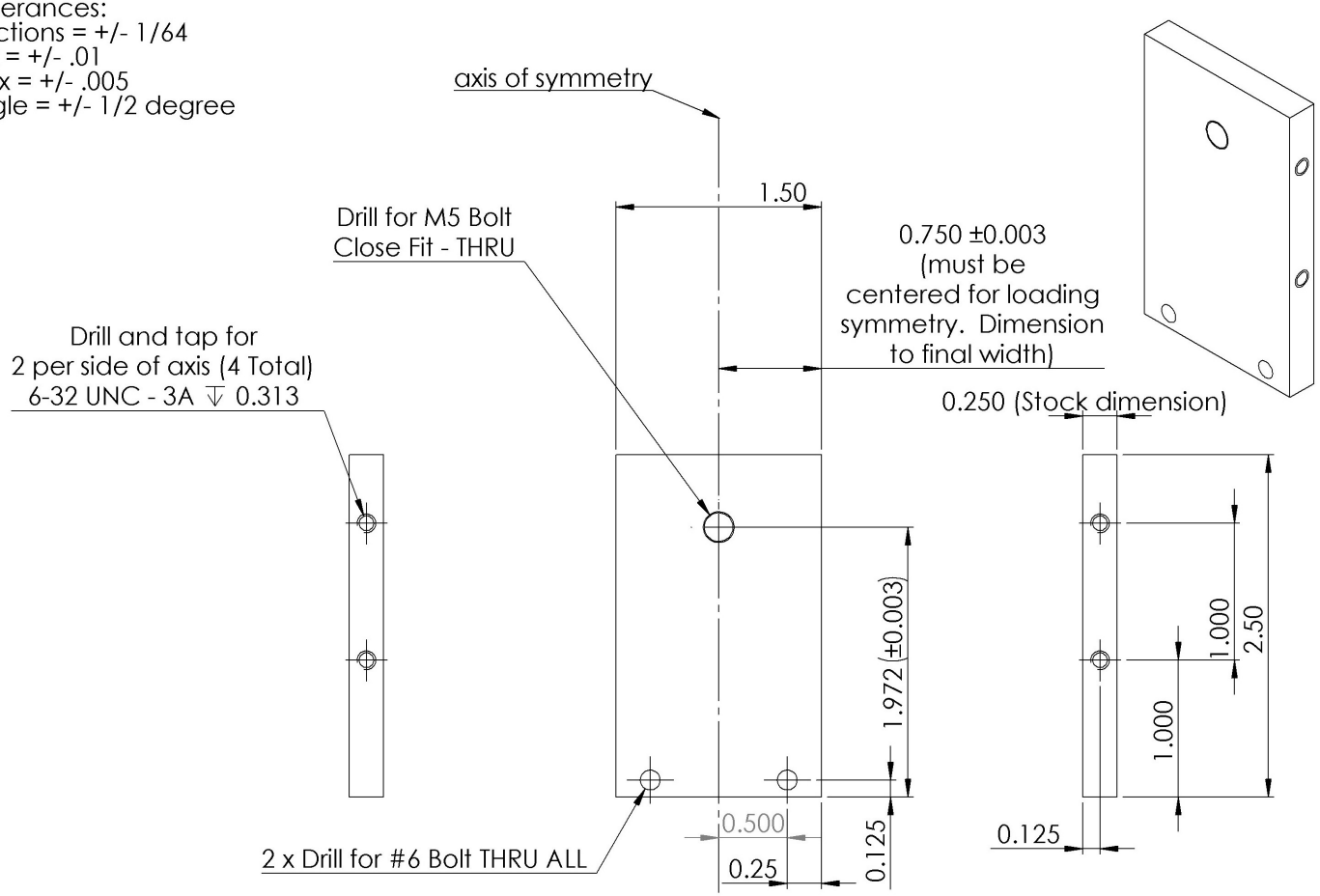

JOEL SCOTT - (902)-579-5922
MATERIAL: Aluminum 5052 - H32 (1/4" Sheet)
DATE: Thursday, Nov 15, 2012
SCALE 1:1, QUANTITY: 1

STATIONARY MOUNT - FRONT

Dimensions are in inches.
Toperances:
Fractions = +/- 1/64
x.xx = +/- .01
x.xxx = +/- .005
Angle = +/- 1/2 degree

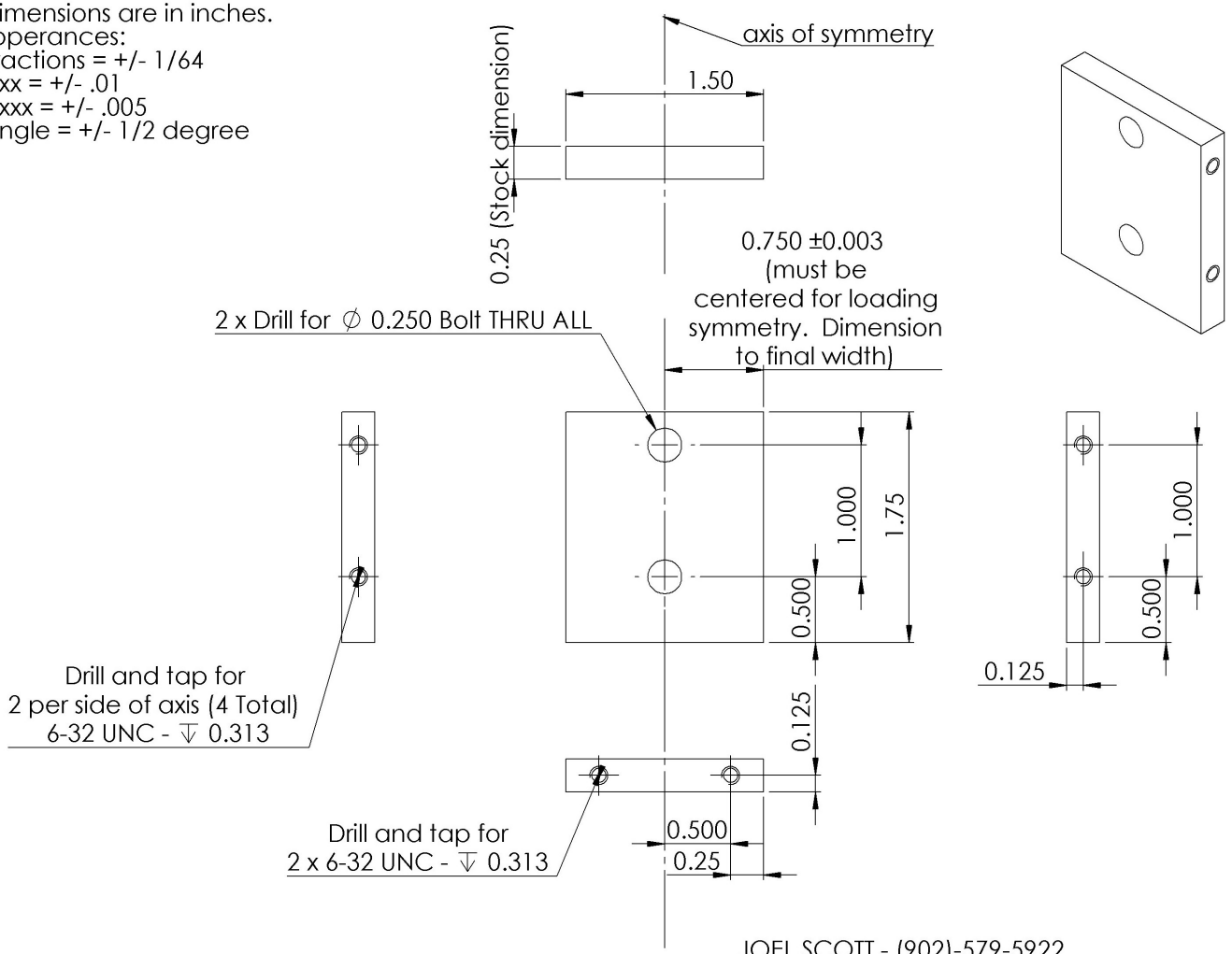

JOEL SCOTT - (902)-579-5922
MATERIAL: Aluminum 5052 - H32 (1/4" Sheet)
DATE: Thursday, Nov 15, 2012
SCALE 1:1, QUANTITY: 1

STATIONARY MOUNT - BOTTOM

Dimensions are in inches.
Toperances:
Fractions = +/- 1/64
x.xx = +/- .01
x.xxx = +/- .005
Angle = +/- 1/2 degree

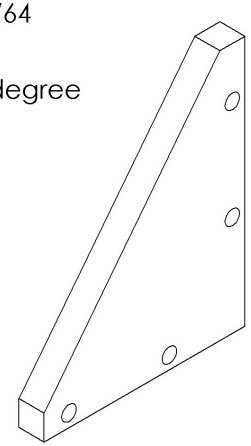

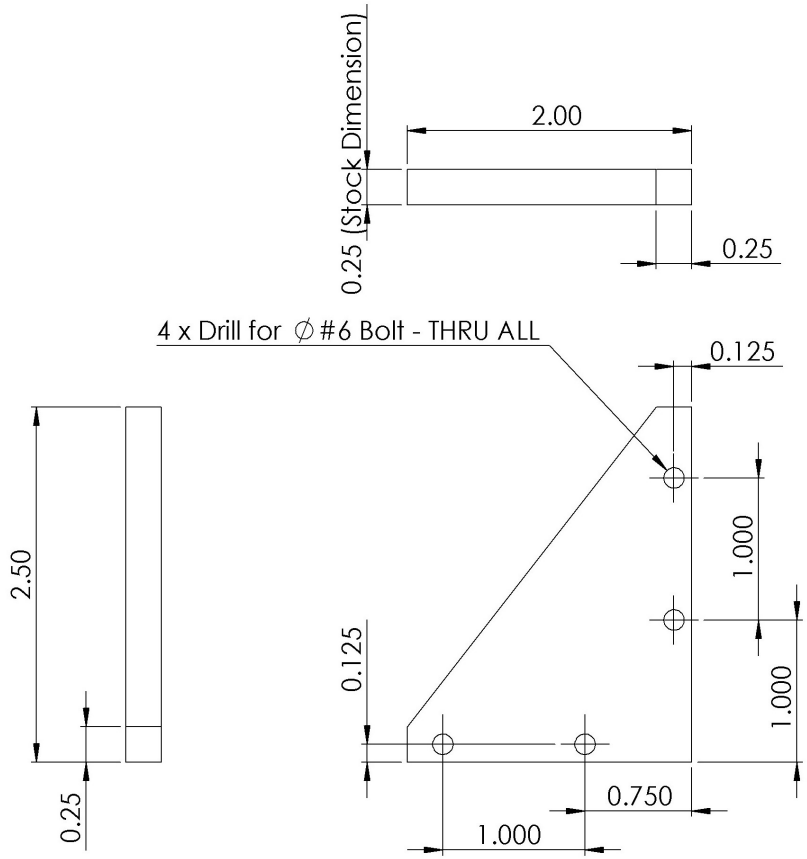

JOEL SCOTT - (902)-579-5922
MATERIAL: Aluminum 5052 - H32 (1/4" Sheet)
DATE: Thursday, Nov 15, 2012
SCALE 1:1, QUANTITY: **2**

STATIONARY MOUNT - SIDES

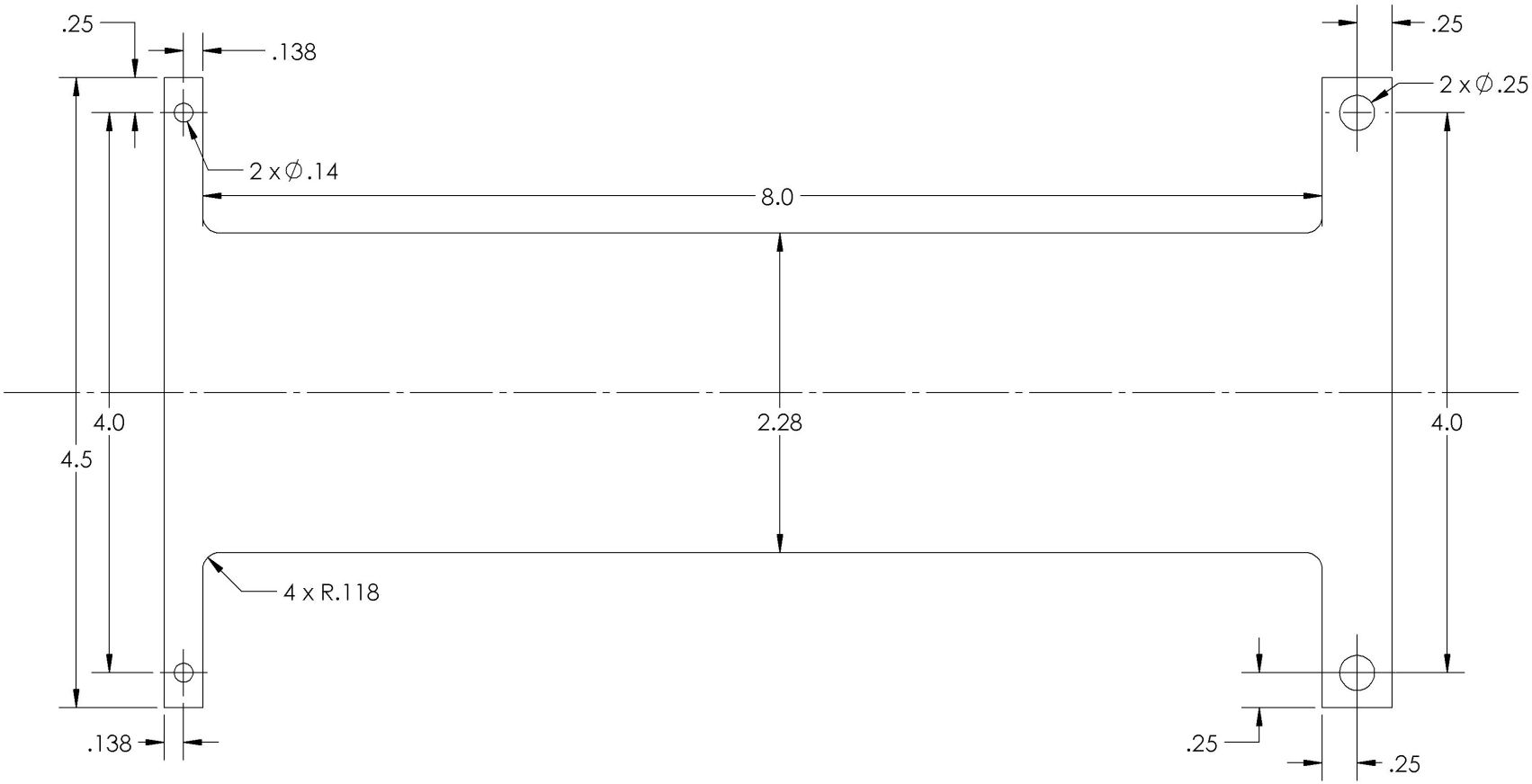

JOEL SCOTT - (902)-579-5922
MATERIAL: Clear Mylar
DATE: Thursday, Nov 15, 2012
SCALE 1:1, QUANTITY: 1
ALL DIMENSIONS ARE IN INCHES

CLEAR MYLAR - LASER CUT

Appendix E

Force Gauge Specification Sheet

O M E G A D Y N E I N C.

LOAD CELL
FINAL CALIBRATION

0.00 - 5.00 KgF
Excitation 10.000 Vdc

Job: RMLS8734 Serial: 282256
Model: LCM703-5 Tested By: CAG
Date: 9/1/2010 Temperature Range: 16 TO 72 C.
Calibrated: 0.00 - 5.00 KgF Specfile: LCM703

Force KgF	Unit Data mVdc
0.00	0.0000
2.50	11.4853
5.00	22.9277
2.50	11.4854
0.00	0.0006

Balance	0.0993	mVdc
Sensitivity	22.9277	mVdc
In Resist	400.90	Ohms
Out Resist	350.90	Ohms
59K Shunt	14.7978	mVdc

ELECTRICAL LEAKAGE: PASS

ELECTRICAL WIRING/CONNECTOR: RED = +INPUT (EXC)
BLACK = -INPUT (EXC)
GREEN = +OUTPUT
WHITE = -OUTPUT

This Calibration was performed using Instruments and Standards that are traceable to the United States National Institute of Standards Technology.

S/N	Description	Range	Reference	Cal Cert
Station 3	100lb Dead-Weights	0 - 45.35924 KgF	C-2691	C-2691
US3612530	AT34401A DMM UUT	Unit Under Test	C-2462	100038

Q.A. Representative : Ed Suchman Jr Date: 9/1/2010
This transducer is tested to & meets published specifications. After final calibration our products are stored in a controlled stock room & considered in bonded storage. Depending on environment & severity of use factory calibration is recommended every one to three years after initial service installation date.
COMMENTS: FINAL TEST IN TENSION.

Omegadyne, Inc., 149 Stelzer Court, Sunbury, OH 43074 (740) 965-9340
http://www.omegadyne.com email: info@omegadyne.com (800) USA-DYNE

Appendix F

Wire Bending Jig Drawings

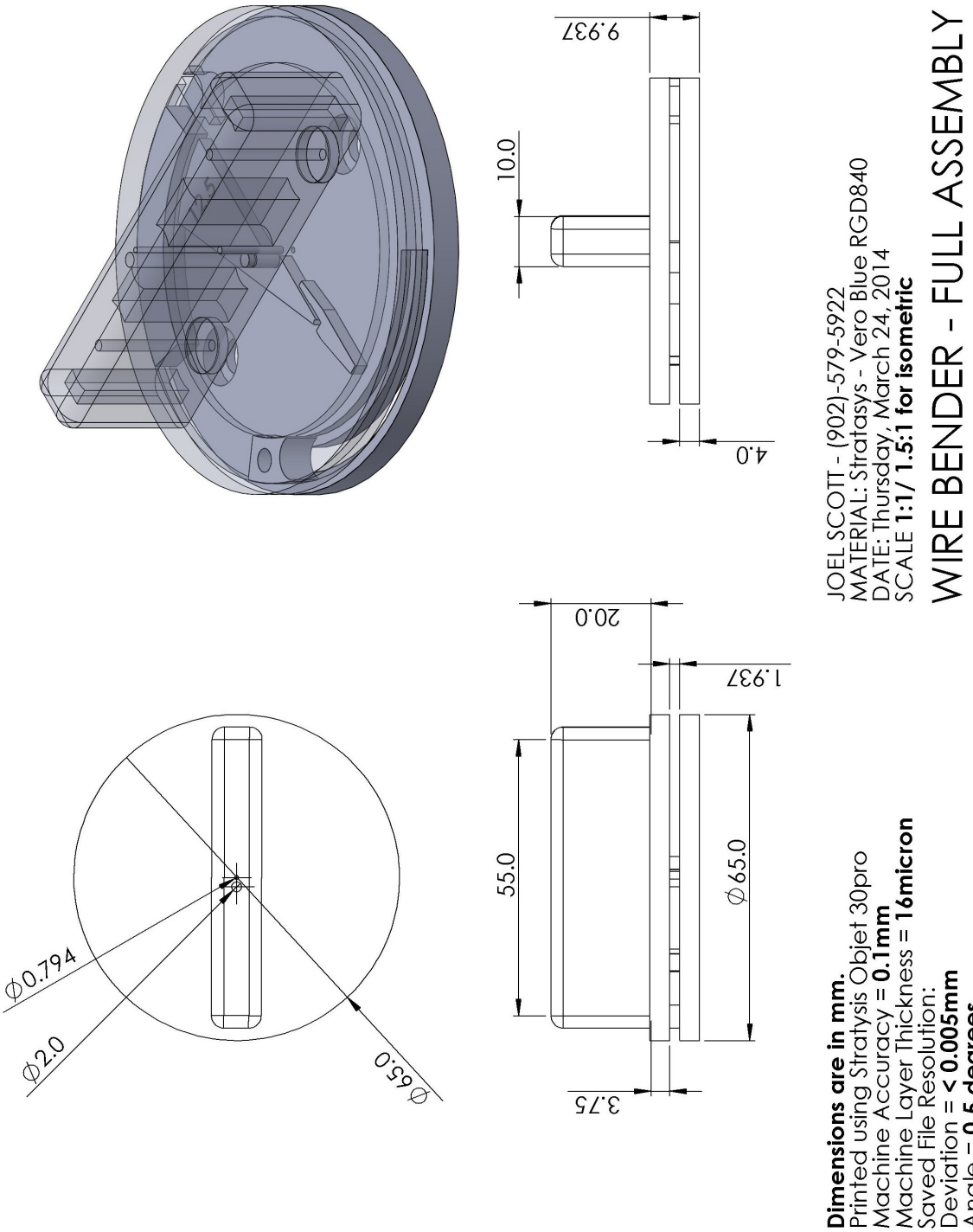

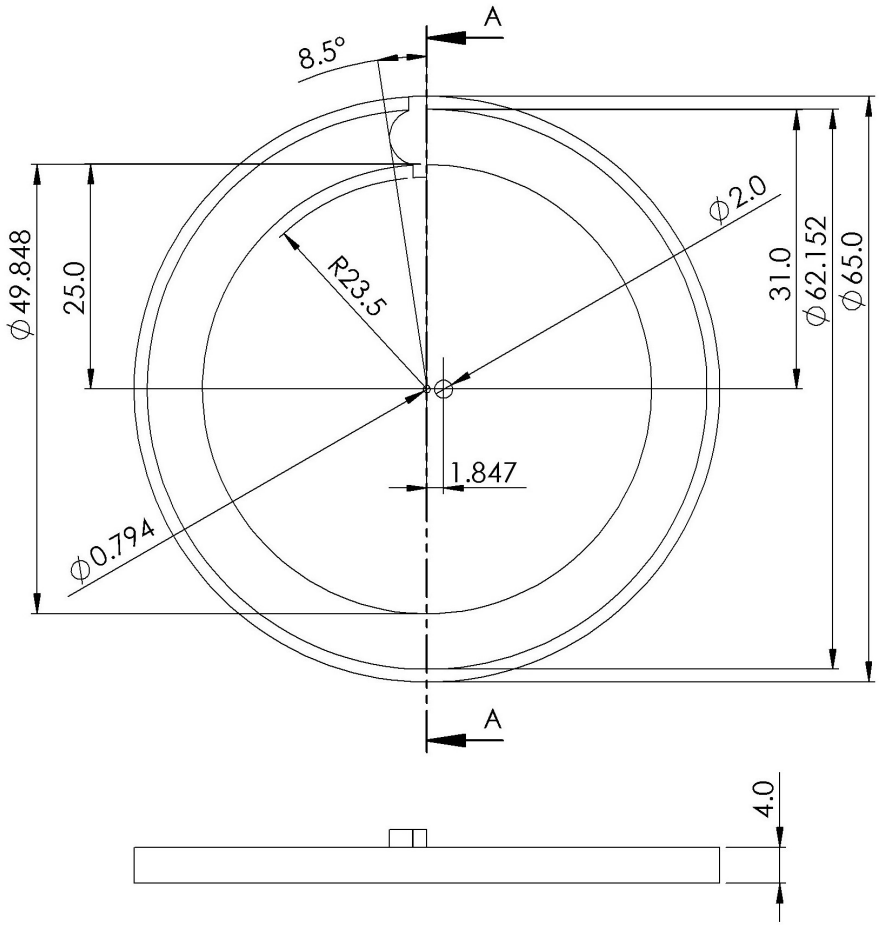

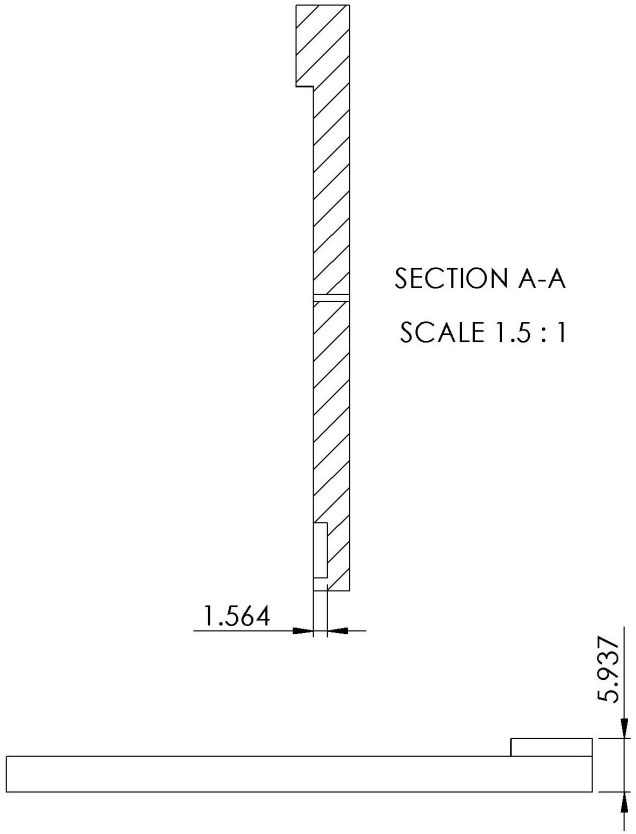

Dimensions are in mm.
Printed using Stratysis Objet 30pro
Machine Accuracy = **0.1mm**
Machine Layer Thickness = **16micron**
Saved File Resolution:
Deviation = **< 0.005mm**
Angle = **0.5 degrees**

JOEL SCOTT - (902)-579-5922
MATERIAL: Stratasys - Vero Blue RGD840
DATE: Thursday, March 24, 2014
SCALE **1.5:1**, QUANTITY: **1**

TOP DISK

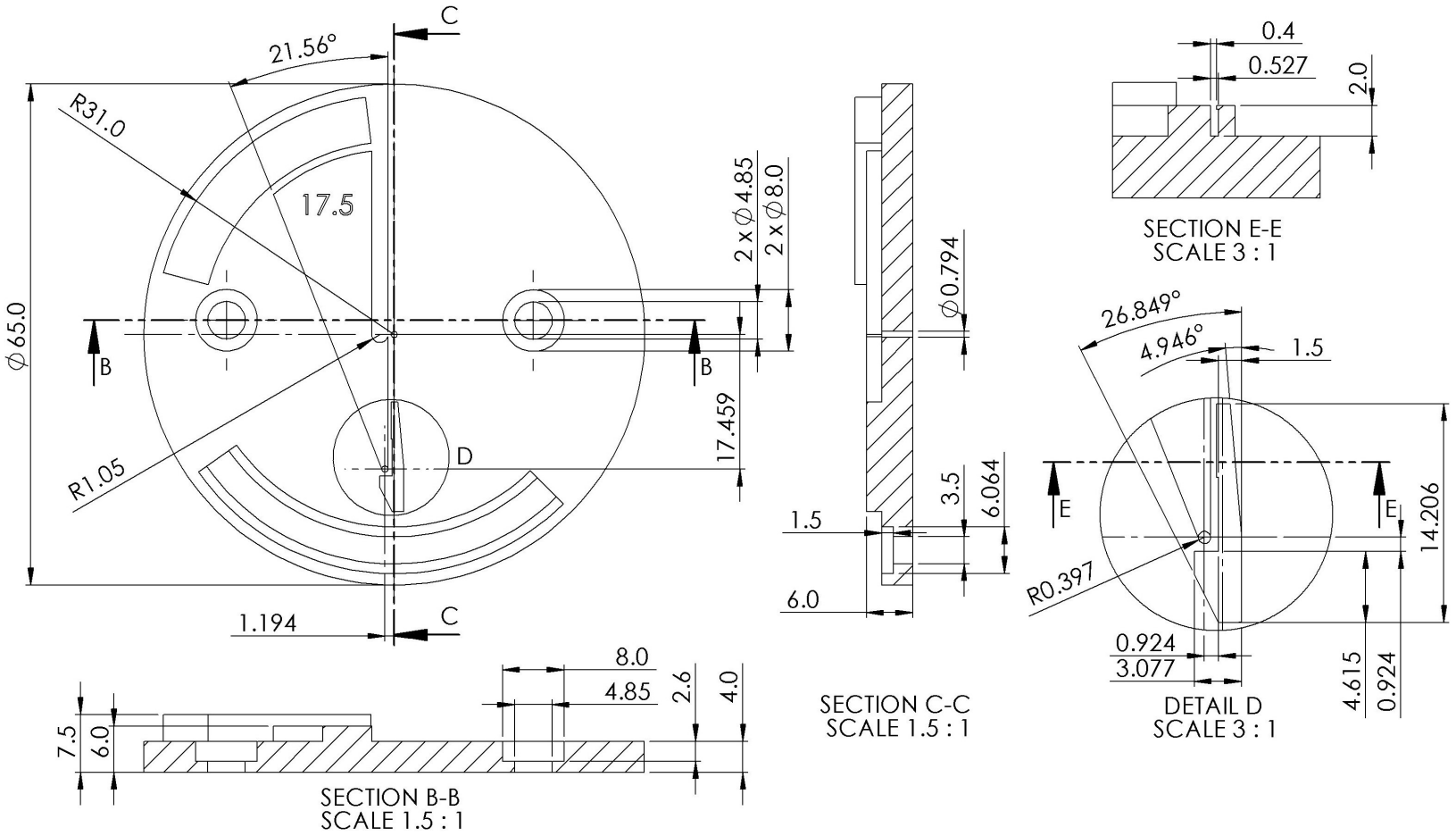

Dimensions are in mm.
Printed using Stratysis Objet 30pro
Machine Accuracy = **0.1mm**
Machine Layer Thickness = **16micron**
Saved File Resolution:
Deviation = **< 0.005mm**
Angle = **0.5 degrees**

JOEL SCOTT - (902)-579-5922
MATERIAL: Stratasys - Vero Blue RGD840
DATE: Thursday, March 24, 2014
SCALE **1.5:1**, QUANTITY: **1**

BOTTOM DISK

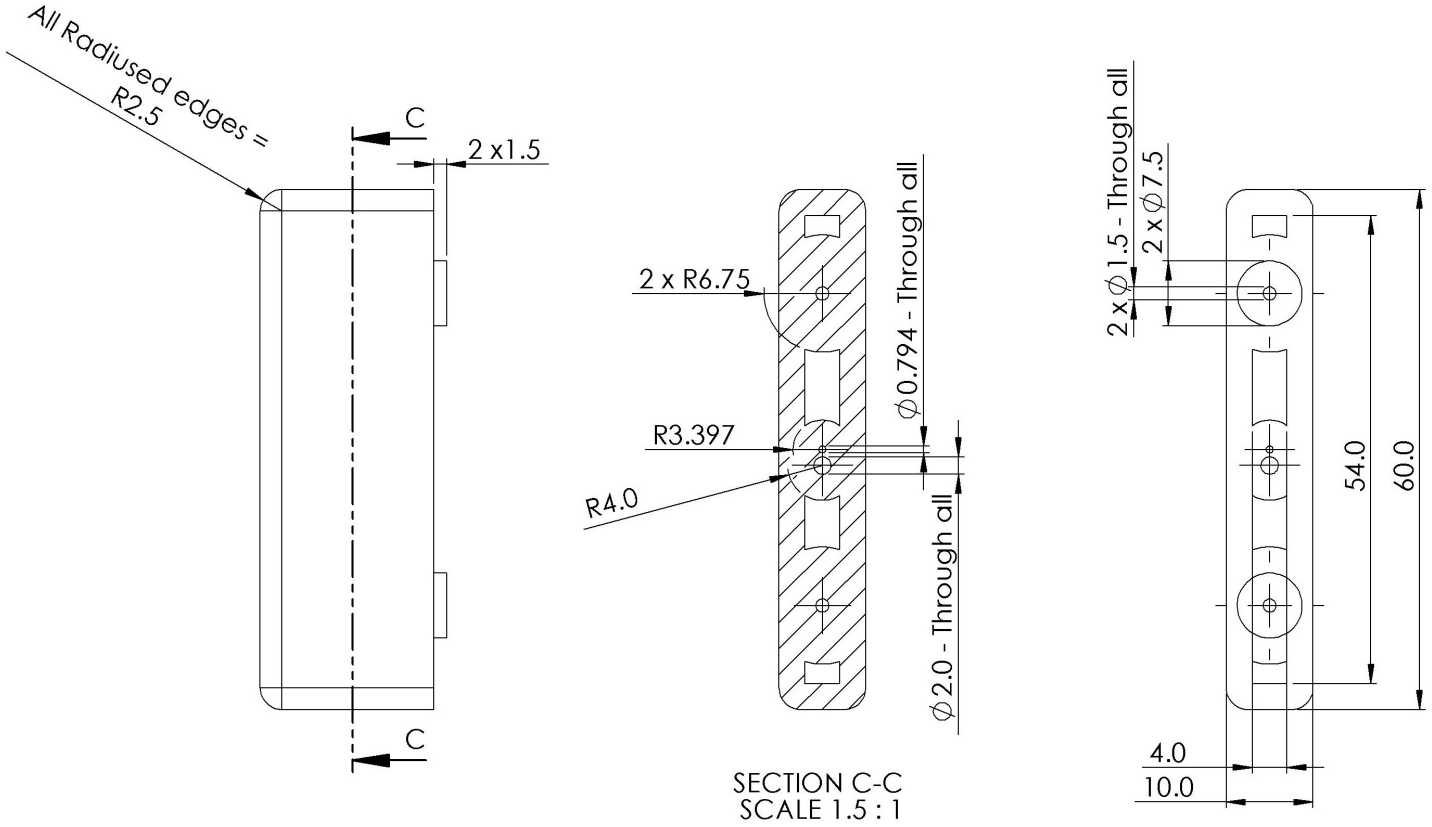

Dimensions are in mm.
Printed using Stratysis Objet 30pro
Machine Accuracy = **0.1mm**
Machine Layer Thickness = **16micron**
Saved File Resolution:
Deviation = **< 0.005mm**
Angle = **0.5 degrees**

JOEL SCOTT - (902)-579-5922
MATERIAL: Stratasys - Vero Blue RGD840
DATE: Thursday, March 24, 2014
SCALE **1.5:1**, QUANTITY: **1**

HANDLE

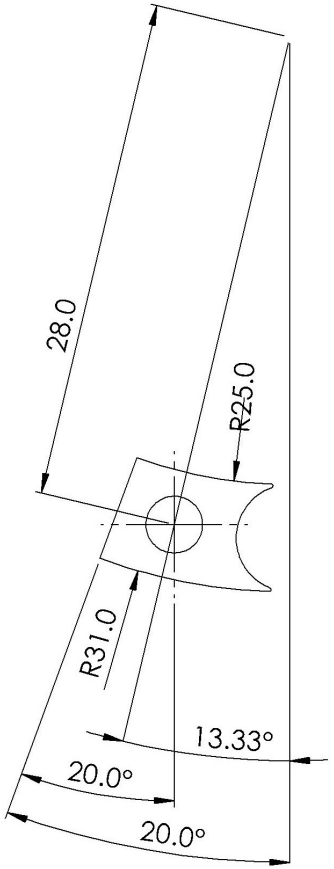

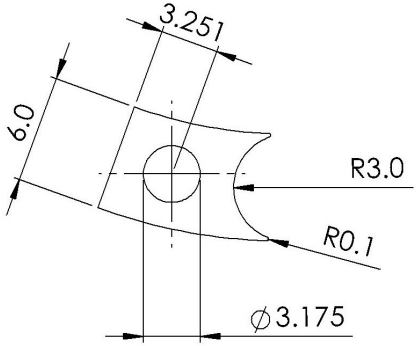

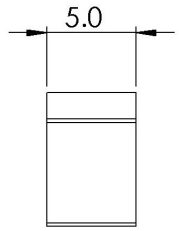

Dimensions are in mm.
Printed using Stratysis Objet 30pro
Machine Accuracy = **0.1mm**
Machine Layer Thickness = **16micron**
Saved File Resolution:
Deviation = **< 0.005mm**
Angle = **0.5 degrees**

JOEL SCOTT - (902)-579-5922
MATERIAL: Stratasys - Vero Blue RGD840
DATE: Thursday, March 24, 2014
SCALE **3:1**, QUANTITY: **1**

STOPPER PLUG

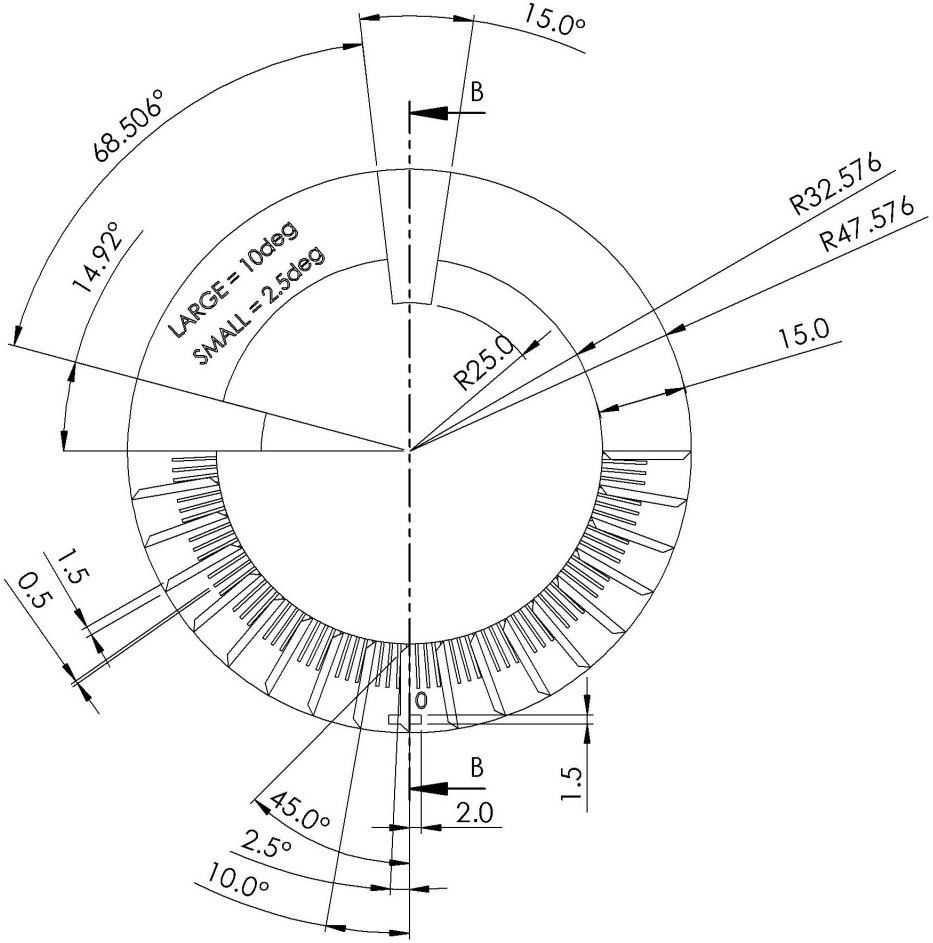

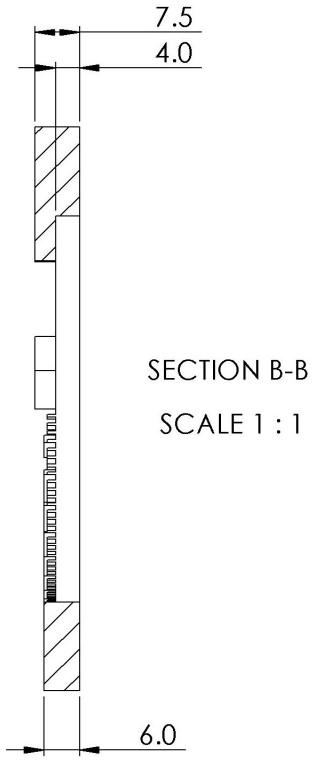

SECTION B-B

SCALE 1 : 1

Dimensions are in mm.
Printed using Stratysis Objet 30pro
Machine Accuracy = **0.1mm**
Machine Layer Thickness = **16micron**
Saved File Resolution:
Deviation = **< 0.005mm**
Angle = **0.5 degrees**

JOEL SCOTT - (902)-579-5922
MATERIAL: Stratasys - Vero Blue RGD840
DATE: Thursday, March 24, 2014
SCALE **1.5:1**, QUANTITY: **1**

ANGULAR PLACEMENT TOOL

Appendix G

Radial Force Prediction Software Code

```
# -*- coding: utf-8 -*-
"""
DALHOUSIE CONFIDENTIAL & PROPREITARY

Created on Sunday, July 19, 2015 at 11:44pm by Joel C.R. Scott.

Use in any form is restricted to JOEL SCOTT or his delegates.
"""

#load required libraries
from numpy import *
from matplotlib.pyplot import *
import matplotlib.patches as mpatches
from scipy import *
from scipy.signal import butter, filtfilt
import sympy as sym
import os, pylab, glob
import wx
from operator import sub
from matplotlib.backends.backend_wxagg import FigureCanvasWxAgg
from matplotlib.figure import Figure
from wx.lib.masked import NumCtrl
from scipy.interpolate import interp1d, griddata
from scipy.optimize import curve_fit
import math

bendrad_dict = {}
wirediam_dict = {}
bendangle_dict = {}
leglength_dict = {}
labcomp_dict= {}

##############################################################################
#                                    INPUT
##############################################################################
# DATA ORIENTATION INPUTS
xax = 5 #x-axis column number from data file
yax = 3 #y-axis column number from data file
poscolumn = 1 #position column to find fully constricted point
OAcolumn = 5 #Original Area Column
timecol = 0 #Time column
forcecol = 3 #Force column

#
```

```
# FILE SIZE ADJUSTMENT INPUTS
match_filesize_from_front = 'no'
match_filesize_from_end = 'yes' #add zeros to the beginning,
                                #after lining up all end values.

#
# TYPE OF PLOT INPUTS


xintegration = 1 #time per step for plotting area under
plotareaunder = 'no' #plot single points showing the area under the force curve

expansion_only = 'yes'  #plot only data during expansion
offset_to_covered = 'no' # Offset plot for uncovered stents so they line up with
                         # the %OA values for a covered stent
                         # Offset can only be done with the expansion only case.
points_plot = 'no' #show a reduced points plot
points_to_show = [20,50,75] #%Area points of interes
pt_average_size = 500 #number of readings to be averaged around areas of interest
original_and_points = 'no'
consistent_colours = 'yes'


curve_fitting = 'no'  #THIS NEEDS TO BE YES FOR CURVE FITTING AND OFF OTHERWISE
fittype = "polynomial" #exponential or polynomial
fitting_degree = 3
fitting_degree_2D = 2
fit_curve_resolution = 225
plot_fit_with_original = 'no' #THIS NEEDS TO BE YES FOR CURVE FITTING ONLY
keep_scatter_plot_with_fit  = 'yes'
put_fit_on_plot = 'no'
xstart = 1
ystart = 2
y_spacing_multiple = 0.25
text_size = 8

#
# FILTERING INPUTS
filterbefore = 'no'  #filter data before or after interpolating and averaging data.
                     #no = after
butterworthvert = 'yes' #lowpass filter data
filterHZvert = 20  #lowpass filter frequency

#
# STENT INPUTS
covered_orig_diam = 14.59
uncovered_orig_diam = 24.02
SA_Stent = 348.49 #Taken from SolidWorks

#
#Simulation inputs
simulate_curve = 'no'
use_saved_input = 'yes'
```

```
98
99  upper_oversize = 1.2
100 lower_oversize = 1.1
101
102 #no longer used
103 high_line = 30.6
104 low_line = 17.3
105 #min_safe_pressure =
106 min_safe_force = 0.6
107 #max_safe_pressure =
108 max_safe_force = 0.8
109
110
111 Points_Per_Percent_initial = 992. #for full
112 Points_Per_Percent_second = 992. #full line plotted on full curve
113 #
114 # PLOT INPUTS
115 tight_plot_border = 'no'
116 show_legend_title = 'no'
117 title_plot = 'yes'
118
119 x_axis_limits = 'no'
120 xlow = 10
121 xhigh = 30
122 y_axis_limits = 'no'
123 ylow = 0
124 yhigh = 0
125
126 save_file = 'no'
127 ###############################################################################
128 #                                  PRESETS
129 ###############################################################################
130
131 #FILES MUST BE ORDERED FROM SMALLEST TO LARGEST OF THE INDEPENDANT VARIABLE
132 #Create a matrix containing all the file names in a directory
133 wirediam_dict = {'loadfiles_trial0': glob.glob('*labmade*.txt'),#3
134                  'loadfiles_trial1': glob.glob('+diam*.txt'),
135                  'loadfiles_trial2': glob.glob('++diam*.txt')}
136
137 leglength_dict = {'loadfiles_trial0': glob.glob('-leg length*.txt'),#3
138                   'loadfiles_trial1': glob.glob('*labmade*.txt'),
139                   'loadfiles_trial2': glob.glob('+leg length*.txt')}
140
141 bendangle_dict = {'loadfiles_trial0': glob.glob('-bend angle*.txt'),#3
142                   'loadfiles_trial1': glob.glob('*labmade*.txt'),
143                   'loadfiles_trial2': glob.glob('+bend angle*.txt')}
144
145 bendrad_dict = {'loadfiles_trial0': glob.glob('*labmade*.txt'),#3
146                 'loadfiles_trial1': glob.glob('+bendrad*.txt'),
147                 'loadfiles_trial2': glob.glob('++bendrad*.txt')}
148
149 labcomp_dict = {'loadfiles_trial0': glob.glob('*labmade*.txt'),#3
150                 'loadfiles_trial1': glob.glob('*Industry*.txt'),#3
```

```
151                 'loadfiles_trial2': glob.glob('*covered*.txt')}
152
153 labonly_dict = {'loadfiles_trial0': glob.glob('*labmade*.txt')}#3
154
155 def plottype(Graph_type):
156     #Plot characteristics
157     if Graph_type == bendrad_dict:
158         legendtitle = "Bend Radius"
159         legendnames = ['14mm','+bend rad','++bend rad']
160
161         xaxislabel = "Percent Reduction in Cross Sectional Area (%)"
162         yaxislabel = "Force (N)"
163         plottitle = "Effect of Altered Bend Radius on Radial Force Profile"
164         plotnumber = 3 #number of files to be plotted
165
166     if Graph_type == wirediam_dict:
167         legendtitle = "Wire Diameter"
168         legendnames = ['14mm','+diam','++diam']
169
170         xaxislabel = "Percent Reduction in Cross Sectional Area (%)"
171         yaxislabel = "Force (N)"
172         plottitle = "Effect of Altered Wire Diameter on Radial Force Profile"
173         plotnumber = 3 #number of files to be plotted
174
175     if Graph_type == bendangle_dict:
176         legendtitle = "Bend Angle"
177         legendnames = ['-bend angle','14mm','+bend angle']
178
179         xaxislabel = "Percent Reduction in Cross Sectional Area (%)"
180         yaxislabel = "Force (N)"
181         plottitle = "Effect of Altered Bend Angle on Radial Force Profile"
182         plotnumber = 3 #number of files to be plotted
183
184     if Graph_type == leglength_dict:
185         legendtitle = "Leg Length"
186         legendnames = ['-leg length','14mm','+leg length']
187
188         xaxislabel = "Percent Reduction in Cross Sectional Area (%)"
189         yaxislabel = "Force (N)"
190         plottitle = "Effect of Altered Leg Length on Radial Force Profile"
191         plotnumber = 3 #number of files to be plotted
192
193     if Graph_type == labcomp_dict:
194         legendtitle = "Cubic fit covered"
195         legendnames = ['Lab made','industry made','covered']
196
197         xaxislabel = "Percent Reduction in Cross Sectional Area (%)"
198         yaxislabel = "Force (N)"
199         plottitle = "Curve Fit (^3): Lab, Industry and covered 14mm Stents"
200         plotnumber = 3 #number of files to be plotted
201
202     if Graph_type == labonly_dict:
203         legendtitle = "Lab Only"
```

```
204         legendnames = ['Lab made']
205
206         xaxislabel = "Percent Reduction in Cross Sectional Area (%)"
207         yaxislabel = "Force (N)"
208         plottitle = "14mm Stent: Lab Data"
209         plotnumber = 1 #number of files to be plotted
210
211     return (legendtitle,legendnames,xaxislabel,yaxislabel,plottitle,plotnumber)
212
213 def orig_type(Graph_type):
214     if Graph_type == bendrad_dict:
215         orig_diams = [24.02, 24.53,24.38 ]
216     if Graph_type == wirediam_dict:
217         orig_diams = [24.02, 24.2772,24.47 ]
218     if Graph_type == bendangle_dict:
219         orig_diams = [17.96 ,24.02, 26.76]
220     if Graph_type == leglength_dict:
221         orig_diams = [19.7,24.02, 25.47]
222     if Graph_type == labonly_dict:
223         orig_diams = [24.02]
224     return orig_diams
225 ###############################################################################
226 #                                   BODY
227 ###############################################################################
228
229 #load the data file and all of its components
230 plothoriz = []
231 plothoriztemp = []
232 plotvert = []
233 plotverttemp = []
234 temphoriz = []
235 tempvert = []
236 area = []
237 fitline = []
238
239 figure(num=None, figsize=(6, 5.8), dpi=100, facecolor='w', edgecolor='k')
240
241 dict2 = {}
242 shapes = ['o','^','s','D','v','p','d','h','+','x','*','2','o','^','s','D','v',
243           'p','d','h','+','x','*','2']
244 colors = ['b','g','r','c','m','y','k']
245
246 vertical = []
247 horizontal = []
248 temp_pos_change = []
249 temp_horiz = []
250 iteration_size = []
251 current_temp = []
252
253 def movingaverage(interval, window_size):
254     window= ones(int(window_size))/float(window_size)
255     return convolve(interval, window, 'same')
256
```

```
257 def fit_the_curve(horiz,vert,fitdeg):
258     tempfit = polyfit(horiz,vert,fitdeg)  #calculate polynomial
259     return poly1d(tempfit)
260 
261 def fit_the_curve2D(stent_char_input,stent_char,vert,fitting_degree_2D):
262     vert_for_z = [list(x) for x in zip(*vert)]
263     poly_coeffs = [polyfit(stent_char,vert_for_z[i],fitting_degree_2D) for i in
264     range(len(vert_for_z))]
265     poly_functions = [poly1d(poly_coeffs[i])(stent_char_input) for i in
266     range(len(poly_coeffs))]
267     return poly_functions
268 
269 def data_manipulation(temp, j, orig_diams):
270     summed_vert_second = []
271     timecollongest = []
272     xolongestsecond = []
273     xomaxsecond = 0.
274     indexval1 = 0.
275 
276     for i in range(len(temp)):
277         #load all files with similar filenames temp in an array and average them
278         print "Filename #{}: {}".format((i+1),temp[i])
279         current_temp = loadtxt(temp[i], skiprows=1)
280 
281         current_vert = current_temp[(len(current_temp)/2)::,forcecol]
282         current_horiz = current_temp[(len(current_temp)/2)::,OAcolumn]
283 
284         Sampling_Rate = len(current_temp[::,forcecol])/amax(current_temp[::,
285 timecol])
286         Sampling_Rate2 = len(current_temp[::,OAcolumn])/amax(current_temp[::,
287 timecol])
288 
289         if len(current_temp[::,timecol]) > len(timecollongest):
290             timecollongest = current_temp[::,timecol]
291 
292         current_horiz = 100 - current_horiz
293         if filterbefore == 'yes':
294             if butterworthvert == 'yes':
295                 nyq=Sampling_Rate/2.0
296                 b,a=butter(3,filterHZvert/nyq,'low')
297                 filtered_data=filtfilt(b,a,current_vert)
298                 current_vert = filtered_data
299 
300             if butterworthhoriz == 'yes':
301                 nyq=Sampling_Rate2
302                 b,a=butter(3,filterHZhoriz/nyq,'low')
303                 filtered_data_horiz=filtfilt(b,a,current_horiz)
304                 current_horiz = filtered_data_horiz
305 
306             if movingfiltervert == 'yes':
307                 current_vert = movingaverage(current_vert, movingavgvert)
308 
309             if movingfilterhoriz == 'yes':
```

```
310                 current_horiz = movingaverage(current_horiz, movingavghoriz)
311
312         current_horiz = current_horiz[::-1]
313         current_vert = current_vert[::-1]
314
315         #to get full line plotted on full curve
316         xo_second = linspace(0.0,floor(max(current_horiz)),
317                              floor(floor(max(current_horiz))
318                              *Points_Per_Percent_second))
319
320         if len(xo_second) > len(xolongestsecond):
321             xolongestsecond = xo_second
322         if max(xo_second) > xomaxsecond:
323             xomaxsecond = max(xo_second)
324
325         yo = griddata(current_horiz,current_vert, xo_second, method='linear',
326                       fill_value= 0.0)
327         indexval = min(range(len(xo_second)),
328                        key=lambda k: abs(xo_second[k]-70.0))
329         if indexval > indexval1:
330             indexval1 = indexval
331
332         if len(summed_vert_second) == 0:
333                 summed_vert_second.append(yo)
334
335                 summed_vert_second = array(summed_vert_second)
336         else:
337             if len(yo) >= len(summed_vert_second[i-1]):
338                 shapetemp = shape(summed_vert_second)
339                 shapetempx = shapetemp[0]+1
340                 shapetempy = len(yo)
341                 summed_vert_temp = zeros((shapetempx, shapetempy))
342                 summed_vert_temp[:(shapetemp[0]),
343                                  :shapetemp[1]] = summed_vert_second
344                 summed_vert_temp[shapetemp[0]] = yo
345                 summed_vert_second = summed_vert_temp
346             else:
347                 shapetemp = shape(summed_vert_second)
348                 yo = array(yo)
349                 yo.resize(len(summed_vert_second[i-1]))
350                 shapetempx = shapetemp[0]+1
351                 shapetempy = shapetemp[1]
352                 summed_vert_temp = zeros((shapetempx, shapetempy))
353                 summed_vert_temp[:shapetemp[0],
354                                  :shapetemp[1]] = summed_vert_second
355                 summed_vert_temp[shapetemp[0]] = yo
356                 summed_vert_second = summed_vert_temp
357
358     averaged_vert_second = []
359     yerror = []
360
361     sumtempsecond = zip(*summed_vert_second)
362
```

```
363     for i in range(len(sumtempsecond)):
364         if sum(sumtempsecond[i]) == 0:
365             yerror.append(std(sumtemp[i], axis = 0))
366             averaged_vert_second.append(mean(sumtempsecond[i], axis=0))
367         else:
368             current_average = average(sumtempsecond[i], axis=0,
369                                       weights=array(sumtempsecond[i])
370                                       .astype(bool))
371             averaged_vert_second.append(current_average)
372             var = (sumtempsecond[i]-current_average)**2
373             yerror.append(sqrt(average(var, axis=0,
374                                        weights=array(sumtempsecond[i])
375                                        .astype(bool))))
376 
377     #Include a fitline based on the _inal dataset
378     fulldatax = xolongestsecond
379 
380     fulldatay = averaged_vert_second
381 
382     Sampling_Rate = len(fulldatax)/amax(timecollongest)
383 
384     if filterbefore != 'yes':
385         if butterworthvert == 'yes':
386             nyq=Sampling_Rate/2.0
387             b,a=butter(3,filterHZvert/nyq,'low')
388             filtered_data=filtfilt(b,a,fulldatay)
389             fulldatay = filtered_data
390 
391     if curve_fitting == 'yes':
392         if fittype == "polynomial":
393             tempfit = polyfit(fulldatax,fulldatay,fitting_degree)
394             #calculate polynomial
395             f = poly1d(tempfit)
396 
397         if fittype == "exponential":
398             testx = [x for x in fulldatax]
399             testx = array(testx)
400             testy = [x*10**6 for x in fulldatay]
401             popt, pcov = curve_fit(func, fulldatax, testy, maxfev = 10000)
402             popt = [x for x in popt]
403 
404         if fittype == "exponential":
405             print(popt)
406         if fittype == "polynomial":
407             print(f)
408         if fittype == "polynomial":
409             fitline = f(fulldatax)  #calculate new x's and y's
410         if fittype == "exponential":
411             fitline = func(testx, *popt)
412             fitline = [x/10**6 for x in fitline]
413         fulldatay = fitline
414 
415     return (fulldatax, fulldatay)
```

```
416
417 def supershape(lo_horiz, lo_vert, wd_vert, ll_vert, ba_vert,
418                br_vert,m, n1, n2, n3):
419     number_of_characteristics = 5
420     characteristic_dict = {'factor0': wd_vert,
421                     'factor1': ll_vert,
422                     'factor2': ba_vert,
423                     'factor3': br_vert,
424                     'factor4': lo_vert}
425
426     xo_second = linspace(0.,50.0,fit_curve_resolution+1)
427
428     for i in range(number_of_characteristics):
429         Graph_Type = factors_dict['factor'+str(i)]
430
431         temparray = []
432         for j in range(len(orig_type(Graph_Type))):
433
434             orig_diams = orig_type(Graph_Type)
435             print(orig_diams)
436             temp = characteristic_dict['factor'+str(i)]
437
438             lo_horiz = array(lo_horiz)
439             temp_horiz = 100*(1-((((pi*covered_orig_diam)-(pi*covered_orig_diam-2*
440             sqrt(abs((100-100-(100-lo_horiz))/100.)*(pi*orig_diams[j]/2)
441             **2)))/(pi*covered_orig_diam))**2))
442
443             if i == 4:
444                 temparray = griddata(temp_horiz,temp[::-1],xo_second,
445                                      method='linear',
446                                      fill_value= 0.0)
447                 print(min(temparray), max(temparray), max(temp), '5')
448
449             else:
450                 print(all(np.diff(temp_horiz)>0), all(np.diff(temp[j])>0),
451                       all(np.diff(xo_second)>0), all(np.diff(lo_horiz)>0))
452                 f = interp1d(temp_horiz,temp[j])
453                 temparray.append(f(xo_second))
454                 print(min(temparray[j]), max(temparray[j]), max(temp[j]), '5')
455
456         characteristic_dict['factor'+str(i)] = temparray
457
458     print(m, n1, n2, n3, wd_factor_values, ll_factor_values,
459           ba_factor_values, br_factor_values)
460     wd_force = fit_the_curve2D(m,wd_factor_values,
461                                characteristic_dict['factor'+str(0)],
462                                                fitting_degree_2D)
463     print(min(wd_force), max(wd_force), 'q')
464     ll_force = fit_the_curve2D(n1,ll_factor_values,
465                                characteristic_dict['factor'+str(1)],
466                                                fitting_degree_2D)
467     ba_force = fit_the_curve2D(n2,ba_factor_values,
468                                characteristic_dict['factor'+str(2)],
```

```
                                                    fitting_degree_2D)
    br_force = fit_the_curve2D(n3,br_factor_values,
                               characteristic_dict['factor'+str(3)],
                                                    fitting_degree_2D)
    lo_vert = characteristic_dict['factor'+str(4)]

    wd_effect = transpose([a - b for a, b in zip(wd_force, lo_vert)])
    ll_effect = transpose([a - b for a, b in zip(ll_force, lo_vert)])
    ba_effect = transpose([a - b for a, b in zip(ba_force, lo_vert)])
    br_effect = transpose([a - b for a, b in zip(br_force, lo_vert)])
    print(max(wd_effect),max(ll_effect),max(ba_effect),max(br_effect),'2')

    simulated_vert = transpose([a + b + c + d + e for
    a, b, c, d, e in zip(lo_vert, wd_effect, ll_effect, ba_effect, br_effect)])
    print(min(simulated_vert), max(simulated_vert), 'sim')

    return simulated_vert

def maxmin_plot_lines():
    Final_D_Covered_H = sqrt(((pi*(covered_orig_diam/2)**2)*
    ((100-high_line)/100))/pi)*2
    High = 100-100*((pi*(Final_D_Covered_H/2)**2)/
    (pi*(uncovered_orig_diam/2)**2))

    Final_D_Covered_L = sqrt(((pi*(covered_orig_diam/2)**2)*
    ((100-low_line)/100))/pi)*2
    Low = 100-100*((pi*(Final_D_Covered_L/2)**2)/(pi*
    (uncovered_orig_diam/2)**2))

    Final_D_Covered_Zero = sqrt(((pi*(covered_orig_diam/2)**2)*
    ((100-0.0)/100))/pi)*2
    Zero = 100-100*((pi*(Final_D_Covered_Zero/2)**2)/(pi*
    (uncovered_orig_diam/2)**2))

    return Low, High, Zero

def mark_for_artery(n4):
    Mark = 100-100*((pi*(n4/2)**2)/(pi*(covered_orig_diam/2)**2))

    return Mark

def compliance_for_artery(Mark, yvalue, n5):
    Pressure = yvalue/(SA_Stent/2)*7500.61561303 #to mmHg
    Compliance_Area_Change = n5*Pressure #to cross sectional area change

    Original_Area = pi*(covered_orig_diam/2)**2
    area_change = Compliance_Area_Change/Original_Area*100

    return Mark-area_change

def rebuild_axes_for_covered(lo_horiz):
    newx = lo_horiz

```

```
522     return newx
523
524 class SuperShapeFrame(wx.Frame):
525     def __init__(self, parent, id, title):
526         wx.Frame.__init__(self, parent, id, title,
527                           style = wx.DEFAULT_FRAME_STYLE ^ wx.RESIZE_BORDER,
528                           size = (650, 775))
529
530         self.m = 0.4
531         self.n1 = 15.32
532         self.n2 = 28.70
533         self.n3 = 0.3975
534         self.n4 = covered_orig_diam
535         self.n5 = 0.0
536
537         self.fig = Figure((6, 6), dpi = 100, facecolor='white',
538                           edgecolor='white')
539
540         panel = wx.Panel(self, -1)
541
542         self.blank = wx.StaticText(panel, label = "")
543         self.blank2 = wx.StaticText(panel, label = "")
544         self.blank3 = wx.StaticText(panel, label = "")
545
546         self.m_label = wx.StaticText(panel, label = "Stent Wire Diameter (mm): ")
547         self.m_text = wx.lib.masked.NumCtrl(panel, -1, self.m, size = (150, -1),
548                                             fractionWidth = 3)
549
550         self.n1_label = wx.StaticText(panel, label = "Stent Leg Length (mm): ")
551         self.n1_text = NumCtrl(panel, -1, self.n1, size = (150, -1),
552                                fractionWidth = 4)
553
554         self.n2_label = wx.StaticText(panel, label = "Stent Bend Angle (deg): ")
555         self.n2_text = NumCtrl(panel, -1, self.n2, size = (150, -1),
556                                fractionWidth = 3)
557
558         self.n3_label = wx.StaticText(panel, label = "Stent Bend Radius (mm): ")
559         self.n3_text = NumCtrl(panel, -1, self.n3, size = (150, -1),
560                                fractionWidth = 4)
561
562         self.n4_label = wx.StaticText(panel, label = "Artery Outer Diam (<{}mm): "
563         .format(covered_orig_diam))
564         self.n4_text = NumCtrl(panel, -1, self.n4, size = (150, -1),
565                                fractionWidth = 3)
566
567         self.n5_label = wx.StaticText(panel, label = "Compliance (mm^2/mmHg): ")
568         self.n5_text = NumCtrl(panel, -1, self.n5, size = (150, -1),
569                                fractionWidth = 4)
570
571         self.button = wx.Button(panel, label="PLOT")
572
573         self.button.Bind(wx.EVT_BUTTON, self.OnButton)
574
```

```
575         sizerv = wx.BoxSizer(wx.VERTICAL)
576         sizerv.Add(FigureCanvasWxAgg(panel, -1, self.fig), 0, wx.TOP | wx.EXPAND)
577 
578         hbox = wx.BoxSizer(wx.HORIZONTAL)
579         fgs = wx.FlexGridSizer(3, 5, 9, 15)
580         fgs.AddMany([(self.m_label), (self.m_text, 1, wx.EXPAND), (self.blank),
581                      (self.n1_label), (self.n1_text, 1, wx.EXPAND),
582                      (self.n2_label), (self.n2_text, 1, wx.EXPAND), (self.blank2),
583                      (self.n3_label), (self.n3_text, 1, wx.EXPAND),
584                      (self.n4_label), (self.n4_text, 1, wx.EXPAND), (self.blank3),
585                      (self.n5_label), (self.n5_text, 1, wx.EXPAND),])
586         hbox.Add(fgs, proportion=
587         1, flag=wx.EXPAND|wx.ALIGN_CENTER|wx.RIGHT|wx.LEFT|wx.TOP, border=10)
588         sizerv.Add(hbox)
589 
590         sizerh3 = wx.BoxSizer(wx.HORIZONTAL)
591         fgs2 = wx.FlexGridSizer(1,2,9,175)
592         fgs2.Add(self.button,0, flag= wx.EXPAND)
593 
594         sizerh3.Add(fgs2, wx.EXPAND)
595         sizerv.Add(sizerh3, flag=
596         wx.ALIGN_CENTER|wx.CENTER|wx.TOP|wx.LEFT|wx.RIGHT, border=10)
597 
598         panel.SetSizer(sizerv)
599         panel.SetBackgroundColour('darkslategray')
600         self.draw_figure()
601 
602     def OnButton(self, e):
603         self.m = self.m_text.GetValue()
604         self.n1 = self.n1_text.GetValue()
605         self.n2 = self.n2_text.GetValue()
606         self.n3 = self.n3_text.GetValue()
607         self.n4 = self.n4_text.GetValue()
608         if self.n4 > covered_orig_diam:
609             self.n4 = covered_orig_diam
610             self.n4_text.SetValue(self.n4)
611         self.n5 = self.n5_text.GetValue()
612         self.refresh_figure()
613 
614     def refresh_figure(self):
615         self.draw_figure()
616 
617     def draw_figure(self):
618         simulated_vert = supershape(lo_horiz, lo_vert, wd_vert, ll_vert, ba_vert,
619                                     br_vert, self.m, self.n1, self.n2, self.n3)
620         ax = self.fig.add_subplot(111)
621         ax.clear()
622 
623         ax.set_ylabel("Force (N)")
624 
625         Low, High, Zero = maxmin_plot_lines()
626 
627         ax.grid(True)
```

```
628
629         xdata = linspace(0., 50.0, len(simulated_vert))
630
631         ax.axvline(x=mark_for_artery(covered_orig_diam/lower_oversize),
632                    linewidth=3., color='k')
633         ax.axvline(x=mark_for_artery(covered_orig_diam/upper_oversize),
634                    linewidth=3., color='k')
635 #
636 #          ax.axvline(x=low_line, linewidth=3., color='k')
637 #          ax.axvline(x=high_line, linewidth=3., color='k')
638         ax.axhspan(0.00, min_safe_force, facecolor='orange', alpha=0.7)
639         ax.axhspan(max_safe_force, max(simulated_vert)+.05, facecolor='orange',
640                    alpha=0.7)
641         ax.axvspan(0.0, low_line, facecolor='r', alpha=0.7,
642                    label = 'Danger Region')
643         ax.axvspan(high_line,100.0, facecolor='r', alpha=0.7)
644         ax.set_xlabel("Percent Area Reduction of Covered Stent (%)")
645         plottitle = "Simulated Force Profile of a Covered {}mm Stent".format(
646         covered_orig_diam)
647         if title_plot == 'yes':
648             ax.set_title(plottitle).set_y(1.02)
649             ax.legend()
650
651         print(max(simulated_vert), len(xdata), len(simulated_vert))
652         self.l, = ax.plot(xdata, simulated_vert, lw = 2.,
653                           label = 'Stent Force Profile')
654
655         Mark = mark_for_artery(self.n4)
656
657         yvalue = argmin(abs(array(xdata)-Mark))
658         yvalue = simulated_vert[yvalue]
659
660         Mark = compliance_for_artery(Mark, yvalue, self.n5)
661         finaldiam = sqrt(((pi*(covered_orig_diam/2)**2)*((100-Mark)/100))/pi)*2
662
663
664         oversize = ((covered_orig_diam/finaldiam)-1)*100
665         yvalue = argmin(abs(xdata-Mark))
666         yvalue = simulated_vert[yvalue]
667
668         self.l, = ax.plot(Mark,yvalue, marker = 'o', markersize = 9,
669                           markeredgewidth = 1.5, markerfacecolor = (1.0,1.0,0.0),
670                           markeredgecolor = 'k',
671                           label = 'Calculated Radial Force')
672
673         self.l.axes.set_xbound(lower=0.0, upper=50.001)
674         self.l.axes.set_ybound(lower=0.0, upper=max(simulated_vert)+.05)
675
676         print(yvalue, Mark)
677         ax.annotate('F = {0:.2f}N, AR = {1:.2f}% \n Oversize = {2:.2f}%'.format(
678         yvalue,Mark,oversize),
679                     ha = 'center', va = 'center',
680                     xytext = (max(xdata)*.806,max(simulated_vert)*.308),
```

```
                    xy = (Mark,yvalue), size = 10,
                    arrowprops = {'facecolor' : 'black', 'arrowstyle' : '->'},
                    bbox = {'facecolor' : 'w', 'edgecolor' : 'k',
                            'boxstyle' : 'square', 'alpha' : '0.5'})
        red_patch = mpatches.Patch(color='r', alpha=0.7,
                                   label='Existing Danger Region')
        orange_patch = mpatches.Patch(color='orange', alpha=0.7,
                                      label='Updated Danger Region')
        circ1 = Line2D([0], [0], linestyle="-", lw = 2., c='b')
        circ2 = Line2D([0], [0], linestyle="none", marker = 'o', markersize = 9,
                       markeredgewidth = 1.5, markerfacecolor = (1.0,1.0,0.0),
                       markeredgecolor = 'k')
        ax.legend((red_patch, orange_patch, circ1, circ2),
                  ('Existing Danger Region',
                  'Additional New Danger Region','Stent Force Profile',
                  'Calculated Radial Force'),
                  numpoints=1,loc = 'upper left',prop={'size':10})

        startx, endx = ax.get_xlim()
        ax.xaxis.set_ticks(arange(startx, endx+0.0001, 10.0))

        starty, endy = ax.get_ylim()
        ax.yaxis.set_ticks(arange(starty, endy+0.0001, 0.25))

        ax.minorticks_on()

        ax.grid(b=True, which='major', axis='both', alpha=1.0)
        ax.grid(b=True, which='minor', axis='both', alpha=0.2)

        self.fig.canvas.draw()
        self.fig.savefig('pics/simulation.png', format='png', dpi=1000)

num_of_factors = 5
factors_dict = {'factor0': wirediam_dict,
                'factor1': leglength_dict,
                'factor2': bendangle_dict,
                'factor3': bendrad_dict,
                'factor4': labonly_dict}
                #calculate polynomial
#load file that gives the values for altered characteristics
factor_values = loadtxt('Altered Dimentions horiz.txt', skiprows=1)
wd_factor_values = factor_values[:,0]
ll_factor_values = factor_values[:,1]
ba_factor_values = factor_values[:,2]
br_factor_values = factor_values[:,3]

#This section decides whether data
if use_saved_input != 'yes':
    saved_input = []

    minhorizlen = []
    #iterate through different characteristics
    for k in range(num_of_factors):
```

```
734
735         print ""
736         print "FILE SET #{}".format(k+1)
737
738         vertical = []
739         horizontal = []
740         horizontalsingle = []
741         verticalsingle = []
742
743         Graph_type = factors_dict['factor'+str(k)]
744
745         legendtitle,legendnames,xaxislabel,yaxislabel,plottitle,
746         plotnumber = plottype(Graph_type)
747         orig_diams = orig_type(Graph_type)
748         print(orig_diams)
749         dict = Graph_type
750
751         temp_pos_change = []
752         temp_horiz = []
753         iteration_size = []
754         current_temp = []
755         summed_vert = []
756         summed_vert_second = []
757         averaged_vert = []
758         averaged_vert_second = []
759         hands = []
760         labs = []
761         xomaxfinal = 0
762
763         #iterate through +- of each characteristic
764         for j in range(plotnumber):
765             temp = dict['loadfiles_trial'+str(j)]
766
767             print ""
768             print "dataset #{}".format(j+1)
769
770             #taking in each file for a specific + or - of each
771             #characteristic and averaging and manipulating them
772             horizontalsingle, verticalsingle = data_manipulation(temp, j,
773                                                                  orig_diams)
774
775             if k == 0 & j == 0 :
776                 minhorizlen = horizontalsingle
777
778             elif len(horizontalsingle) > len(minhorizlen):
779                 minhorizlen = horizontalsingle
780
781             if len(saved_input) == 0:
782                     saved_input.append(verticalsingle)
783                     vertical.append(verticalsingle)
784                     horizontal.append(verticalsingle)
785
786             else:
```

```
787                 if len(verticalsingle) >= len(saved_input[j-1]):
788                     shapetemp = shape(saved_input)
789                     shapetempx = shapetemp[0]+1
790                     shapetempy = len(verticalsingle)
791                     summed_vert_temp = zeros((shapetempx, shapetempy))
792                     summed_vert_temp[:shapetemp[0],:shapetemp[1]] = saved_input
793                     summed_vert_temp[shapetemp[0]] = verticalsingle
794                     saved_input = summed_vert_temp
795                     vertical = summed_vert_temp
796                     horizontal = summed_vert_temp
797 
798                 else:
799                     shapetemp = shape(saved_input)
800                     verticalsingle = array(verticalsingle)
801                     verticalsingle.resize(len(saved_input[j-1]))
802                     shapetempx = shapetemp[0]+1
803                     shapetempy = shapetemp[1]
804                     summed_vert_temp = zeros((shapetempx, shapetempy))
805                     summed_vert_temp[:shapetemp[0],:shapetemp[1]] = saved_input
806                     summed_vert_temp[shapetemp[0]] = verticalsingle
807                     saved_input = summed_vert_temp
808                     vertical = summed_vert_temp
809                     horizontal = summed_vert_temp
810 
811             print(shape(saved_input))
812 
813         if Graph_type == wirediam_dict:
814             wd_vert = vertical[-3::]
815             wd_horiz = horizontal[-3::]
816             print(shape(wd_vert))
817 
818         if Graph_type == leglength_dict:
819             ll_vert = vertical[-3::]
820             ll_horiz = horizontal[-3::]
821 
822         if Graph_type == bendangle_dict:
823             ba_vert = vertical[-3::]
824             ba_horiz = horizontal[-3::]
825 
826         if Graph_type == bendrad_dict:
827             br_vert = vertical[-3::]
828             br_horiz = horizontal[-3::]
829 
830         if Graph_type == labonly_dict:
831             lo_vert = vertical[-3::]
832             lo_horiz = horizontal[-3::]
833 
834     print(len(minhorizlen))
835     shapetemp = shape(saved_input)
836     shapetempx = shapetemp[0]+1
837     shapetempy = len(minhorizlen)
838     summed_vert_temp = zeros((shapetempx, shapetempy))
839     summed_vert_temp[:(shapetemp[0]),:shapetemp[1]] = saved_input
```

```
840     summed_vert_temp[shapetemp[0]] = minhorizlen
841     saved_input = summed_vert_temp
842 
843     saved_input = zip(*saved_input)
844 
845     savetxt('savedinputhoriz.txt', zip(*saved_input), delimiter=" ", fmt='%5.5f')
846 
847 else:
848     saved_input_data = transpose(loadtxt('savedinputhoriz.txt'))
849     wd_vert = [saved_input_data[:,i] for i in range(3)]
850     ll_vert = [saved_input_data[:,3+i] for i in range(3)]
851     ba_vert = [saved_input_data[:,6+i] for i in range(3)]
852     br_vert = [saved_input_data[:,9+i] for i in range(3)]
853 
854     lo_vert = saved_input_data[:,12][::-1]
855     lo_horiz = saved_input_data[:,13]
856 
857 app = wx.PySimpleApp()
858 top = SuperShapeFrame(None, -1, 'SuperShape')
859 
860 top.Show()
861 app.MainLoop()
```